creative commons
COMMONS DEED

저작자표시-비영리-변경금지 2.0 대한민국

이용자는 아래의 조건을 따르는 경우에 한하여 자유롭게

- 이 저작물을 복제, 배포, 전송, 전시, 공연 및 방송할 수 있습니다.

다음과 같은 조건을 따라야 합니다:

저작자표시. 귀하는 원저작자를 표시하여야 합니다.

비영리. 귀하는 이 저작물을 영리 목적으로 이용할 수 없습니다.

변경금지. 귀하는 이 저작물을 개작, 변형 또는 가공할 수 없습니다.

- 귀하는, 이 저작물의 재이용이나 배포의 경우, 이 저작물에 적용된 이용허락조건을 명확하게 나타내어야 합니다.
- 저작권자로부터 별도의 허가를 받으면 이러한 조건들은 적용되지 않습니다.

저작권법에 따른 이용자의 권리는 위의 내용에 의하여 영향을 받지 않습니다.

이것은 이용허락규약(Legal Code)을 이해하기 쉽게 요약한 것입니다.

Disclaimer

dCollection

공학박사학위논문

수치해석 기법을 이용한 가솔린 엔진에서 난류 유동이 연소의 사이클 편차에 미치는 영향에 대한 연구

The Effect of Turbulent Flow on the Combustion Cyclic Variation in a Spark Ignition Engine using Large-Eddy Simulation

2020 년 8 월

서울대학교 대학원

기계항공공학부

고 인 석

수치해석 기법을 이용한 가솔린 엔진에서 난류 유동이 연소의 사이클 편차에 미치는 영향에 대한 연구

The Effect of Turbulent Flow on the Cyclic Variation in a Spark Ignition Engine using Large-Eddy Simulation

지도교수 민 경 덕

이 논문을 공학박사 학위논문으로 제출함

2020 년 4 월

서울대학교 대학원

기계항공공학부

고 인 석

고인석의 공학박사 학위논문을 인준함

2020 년 6 월

위 원 장 : 송 한 호 (인)

부위원장 : 민 경 덕 (인)

위 원 : 도 형 록 (인)

위 원 : 이 복 직 (인)

위 원 : 최 회 명 (인)

Abstract

The Effect of Turbulent Flow on the Combustion Cyclic Variation in a Spark Ignition Engine using Large-Eddy Simulation

Insuk Ko

Department of Mechanical and Aerospace Engineering
The Graduate School
Seoul National University

At the present, the problem of worldwide air pollution has emerged as an important issue and many countries are trying to solve the problem. Emission regulations have been tightened around the world in an effort to reduce emissions from internal combustion engine (ICE) vehicles. From 2014, Tier 3 emissions standards in the United States (U.S.) and EURO6 regulations in the European Union (EU) are adopted. Currently, CO2 is also being strongly enforced annually. To meet the tightened CO2 regulations, the development of high efficiency engines is actively being carried out by each vehicle manufacturer. In the development of high efficiency engines, the key point is the increase in thermal efficiency. Many technologies have been developed to increase thermal efficiency and are being applied to mass-production engines. However, there is currently a cycle-to-cycle variation (CCV) of combustion as

the biggest obstacle to engine development. Therefore, research on the CCV is also being actively carried out. Because the causes that affect the cycle deviation are various and complex, it is difficult to conduct detailed research on the source of the CCV through experimental studies. Therefore, the 3D simulation is actively carried out as an alternative.

In the present study, the CCV phenomenon of combustion was reproduced using large-eddy simulation (LES) approach and the investigation on the source of CCV are conducted. Currently, the engine simulation using LES is immature. Therefore, it is necessary to consider each sub-model for accurate simulation. First, three Sub-grid scale (SGS) turbulence models were evaluated with particle image velocimetry (PIV) data from the single-cylinder transparent combustion chamber (TCC-III) engine. The dynamic structure model (DSM) was adopted for this study, based on the analysis of the flow field and the predicted SGS turbulent velocity compared to the PIV data.

Secondly, the G-equation was employed as a combustion model. The model can be used in the corrugated flamelets regime and the thin reaction flamelets regime. The turbulent burning velocity of the model is quite complicated to simulate the turbulent flame included in the two regimes. Therefore, in this study, the combustion regime of the target engine operating condition was found by using Reynolds averaged navier-stokes equation (RANS) approach and was identified to the corrugated flamelets regime. Thus, the G-equation was modified for the corrugated flamelets regime.

Thirdly, an ignition model reflecting the characteristics of LES was developed. The lagrangian particles were employed to realize the ignition channel and the secondary electric circuit model was implemented to predict the spark energy, restrikes phenomena and the end of ignition time. The one of the key features of the ignition model developed in this study is that a

simplified empirical function is implemented to realize the thermal diffusion during arc phase. After ignition phase, the channel grows by chemical reaction and the flame propagation progresses. The turbulent flame brush thickness term is introduced to predict the transition state between the laminar flame propagation and the turbulent flame propagation. Finally, when the channel is grown sufficiently, flame is propagated in the 3D field by the G-equation

Finally, 30 LES cycles were performed to identify the cause of the CCV and validated against the experimental data. The sources of the CCV are mainly from the small scale turbulent flow and the large scale turbulent flow. The small scale turbulent flow effect was investigated and the fact that the small scale turbulent flow is related to the tumble motion is identified. In terms of the large scale turbulent flow, the effect of the local vortex on the flame propagation was found through the detailed analysis of the flow field. In particular, the vortex produced by wall flow on the secondary tumble plane is an important factor. A new piston shape was designed to strengthen the vortex formation by wall flow. The result of new piston case shows the reduced combustion CCV than the base case. This research provides the guide how to investigate the sources of the combustion CCV and how to reduce the combustion CCV for the future engine development

Keywords: SI engine, LES, CFD (Computational Fluid Dynamics), CCV (Cycle-to-cycle variation), Ignition model, SGS model

Student Number: 2013-20641

Contents

List of Figures

List of Tables

Nomenclature

Acronyms

AKTIM	the arc and kernel tracking ignition model
ALE	arbitrary lagrangian-eulerian
AMR	adaptive mesh refinement
ASI	arbitrary sliding interface
BDC	bottom dead center
BEV	battery electric vehicle
BML	Bray-Moss-Libby
CA	crank angle
CARB	California air resources board
CCV	cycle-to-cycle variation
CFD	computational fluid dynamics
CFL	Courant-Friedrichs-Lewy
CFM	coherent flame model
COV	coefficient of covariation
CSD	circular standard deviation
DI	direct injection
DNS	direct numerical simulation
DPFI	dual-port fuel injection
DPIK	the discrete particle ignition kernel model
DSM	dynamic structure model
EBU	eddy-break-up
ECFM	the extended coherent flame model
EDM	eddy dissipation model
EGR	exhaust gas recirculation

EPA	environmental protection agency
FAS	fleet average system
FEV	hybrid electric vehicle
FSD	flame surface density
FTP	federal test procedure
HEV	hybrid electric vehicle
ICE	internal combustion engine
ISSIM-LES	the imposed stretch spark ignition model for LES
LCA	life cycle assessment
LEM	linear eddy model
LES	large-eddy simulation
MARS	monotone advection and reconstruction scheme
MFB	mass burned fraction
MUSCL	monotonic upstream-centered scheme for conservation laws
NA	naturally aspirated
NEDC	new European driving cycle
nIMEP	indicated mean effective pressure
NMOG	non-methane organic gas
PDF	probability density function
PISO	pressure implicit with splitting of operator
PIV	particle image velocimetry
PRF	primary reference fuel
RANS	Reynolds averaged navier-stokes equation
RCM	rapid compression machine
RED	real driving emissions
RMSd	root-mean-square deviation
rpm	revolution per minute
SGS	sub-grid scale
SI	spark ignition

SparkCIMM	the spark-channel ignition monitoring model
TCC	transparent combustion chamber
TRF	toluene reference fuel
U.S.	the United States
WLTC	worldwide harmonized light-duty vehicles test cycles

Chapter 1. Introduction

1.1 Background and Motivation

At the present, the problem of worldwide air pollution has emerged as an important issue and many countries are trying to solve the problem. There are lots of man-made air pollutant sources including power station, manufacturing facilities, waste incinerators, agriculture, food as well as transportation. In the transportation system, the internal combustion engine (ICE) equipped vehicles are considered to be a major source of air pollution. Therefore, emission regulations have been tightened around the world in an effort to reduce emissions from ICE vehicles.

In 1973, the United States (U.S.) firstly adopted Tier 0 standards for railroad locomotives and locomotive engines fueled by diesel and by other fuels. The emission regulations have become stricter and Tier 3 emissions standards from the U.S. Environmental Protection Agency (EPA) were adopted in March 2014 and have been enforced from 2017 to 2025. In European Union, the first EURO1 regulations were introduced in 1992, and currently EURO6 regulation has been effective. In 2009, Republic of Korea adopted California Air Resources Board (CARB)'s non-methane organic gas (NMOG) fleet average system (FAS) for gasoline-fueled vehicles. Currently, K-LEV III standards have been enforced. To assess the emission levels of vehicle engines and fuel economy in passenger cars, the New European Driving Cycle (NEDC) and the EPA Federal Test Procedure (FTP) were introduced in European Union and the U.S., respectively. From 2017, the NEDC was replaced with the worldwide harmonized light-duty vehicles test cycles (WLTC) for all types of vehicles. There is a difference between the driving mode and the driving

conditions of the actual road. To evaluate these differences, the real driving emissions (RDE) test has been introduced to reflect the real road conditions. As above, regulations on emissions are being tightened in countries around the world. According to the U.S. EPA, CO2 emissions from the transportation sector in the U.S. account for 28 percent of the total industrial sector in 2018 [1]. Therefore, the European Union regulates CO2 emissions, reducing by about 27% from 130g/km in 2015 to 95g/km by 2021 as shown in Figure 1.1 [2]. Furthermore, the regulations on CO2 emissions will be greatly tightened by 2030, down about 37.5 percent to 59g/km. In the U.S., the regulations on CO2 emissions reduction were eased to 89g/km by 2025, 102.5g/km by 2026. The U.S. had previously planned to impose very strict regulations on CO2 emissions of 89 g/km by 2025. However, in March 2020, the government announced eased the regulations to limit CO2 emissions to 102.5g/km by 2026, reflecting more practical difficulties. Republic of Korea has regulated the amount of CO2 emissions from 140g/km in 2015 to 97g/km in 2020, which is about 31% tightened. Due to the tightened CO2 regulations, many car manufacturers are putting a lot of effort into developing eco-friendly internal combustion engines to meet the future regulations.

In addition, there has been lots of effort to develop the alternative powertrains such as the battery electric vehicle (BEV), the fuel cell electric vehicle (FEV) and the hybrid electric vehicle (HEV). Thus, many outlooks have predicted that the market sharer of the ICE would be diminished. In the past, the tank-to-wheel emissions have been mainly dealt, but recently the importance of well-to-wheel emissions have emerged through the life cycle assessment (LCA). In Figure 1.2, the well-to-wheel CO2 emission from the BEV and the ICE obtained through the LCA is shown. Depending on the energy source, the CO2 emissions of the BEV are in a wide range of approximately 50 to 170g/km. The reason is that the well-to-tank CO2

emissions of the BEV is very dependent on the generation system of electricity. The CO2 emissions of the conventional ICEs such as natural gas, diesel and gasoline are about 125-160g/km, which is higher than the BEV. However, if the ICEs are hybridized, the HEV's CO2 emissions are approximately 105 to 125g/km, which is equivalent to the BEV. The market share prediction in 2025 in major markets is shown in Figure 1.3. The market share of conventional ICEs is very small, but the increase in the HEVs is a noticeable. Since the HEVs are equipped with the ICE, the ICEs is still considered as the mainstream of the vehicle market. Therefore, continuous research on the ICE engines is needed.

The ICE converts the chemical energy of hydrocarbon fuel into the thermal energy by combustion, and thereby into the mechanical energy by the reciprocating piston movement, of which the latter efficiency is called thermal efficiency [3]. The increase of the thermal efficiency plays a key role to reduce CO2 emissions. Through the Otto cycle, theoretical maximum thermal efficiency can be obtained as equation (1.1). The thermal efficiency is a function of the compression ratio and the specific heat ratio. The higher the compression ratio and the lower the specific heat ratio, the greater the thermal efficiency. To lower the specific heat ratio, lowering the equivalence ratio is mainly adopted. However, the higher the compression ratio, the more vulnerable it becomes to knocking, and the lower the equivalence ratio, the lower the combustion stability. Therefore, many technologies are being introduced to overcome these problems. For instances, the downsized engine with the direct injection (DI) and the turbocharging system to achieve the utilization of the sweet spots and the high compression ratio and the burn engines, which reduce pumping loss and lowers the specific heat ratio to increase the thermal efficiency. The direction of the engine development is in

line with the method of increasing the thermal efficiency in the Otto cycle, which is the theoretical thermal efficiency.

$$\eta = 1 - \frac{1}{r_c^{k-1}} \tag{1.1}$$

Where, η: thermal efficiency

r_c: compression ratio

k: specific heat ratio

There is a major obstacle which is a cycle-to-cycle variation (CCV) phenomena to the development of the spark ignition (SI) engine to improve efficiency using these latest technologies. Generally, engine studies develop using the average of several cycles as a representative value. However, the actual engine operation shows different behavior for each cycle, called the CCV as shown in Figure 1.4. As shown in Figure 1.4, combustion is a behavior within a large range, largely up and down, and the larger this range results in abnormal combustion and combustion instability. There are lots of causes of the CCV, coming from the external environment to inside the engine. For example, the external environments include conditions of ambient air, and internal sources of the CCV are revolution per minute (rpm) fluctuation, fuel injection, deviation of mechanical movement such as valves and pistons, etc. During the four strokes, the effects of each factors are intertwined, finally the combustion CCV occurs. Since the CCV is such a complex phenomenon, it is now considered an uncontrollable obstacle. However, many studies have begun in recent years, as a must-over for the future high-efficiency engine

development. Experimental studies [4-7], especially using a optical engine to reproduce the CCV and find the causes of it, have been carried out but the limitations of information make it difficult to identify the causes and assess the impact of the factors. Therefore, a lot of research have been conducted using 3D simulation.

In the 3D simulation, information on the factors that are difficult to measure in the experiment can be obtained, visualized and quantified. One of the most widely used techniques in the 3D simulation is Reynolds averaged navier-stokes equation (RANS) approach. RANS is a technique that simulates turbulence using averaging method, and there is a limit to the implementation of chaotic behavior of flow from the outside, one of the causes of the CCV. There is another turbulence model, called the large-eddy simulation, as a method to overcome these limitations. In LES, the large scales of turbulence which are larger than a LES filter size can be resolved, and the small turbulence scales which are smaller than the LES filter size is modeled. Due to the characteristic of resolving the large scale turbulence, it is possible to reproduce the randomness behavior of flow that is difficult in RANS. Thanks to these characteristics, research on the CCV phenomenon in the ICE using LES has been actively carried out [8-11]. Currently, however, LES research in the ICE community is still in its early stages, and a model study is still underway to implement physical phenomena during the combustion process based on LES. Therefore, the present study analyzes the causes of the CCV with LES based physical models, especially for the ignition and the combustion processes.

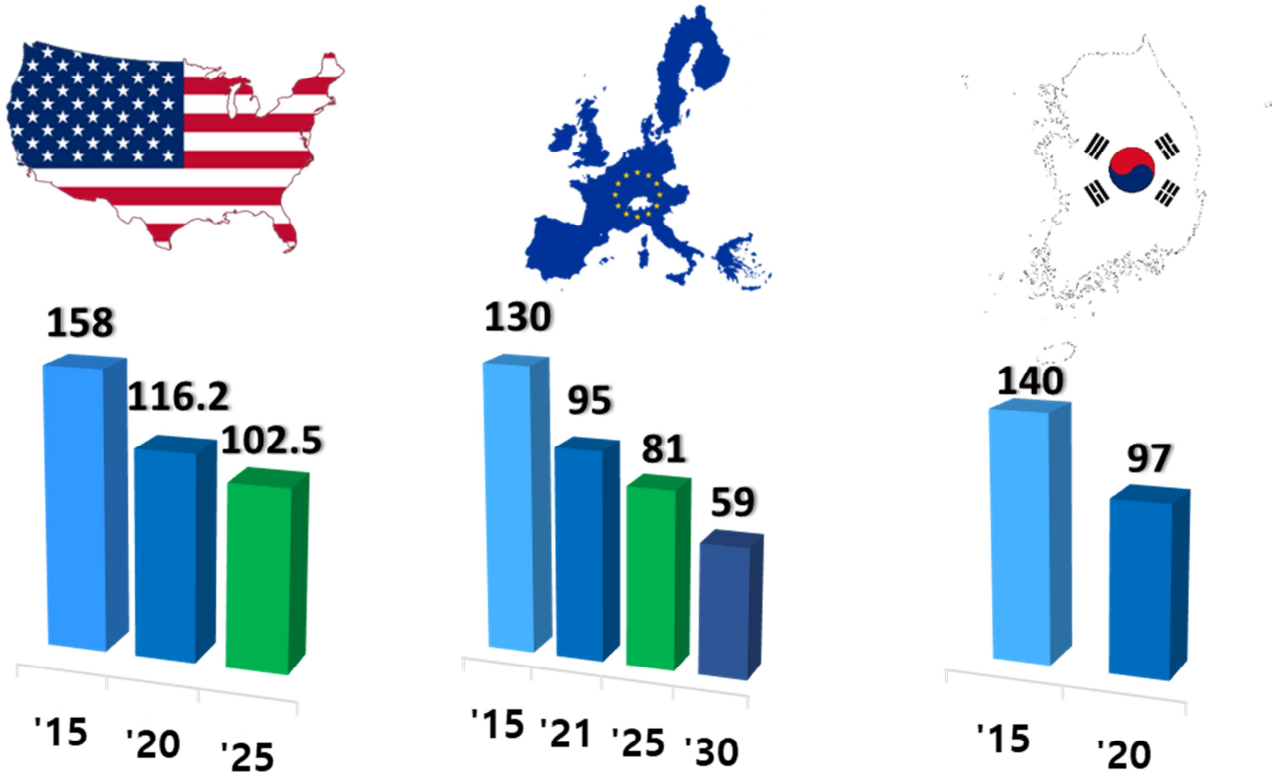

Figure 1.1 CO2 regulations in global markets [2]

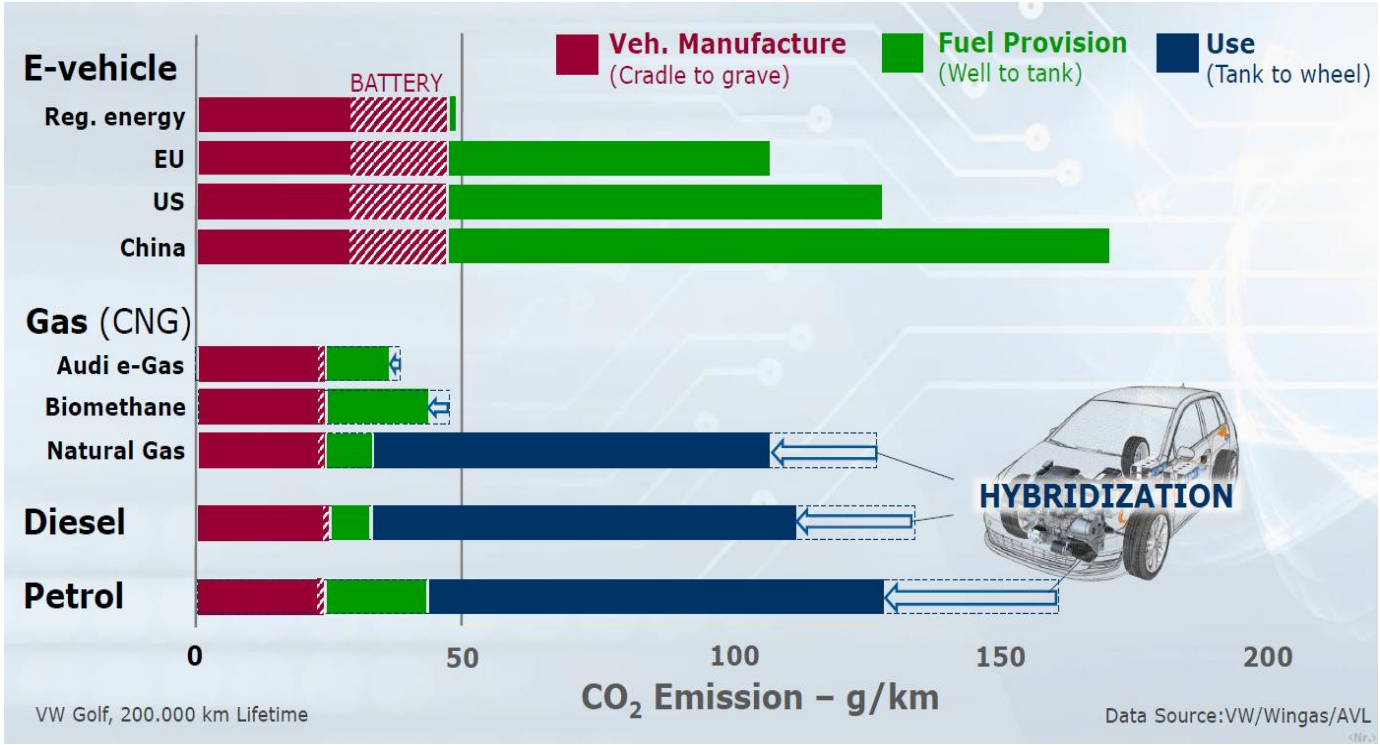

Figure 1.2 Life cycle assessment of CO2 emission from internal combustion engine vehicle and battery electric vehicle [2]

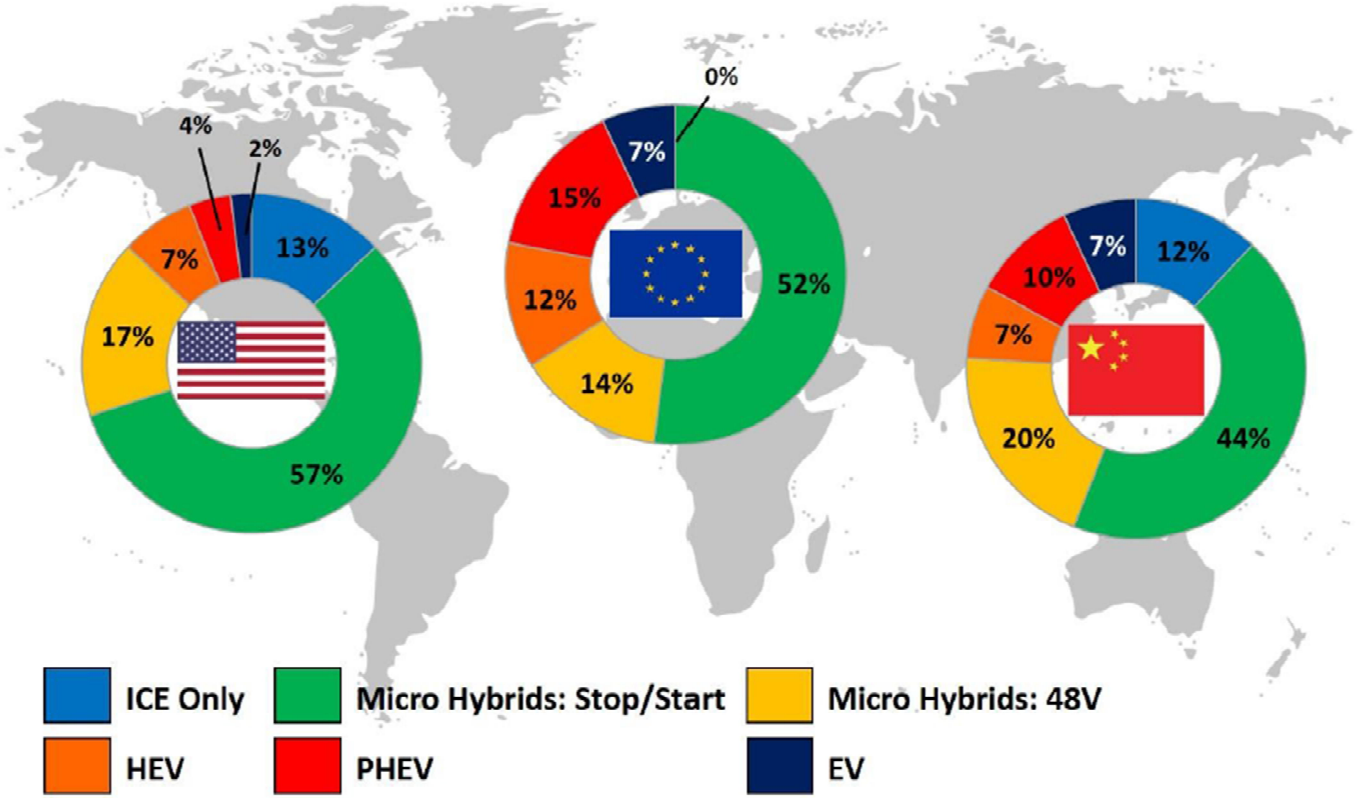

Figure 1.3 Outlook of future market share of powertrain types in 2025 [12]

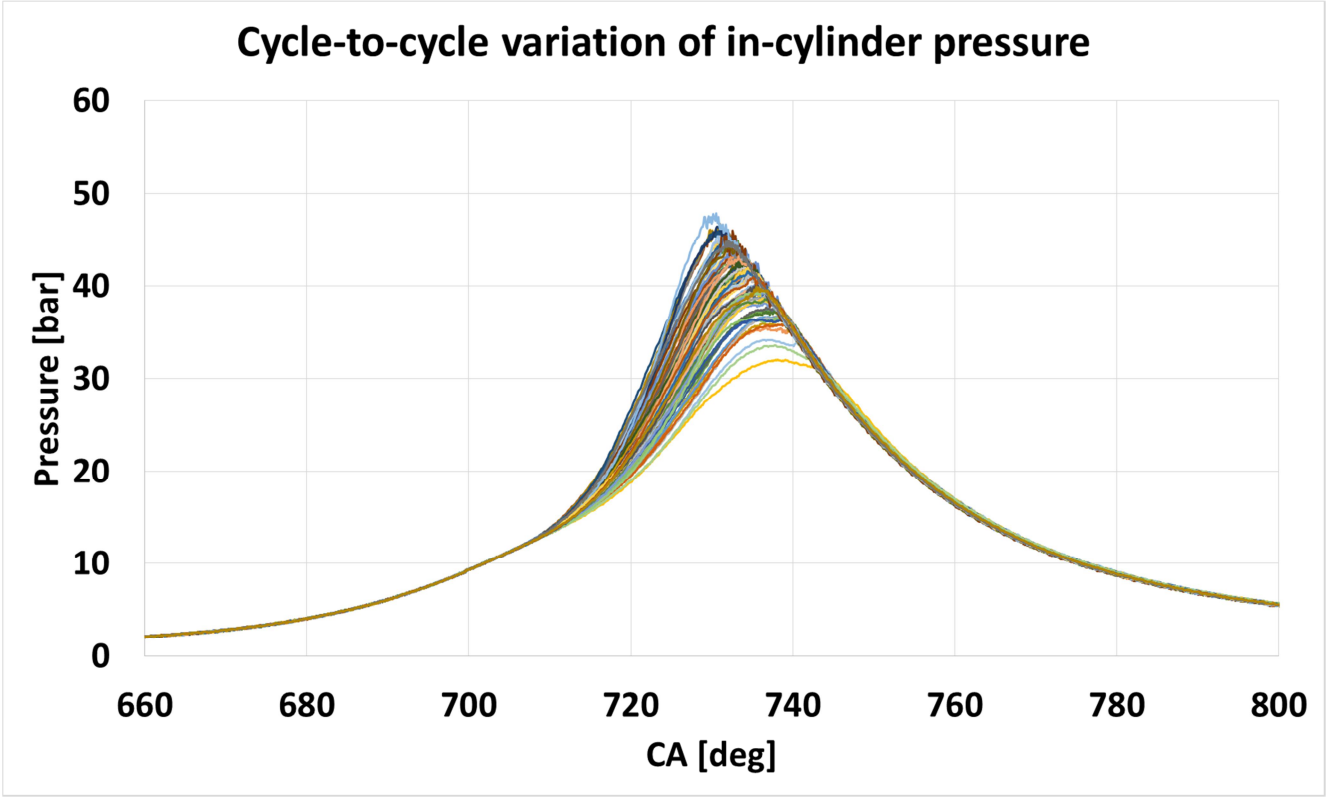

Figure 1.4 Cycle –to-cycle variation of in-cylinder pressure in a SI engine

1.2 Literature Review

1.2.1 Cycle-to-cycle variation in engine combustion

The combustion CCV in engines means different behavior in every cycle, not always reproducing the same combustion behavior, even under the same operating conditions. The combustion CCV is a major obstacle to the development of high-efficiency, high-performance engines, and many studies have been conducted recently. First of all, experimental studies have been conducted to analyze the combustion CCV using engine combustion deviations. Zervas [13] evaluated the coefficient of covariation (COV) of the beginning and the end of the combustion, and the mass fraction burnt (MFB) 50% to assess the combustion CCV. Huang et al. [14] investigated the exhaust gas recirculation (EGR) effect on the CCV in a SI engine fueled with natural gas-hydrogen blends. Chen et al. [15] conducted the statistical analysis to find correlations between combustion parameters, such as burning rate and knock, and COV of net indicated mean effective pressure (nIMEP) and peak pressure. However, in experimental studies, there is a lack of information on the correlation between factors affecting the CCV and difficulty in controlling the variables. Therefore, the 3D simulation research is drawing attention as an excellent method of study of the CCV research.

Among several turbulence modelling approaches in the 3D simulation, LES is widely used in an engine CCV research because of the advantage of being able to simulate the chaotic flow of the large turbulence. In the early stage of LES research in the ICE, studies on engine like geometries were conducted to verify the possibility of LES approach [16, 17]. Next, studies were conducted on the cyclic deviation of the flow in the engine through multi-

cycle analysis under the cold flow condition using LES. Enaux et al. [18] evaluated a numerical strategy including mesh movement and specific treatments of boundary conditions to realize the CCV in the ICE. Van Dam et al. [11] conducted multi-cycle LES of motored flow in an optical engine. The simulation result is compared against the particle image velocimetry (PIV) data. The author suggested that analysis of the circular standard deviation (CSD) is a promising method to identify critical points such as vortex centers or stagnation points which may be useful for engine designation. Angelberger et al. [19] found the correlation of CCV between the in-cylinder swirl ratio and the polar velocity profile in the valve seat region using LES and the PIV results. Early studies were mainly conducted to successfully simulate the flow CCV using LES and comparing it with the PIV results.

Next to the studies of the flow CCV, Goryntsev et al. [9] conducted a study on the flow CCV on the fuel-air mixing in a direct injection engine that is important for combustion. Several researches have been conducted to reproduce the combustion CCV in SI engines [10, 20-24]. Fontanesi et al. evaluated the boundary condition effect on the combustion CCV in a SI engine. The authors compared the CCV result of cycle-specific boundary condition from experiment and that of cycle constant boundary condition from the 1D simulation. It was found that the impact of the boundary condition on the CCV is modest. Gharderi et al. [25] conducted the study on the assumption that the rpm and the flow of ignition timing had a great effect on the combustion CCV and evaluated its influence. Fontanesi et al. [8] reproduce the combustion CCV and knock in a SI engine. Fontanesi et al. [26] assessed the effect of the spark plug location and direction on the combustion CCV and knock phenomena. Robert et al. [27] evaluate the effect of spark timing on the combustion CCV and knock with experimental data. Chen et al. [28] found the correlation between knock intensity and, combustion phase and peak pressure. In LES

research on the CCV, multi-cycle simulation must be conducted, so high computational costs are required. There are some researches [29, 30] focusing on reduction of computational cost using parallel perturbation methodology. This method implements the CCV by imposing perturbation at the initial conditions, allowing multiple cycles to be carried out simultaneously in parallel rather than consecutive cycle simulations. Researches on the CCV using LES have mainly shown the potential for the CCV reproduction and analyzed the causes of the CCV through statistical analysis. However, since research on LES-based physical models is still in its infancy, there is a limit to the lack of consideration for models.

1.2.2 Turbulence Modeling

Turbulent flow represents to irregular random flow movements depending on the time and the space of large and small eddies. Thanks to this movement of randomness, it is characterized by active transport and mixing of fluid compared to laminar flow. This is particularly important in combustion phenomenon, and a turbulence model that can be accurately predicted in computational fluid dynamics (CFD) is very important. There are three main ways to simulate turbulence in the CFD: Reynolds averaged navier-stokes equation, large-eddy simulation and direct numerical simulation (DNS) as shown in Figure 1.5. Characteristic of each methods is that RANS simulates all turbulence length scales through modeling [31] and the calculation is very fast, but the accuracy is relatively lower than other methods. DNS is the high fidelity method to resolve all turbulence length scales, as opposed to RANS. The disadvantage is that a grid size of simulation domain must be smaller than the Kolmogorov scale to resolve all turbulence scales, so it is the most accurate,

but due to calculation cost, DNS is not applicable to engineering application. LES is a method that utilizes the advantages and complements the disadvantages of these two methods, LES predicts the turbulence length scales smaller than a certain size (filter) through a sub-grid scale (SGS) model, and turbulence scales larger than the filter size are resolved. Thus, LES is an appropriate modeling approach that can reduce calculation time while simultaneously reproduce the randomness of turbulence flow. Because of these characteristics, the turbulence modeling method using LES is suitable for the CCV study of engines.

The turbulence model of LES is called the SGS model, and there are the zero-equation and the one-equation models. The first SGS model was introduced in 1963 by Smagorinsky [32]. The Smagorinsky model is a representative zero-equation model and adopts the eddy-viscosity hypothesis to predict the SGS turbulence viscosity. Fundamental studies using the Smagorinsky model have suggested model coefficients for various condition [33-37]. However, the model has a drawback to predict turbulence in strong transient condition because a constant value of the SGS model coefficient is used. There is a method of dynamically calculating the SGS model coefficient locally using double filters introduced by Germano to overcome the drawback of the Smagorinsky model [38]. This model uses dynamic coefficients, reflecting local characteristics so that non-steady flows can be better predicted than the conventional Smagorinsky model.

The one-equation model improves the accuracy of prediction of the SGS turbulence terms by adding a transport equation for the SGS kinetic energy. The transport equation has a SGS turbulent kinetic energy budget which is available for the formulation of the SHS models. Therefore, the use of the transport equation for the SGS turbulent kinetic energy makes it possible to use

relatively coarser grids compared to the zero-equation model. The one-equation was derived by Yoshizawa [39] and by Yoshizawa and Horiuti [40], on the basis of the Kraichnan's direct-interaction approximation [41]. In 1992, Wong first introduced the dynamic modeling approach to the one-equation model [42]. The transportation equation is defined by the source and sink terms that require dynamic model coefficient. Ghosal et al. [43] proposed the advanced dynamic one-equation model to calculate the dynamic model coefficient using a iterative method. However, there is a problem that the iterative solution do not always converge and scaling issues that the dynamic modeling approach depends on are not considered. To overcome the problem, the dynamic structure model (DSM) has been introduced by Pomraning [44]. This is the one-equation non-viscosity dynamic model which estimates the stress tensor directly instead of modeling the stress tensor with the SGS viscosity. The transportation equation for the SGS turbulent kinetic energy is added to give the energy flow of the SGS turbulent kinetic energy between the resolved and the sub-grid scales.

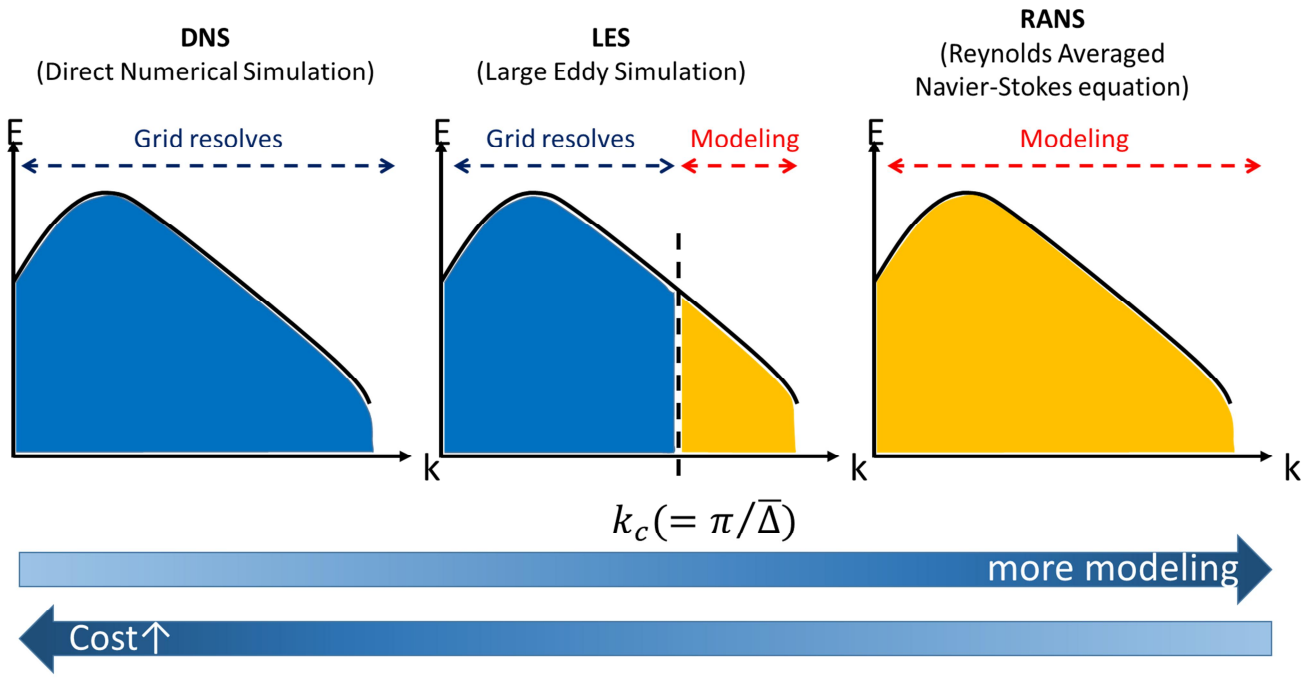

Figure 1.5 Three main ways to simulate turbulence in computational fluid dynamics: RANS, LES and DNS

1.2.3 Combustion Modeling

Combustion is a phenomenon in which flames are propagated in chemical reactions of fuel and air mixtures. In order to realize combustion with flow, an additional scalar reaction equation (equation. (1.2)) is needed to calculate chemical reactions and their source terms. In turbulent combustion, there is a closure problem to solve the scalar reaction equation, because chemical reactions which are complex non-linear function of chemical species are strongly coupled with turbulent fluid dynamics. Therefore, the main objective of turbulent combustion modelling is to close the problem with appropriate assumptions in order to reproduce turbulent combustion phenomenon [45].

$$\rho \frac{\partial \psi_i}{\partial t} + \rho v \cdot \nabla \psi_i = \nabla \cdot (\rho D_i \nabla \psi_i) + \omega_i \qquad (1.2)$$

Where ω_i: chemical source term.

Spalding [46] attempted to solve the closure problem of chemical source term. The author assumed that turbulent mixing is a cascade process from the integral length scales to the molecular scales and therefore the cascade process also controls chemical reactions. This model is called the Eddy-break-up (EBU) model. The turbulent mean reaction rate of products is related with the variance of the product mass fraction and the EBU model constant. Magnussen and Hjertager [47] have modified the EBU model by replacing the variance of the product mass fraction to the mean mass fraction of the deficient species, so called the Eddy dissipation model (EDM). The model requires at least three rates defined with the mean fuel mass fraction, the mean oxidizer mass fraction and the product mass fraction in order to calculate the mean chemical source term. The main idea of these two models is to replace the chemical time by the

turbulent time scale. The model is based on the fast chemistry limit without the influence of the chemical kinetics. The model constant for the EBU or the EDM must be tuned for a particular combustion condition. However, since the models assume the fast chemistry and the chemical equilibrium [48], the models overestimate the reaction rate in certain situations.

Another approach based on statistics was introduced by Pope [49]. The model adopts a probability density function (PDF) transport equation for the velocity and the reactive scalars formulated for one-point statistics. The early model uses only the joint pdf equation of velocity, viscous dissipation and reactive scalars which does not include scalar gradients and therefore it does not include information about the mixing time scale. Therefore, Dopazo [50] propose a transport equation for the joint statistic of velocity, velocity gradient, reactive scalars and their gradients. In addition to the closure of chemical source term, it describes the straining and rotation of scalar gradients, the properties are considered necessary in turbulent reacting flows. In the slow chemistry condition, Hulek and Lindstedt [51] showed a very good agreement with experimental data using the joint scalar-velocity approach. However, in the fast chemistry, molecular mixing and chemical reaction arise in thin layers where the molecular transport and the chemical source term balance each other. Therefore, the molecular mixing term and the chemical source term are closely related to each other. However, from a numerical point of view, the pdf transport equation is not attractive because its requirement of memory increase approximately exponentially with dimensionality in finite volume and finite-difference techniques. To overcome the memory problem, Monte-Carlo method which adopts the lagrangian algorithm was introduced [52, 53]. But this method is suffered from a statistical error with the small number of lagrangian particles.

The Linear Eddy Model (LEM) approach is also used to deal with a non-equilibrium chemistry in turbulent combustion. At first, it was developed for non-reacting flows by Kerstein [54-57] and was improved for reactive scalars by Kerstein [58]. This approach obtains an information of molecular mixing by simulating the molecular mixing on a one-dimensional domain. Two processes are conducted simultaneously to calculate the reactive scalars. In the first process, the evolution of the reactive scalar field is described in the one dimension. In the second process, a stochastic procedure of instantaneous, statistically independent "rearrangement events" is occurred. McMurtry et al. [59] applied the LEM to hydrogen-air combustion and Menon and Kerstein [60] used the LEM on the G-equation. However, there is a limitation on the LEM that the calculation of molecular mixing should be performed at the finest scales of turbulent flow in physical space, so that LES requires high computational cost.

The flamelet concept is widely used to reproduce the turbulent combustion phenomenon. The flamelets are defined as thin reactive-diffusive layers where are embedded in turbulent flow field. It assumes that the flame structure is infinitely thin and there is no intermediate temperature between unburnt mixture gas and burnt gas. The progress variable is introduced to separate unburnt mixture and burnt gas in a mixture field. The Bray-Moss-Libby (BML) model is one of the popular method in the flamlets approach [61]. This model adopts the progress variable as a scalar quantity which is normalized by temperature or product mass fraction. The transport equation for the progress variable is adopted instead of the reactive scalar transport equation. There is also closure problem in chemical source term. The chemical source term is modeled by the mean chemical reaction rate which is related to the un-stretched laminar burning velocity, a stretch factor and the crossing length scale which needs to be modeled [62, 63].

Alternative approach for the chemical source term is the Coherent flame model (CFM) which defines the chemical source term with the flame surface density. In the CFM, there is an additional transport equation for the flame surface density [64, 65]. Formulations of the CFM are discussed by Duclos [64].

More recently, the level-set approach using the non-reacting scalar G rather than the progress variable is widely adopted for premixed combustion. This model is called the G-equation. Since the G-equation adopts the non-reacting scalar G, there is no need to consider the complications related with closure problem of chemical source term. Because of this advantage, the present study adopts the G-equation model as a combustion model. So far, most combustion models have been developed as RANS base. In contrast to RANS approach which is modelling all turbulent scales, LES resolve the turbulent scales larger than the filter size and the smaller turbulence scales are modeled. Therefore, the existing combustion models have been re-developed to fit the characteristics of LES [66, 67]. The detailed information of the G-equation for LES will be described in Chapter 4.

1.3 Research Objective

Research on the CCV is essential in the development of high efficiency engines. LES approach has been spotlighted as a useful way to investigate the CCV. Therefore, nowadays a lot of researches using LES are actively underway, but it is still immature. Sub-models, such as spray model, ignition model, combustion model and etc., considering the characteristics of LES have been developed, but there are still lots of rooms to be developed in order to improve the accuracy of LES simulation on engine research. Apart from the accuracy of sub-models, many studies are currently underway to find the causes of the CCV, but so far there are lack of researches on how each causes is generated and how it affects the CCV. Therefore, this study consists of two main parts: development of highly accurate models, and analysis of the causes of the CCV and suggestion how to reduce the CCV. The detailed objectives are as followed:

1. Selection of the SGS turbulent model

    - LES with three SGS models are performed to evaluate the SGS model effect on in-cylinder flow under motored condition.

2. Development of ignition mode

    - The lagrangian ignition model for LES is developed.

3. Investigation of cycle-to-cycle variation

    - The cycle-to-cycle variation is reproduced using LES.

- Root of the cycle-to-cycle variation is investigated.

4. Suggestion to reduce the CCV
    - Provision of a guide on how to reduce the CCV using LES simulation of new designed hardware with reduced the CCV.

1.4 Structure of the Thesis

The present study consists of eight main chapter. In chapter 2, the evaluation of the SGS model effect under motored condition is described. The results of three SGS models are compared with PIV data, and finally one model is selected. In chapter 3, the modeling of gasoline surrogate fuel is introduced. In chapter 4, the flamelets regime in engine condition is investigated. A level-set method for the corrugated flamelets regime is described. In chapter 5, the lagrangian concept of ignition model for LES is introduced. At first, the model concept is described and the detailed description for each sub-model is illustrated. In chapter 6, the experimental and the numerical configuration for the target engine are introduced. In chapter 7, the multi-cycle LES simulation is performed and the CCV phenomenon is reproduced and validated against the measured data from the single-cylinder port fuel injection engine experiment. Investigation of source of the CCV is conducted to find the controllable cause. The way to reduce the CCV is introduced. Finally, the study closes with a summary and conclusions in chapter 8.

Chapter 2. Sub-grid Scale Turbulence Model

In this section, the theory of turbulent flow is described. From the point of LES, the SGS turbulence model and the grid size are very important factor to realize turbulence flow. Therefore, three SGS turbulence models are introduced and LES quality assessment to select the SGS turbulence model is introduced.

2.1 The Fundamentals of Turbulent Flow

2.1.1 The Energy Cascade

Turbulent flow is an unpredictable flow which is called the stochastic flow. The stochastic behavior of turbulent flow enhances the transport and mixes fluid much more effective than laminar flow. In the Pope' text book [68], the stochastic behavior is caused by 'eddy' which contains turbulence energy. Turbulent flow is composed of various size of eddies and the large eddy can contain the smaller eddies. Each eddies has a characteristic length ℓ, velocity $u(\ell)$ and timescale $\tau(\ell) \equiv \ell/u(\ell)$. In Figure 2.1, eddy sizes and ranges at high Reynolds number are shown [68]. $\mathcal{L}$ is the flow scale, ℓ_0 is the length scale of the largest eddy size which is comparable to the flow scale. ℓ_{EI} is the demarcation between the anisotropic large eddies in the energy-containing range and the isotropic small eddies in the universal equilibrium range, and it is estimated with $\ell_{EI} = \frac{1}{6}\ell_o$. ℓ_{DI} (with $\ell_{DI} = 60\eta$) is the demarcation between the inertial subrange and dissipation range in the universal equilibrium range. η is the characteristic length scale of the smallest turbulent

motions, called the Kolmogorov length scale. The Kolmogorov scale is defined from dissipation (ε) and viscosity (ν):

$$\eta \equiv \left(\frac{\nu^3}{\varepsilon}\right)^{1/4} \tag{2.1.1}$$

$$\tau_\eta \equiv \left(\frac{\nu}{\varepsilon}\right)^{1/2} \tag{2.1.2}$$

$$u_\eta \equiv (\nu\varepsilon)^{1/4} \tag{2.1.3}$$

The larger eddies are unstable and break up to the smaller eddies with transferring their energy. This process is continued until the eddy motion is stable and molecular viscosity is effective to dissipate the kinetic energy. This process is called the energy cascade and its schematic diagram is shown in Figure 2.2. The energy-containing range contains most of the energy and it is transferred to the smaller scales by the transfer rate $\mathcal{T}(\ell)$. The transfer rate is independent of ℓ in the inertial subrange as below.

$$\mathcal{T}_{EI} \equiv \mathcal{T}_{(\ell_{EI})} \equiv \mathcal{T}_{(\ell)} \equiv \mathcal{T}_{DI} \equiv \mathcal{T}_{(\ell_{DI})} \equiv \varepsilon \tag{2.1.4}$$

Hence, the energy is transferred from the large scales to the small scales by the constant rate of the dissipation rate ε.

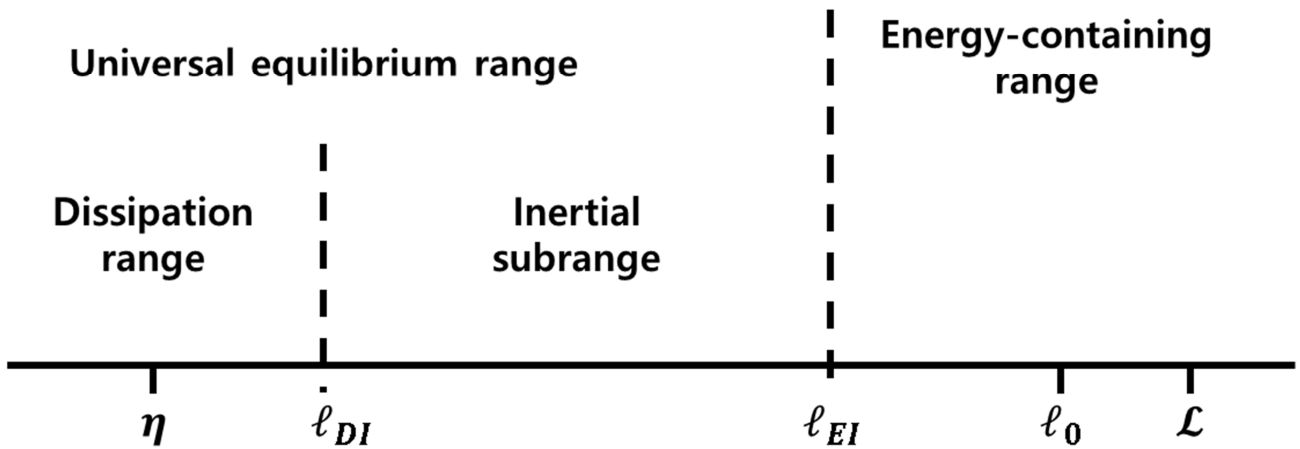

Figure 2.1 Eddy sizes at very high Reynolds number, showing the various length scales and ranges [68]

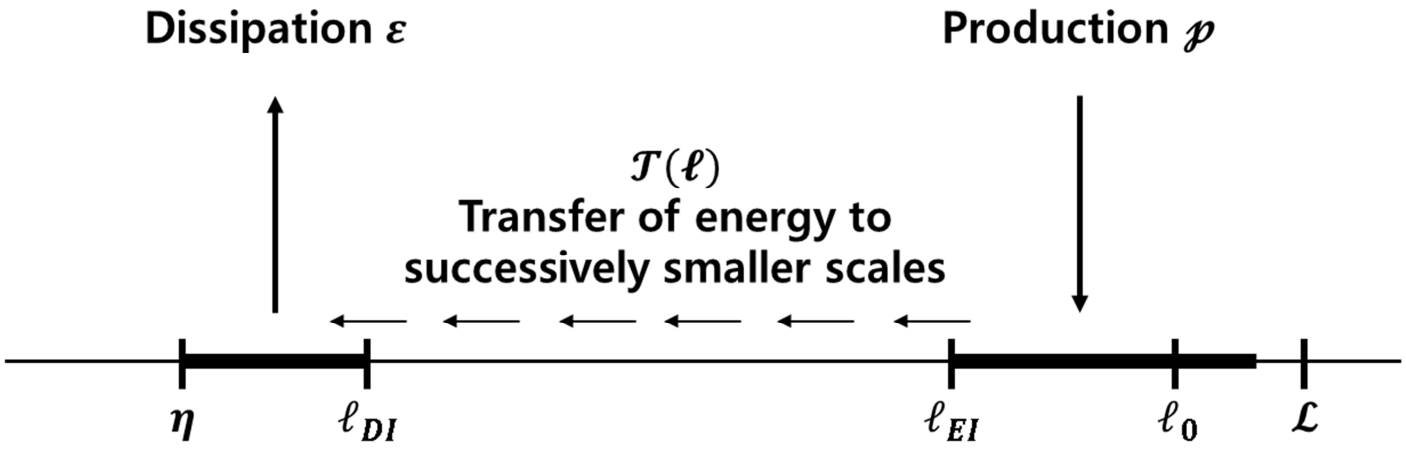

Figure 2.2 A Schematic diagram of the energy cascade at very high Reynolds number [68]

2.1.2 The Energy Spectrum

Turbulent flow is composed of different scales of eddy and the turbulent kinetic energy is distributed among the different scales [68]. In the Kolmogorov hypothesis, the turbulent kinetic energy among different eddy scales can be described as below Figure 2.3. The turbulent length scale ℓ (characteristic eddy size) is transformed to wave length κ domain. The energy spectrum function $E(\kappa)$ is formed from the dissipation rate ε and wave length κ as below.

$$E(\kappa) = C\varepsilon^{2/3}\kappa^{-5/3} \tag{2.1.5}$$

The region of $E(\kappa)\sim\kappa^{2}$ is at the low wave lengths (large turbulent lengths) which have most of turbulent kinetic energy and $E(\kappa)\sim\kappa^{-5/3}$ is in the inertial subrange. Because, in LES, a filter size determines the resolved turbulent length scale, it is very important to understand the energy cascade and the energy spectrum. Following section derives the governing equation of LES and highlights the importance of a grid size for the LES filter.

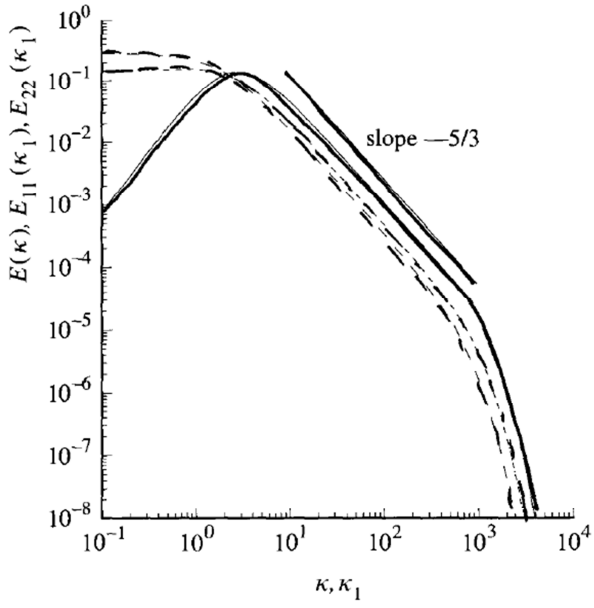

Figure 2.3 Comparison of spectra in isotropic turbulence at $R_\lambda = 500$ [68]

2.2 Sub-grid Scale Turbulence Model

The governing equations of mass and momentum conservation are described as equations (2.2.1) and (2.2.2) [69]

$$\frac{\partial \rho}{\partial t} + \frac{\partial (\rho u_i)}{\partial x_i} = \dot{m} \tag{2.2.1}$$

$$\frac{\partial (\rho u_i)}{\partial t} + \frac{\partial}{\partial x_i}\left(\rho u_j u_i - \tau_{ij}\right) = -\frac{\partial P}{\partial x_i} + \dot{M}_\iota \tag{2.2.2}$$

Where, t: time

ρ: density

x_i: Cartesian coordinate (i= 1, 2, 3)

u_i: velocity component

P: pressure

τ_{ij}: stress tensor

$\dot{m}$: mass source term

$\dot{M}_\iota$: momentum source term

In LES approach, the flow field is decomposed into a resolved (filtered) part and a SGS part by the LES filter as equation (2.2.3).

$$u_i = \bar{u}_i + \acute{u}_\iota \tag{2.2.3}$$

Where, u_i: velocity

$\bar{u}_i$: resolved (filtered) velocity

$\acute{u}_i$: sub-grid scale velocity

The resolved part is defined as a spatial average of the actual velocity field. Unlike RANS, LES filter has below properties.

$$\overline{\bar{u}_i} \neq \bar{u}_i \tag{2.2.4}$$

$$\overline{\acute{u}_i} \neq 0 \tag{2.2.5}$$

The filtered momentum equation is derived as equation (2.2.6). $\bar{}$ is used to denote the grid filter and $\tilde{}$ indicates the Favere-averaged term.

$$\frac{\partial \bar{\rho}\widetilde{u_i}}{\partial t} + \frac{\partial \bar{\rho}\widetilde{u_i}\widetilde{u_j}}{\partial x_j} = -\frac{\partial \bar{P}}{\partial x_i} + v\frac{\partial^2 \overline{u_i}}{\partial x_j \partial x_j} - \frac{\partial \tau_{ij}}{\partial x_j} \tag{2.2.6}$$

Where, v: kinematic viscosity

and

$$\widetilde{u_i} \equiv \frac{\overline{\rho u_i}}{\bar{\rho}} \tag{2.2.7}$$

$$\tau_{ij} = L_{ij} + C_{ij} + R_{ij} \tag{2.2.8}$$

Where,

$$L_{ij} = \overline{\bar{u}_i \bar{u}_j} - \bar{u}_i\,\bar{u}_j \tag{2.2.9}$$

$$C_{ij} = \overline{\bar{u}_i \acute{u}_j} + \overline{\acute{u}_i \bar{u}_j}$$
(2.2.10)

$$R_{ij} = \overline{\acute{u}_i \acute{u}_j}$$
(2.2.11)

L_{ij}, C_{ij} and R_{ij} are called the Leonard stresses, the sub-grid cross stresses and the sub-grid Reynolds stresses [70] respectively. Sub-grid scale stress tensor (Equation (2.2.8)) can be simplified to equation (2.2.12)

$$\tau_{ij} = \overline{u_i u_j} - \bar{u}_i \, \bar{u}_j$$
(2.2.12)

Because equation (2.2.12) cannot be calculated from the resolved field, it is necessary to model the sub-grid scale stress tensor. There are two approaches to model the sub-grid scale stress tensor: zero-equation and one-equation. In this study, two kinds of zero-equation and one-equation models are assessed with PIV results. Before discussion of results, LES models are briefly introduced.

2.2.1 Zero-equation Model

2.2.1.1 Smagorinsky Model

In 1963, Smagorinsky proposed a SGS model based on the assumption of eddy-viscosity[32]. The Smagorinsky model is the simplest and widely used. It is derived from a local equilibrium assumption that production and dissipation of the SGS turbulent kinetic energy are equal. The sub-grid stress tensor is derived as equation (2.2.13).

$$\tau_{ij} - \frac{1}{3}\tau_{kk}\delta_{ij} = -v_t\overline{S_{ij}}$$

(2.2.13)

Where, δ_{ij}: kronecker delta

v_t: sub-grid turbulent viscosity

S_{ij}: strain rate tensor

$$\overline{S_{ij}} = \frac{1}{2}\left(\frac{\partial\overline{u_i}}{\partial x_j} + \frac{\partial\overline{u_j}}{\partial x_i}\right)$$

(2.2.14)

$$v_t = 2C_s\Delta^2\left\|\overline{S_{ij}}\right\|$$

(2.2.15)

Where, C_s: model coefficient for sub-grid turbulent viscosity

Δ: filter size

$\left\|\overline{S_{ij}}\right\|$: Frobenius norm of the strain rate tensor

It is important to note that a priori knowledge for the flow field to determine the constant model coefficient for sub-grid turbulent viscosity. In addition, for a complex flow system such as in-cylinder flow, it may suffer from some severe drawbacks such as wall-bounded flow, flow involving a laminar/turbulent transition region, back scattering and excessive damping of large scale fluctuation in the presence of mean shear [71, 72].

2.2.1.2 Dynamic Smagorinsky Model

Germano et al. [38] suggested a dynamic version of Smagorinsky model which dynamically calculates model coefficient as a function of space and time from the resolved field. This approach assumes that different scales of resolved and sub-grid scale are mathematically identified. The advantage of dynamic model is that it doesn't require a priori knowledge of the flow to set the model coefficient.

Two different size of LES filters are used to calculate model coefficient. One is the 'test' filter and the other is called the 'grid' filter. The typical size of the test filter is twice that of the grid filter. The grid filtered stress tensor is given as equation (2.2.16) and the double (grid and test) filtered stress tensor is shown in equation (2.2.17). $\widehat{\ }$ denotes the test filter.

$$\tau_{ij} = \overline{u_i u_j} - \overline{u}_i \, \overline{u}_j \quad (2.2.16)$$

$$T_{ij} = \widehat{\overline{u_i u_j}} - \widehat{\overline{u}}_i \widehat{\overline{u}}_j \quad (2.2.17)$$

The Germano identity relates the test filtered stress tensor and the grid filtered stress tensor as equation (2.2.18).

$$L_{ij} = T_{ij} - \widehat{\tau_{ij}} = \left(\widehat{\overline{u_i u_j}} - \widehat{\overline{u}}_i \widehat{\overline{u}}_j\right) - \left(\widehat{\overline{u_i u_j}} - \widehat{\overline{u}_i \overline{u}_j}\right) = \widehat{\overline{u_i u_j}} - \widehat{\overline{u}}_i \widehat{\overline{u}}_j \quad (2.2.18)$$

where L_{ij}, is the Leonard stress term. The test filtered Smagorinsky equation is shown in equation (2.2.19). In the dynamic Smagorinsky model, the Leonard stress term is derived by subtracting equation (2.2.13) from equation (2.2.19) as equation (2.2.20).

$$T_{ij} - \frac{1}{3}T_{kk}\delta_{ij} = -2C_s\hat{\Delta}^2\|\widehat{S_{ij}}\|\widehat{S_{ij}}$$

(2.2.19)

$$L_{ij} - \frac{1}{3}L_{kk}\delta_{ij} = C_s M_{ij}$$

(2.2.20)

Where,

$$M_{ij} = -2\left(\hat{\Delta}^2\|\widehat{S_{ij}}\|\widehat{S_{ij}} - \Delta^2\widehat{\|S_{ij}\|S_{ij}}\right)$$

(2.2.21)

Finally, the dynamic model coefficient is obtained as equation (2.2.22).

$$C_s = \frac{L_{ij}M_{ij}}{M_{ij}M_{ij}}$$

(2.2.22)

2.2.2 One-equation and Non-viscosity Model

2.2.2.1 Dynamic Structure Model

Above two models adopt the eddy-viscosity hypothesis. However, Liu et al. show little correlation between the eddy-viscosity assumption and the actual sub-grid stress tensor. To overcome the problem, there is an attempt to estimate the sub-grid stress tensor directly. The DSM also adopts ‘test’ and ‘grid’ stress tensors as equation (2.2.23) and (2.2.24)

$$\tau_{ij} = c_{ij}k$$

(2.2.23)

$$T_{ij} = c_{ij}K$$

(2.2.24)

Where, τ_{ij}: 'grid' filtered stress tensor

T_{ij}: 'test' filtered stress tensor

k: sub-grid scale turbulent kinetic energy of 'grid' filter

K: sub-grid scale turbulent kinetic energy of 'test' filter

c_{ij}: tensor coefficient

Where the SGS turbulent kinetic energy with the 'grid' and the 'test' filters are shown as equation (2.2.25) and (2.2.26).

$$k \equiv \frac{1}{2}(\overline{u_\iota u_\iota} - \overline{u}_\iota\,\overline{u}_\iota)$$

(2.2.25)

$$K \equiv \frac{1}{2}(\widehat{\overline{u_\iota u_\iota}} - \widehat{\overline{u}_\iota}\widehat{\overline{u}_\iota})$$

(2.2.26)

Because this model doesn't employ the eddy-viscosity hypothesis, the sub-grid stress tensor can be obtained from a tensor coefficient. The tensor coefficient is derived as equation (2.2.27) by using the Germano identity.

$$L_{ij} = T_{ij} - \widehat{\tau_{ij}} = Kc_{ij} - \widehat{kc_{ij}}$$

(2.2.27)

Inserting equation (2.2.23) and (2.2.24) into equation (2.2.27), then the tensor coefficient has a relation with the Leonard stresses and the SGS turbulent kinetic energy as equation (2.2.28).

$$c_{ij}(K - k) = L_{ij}$$

(2.2.28)

Substituting the SGS turbulent kinetic energy (equations (2.2.25) and (2.2.26)) into equation (2.2.28), gives the tensor coefficient as equation (2.2.29).

$$c_{ij} = 2\frac{L_{ij}}{L_{kk}}$$

(2.2.29)

Finally, the SGS stress tensor is obtained as equation (2.2.30).

$$\tau_{ij} = 2k\frac{L_{ij}}{L_{kk}}$$

(2.2.30)

The DSM adopts a transport equation for the SGS turbulent kinetic energy and it is called one-equation model. The transport equation of the SGS turbulent kinetic energy is described as equation (2.2.31) [37, 60]

$$\frac{\partial(\bar{\rho}k)}{\partial t} + \frac{\partial(\bar{\rho}\,\overline{u_j}k)}{\partial x_j} = -\bar{\rho}\tau_{ij}\frac{\partial \overline{u_j}}{\partial x_j} - \bar{\rho}\varepsilon + \frac{\partial}{\partial x_j}\left(\bar{\rho}\,\overline{u_j}v_t\frac{\partial k}{\partial x_j}\right)$$

(2.2.31)

with the dissipation rate and the sub-grid turbulent viscosity as equation (2.2.32) and (2.2.33), respectively.

$$\varepsilon = C_1 \frac{k^{3/2}}{\Delta} \quad (2.2.32)$$

$$v_t = C_2 \Delta \sqrt{k} \quad (2.2.33)$$

Where, C_1: model coefficient for dissipation rate

C_2: model coefficient for sub-grid turbulent viscosity.

By adding the transport equation for the SGS turbulent kinetic energy, a kinetic energy budget serves that the information of the SGS turbulent kinetic energy is transferred to neighbors and it improves the numerical stability. Therefore, the accuracy of the SGS model is improved with coarser grids than the zero-equation models.

2.3 Evaluation of Turbulence Models

In the previous section, three SGS models were introduced. Three SGS models were evaluated with PIV results in the author's previous publications [73, 74]. The target engine is a single cylinder engine with transparent combustion chamber (TCC-III) which was designed for LES research by University of Michigan and GM Global R&D center [75, 76]. It consists of two valve head and a simple combustion chamber of pancake shape. Each intake and exhaust port is connected to a plenum. The schematic of the TCC-III engine is shown in Figure 2.4 [75]. The pressure signals were measured at inlet of intake plenum, outlet of exhaust plenum, intake port, exhaust port and in-cylinder every 0.5 crank angle (CA) degrees as shown in Figure 2.4 with a red dots. Detailed engine specifications are listed in Table 2.1. PIV measurements were conducted on four different section planes as shown in Figure 2.5. A monochrome high-speed camera (Vision Research, Phantom v1610) was used to record images measured every 5 CA degrees. Silicon-oil droplets (1μm) were used as seeding parcels and a ND:YLF laser (Darwin Duo, Quantronix) was used to illuminate the parcels. A DaVis 9.x which is a commercial PIV post-processing code made of LaVision was adopted to generate vector field from recorded images. A detailed information of the TCC-III engine and the PIV setup can be found in [75].

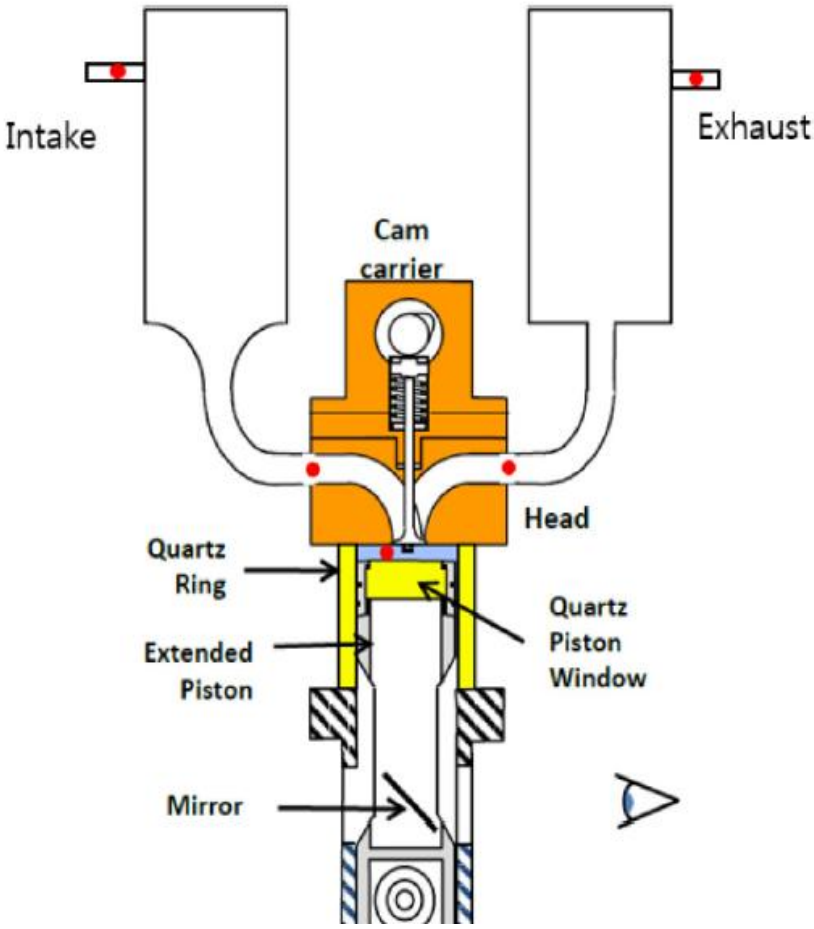

Figure 2.4 The schematic of TCC-III engine. The pressure signals are measured at red dots [75].

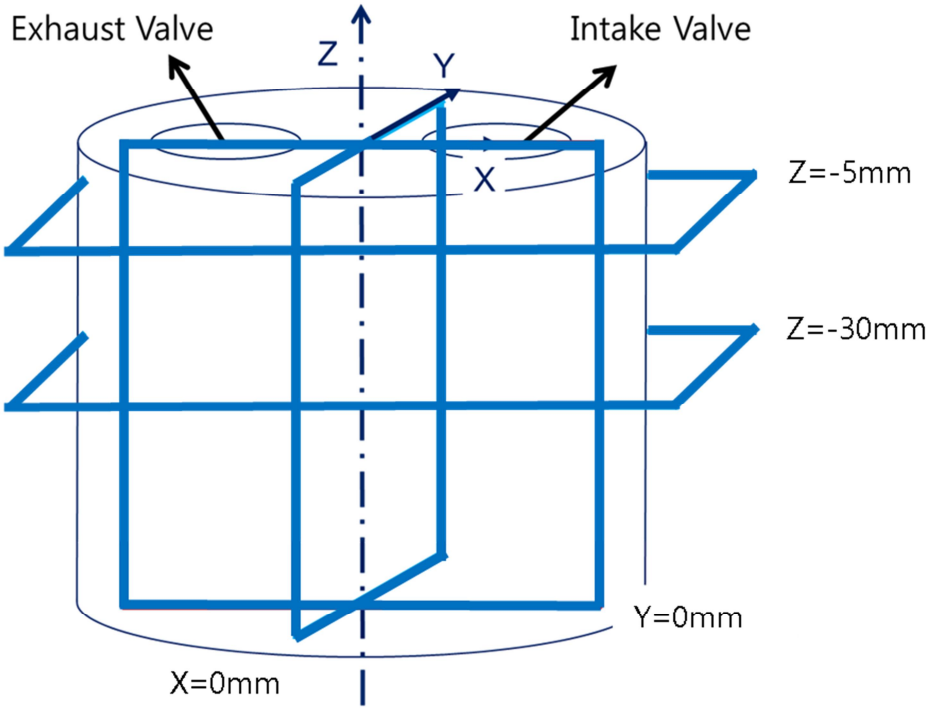

Figure 2.5 PIV measurement planes [75]

Table 2.1 The TCC-III engine specification

Parameter	Specification
Engine	TCC-III engine
Displacement Volume	570 cc
Bore	92 mm
Stroke	86 mm
Compression Ratio	10.0
Engine Speed	1300 RPM
Intake Pressure	0.4 bar

2.3.1 Numerical Configuration

The assessment of the SGS models was performed using STAR-CD v4.22 licensed by Siemens PLM. The numerical domain was meshed using trim method as Figure 2.6. To save the computational cost, a grid size of the intake and exhaust plenums was 6mm and that of the ports was 1.5mm. A mean grid size of the in-cylinder was 1mm. The high velocity gradient regions such as near the valve regions and the spark plug region were meshed with 0.4mm and 0.6mm, respectively. A single layer of prismatic cells aligned to the walls was used to construct mesh of near-wall regions. The total number of cells was approximately 1.15 million at bottom dead center (BDC) with 1 million cells of the intake and exhaust plenums. The arbitrary lagrangian-eulerian (ALE) formation and the arbitrary sliding interface (ASI) were adopted to deal with moving-boundary and mesh motion. The pressure implicit with splitting of operator (PISO) algorithm, which is optimized for transient flow, was employed for temporal discretization. The monotone advection and

reconstruction scheme (MARS) was used for spatial discretization. The standard wall function was adopted for near-wall treatment.

Time-dependent pressure and boundary conditions were adopted for inlet and outlet condition. At first, pressure signals were measured at the inlet of plenum, the outlet of plenum, the intake, the exhaust and the in-cylinder as shown in Figure 2.4 [75]. The 1D (GT-power) simulation was conducted to obtain intake pressure and temperature, exhaust pressure and temperature and wall temperatures [75]. As shown in Figure 2.7, the discrepancy between the pressure of the inlet and the outlet in the experiment and the simulation was negligible. Therefore, the implementation of boundary conditions obtained from GT-power is reasonable choice.

To evaluate the SGS model effects, the vector fields were compared with the PIV result. Basically, the simulations and the PIV result were compared with the analysis of vector field and root-mean-square deviation (RMSd) of velocity vector. The definition of RMSd is as equation (2.3.1).

$$u' = \sqrt{\frac{1}{n-1}\sum_{i=1}^{n}(u_i - \langle u \rangle)^2} \tag{2.3.1}$$

Where, u': root-mean-square deviation of velocity

u_i: instantaneous velocity

$\langle \ \rangle$: ensemble or phase average

n: total number of cycle

In addition, the alignment parameter and the LES quality index was used to assess the SGS models quantitatively. The alignment parameter is a very

simple and effective method to quantify the local derivation of the simulated vector field with respect to the PIV vector field, which is assumed as a reference. The definition is formulated as equation (2.3.2).

$$\frac{\vec{A}\cdot\vec{B}}{\|\vec{A}\|\|\vec{B}\|} = \frac{\|\vec{A}\|\|\vec{B}\|\cos(\alpha)}{\|\vec{A}\|\|\vec{B}\|} = \cos(\alpha) \quad \in \quad [-1,1] \tag{2.3.2}$$

Where, $\vec{A}$: reference vector

$\vec{B}$: comparable target vector

α: angle between reference and comparable target vectors

If the parameter equals 1, it means that direction of the PIV (reference) vector field and the LES vector (comparable target) field is exactly aligned. While if the parameter equals -1, their vector has totally opposite direction. The value of 0 indicates that they have orthogonal direction.

Finally, the LES quality index was used to evaluate the level of resolved flow field. As mentioned before, the grid size determines the resolved flow field and the contribution of the SGS model. Therefore, the LES quality index is very useful tool to determine the grid size and the SGS model. The LES quality index, M, is defined as equation (2.3.10) [77, 78].

$$M = \frac{k_{res}}{k_{res}+k_{sgs}} \tag{2.3.10}$$

Where, $\langle \quad \rangle$ indicates the ensemble or phase average.

$$k_{res} = \frac{1}{2}(\langle \overline{u_i} - \langle \overline{u_i} \rangle \rangle^2)$$

(2.3.11)

$$k_{sgs} \equiv \frac{1}{2}(\overline{u_i u_i} - \overline{u_i}\ \overline{u_i})$$

(2.3.12)

The index provides two aspects of significant information. It indicates whether the grid size is sufficient to resolve turbulence flow. The high value of index means that almost turbulence flow is resolved and only small turbulence scale is modeled by the SGS model. However, even though the grid size is small enough to resolve turbulent flow, the SGS models sometimes cannot predict turbulent flow field properly. Then, the index indicates low value regardless of grid resolution. So, the index also provides whether the SGS turbulent flow is adequately predicted by SGS models.

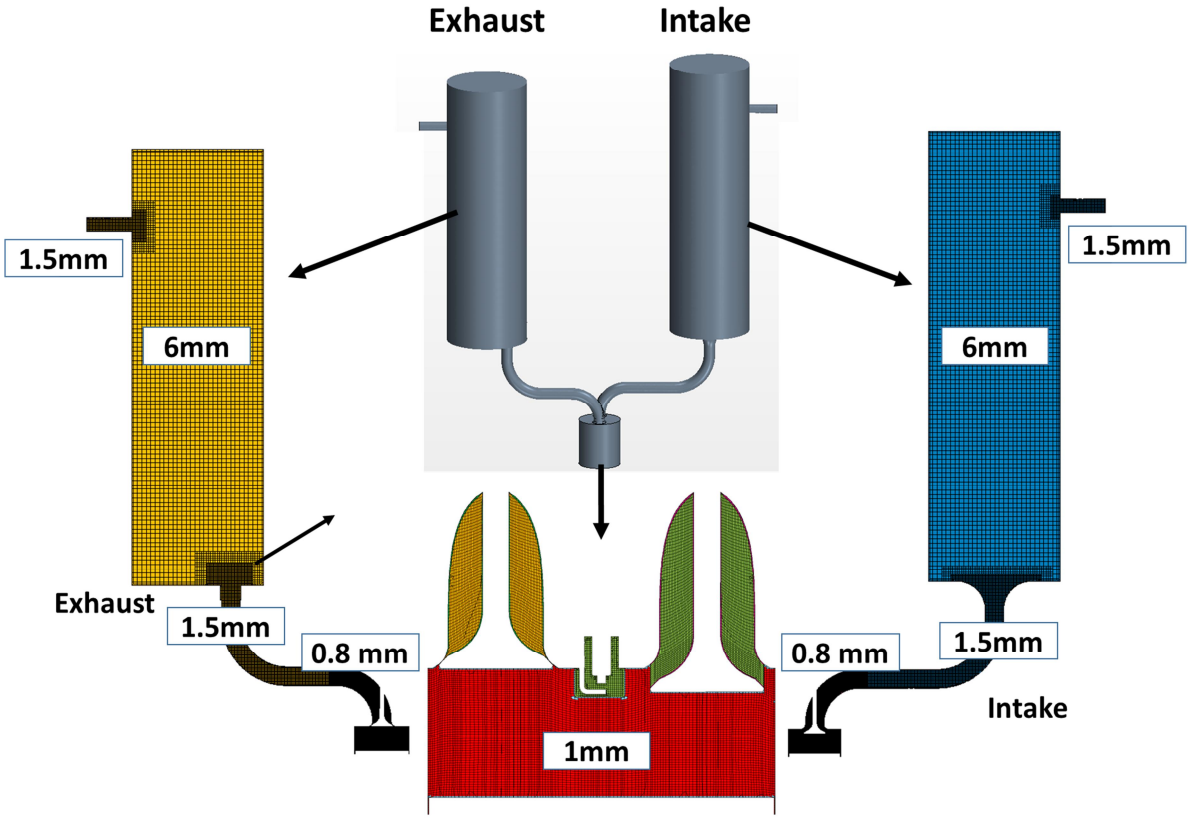

Figure 2.6 The computational domain of the TCC-III engine [73]

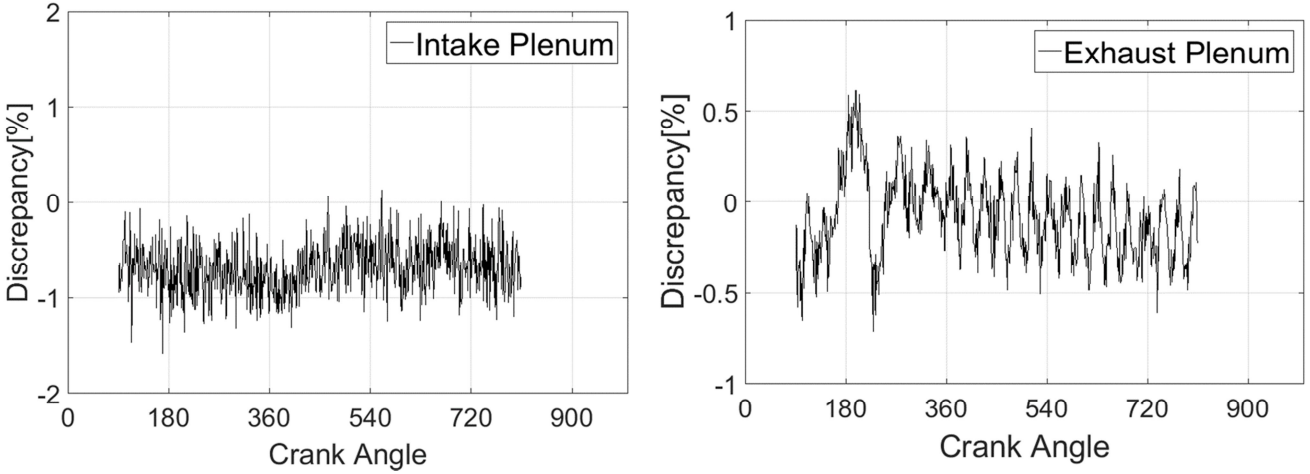

Figure 2.7 The discrepancies of pressure between experiment data and GT-power data [73]

2.3.2 Comparison of Sub-grid Scale Model

The comparison of the SGS model with the PIV result was mainly conducted under following condition. The engine operation speed was 1,300 rpm under about 0.4 bar of intake pressure. To obtain a stable initial condition, one cycle was performed using RANS approach for each SGS model case and it was used as an initial condition of LES cycle. The three sets of 51 consecutive LES cycles were conducted. The first cycle of each LES case was discarded to remove the unstable transition state between RANS and LES cycle. Figures 2.8 and 2.9 show the peak pressure and trapped mass for the 52 cycles including RANS cycle. The peak pressure results show convergence in 51 LES cycles, but in terms of trapped mass, the first cycle of LES is slightly deviated from the 51 cycle average. Therefore, the first cycle of three LES cases was discarded to remove the unstable cycle. Finally, three sets of effective 51 LES cycles were obtained. The measurement plane is Y=0mm section plane shown in Figure 2.5. The vector fields were evaluated at four different crank angle positions. The chosen crank angles represent significant engine events:

- Middle of exhaust stroke at 245 CA
- Middle of intake stroke at 475 CA
- BDC, 540CA
- Middle of compression stroke at 630CA

Figure 2.10 shows the vector fields of LES and the PIV results at four different CA on Y=0mm section plane. At 245 CA, the dynamic Smagorinsky model and the DSM cases are well matched with PIV data. However, the static

Smagorinsky model case shows that a wall flow near left liner is relatively stronger than the PIV and other LES results. At 540 CA and 630 CA, there is no significant difference between LES results. At 475 CA, an intake jet flow is observed in the PIV and LES results. All of the SGS model cases are well matched with the PIV data. Figure 2.11 shows the RMSd field of velocity for three LES cases and the PIV data. The LES cases slightly underestimate the magnitude of the RMSd velocity compared with the PIV data. The estimation of turbulent flow in LES can be divided into two types: large scale turbulent flow resolved by grid and small scale turbulent flow predicted by the SGS model. Thus, while only the large scale turbulent flow is reflected in the RMSd velocity field in LES, both the large and small scale turbulent flow are contained in the RMSd velocity field in PIV. This is why LES results underestimate the RMSd velocity field of the PIV. Except for this discrepancy between LES cases and the PIV data, there is no noticeable difference between LES results at 245 CA, 540 CA and 630 CA. However, there is noticeable difference among LES results at 475 CA. While the static Smagorinsky result predicts the wider and longer shape of intake jet flow than the PIV data, the dynamic Smagorinsky and the DSM cases are well matched with the PIV data. The results of alignment parameter are shown in Figure 2.12. At 245 CA, vector fields of the dynamic Smagorinsky model and the DSM cases are well aligned with the PIV result. However, the wide region of discrepancy is shown in the static Smagorinsky model case. At 475 CA, two discrepancy regions can be found in three SGS model cases. Because the intake jet flow of LES slightly leans to the left compared to the PIV counterpart, two regions of very poor alignment appear. The parameter values are spatial averaged and presented in Table 2.2. The spatial averaged value of alignment parameter for the dynamic Smagorinsky model and the DSM case show a good agreement with the PIV data.

In terms of the LES quality, the DSM case has the very high contribution of resolved part on turbulent flow field and the dynamic Smagorinsky model case also show high quality as shown in Figure 2.13. The remarkable point is that the dynamic Smagorinsky model case predicts abnormally the high SGS turbulent kinetic energy in the high velocity gradient region near the valve at 245 CA. On the contrary, the DSM case can predict the reasonable SGS turbulent kinetic energy relative to the surrounding field. Except near the valve region, the level of grid resolution is enough to predict flow field for both the dynamic Smagorinsky model and the DSM case as Table 2.3 which summarizes the spatial averaged value of the LES quality index. In terms of the accuracy of flow field and prediction of the SGS turbulent kinetic energy, the dynamic Smagorinsky model and the DSM are superior model than the static Smagorinsky model. Furthermore, the DSM model was adopted in this study in consideration of the theoretical advantages of calculating the transport equation of the SGS turbulent kinetic energy.

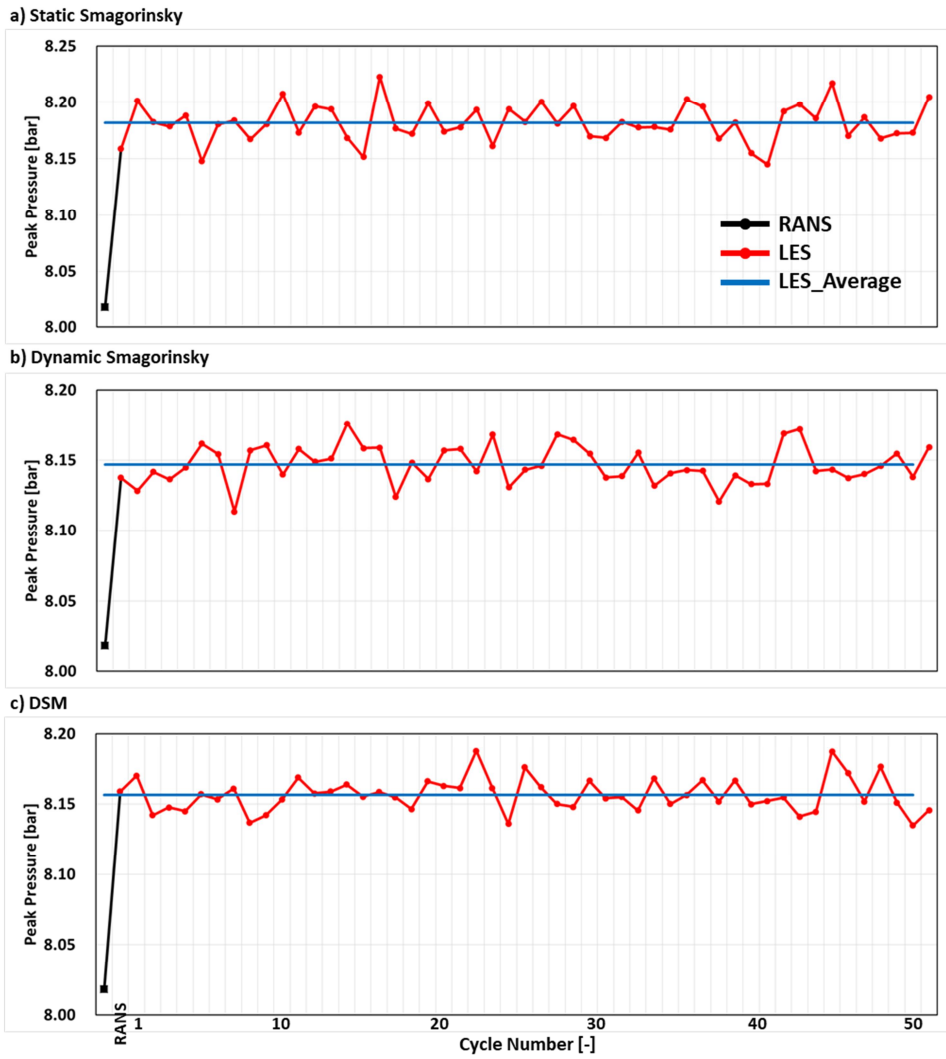

Figure 2.8 Peak pressure for the 52 cycles. The black circle identifies the discarded LES cycle for a) Static Smagorinsky, b) Dynamic Smagorinsky, c) DSM [74]

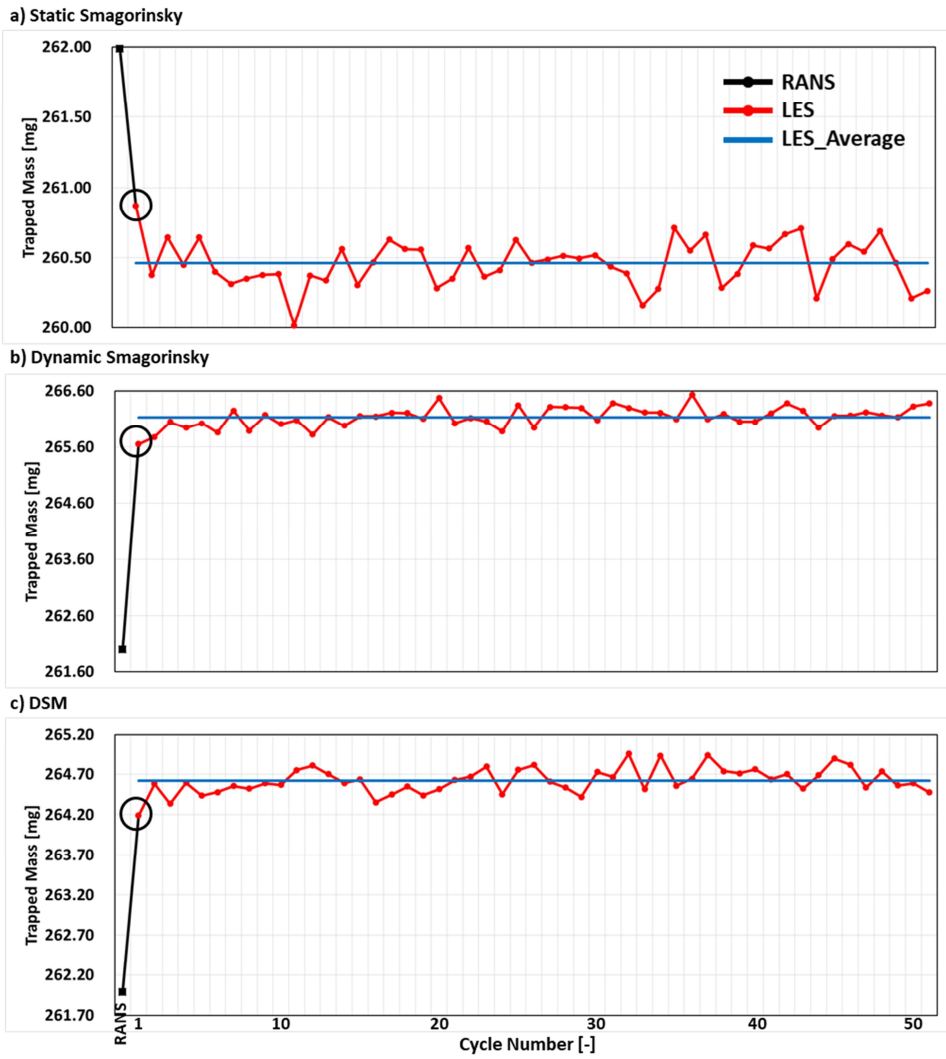

Figure 2.9 Trapped mass for the 52 cycles. The black circle identifies the discarded LES cycle for a) Static Smagorinsky, b) Dynamic Smagorinsky, c) DSM [74]

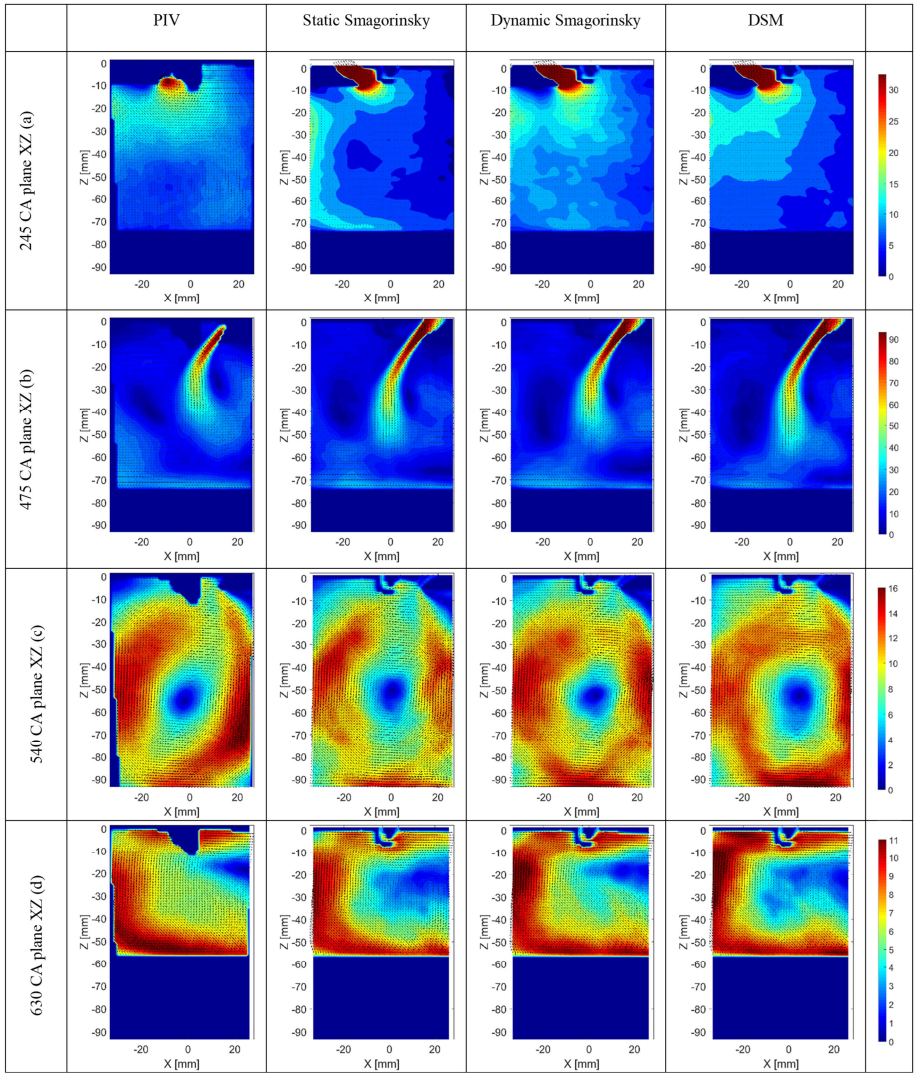

Figure 2.10 Averaged velocity field of PIV, static Smagorinsky, dynamic Smagorinsky and DSM cases at four different CA positions on section plane Y=0mm [74]

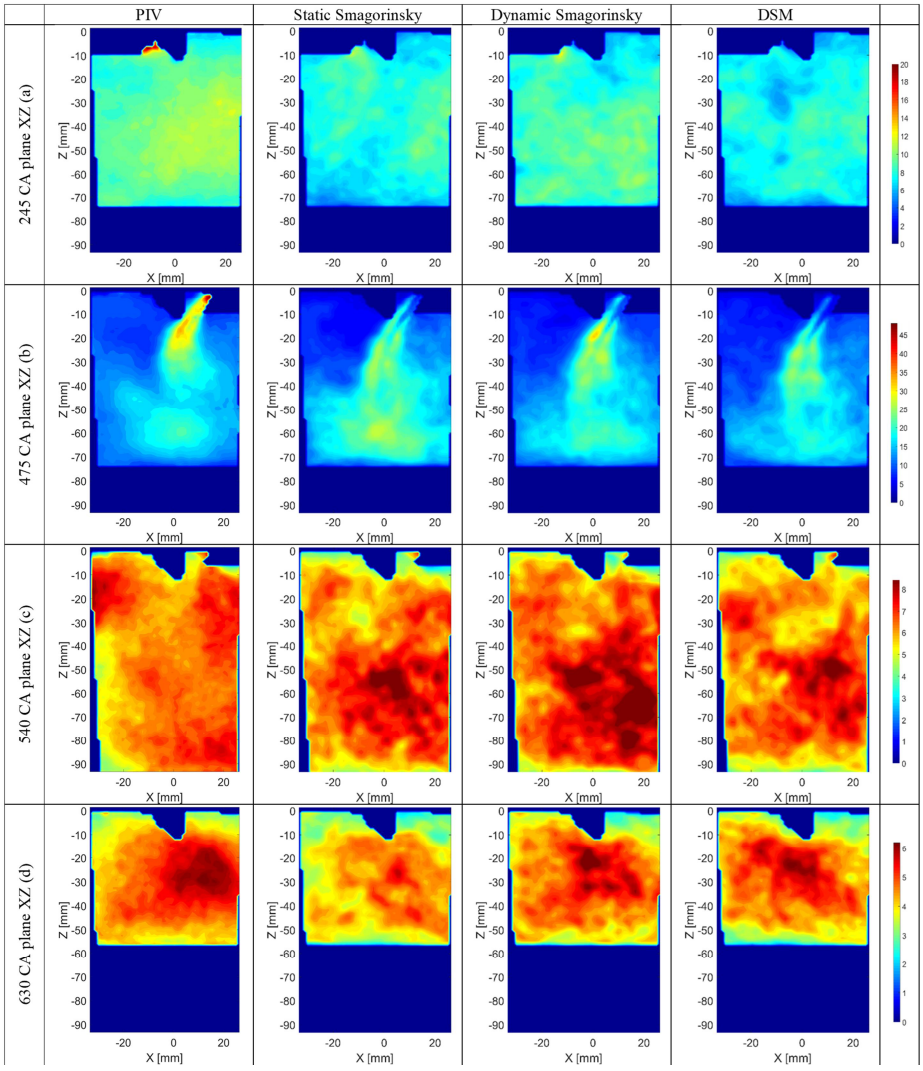

Figure 2.11 RMSd velocity field of PIV, static Smagorinsky, dynamic Smagorinsky and DSM cases at four different CA positions on section plane Y=0mm [74]

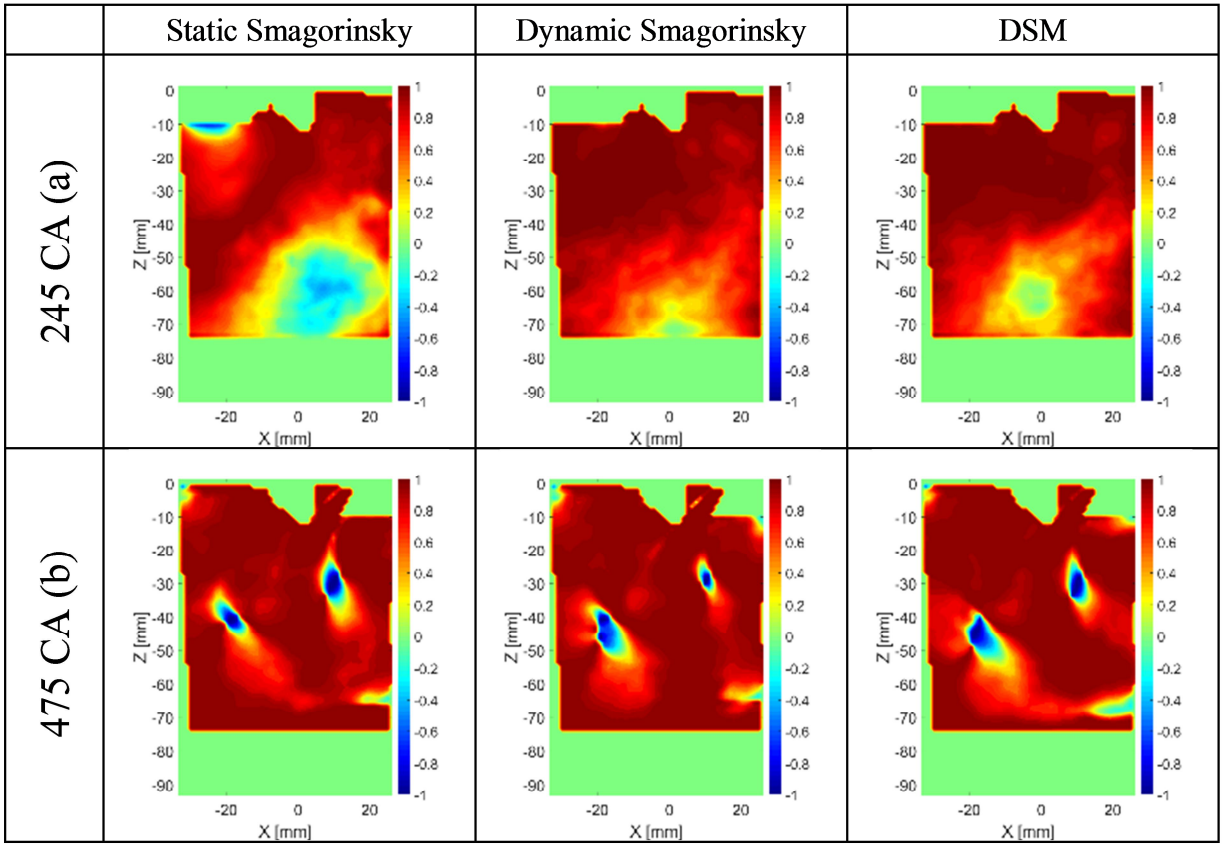

Figure 2.12 Alignment parameter representation on section plane Y=0mm at (a) 245 CA and (b) 475CA [74]

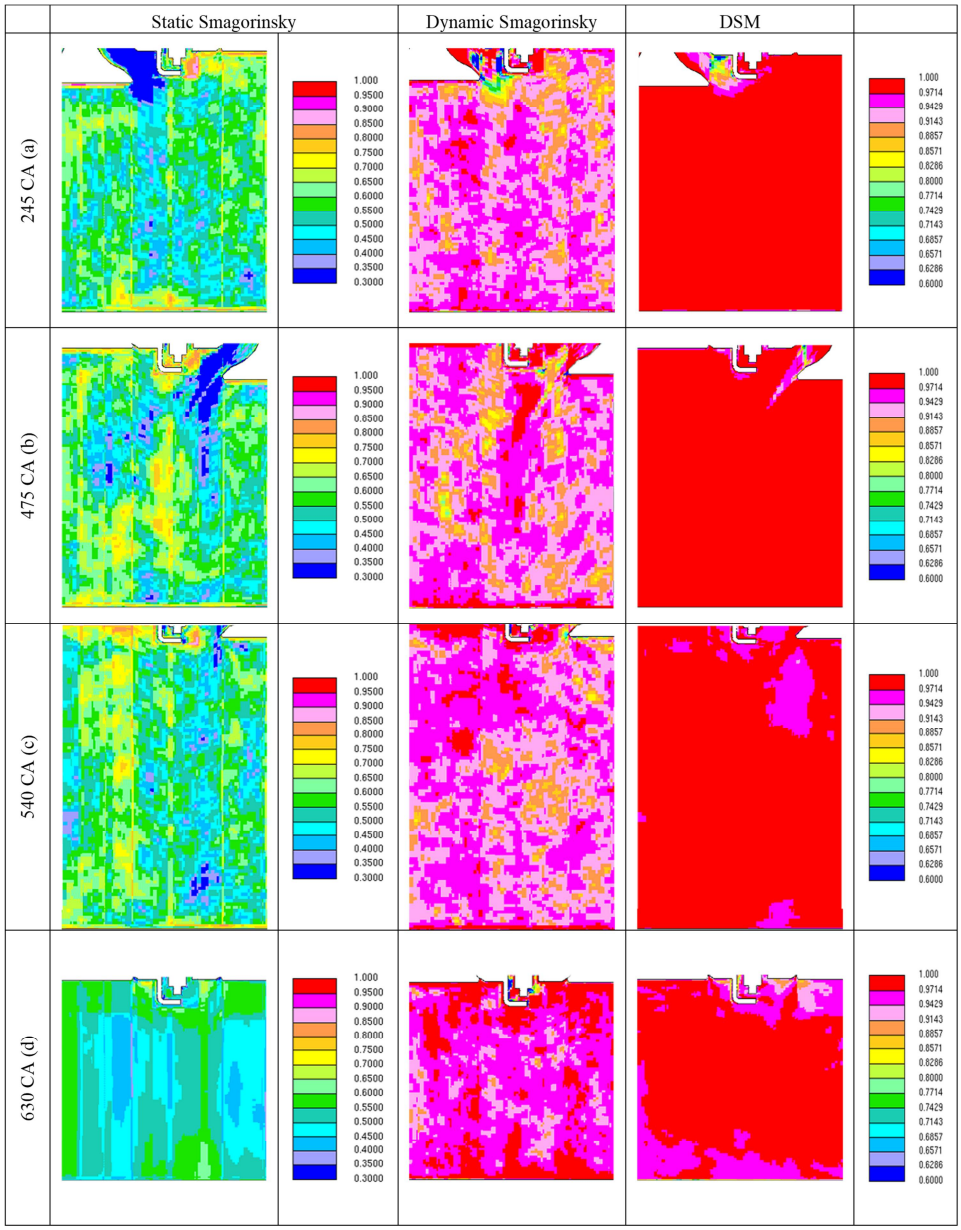

Figure 2.13 LES quality result of static Smagorinsky, dynamic Smagorinsky and DSM at four different CA positions on section plane Y=0mm [74]

Table 2.2 The spatial averaged value of alignment parameter at Y=0mm plane [74]

	Static Smagorinsky	Dynamic Smagorinsky	DSM
245 CA	0.5344	0.9383	0.9388
475 CA	0.4968	0.9265	0.9146
540 CA	0.5688	0.9329	0.9482
630 CA	0.6129	0.9511	0.9528

Table 2.3 The spatial averaged value of LES quality index at Y=0mm plane [74]

	Static Smagorinsky	Dynamic Smagorinsky	DSM
245 CA	0.611	0.831	0.808
475 CA	0.869	0.876	0.839
540 CA	0.956	0.962	0.939
630 CA	0.948	0.982	0.967

Chapter 3. Modeling of Gasoline Surrogate Fuel

Real gasoline consists of hundreds of hydrocarbon species which vary in the number of carbon atoms and various chemical families: paraffins, naphthenes, olefins and aromatics. And the composition of fuel depends on the crude oil origin and the refinery system [79]. There are many attempts to make surrogate fuels to predict real gasoline properties. A surrogate fuel which realizes many aspects of gasoline properties needs many amount of chemical species and reactions and extremely high computational cost to solve reactions. The important properties of gasoline are flame propagation, auto-ignition, distillation and emissions. However, it is very inefficient to use the surrogate fuel to predict all of gasoline properties for the 3D simulation. Considering computational cost, the surrogate fuel should be aimed to target properties. In this study, the engine operates with dual-port fuel injection (DPFI) system and emissions are not considered. Therefore, the target properties are flame propagation and auto-ignition.

In this chapter, the gasoline surrogate fuel is formulated by following steps. At first, the literature review for target properties are conducted. Next, the surrogate fuel and its mechanism are chosen for auto-ignition property of domestic gasoline fuel based on the literature review.

3.1 Literature Review

In SI engines, the combustion process starts from the electrical spark discharge. Then, the electrical energy transfers to the air-fuel mixtures in the spark channel and starts the flame propagation with turbulent flame speed. The turbulent flame speed is related to the laminar burning velocity and flow

structures. So, the laminar burning velocity is a key feature of the surrogate fuel. As the flame propagates with the turbulent flame speed, the temperature of burned gas and on flame region elevates to the flame temperature. Since the laminar burning velocity can be formulated by semi-empirical correlation, it will be discussed in Chapter 4. The flame temperature is related to the lower heating value. The low heating value of gasoline is around 42.8 MJ/kg. The primary reference fuel (PRF), a mixture of iso-octane and n-heptane, is a representative chemical species to formulate the surrogate fuel [80, 81].

3.2 Determination of Surrogate Component

In the previous section, the major chemical properties for the present study were introduced. The laminar burning velocity can be obtained by semi-empirical correlation. The toluene reference fuel (TRF) can mimic the lower heating value of gasoline and other chemical properties. Therefore, the TRF which consists of n-heptane, iso-octane and toluene meets the chemical property used in this study. In addition to the surrogate component, the selection of reaction mechanism and surrogate composition is important to predict the flame temperature.

There are several researches for development of detailed chemical mechanism. Detailed mechanisms of iso-octane [82] and PRF [83] developed by Lawrence Livermore National Laboratory were widely used. And Mehl et al. [84] introduced a detailed mechanism of PRF focused on a low-temperature heat release for an HCCI engine. Naik et al. [85] also developed a detailed mechanism of surrogate fuel which consists of iso-octane, n-heptane, 1-pentene, toluene and methyl-cyclohexane for an HCCI engine. However, even though these mechanisms have high accuracy and meet many aspects of fuel properties, they have too many reactions and species to apply on 3D simulation.

Therefore, reduced mechanism has been developed as an alternative chemical mechanism.

Andrae [86] developed reduced mechanism of the TRF focusing on the ignition delay and the laminar burning velocity for gasoline at engine-relevant conditions. This mechanism is relatively heavy for the reduced mechanism due to prediction of two properties: the ignition delay and the laminar burning velocity. Lee et al. [87] conducted a rapid compression machine (RCM) experiment to obtain engine-relevant conditions and developed the reduced mechanism of the TRF focusing on the ignition delay time of Korean domestic gasoline with the RCM data. They validated iso-octane, n-heptane and toluene with experimental and detailed mechanism data, respectively. Even though the mechanism was built to predict ignition delay time, the mechanism was also composed to meet the properties of Korean gasoline as shown in Table 3.1. In their work, the selected composition of TRF is 54% iso-octane, 22% n-heptane and 24% toluene by liquid volume fraction. The properties of surrogate fuel are listed in Table 3.2 and good agreement with Korean gasoline. Therefore, the TRF mechanism of the introduced composition ratio (54% iso-octane, 22% n-heptane and 24% toluene by liquid volume fraction) is adopted in this study.

Table 3.1 The properties of Korean gasoline

Item	Value
ON(RON)	92
Density (g/cm3 at 15°C)	0.733
Vapor pressure (37.8°C, kPa)	55
Lead content (g/L)	Below 0.013
Surfer content (ppm)	19
Aromatic compound content (Vol %)	19.7
Benzene content (Vol %)	0.4
Olefin content (Vol %)	14.5
Oxygen content (wt %)	2.05
Methanol content (wt %)	Below 0.1

Table 3.2 The properties of TRF surrogate fuel

Item	Value
RON	87
MON	82
Density (g/cm3 at 15°C)	730.4
Lower heating value (MJ/kg)	44.03

Chapter 4. Combustion Model for LES

In SI engines, it is well known that the turbulent flame propagation is a comprehensive phenomenon which is affected by the thermo-chemical reaction of the air-fuel mixture and turbulent flow [45]. The laminar burning velocity is a pure propagation speed of chemical reactions. Therefore, it is a fuel property. Many researches have been conducted to measure the laminar burning velocity of pure hydrocarbons and develop the chemical mechanisms. Turbulence also affects the flame propagation by a convection, a kinematic interaction between turbulent eddies and the laminar flame, and an increase of scalar mixing. Therefore, the laminar burning velocity and the interaction between chemical reaction and turbulent flow are key role to predict the turbulent flame propagation.

In this chapter, the combustion model is described. At first, the laminar burning velocity is introduced based on literature review. Secondly, the G-equation model considering the characteristic of LES is described. Finally, the turbulent burning velocity for LES is illustrated.

4.1 The Laminar Burning Velocity

4.1.1 Literature Review

The laminar burning velocity is a fuel property as discussed in section 3.1.1. Many chemical mechanisms have been proposed to predict the laminar burning velocity of the gasoline surrogate fuel: detailed or semi-detailed mechanisms [88-90] and reduced mechanism [91]. However, these

mechanisms have too many species and reactions to apply on the 3D engine simulation due to enormous computational cost. Therefore, empirical (or semi) empirical correlation of the laminar burning velocity has been proposed [92]. The simplest and widely used form of empirical correlation is a function of the unstretched laminar burning velocity, temperature, pressure and residual gas fraction as equation (4.1.1).

$$s_L = s_{L,0}(T/T_0)^{\alpha}(P/P_0)^{\beta}(1-\gamma Y_{dil}) \quad (4.1.1)$$

Where, s_L: laminar burning velocity

$s_{L,0}$: unstreched laminar burning velocity

T_0: reference temperature

P_0: reference pressure

α: coefficient of temperature dependency

β: coefficient of pressure dependency

γ: coefficient of residual gas effect

Y_{dil}: residual gas fraction

The formulation of the unstreched laminar burning velocity and coefficients of temperature, pressure and residual gas dependency were based on the experimental or numerical researches [92-94].

Gulder [92] proposed a semi-empirical correlation of various pure hydrocarbons and binary mixtures. However, they were verified at low temperature (less than 600 K). Metgalchi and Keck [93] also developed

correlation for methanol, iso-octane and indolene at high pressure and temperature. But, a single hydrocarbon has a limitation that it cannot satisfy the wide range of engine operation conditions. Yang and Reitz [94] suggested an empirical correlation of various the PRF mixtures based on the experimental data and integrated the correlation with the G-equation combustion model for an engine simulation. However, its limitation is also that the correlation is based on the PRF. There are two experimental [95] and numerical [96] researches about the validation between the laminar flame speed of the PRF and real gasoline. While the PRF shows good agreement with real gasoline in their works, there is still a deviation with real gasoline under stoichiometric and rich mixtures.

To overcome the limitation of the PRF, many works with additional hydrocarbon (toluene), the TRF, have been conducted. Mannaa et al. [97] conducted experimental study on the laminar burning velocity of the PRF, the TRF and the real gasoline under various RON. In their work, the laminar burning velocity of TRF shows better agreement with gasoline result. Sileghem et al. [98] investigated the TRF mechanism to compare with the laminar flame speed of gasoline. The authors obtained the composition of a mixture of iso-octane, n-heptane and toluene by a mixing rule. Liao and Roberts [99] measured the laminar burning velocity of various compositions of the TRF with the flat flame method. The TRF results retains the satisfactory agreement and it is found that the deviation among various compositions of the TRF is negligible. Kim and Min [100] developed a new correlation using an energy fraction-based mixing rule approach. The correlations were derived for each surrogate fuel component with consideration for the effect of temperature, pressure and diluent. Because of mixing rule, the correlation can consider the various composition of the TRF. In this paper, the composition of the TRF is already determined to predict the auto-ignition phenomena. Therefore, the

correlation for the laminar burning velocity is obtained by the mixing rule approach. The detailed process for the correlation is described in following section.

4.1.2 The Correlation for the Laminar Flame Speed

As aforementioned, the TRF which is composed of 54% iso-octane, 22% n-heptane and 24% toluene by liquid volume fraction is adopted as the gasoline surrogate fuel in this study. The correlation of the laminar burning velocity for the surrogate fuel is determined by mixing-rule approach[100]. In general, the mixing rule is described as equation (4.1.2).

$$s_{L,blend} = \sum_{i=1}^{n} \alpha_i s_{L,i} \tag{4.1.2}$$

Where, $s_{L,blend}$: the laminar burning velocity of surrogate fuel

$s_{L,i}$: the laminar burning velocity of each component

i: ith fuel component

α_i: blending factor of ith fuel component

The energy fraction-based mixing rule is used to calculate blend factor as equation (4.1.3).

$$\alpha_i = \frac{\Delta H_{c,i} x_i}{\sum_{i=1}^{n} \Delta H_{c,i} x_i} \tag{4.1.3}$$

Where, $\Delta H_{c,i}$: the heat of combustion

x_i: the mole fraction

Then, the correlation of the laminar burning velocity for each component follows the basic form as equation (4.1.1) and residual gas effect is neglected. The reference temperature and pressure are 600 K and 5 bar, respectively. An algebraic equation is introduced to reproduce the unstretched laminar burning velocity of each component as equation (4.1.4)

$$s_{L,0,i} = a_i\left[1 - exp\{b_i(\phi - \phi_m)\} - exp\{\{-\xi(\phi - \phi_m)\}\} + \xi(\phi - \phi_t)^2\right] \quad (4.1.4)$$

Where, ϕ: equivalence ratio

$a_i,\ b_i,\ \phi_m,\ \phi_t,\ \xi$: model constants

The model constants are listed in Table 4.1.

The coefficients of temperature and pressure dependency are function of equivalence ratio. The coefficients are curve-fitted with a fifth-order polynomial as equations (4.1.5) and (4.1.6), respectively, and the temperature range is divided into low and high temperature regime.

$$\alpha(\phi) = \sum_{j=0}^{5} A_j \phi \quad (4.1.5)$$

$$\beta(\phi) = \sum_{j=0}^{5} B_j \phi \quad (4.1.6)$$

Where, A_j: coefficients of temperature dependency

B_j: coefficients of pressure dependency

The coefficients for polynomial equation are listed in Table 4.2 and 4.3.

Finally, the laminar burning velocity of the surrogate fuel with consideration of residual gas effect is obtained with determined component ratio of the TRF as equation (4.1.7).

$$s_L = \sum_{i=1}^{n} \alpha_i s_{L,i} (1 - \gamma Y_{dil}) \quad (4.1.7)$$

The laminar burning velocity under various conditions is verified against the measurement data from various literatures as Figures 4.1-4.3. The component of gasoline varies according to the crude oil origin and the refining process. In European Union, the aromatic content of commercial gasoline is limited under 35% of volume fraction. While, in South Korea, the content of aromatic is regulated that it does not exceed 22% of volume fraction. Thus, the laminar burning velocity of Korean gasoline may be faster than literature sources. Considering the difference, it is found that the laminar burning velocity of the surrogate fuel is well matched with that of real gasoline.

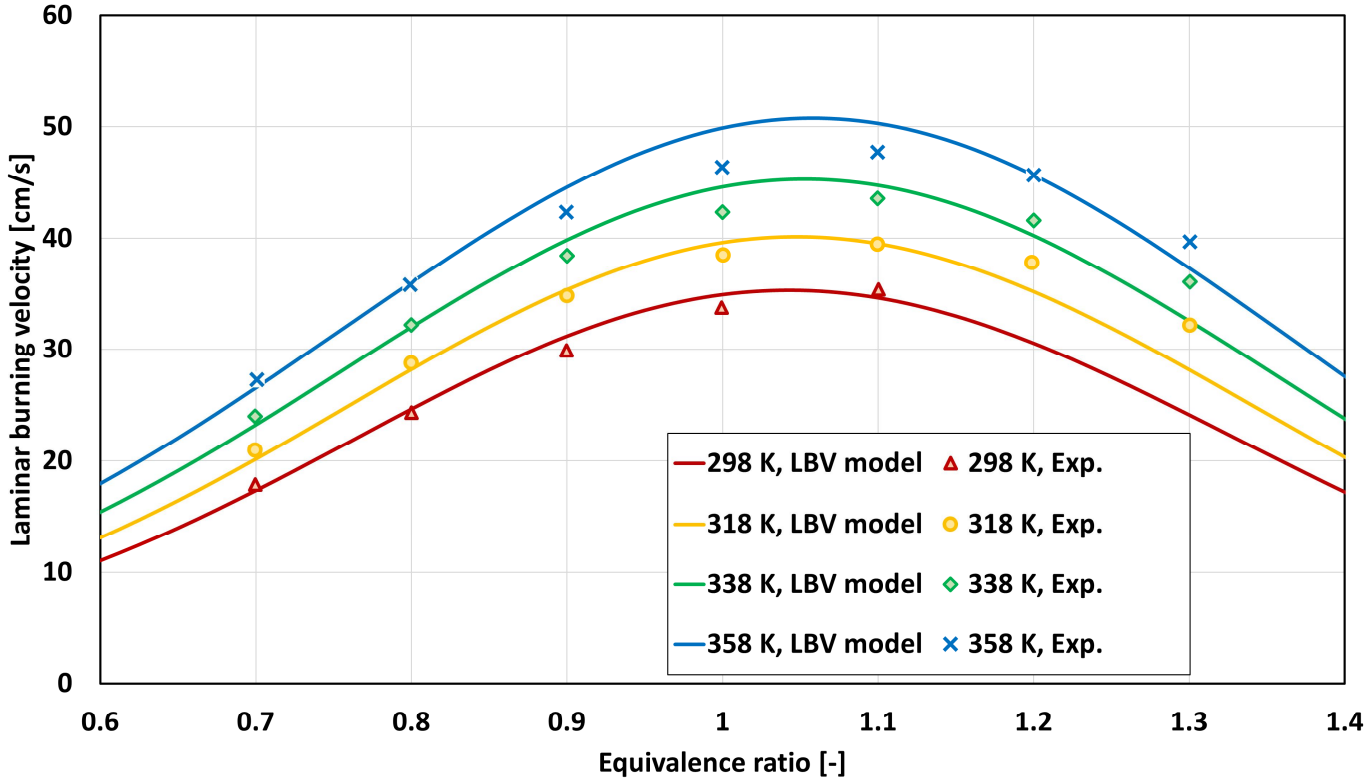

Figure 4.1 Validation of LBV model of this study (line) against the measurement data from literature source (symbol): Sileghem et al. @ p=1atm [98]

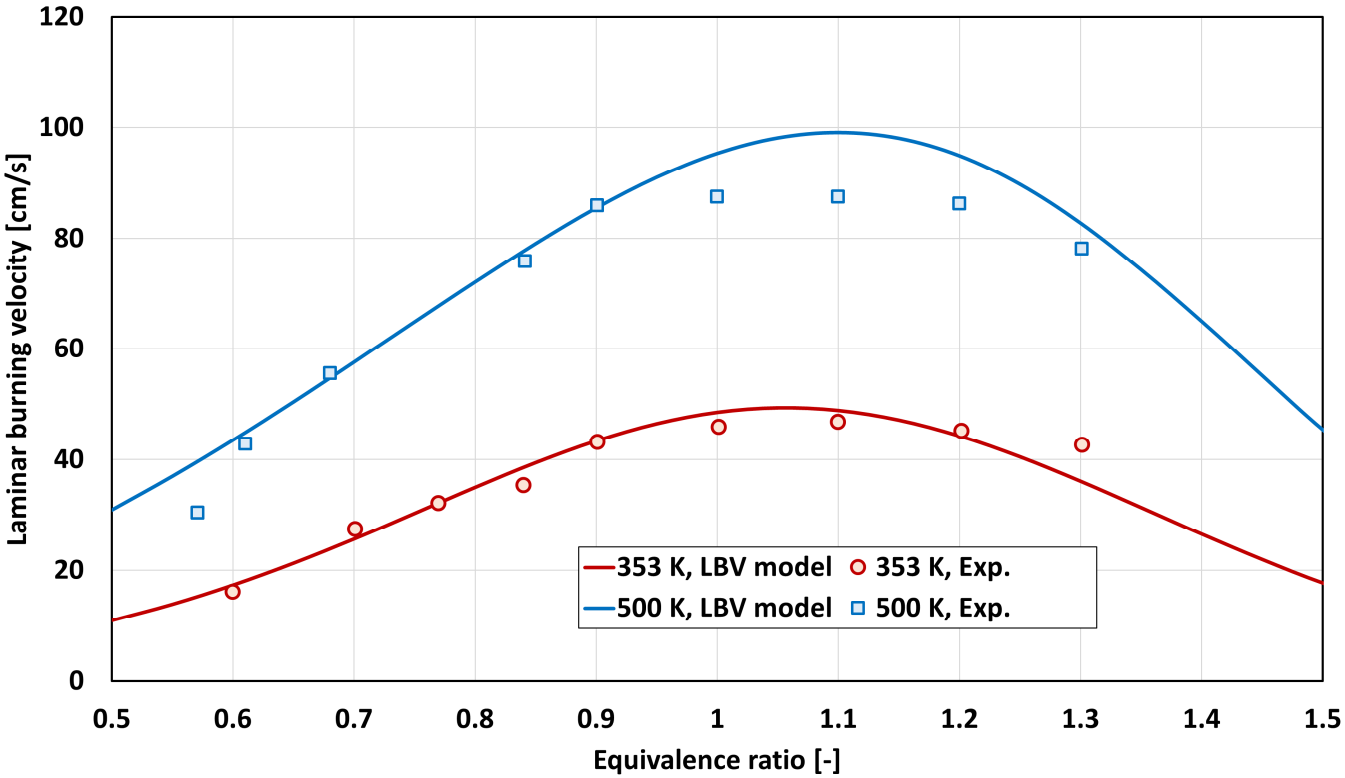

Figure 4.2 Validation of LBV model of this study (line) against the measurement data from literature source (symbol): Zhao et al. @ p=1 bar [95]

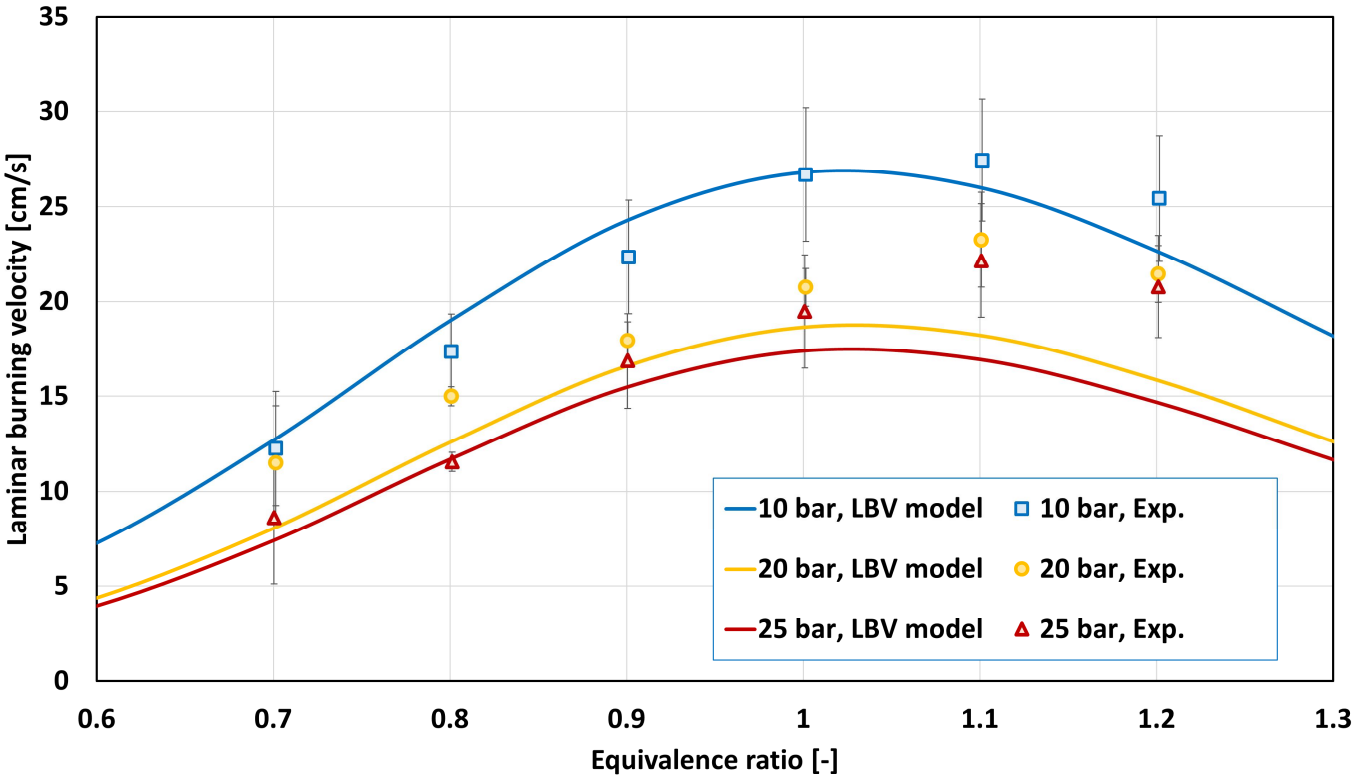

Figure 4.3 Validation of LBV model of this study (line) against the measurement data from literature source (symbol): Jerzembeck et al. @ T_u=373K [96]

Table 4.1 The model constants for laminar burning velocity

	iso-octane	n-heptane	Toluene
a_i	2.25	2.5	2.35
b_i	1.95	1.9	2
ϕ_m	1.1		
ϕ_t	1.5 (if ϕ>1.5, otherwise 0)		
ξ	9		

Table 4.2 Coefficients for fitting temperature dependence, $\alpha_i(\phi) = \sum_{j=0}^{5} A_{i,j}\phi^i$

$\alpha_i(\phi)$	$A_{i,0}$	$A_{i,1}$	$A_{i,2}$	$A_{i,3}$	$A_{i,4}$	$A_{i,5}$
High temperature regime (600-900 K)						
iso-octane	-2.564	40.879	-94.888	92.663	-40.318	6.488
n-heptane	6.253	-3.876	-8.627	13.795	-6.094	0.818
toluene	1.450	16.212	-40.638	37.634	-14.632	1.892
Low temperature regime (400-600 K)						
iso-octane	-0.610	29.461	-75.525	78.128	-35.367	5.856
n-heptane	2.368	14.331	-45.612	50.307	-23.321	3.901
toluene	0.105	24.815	-63.708	64.374	-28.146	4.469

Table 4.3 Coefficients for fitting pressure dependence, $\boldsymbol{\beta}_i(\phi) = \sum_{j=0}^{5} B_{i,j}\phi^i$

$\beta_i(\phi)$	$\mathbf{B}_{i,0}$	$\mathbf{B}_{i,1}$	$\mathbf{B}_{i,2}$	$\mathbf{B}_{i,3}$	$\mathbf{B}_{i,4}$	$\mathbf{B}_{i,5}$
iso-octane	-1.299	0.601	5.019	-8.817	5.203	-1.024
n-heptane	-0.954	-1.319	8.365	-11.400	6.147	-1.161
toluene	0.135	-6.040	16.668	-18.303	8.776	-1.527

4.2 G-equation Model for LES

The flame propagation is occurred with an interaction of transport processes and chemical reaction within the flame front. In the flamelet models, these processes are expressed by the flame front as a thin flame sheet propagating with the laminar burning velocity. Williams [101] first introduced a level set approach, so called the G-equation, based on the flamelet model to reproduce the behavior of the flame front. The flame front is defined by the iso-surface of non-reacting scalar G. The scalar G is defined that the flame front position is at $G = G_0$, the unburned region is in $G < G_0$ and the burned region is in $G > G_0$. Peters [45] developed the formulation based on the Reynolds-averaged approach for the corrugated flamelets and the thin reaction zone regimes. Pitsch [67] proposed the spatially filtered G-equation for LES. For the sake of brevity, the derivation procedure is briefly introduced in this study and the detailed information is referred to the original publication [67]. Prior to using the filtered g-equation model proposed by Pitsch, the combustion regime of the target engine was investigated as shown in Figure 4.4. RANS approach was used to simulate the combustion in the SI engine under the operating condition of the target engine described in the chapter 6. The numerical setup is shown in Table 4.4. According to the result, the combustion regime of the target engine condition is under the corrugated flamelets regime. Therefore, the filtered G equation for the corrugated flamelets is derived as equation (4.2.1).

$$\frac{\partial \check{G}}{\partial t} + \hat{v} \cdot \nabla \check{G} = -\widehat{S_L \boldsymbol{n}} \cdot \nabla \check{G} \tag{4.2.1}$$

Where, $\widehat{G}$: the filtered flame front location

$\widehat{v}$:the filtered velocity

S_L:the flame propagation term for the corrugated flamelets regime

n:the normal vector of the filtered flame front position

The flame propagation term for the corrugated flamelets regime $\widehat{s_L \boldsymbol{n}}$ can be modeled by the filtered laminar burning velocity $\widehat{s_L}$ and the sub-filter turbulent burning velocity s_T as equation (4.2.2).

$$\widehat{S_L \boldsymbol{n}} = \left(\widehat{S_L} + S_T\right)\boldsymbol{n} \tag{4.2.2}$$

The sub-filter turbulent burning velocity is described in the next section.

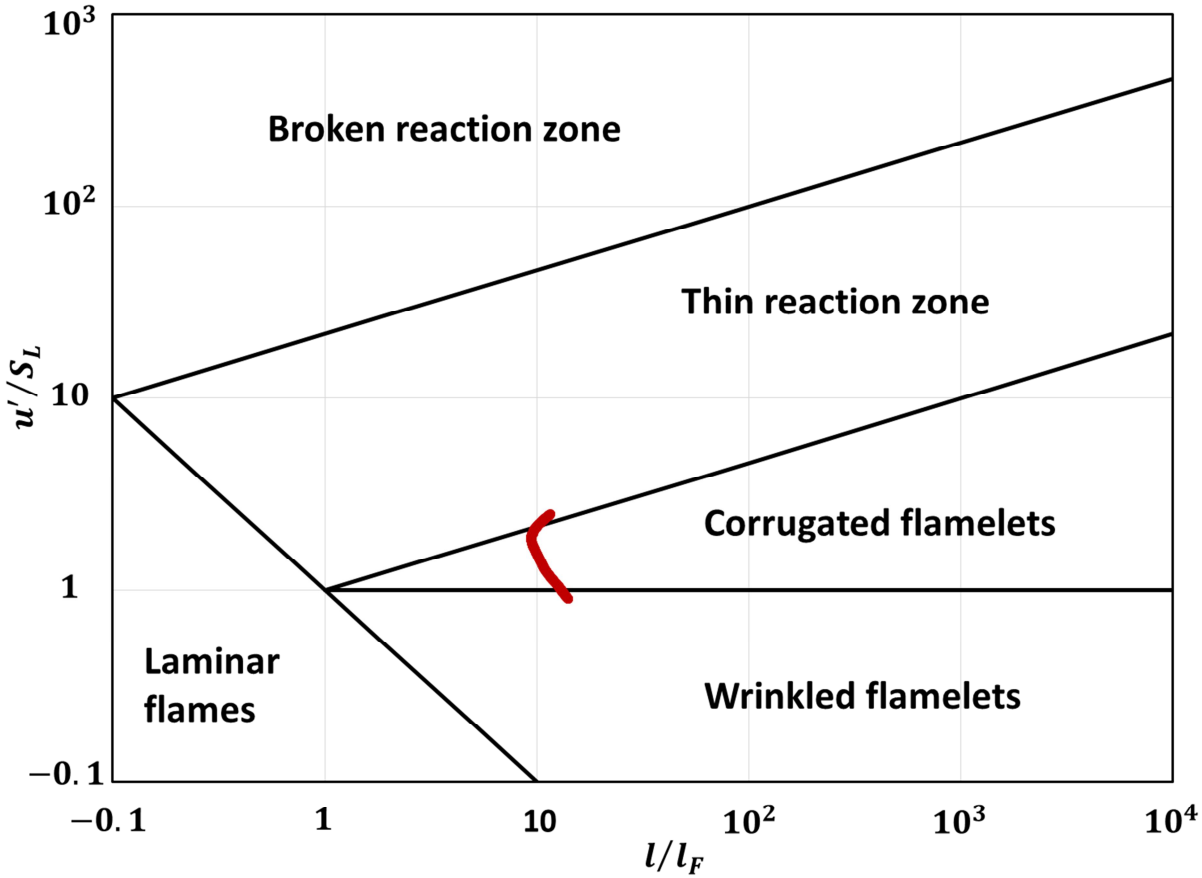

Figure 4.4 Regime diagram for premixed turbulent combustion

Table 4.4 The numerical setup of RANS approach

Parameter	Specification
Turbulent model	k-epsilon / RNG
Combustion model	G-equation (Level-set)
Ignition model	Single flame kernel model
Wall model	Standard wall function
Heat transfer model	GruMo-UniMORE
Fuel	TRF surrogate fuel

4.3 Sub-filter Turbulent Burning Velocity

The sub-filter turbulent burning velocity is derived from the sub-filter flame front fluctuations l [67]. For the sake of brevity, the derivation procedure is briefly introduced in this study and the detailed derivation procedure is described in the original publication [67]. The sub-filter flame front fluctuation is determined by the distance of the instantaneous to the filtered flame front as equation (4.3.1) and is schematically shown in Figure 4.5.

$$l = |\mathbf{l}| \text{ with } \mathbf{l} = x_f - \widehat{x_f} \tag{4.3.1}$$

A transport equation for the sub-filter flame front fluctuation is derived by the difference of the displacement speed between the instantaneous flame front and the filtered flame front as equation (4.3.2).

$$\frac{dl}{dt} = \frac{dx_f}{dt} - \widehat{\frac{dx_f}{dt}} \tag{4.3.2}$$

The equation (4.3.2) can be described with the kinematic restoration term and the scalar dissipation term as equation (4.3.3).

$$\frac{dl}{dt} = v - \hat{v} + S_L n - \widehat{S_L n} \tag{4.3.3}$$

The length scale of the sub-filter flame front fluctuation can be derived by multiplying equation (4.3.3) with $\mathbf{l}$ and applying the filtering operation as equation (4.3.4).

$$\widehat{\frac{dl^2}{dt}} = 2\widehat{l \cdot v'} + 2l \cdot \widehat{(S_L \boldsymbol{n})}' \tag{4.3.4}$$

The first term on the right-hand side means the production of flame front wrinkling due to turbulence. The second term describes the flame surface dissipation due to the flame propagation. The production term can be defined as equation (4.3.5).

$$\mathbf{l}\cdot\widehat{\dot{u}} = C_1 C_s \Delta u'_\Delta \tag{4.3.5}$$

Where, c_1: model coefficient

c_s: Smagorinsky constant

Δ: filter size

u'_Δ: SGS velocity

The flame surface dissipation term can be modeled as equation (4.3.6).

$$\mathbf{l}\cdot\widehat{(s_L\boldsymbol{n})}' = -c_2 c_s \Delta s_T \tag{4.3.6}$$

Substituting equation (4.3.5) and (4.3.6) into equation (4.3.4), and assuming that production term equals dissipation terms, equation (4.3.7) can be obtained.

$$S_T = \frac{c_1}{c_2} u'_\Delta \tag{4.3.7}$$

The constants for the equation can be replaced as equation (4.3.8).

$$\frac{c_1}{c_2} = b_1 \tag{4.3.8}$$

Where, b_1 the model constant

Finally, the sub-filter turbulent burning velocity can be written as equation (4.3.9).

$$\frac{s_T}{s_L} = b_1 \frac{u'_\Delta}{s_L} \tag{4.3.9}$$

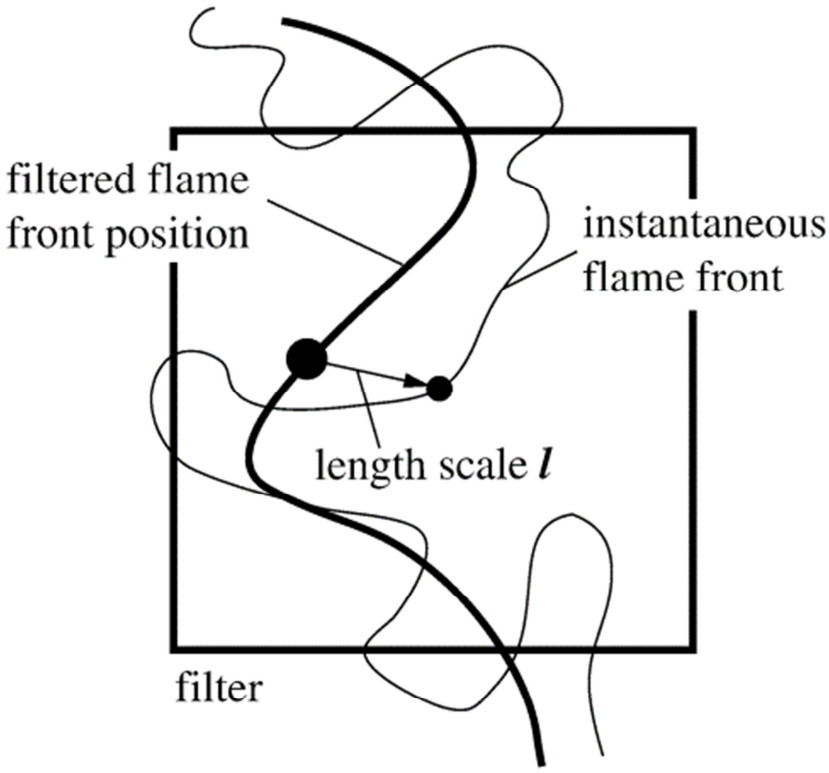

Figure 4.5 Instantaneous and filtered flame front position [67]

Chapter 5. Lagrangian Ignition Model

5.1 Literature Review

The spark ignition process is a very complicated phenomenon in which many different physical processes, such as electric circuit, chemical reaction and interaction of ignition channel and turbulent flow, take place within a short time. The spark ignition process is divided into three phases as shown in Figure 5.1 [102]: the breakdown phase, the arc phase and the glow discharge phase. During the breakdown phase, the voltage rapidly increases up to ~10kV and the current is about 200 A. The spark channel with a diameter of about 40μm and a temperature of about 60,000K is generated. The gas molecules in the channel are fully dissociated and ionized. The duration of the breakdown phase is very short, from 1 to 10 ns. As soon as the breakdown phase is over, the arc phase follows. The arc phase is characterized by very low voltage (<100V) due to voltage drop and high current. And small portion of gases are ionized, but dissociation is quite high in the central region of channel. The spark channel expands due to heat conduction and mass diffusion. Due to the heat loss to anode, cathode and surrounding gases, the temperature is decreases to 6,000K. The arc phase lasts in μs. The voltage increases to 300 to 500V and the current decreases to less than 200mA, moving over to the glow discharge phase. The characteristic of glow discharge phase is very similar with the arc phase. Due to the larger heat loss than the arc phase, the temperature of spark channel is about 3,000K. Due to the long duration (~ms) of glow discharge phase, most of the spark energy is transferred to the surrounding gases during this phase. The detailed characteristics of spark ignition process depends on the spark ignition system and surrounding gas condition. In the 3D simulation for

the ICE, the spark ignition process is very complicated and short duration. Therefore, most ignition models have been modeled by simplifying physical phenomena after the breakdown phase. The description of typical ignition models is followed.

The discrete particle ignition kernel model (DPIK) that was first developed by Fan et al. [103], is a spark ignition model that considers only one single flame kernel. The lagrangian particles are adopted to reflect the local condition at the flame surface of spherical single flame kernel. The particles expand in the radial direction by turbulent velocity and laminar flame speed. In this model, the breakdown, the spark-channel and the deflection of the spark-channel are not taken into account. Therefore, there is a limitation that the ignition simulation in the DPIK model cannot reflect the spark channel elongation by flow field.

Duclos et al. [104] proposed the arc and kernel tracking ignition model (AKTIM). The secondary electric circuit model is adopted to simulate the electrical energy for the spark ignition. To reflect the flow effect on the flame kernel, a set of lagrangian particles are generated between the electrodes. Unlike the DPIK, each of particles represents the gravity center of the flame kernel. The flame kernel propagation takes place as soon as an ignition spot has been formed. However, the model does not take into account the thermal expansion, mainly occurred during the arc phase.

The spark-channel ignition monitoring model (SparkCIMM), derived by Dahms et al. [105, 106], simulates the spark ignition process for a wide range of conditions. The model describes the spark channel dynamics using lagrangian particles. A set of lagrangian particles represents the spark channel like the AKTIM. The flamelet equations are adopted to evaluate the local ignitibility. If the kernels meet the criteria of ignitibility, quasi-spherical flame

kernels are launched at the position of the spark channel and the kernels grow by chemical reactions. When the surface of the flame kernels can be resolved on the computational grid, the particle tracking model is deactivated and the level-set approach is used to simulate the transportation of the mean turbulent flame front. This model reflects the local characteristics of spark channel, but it is a quite complicated and developed for RANS approach.

These introduced ignition models generally successfully realize ignition phenomena in RANS approach. In LES, however, the way to define turbulence is different from RANS, so it is difficult to use the introduced ignition model directly in LES approach. The imposed stretch spark ignition model for LES (ISSIM-LES) is suggested by Colin et al. [107]. This model is based on the same electrical circuit description as the AKTIM [104] and allows multi-ignition description without any ad hoc adaptation since the different ignitions are directly controlled by the flame surface density (FSD) equation, which is modified during early flame ignition. However, this model is suitable for the extended coherent flame model (ECFM) combustion model and requires a suitable LES ignition model for the G-equation.

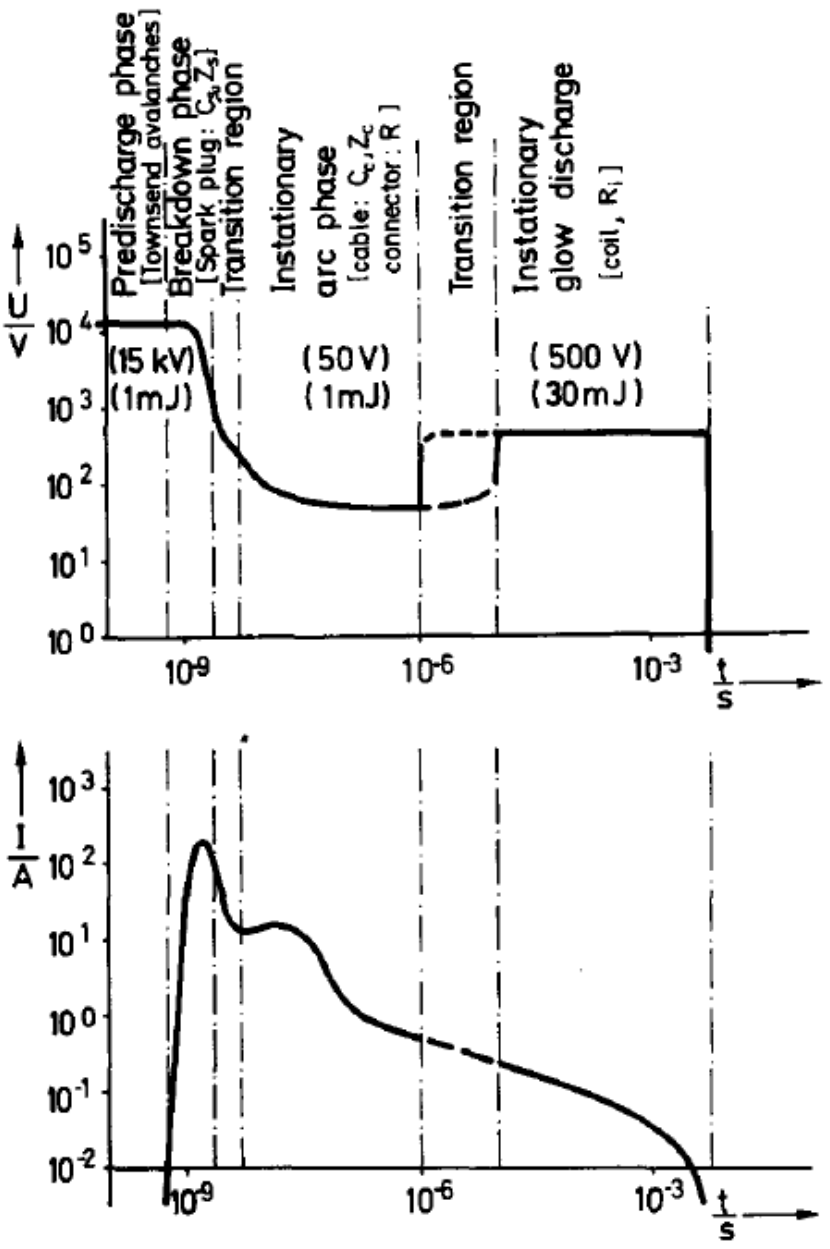

Figure 5.1 Schematic diagram of voltage and current of typical ignition system as functions of discharge time [102]

5.2 Modeling of Ignition

In the present study, lagrangian concept of ignition model is adopted to predict the initial stage of the combustion process in a spark-ignition engine. The spark-channel is initially represented by a set of lagrangian particles that are initially placed along a line between the two electrodes. Particles are convected by mean and turbulent flow and flame kernel grows simultaneously. Specific sub-models are implement to reproduce the ignition phenomenon. The sub-models are:

1. Initialization of particles (spark channel): A set of lagrangian parcels represents the spark channel.

2. Channel elongation: Particles are convected by mean and turbulent flow.

3. Electric circuit: The electrical energy is calculated by the secondary electric circuit model.

4. Plasma channel expansion: After the breakdown phase, the spark channel grows by the thermal diffusion.

5. Spark channel development: The ignition channel is developed by chemical reactions.

6. Restrike: Restrike is reproduced by the secondary electric circuit model.

7. Transition between the ignition model and the flame propagation.

5.2.1 Initialization of Particles

Among the three characteristic stages of ignition in SI engines, namely the breakdown, the arc and the glow discharge, only the last two are modeled because of the very short duration (~ns) of the breakdown phase. At ignition timing, the set of lagrangian particles are generated along the spark-gap centerline. In this study, ten particles are generated and a particle is added if the distance between neighboring two particles exceed 0.2 mm. The initial temperature and the diameter of the particles are estimated the following equations (5.2.1) and (5.2.2) [108, 109]. The breakdown temperature, T_{bd}, is 60,000 K suggested by Refael et al. [109] and the plasma channel specific heat ratio, k, is equal to 1.66. The breakdown energy is computed by the electrical circuit model and it will be explained further in detail.

$$T_i = \left[\frac{1}{k}\left(\frac{T_{bd}}{T_u} - 1\right) + 1\right] T_u \tag{5.2.1}$$

$$d_i = 2\left[\frac{k-1}{k}\frac{E_{bd}}{p d_{gap}\left(1-\frac{T_u}{T_i}\right)\pi}\right]^{1/2} \tag{5.2.2}$$

Where, T_u: unburned temperature

. T_{bd}: breakdown temperature

k: plasma channel specific heat ratio

E_{bd}: breakdown energy

d_{gap}: length of spark plug gap

5.2.2 Channel elongation

The motion of the spark channel, including the turbulent stretch and wrinkle effect, is modeled by the following convection equation solved for each representative lagrangian particle, p. The indices (p) and (cell) refer to the particle and to the computational grid cell value, respectively. The SGS turbulent velocity is denoted by u'_{SGS}. $x_{p,cell}$ is the local distance vector between the particle location and the corresponding grid cell center. $\widetilde{\ }$ indicates the sub-filtered value and $\overrightarrow{\ }$ denotes the vector. The rand-operator provides a random number between [-1, 1] to reflect the SGS turbulent velocity effect.

$$\widetilde{\overrightarrow{u_p}} = \widetilde{\overrightarrow{u_{cell}}} + \nabla\widetilde{\overrightarrow{u_{cell}}} \cdot \Delta\overrightarrow{x_{p,cell}} + \left(\widetilde{\overrightarrow{u'_{sgs}}} + \nabla\widetilde{\overrightarrow{u'_{sgs}}} \cdot \Delta\overrightarrow{x_{p,cell}}\right) \cdot sign(rand) \tag{5.2.3}$$

5.2.3 Electric circuit model

The energy transferred from the electrical circuit to the gas phase might affect significantly the flame kernel development. For this reason, the effects of electrical circuit on the flame kernel growth process need to be taken into account. Generally, the electric system of the spark plug is composed by the primary and the secondary circuit [104, 110], as illustrated in Figure 5.2.

The energy is sufficiently stored in the primary inductance before ignition timing. Therefore, only the secondary electric circuit is modeled in detail. In fact, the known amount of energy stored in the primary circuit at spark time is transferred to the secondary circuit as shown in equation (5.2.4).

$$E_S' = C_{eff} E_p \tag{5.2.4}$$

Where, E_S': initial secondary electric circuit energy for the breakdown phase

E_p: primary electric circuit energy

C_{eff}: transmission coefficient

Here, the transmission coefficient models the secondary inductance dissipation during the energy transfer from the primary to the secondary circuit and 0.6 was estimated by Duclos et al. [104]. Due to the very short duration of the breakdown phase, the breakdown phase effect is considered only as an initial condition of arc phase. The breakdown energy is calculated by equation (5.2.5) [111].

$$E_{bd} = \frac{V_{bd}^2}{C_{bd}^2 d_{gap}} \tag{5.2.5}$$

Where, E_{bd}: breakdown energy

V_{bd}: breakdown voltage [kV]

C_{bd}: breakdown constant [kV]

d_{gap}: inter-electrode distance [mm]

The breakdown voltage is computed as follows

$$V_{bd} = \mathrm{a} + \mathrm{b}\frac{p}{T_u} + c\frac{p}{T_u} d_{gap} \tag{5.2.6}$$

as reported in [111], the coefficient values of equation (5.2.6) are the following: a = 4.3 kV , b = 136 (kV·K)/bar and c = 324 (kV·K)/(bar·mm).

Consequently, the secondary circuit energy, E_s, at the beginning of the arc phase is obtained from equations (5.2.4) and (5.2.5) as

$$E_s = E_S' - E_{bd} \tag{5.2.7}$$

The time variation of secondary circuit energy is calculated as equation (5.2.5)

$$\frac{dE_S(t)}{dt} = -R_S i_S^2(t) - V_{IE}(t) i_S(t) \tag{5.2.8}$$

Where, R_S: Resistance of secondary electric circuit

i_S: current of secondary electric circuit

V_{IE}: voltage between the electrodes

The current of secondary electric circuit and the voltage between the electrodes are time-dependent parameters computed at each time-step as

$$i_S(t) = \sqrt{\frac{2E_S(t)}{L_S}} \tag{5.2.9}$$

$$V_{IE}(t) = V_{cf} + V_{af} + V_{gc}(t) \tag{5.2.10}$$

Where, L_S: impedance of the secondary electric circuit

V_{cf}: cathode voltage fall, 252 [V] [112]

V_{af}: anode voltage fall, 8.45 [V] [112]

V_{gc}: gas-column voltage fall [V]

The gas-column voltage fall is obtained as below equation.

$$V_{gc}(t) = a_{gc} l_{spk}(t) i_S^{b_{gc}}(t) p^{c_{gc}}$$

(5.2.11)

with the spark channel length (l_{spk}) in mm, the pressure (p) in bar and the coefficients (a_{gc} = 6.31, b_{gc}=-0.75 and c_{gc} = 0.51) for the glow discharge phase.

The spark discharging energy from the secondary electric circuit to the mixture gas is estimated as following equation (5.2.12) [104].

$$\dot{Q}_{spk} = \eta_{eff} V_{gc}(t) i_S(t)$$

(5.2.12)

During the spark discharge, there is heat loss to the electrodes. Therefore, the efficiency of the energy transfer process from the electrical circuit to the mixture gases is estimated as following equation (5.2.13) [110, 113].

$$\eta_{eff} = \eta_0 + \frac{(\eta_\infty - \eta_0) U^3}{A + U^3}$$

(5.2.13)

Where, η_0: energy transfer efficiency under quiescent mixture condition, η_0=8

η_∞: energy transfer efficiency under high velocity flow condition, η_∞=30

A: constant coefficient, 700 [m^3/s^3] for the glow discharge phase

U: average velocity at which channel is located

The spark discharge is maintained until the secondary circuit energy (E_s) reaches 0.

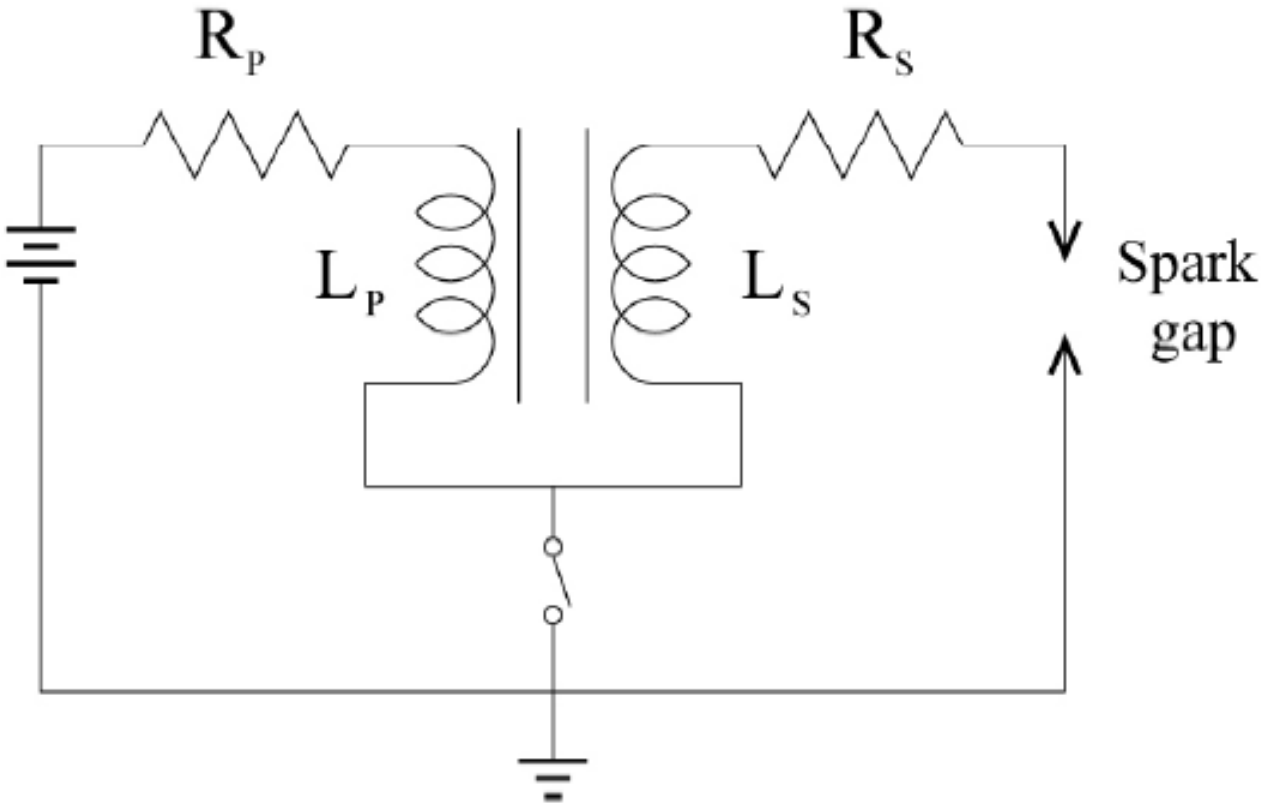

Figure 5.2 Schematic of primary and secondary electric circuit [110]

5.2.4 Plasma channel expansion.

After the breakdown phase, the initial temperature and the radius of the spark channel are obtained by equations (5.2.1) and (5.2.2). Although slightly different depending on the ambient temperature and pressure, the initial temperature and radius are about 40,000K and 0.2mm. When the temperature is high, generally $T_p > 3T_{ad}$, the heat conduction from the hot plasma channel to the unburnt mixture is important and expansion due to chemical reactions and heat transfer from the electric circuit is neglected [110]. Until the channel temperature remains higher than $3T_{ad}$, the plasma channel temperature is computed by solving the heat conduction equation as below equation (5.2.14) [113].

$$\frac{\partial T_{pl}}{\partial t} = \alpha \cdot \nabla^2 T_{pl} + \frac{\dot{Q}_{spk}}{\rho_{pl} \cdot c_{p,pl} \cdot V_{pl}} \quad (5.2.14)$$

Where, T_{pl}: plasma channel temperature

α: plasma thermal diffusivity

$\dot{Q}_{spk}$: spark discharging energy

ρ_{pl}: density under plasma

$c_{p,pl}$: specific heat under plasma

V_{pl}: volume of plasma channel

A sub-cycling procedure ($\Delta t < 0.1$ ns) between CFD iterations is used to solve equation (5.2.14). The domain is discretized on a 1D, axisymmetric grid

representing the mixture gas region that surrounds the spark electrodes. The grid height is set to be equal to the distance between the electrodes, while the radial length of the computational domain is set to 10 mm, which is sufficiently longer than the maximum diameter of the plasma channel that is reached during arc phase. The grid size is 10 µm and the following initial and boundary conditions are imposed at spark time:

$$\mathrm{t} = t_0 : T_{pl} = T_i \; if 0 < r < r_i ; \; T_{pl} = T_u \; if \; r < r_i ; \;\; r = r_\infty : T_{pl} = T_u$$

At each time-step, the channel radius r_{ch} is identified at the location where the plasma temperature equals to the adiabatic flame temperature in the 1D domain.

The properties such as thermal diffusivity α, heat capacity $C_{p,pl}$ and density $\rho_{p,pl}$ need to be known. During the thermal expansion, the plasma temperature is very high, and dissociation of molecules and atom ionization play a very important role. These phenomena are considered by assuming chemical equilibrium and neglecting fuel contribution. In this way, the thermodynamic and transport properties functions provided by D'Angola et al. [114] are employed to calculate heat conduction equation. The heat conduction equation is solved until the temperature is below three times of adiabatic temperature ($T_{pl} < 3T_{ad}$).

Figure 5.3 shows the spatial distribution of temperature in the plasma channel calculated by 1D axisymmetric simulation. The ambient temperature is 700 K and the ambient pressure is 10 bar. Over time, the mean temperature of plasma channel decreases and the plasma channel widens to radial direction. At each given time, the *r* at the point where the plasma temperature $T_{pl}(r)$equals the adiabatic temperature is the radius of the plasma channel. After about 10 µs, the mean temperature of the plasma channel is less than three times the

adiabatic temperature, growth by chemical reactions is dominant rather than growth by the thermal expansion, hence the thermal expansion model is deactivated.

The plasma thermal expansion is actually a very short time (~10ms), but because of the very short time step and the small grid size of the sub-model, the required CPU time is very large. Furthermore, the plasma channel expansion model is only effected by the ambient temperature and pressure. Therefore, in this study, the required time and the radius of the ignition channel after the plasma channel expansion is calculated in advance and the database is built at the wide range of temperature (600 – 800K) and pressure (6 – 26 bar) conditions as shown in Figure5.5. Finally, the channel radius is derived from a time-based correlation function to predict the radius after the plasma thermal expansion (Arc phase).

The time when the plasma temperature is less than three times of adiabatic temperature is obtained as equation (5.2.15).

$$\mathrm{t} = t_{ref}\left(\frac{P}{P_0}\right)^{\alpha}\left(\frac{T}{T_0}\right)^{\beta} \qquad (5.2.15)$$

Where, $\alpha(P) = -6.3644e^{-5}P^2 + 3.6235e^{-2}P + 8.0157e^{-1}$

$\beta = -2$

$t_{ref=1.1939e^{-2}}\ [ms]$

At that time, the radius is obtained by below equation (5.2.16).

$$\mathrm{r} = r_{ref}\left(\frac{P}{P_0}\right)^{\alpha}\left(\frac{T}{T_0}\right)^{\beta} \qquad (5.2.16)$$

Where, $\alpha(P) = -1.0914e^{-5}P^3 + 1.8395e^{-4}P^2 + 1.1632e^{-2}P - 3.8142e^{-2}$

$\beta(T) = -1.0860e^{-3}\mathrm{T} - 5.6300e^{-2}$

$r_{ref} = 3.4232e^{-3}$ [m]

$T_0 = 700$ [K]

$P_0 = 10$ [bar]

The channel temperature is approximated by three times the adiabatic temperature.

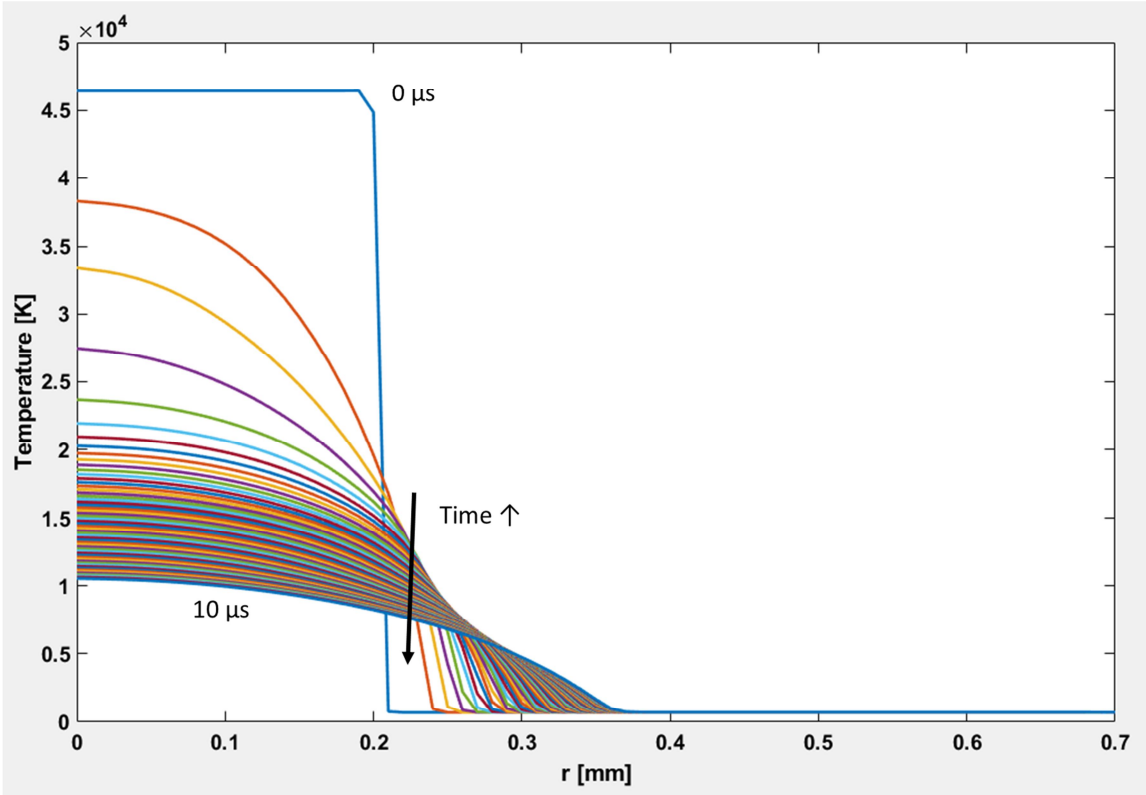

Figure 5.3 The spatial distribution of temperature in the plasma channel calculated by 1D axisymmetric simulation. The ambient temperature is 700 K and the ambient pressure is 10 bar.

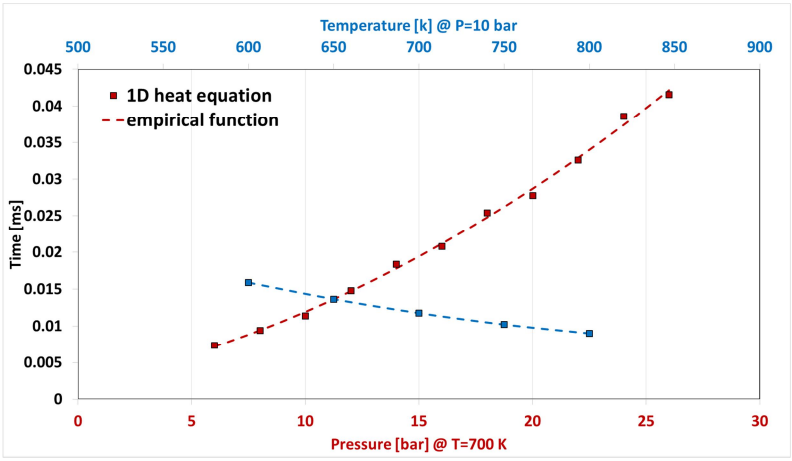

(a)

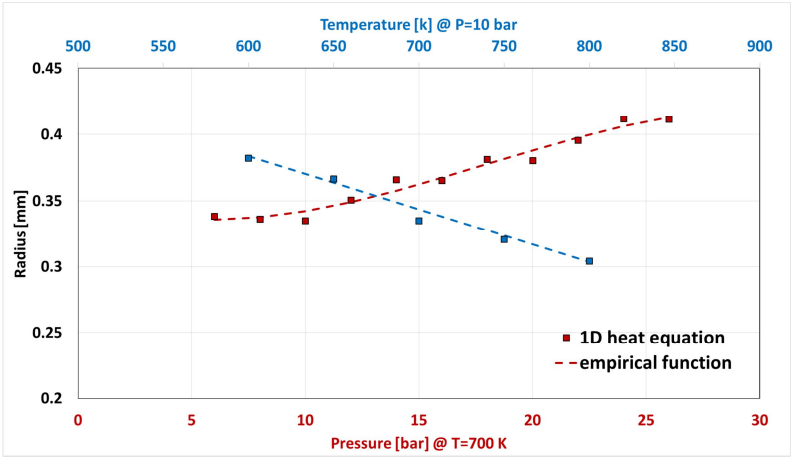

(b)

Figure 5.4 The required time for thermal expansion (arc phase) and the channel radius after thermal expansion. Dots represent the result of 1D heat conduction equation and solid lines indicate the result of empirical function. (a) The required time for thermal expansion, (b) the channel radius after thermal expansion.

5.2.5 Ignition channel development

After the plasma channel expansion, the ignition channel is developed by chemical reactions. The ignition channel is generated in a cylinder shape between the anode and the cathode of spark plug. Each lagrangian particles represents the channel location and interacts between the ignition channel and the 3D domain. The sum of the distances between particles means the length of the ignition channel. The particles are stretched by mean and turbulent flow as described in equation (5.2.1). At the same time, the ignition channel grows by chemical reactions. In this model, the properties of ignition channel are assumed uniform, thus the averaged properties in each particles represent the ignition properties.

The radius of ignition channel is calculated following

$$r_{ch} = \sqrt{\frac{m_{ch}}{\rho_{ch}\pi l_{ch}}} \quad (5.2.17)$$

Where, r_{ch}: ignition channel radius

m_{ch}: ignition channel mass

ρ_{ch}: density in the ignition channel

l_{ch}: ignition channel length

And the density in the ignition channel is obtained by equation (5.2.18)

$$\rho_{ch} = \frac{P}{R_b \cdot T_{ch}}$$

(5.2.18)

Where, R_b: specific gas constant of burned gas

T_{ch}: ignition channel temperature

The temperature is calculated from the following channel temperature equation:

$$\frac{d}{dt}T_{ch} = -\frac{\dot{m}_{ch}}{m_{ch}}(T_{ch} - T_{ad}) + \frac{\eta_{eff}}{m_{ch}C_p} + \frac{1}{\rho_{ch}C_p}\frac{dp}{dt}$$

(5.2.19)

The mass consumption rate of the ignition channel is calculated by equation (5.2.20),

$$\frac{d}{dt}m_{ch} = \dot{m}_{ch} = 2\pi r_{ch} l \rho_u S_T$$

(5.2.20)

The detailed description of the turbulent burning velocity is in chapter 5.2.7.

5.2.6 Restrike

The restrike is the phenomenon that when the spark channel length increase by interaction with flow, the spark channel is cut off and reformulated between the electrodes. There are two way to model the restrike. First, experimental research [115] shows that the gas-column voltage increase as the

spark channel increase. If the voltage becomes greater than the breakdown voltage, the restrike occurs [110]. Secondly, if the spark channel length becomes longer than a threshold value, then the restrike occurs [105, 116]. The threshold value is determined by the experimental observation. The first way is applicable if the detailed information of spark system is provided. Otherwise, if the information is not provided sufficiently, then the second way may be an alternative. In this study, the first method is adopted with the general information of spark system from literature [14]. In this model, when the restrike occurs, the existing particles representing the spark channel remain without the spark energy from the spark system and a new set of particles is created between the electrodes.

5.2.7 Transition between ignition and flame propagation

When the ignition channel grows by chemical reactions shortly after the plasma expansion, the flame is very thin and unstable, taking time to form a fully turbulent flame brush thickness. For modeling purposes, a one-dimensional steady planar flame is assumed. Then, the turbulent flame brush thickness is obtained as following equation (5.2.21).

$$\ell_{f,t} = b_2 \ell [1 - exp(-C_s/\tau)]^{1/2} \quad (5.2.21)$$

The detailed description is in [45]. The original equation of the turbulent flame brush thickness is derived for RANS approach. In RANS approach, the turbulent flame brush thickness is larger than grid size and takes a long time to fully develop, as the modelling term represents all length scales of turbulence. However, in LES, the turbulence scales less than the grid size (filter size) is modelled and others are resolved. Therefore, the turbulent flame thickness is

smaller than the grid size and it requires a shorter time than RANS to be fully developed.

According to the equation (5.2.21), the fully developed turbulent flame brush thickness is expressed as $b_2 l$ with $b_2 = 2.0$ and l is the integral length scale [117]. Then, the normalized turbulent flame brush thickness is introduced as

$$\ell^* \equiv \ell_{f,t}/(b_2 \ell) \quad (5.2.22)$$

$$\ell^* = [1 - exp(-C_s/\tau)]^{1/2} \quad (5.2.23)$$

In the corrugated flamelets regime, the turbulent burning velocity is assumed to be independent on Damkohler number at high Damkohler number and a fully developed flame is shown in equation (5.2.24).

$$\sigma_t = b_1 v^{'}/S_L \quad (5.2.24)$$

It assumes that only small scale turbulent eddies smaller or equal to the flame brush thickness in the inertial range of the energy cascade shown in Figure 2.1 are able to effect on the flame surface. The small scale turbulent eddies are represented by the SGS turbulent length. Therefore, using a relationship of equation (5.2.25) [68], a scaling of the SGS turbulence velocity down to a given turbulent velocity scale, whose the turbulent length scale is smaller than the LES filter, in the inertial range of the turbulent energy spectrum is shown in equation (5.2.26).

$$v' \sim v_0' (l/l_0)^{1/3}$$

(5.2.25)

Where, v': turbulent velocity of a given eddy size l

v_0': turbulent velocity of a given eddy size l_0

$$v' = \left(l/\ell_{f,talg}\right)^{1/3} v_{\text{sgs}}^{'}$$

(5.2.26)

Where, v': turbulent velocity of a given eddy size

$v_{\text{sgs}}^{'}$: SGS turbulent velocity

l: turbulent length scale smaller than the LES filter (grid size)

$\ell_{f,talg}$: fully developed flame brush thickness resolved by grid size

Finally, the turbulent burning velocity is derived by equation (5.2.27).

$$\frac{S_T}{S_L} = b_1 \frac{u_\Delta'}{S_L} \ell^*$$

(5.2.27)

Here, l^* reproduce the transition state between the laminar flame propagation and the fully turbulent flame propagation. In this study, when the $(l^*)^{1/3}$ reaches 0.5, then the lagrangian ignition model is deactivated and the level-set approach is used to numerically transport the turbulent flame front.

Chapter 6. Experimental and Numerical Setup

6.1 Experimental Setup

A 0.5 L single cylinder engine equipped with the DPFI and a naturally aspirated (NA) system was used [118]. The detailed engine specifications and operating conditions are shown in table 6.1. The length of bore and stroke was 81 mm and 97 mm, respectively. The compression ratio was directly measured and it was 11.91. The engine was operated at 1500 rpm and the load was nIMEP 5.4 bar.

The schematic diagram of the engine testing system is shown in Figure 6.1. A Kistler 6056A piezoelectric pressure sensor was mounted flush in the cylinder head. AVL IndiMicro IFEM amplifier was used to amplify the in-cylinder pressure signal. A Kistler 4045A2 absolute pressure sensor was implemented in to the intake manifold to measure the intake pressure and the signal was amplified by a Kistler 4603 piezo-resistive amplifier. AVL IndiModule acquired the in-cylinder and intake pressure signals and analyzed the characteristics of combustion. Air, oil and coolant temperature were controlled by external control system. Oil pressure was controlled by an oil pump system with inverter and was supplied into the engines. A flow meter, OVAL CA001, was used to obtain fuel flow rate. Horiba MEXA-110λ and ETAS ES631.1 were used to monitor the air-fuel ratio during operation to obtain the stoichiometric condition. A Horiba MEXA-7100DEGR exhaust gas analyzer was used not only to measure emissions but also to validate the air-fuel ratio.

The K-type thermocouples were implemented to measure the head, piston and liner surface temperature [118]. The measuring points are shown in Figure 6.2. A special linkage system was developed for the reciprocating piston moving motion. The measured boundary temperatures are listed in Table 6.2 and they were used for the boundary condition of the 3D simulation.

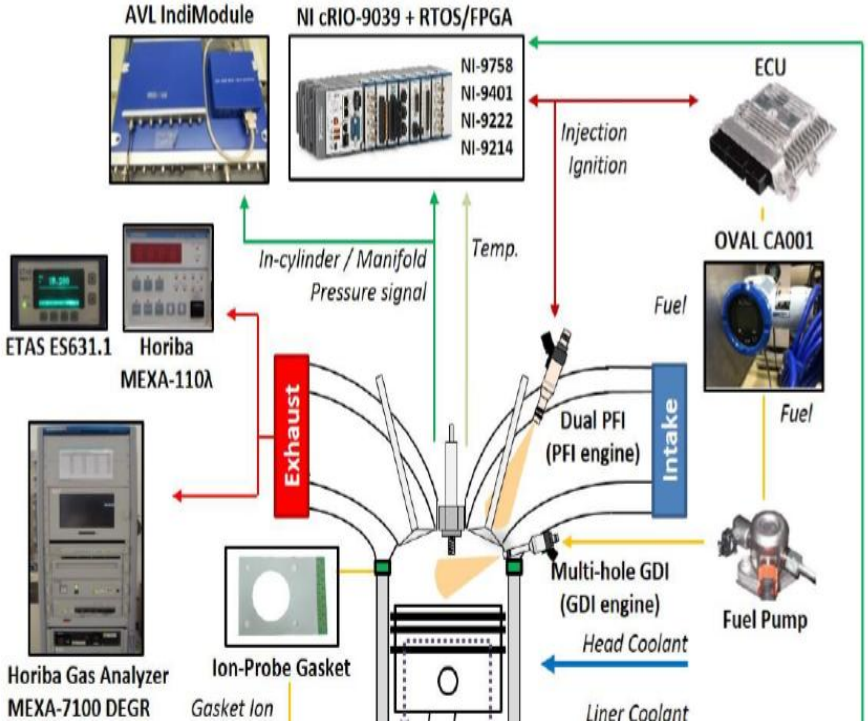

Figure 6.1 Schematic diagram of experimental system [118]

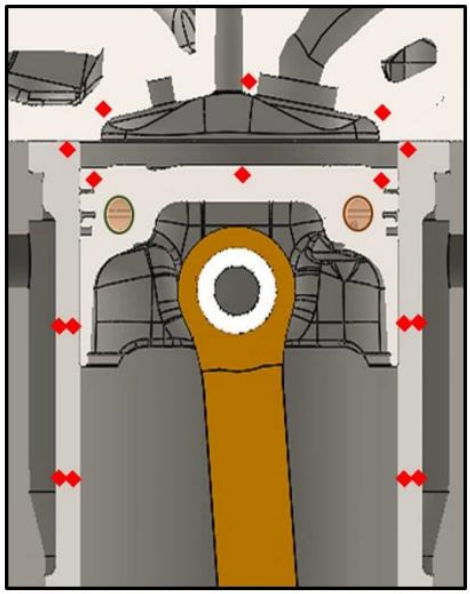

(a)

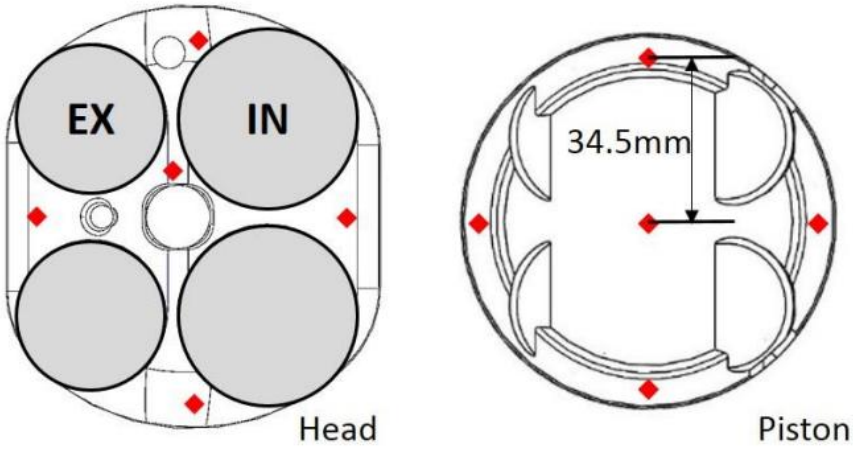

(b)

Figure 6.2 Temperature measurement points on the liner, head and piston. (a) Side view of combustion chamber, (b) Head and piston [118]

Table 6.1 Engine specification

Parameter		Specification
Engine		Single-cylinder N/A dual CVVT
Displacement volume [cc]		499.8
Stroke [mm]		97
Bore [mm]		81
Compression ratio		11.91
RPM [rev/min]		1500
Load		nIMEP 5.4 bar
Spark timing		21CA bTDC
Injection timing		540 CA bTDC
Valve timing (@ 0.1mm)	EVO	68 CA bBDC
	EVC	1 CA aTDC
	IVO	10 CA aTDC
	IVC	67CA aBDC
Maximum valve lift [mm]		10

Table 6.2 The measured Wall boundary temperature

Region	Temperature [K]	Region	Temperature [K]
Liner	393	Intake valve	403
Piston	453	Exhaust valve	513
Head	403	Intake port	373
		Exhaust port	473

6.2 Numerical Setup

In the present study, the CONVERGE v2.4.27 solver is used to calculate the mass, momentum and enthalpy equations of LES. And the ignition model is coupled to the CONVERGE solver by using user defined function. The grid size in the intake port and the cylinder consists of grid of 1 mm, and the exhaust port is 2 mm. The valve sheet is 0.5mm and the region around the spark plug is 0.125mm. Thanks to the adaptive mesh refinement (AMR) function, which is an advantage of CONVERGE, the region with large velocity gradient is refined to 0.5mm and the region around the flame surface is 0.25mm. Therefore, the grid size is refined to suit the transient characteristics of the engine, enabling efficient calculation.

The PISO algorithm and 2nd order monotonic upstream-centered scheme for conservation laws (MUSCL) scheme are employed as the Temporal and spatial discretization scheme. SOR scheme is applied to momentum, mass, energy and SGS turbulent kinetic energy equations. The time step is determined by the Courant-Friedrichs-Lewy (CFL) number. Basically the number of CFL 1 is the criterion for the determination of the time step. During the valve opening and closing time, the CFL number of 0.5 is used to calculate the time step due to very fast flow near valves. The DSM is adopted for the SGS turbulent model and the G-equation is employed as a combustion model. The turbulent burning velocity model for the corrugated flamlets regime is used. The ignition model, developed in this study, is adopted to realize the ignition phenomena. Werner and Wengle model is used for near wall treatment and GruMo-UniMORE model is employed to calculate wall heat transfer. The TRF surrogate fuel is adopted to mimic the domestic gasoline fuel. The described sub-models used for simulation are listed in Table

6.3. As a boundary condition, the intake pressure was obtained directly from the experiment (Figure 6.3) and the exhaust pressure was calculated by GT-power (Figure 6.4). Wall temperature conditions were measured as shown in Table 6.3.

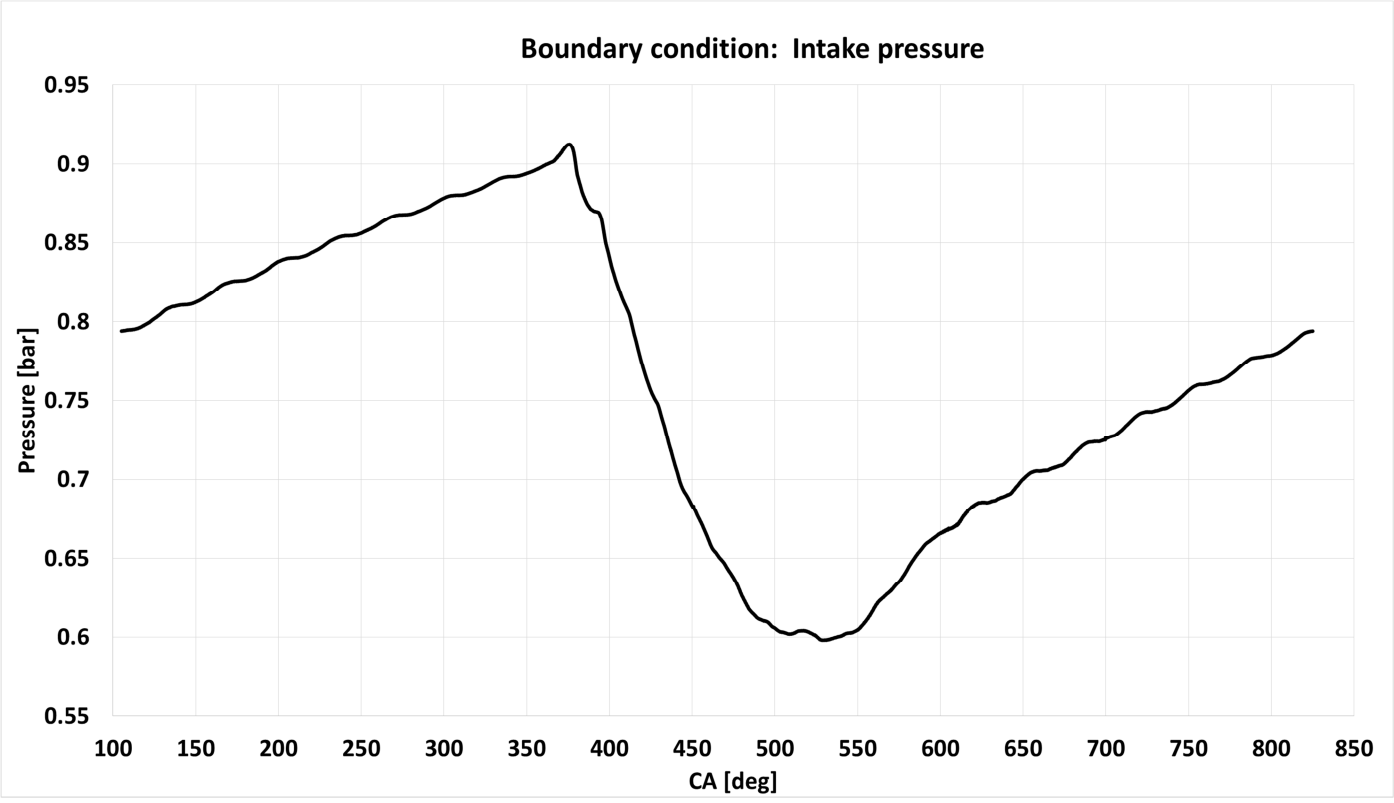

Figure 6.3 Boundary condition of intake pressure measured by experiment

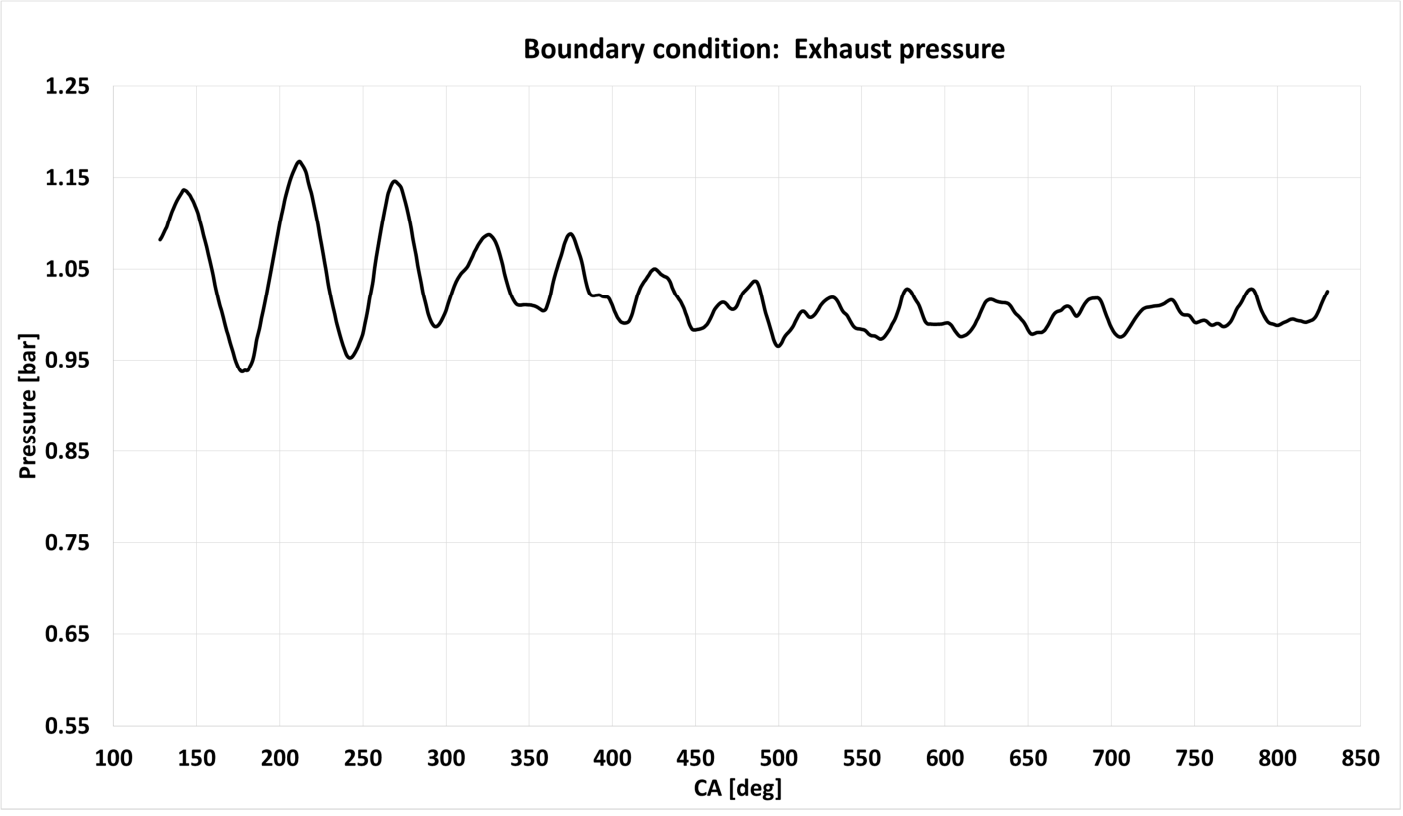

Figure 6.4 Boundary condition of exhaust pressure calculated by GT-power

Table 6.3 Adopted sub-models for simulation

Parameter	Specification
SGS turbulent model	DSM
Combustion model	G-equation (Level-set)
Turbulent burning velocity model	$S_T = b_1 u'_\Delta$ (b_1=3.4) Corrugated flamelets regime
Ignition model	In-house model
Heat transfer model	GruMo-UniMORE
Fuel	TRF surrogate fuel

Chapter 7. Simulation Results of Combustion CCV

In this chapter, the results of the 30 LES cycles are verified using in-cylinder pressure data from experimental data. In addition, the reproduced CCV phenomenon are analyzed in detail to evaluate the factors affecting the CCV. Finally, the most important factor to reduce the CCV is investigated and a guide on how to reduce the CCV is provided with an example of a re-designed piston case.

7.1 Validation of Simulation Results

As the first step of verification, the range of in-cylinder pressure predicted in LES is compared to the in-cylinder pressure range measured in the experiment. In Figure 7.1, the dotted line means the fastest and the slowest value of the experiment and the average value of 100 cycles, while the solid line represents the individual cycles of LES. The in-cylinder pressure of LES cycles fall within the range of cycle deviation of the experiment results, but the range of cyclic variation of LES cycles is slightly narrower than the cyclic variation of experiments. For reasons, the prediction of the cycle deviation of LES may be somewhat underestimated compared to the experiment, as there are many factors affecting the cycle deviation in the actual engine operation, but only the deviation of turbulence flow is considered in LES. And another possibility is that the number of cycles in LES is 30 cycles, less than the 100 cycles in the experiment. Therefore, discrepancy can occur due to differences in the number of samples. Given the differences between experiments and LES, the LES results are well matched with the experimental data in both terms of the combustion accuracy and the cycle-to-cycle variability.

Next, in Figure 7.2, the accuracy of LES for combustion phase is compared with the experimental data with the comparison of the MFB indicating the combustion phase. As noted in the previous comparison of pressure curves, the averaged value is very well simulated, but for the fastest and the slowest cycles, LES predicts slightly slower and faster, respectively.

In general, the CCV of the engine combustion is defined using the deviation of IMEP and peak pressure. IMEP is important parameter in terms of engine efficiency and performance, reflecting all four-stroke in addition to combustion, and peak pressure represents the characteristics of combustion because of variations caused by combustion phenomenon. Therefore, in the present study, the CCV of engine combustion is defined by the deviation of peak pressure for the analysis of the CCV occurring in the combustion phase.

The cycle-to-cycle variation is mainly defined using the COV. The COV is defined in the following equation:

$$\mathrm{COV} = \frac{\sigma}{\mu} \qquad (7.1)$$

Where, σ: standard deviation

μ: mean value

Table 7.1 shows the COVs of each combustion phase and peak pressure measured in LES and in the experiment. In the MFB 5, which indicates the early flame propagation, LES predicts slightly higher deviations, but as flame propagated, LES finally predicts slightly lower deviations of the peak pressure. There are two reasons for the slight discrepancy between the experiment and LES. One is that the sample of LES is smaller than the experiment and, unlike the experiment in LES, only the variation due to the flow is considered. As a

result, although slight difference exists, the CCV of LES has a good agreement with the CCV phenomenon found in the experiment.

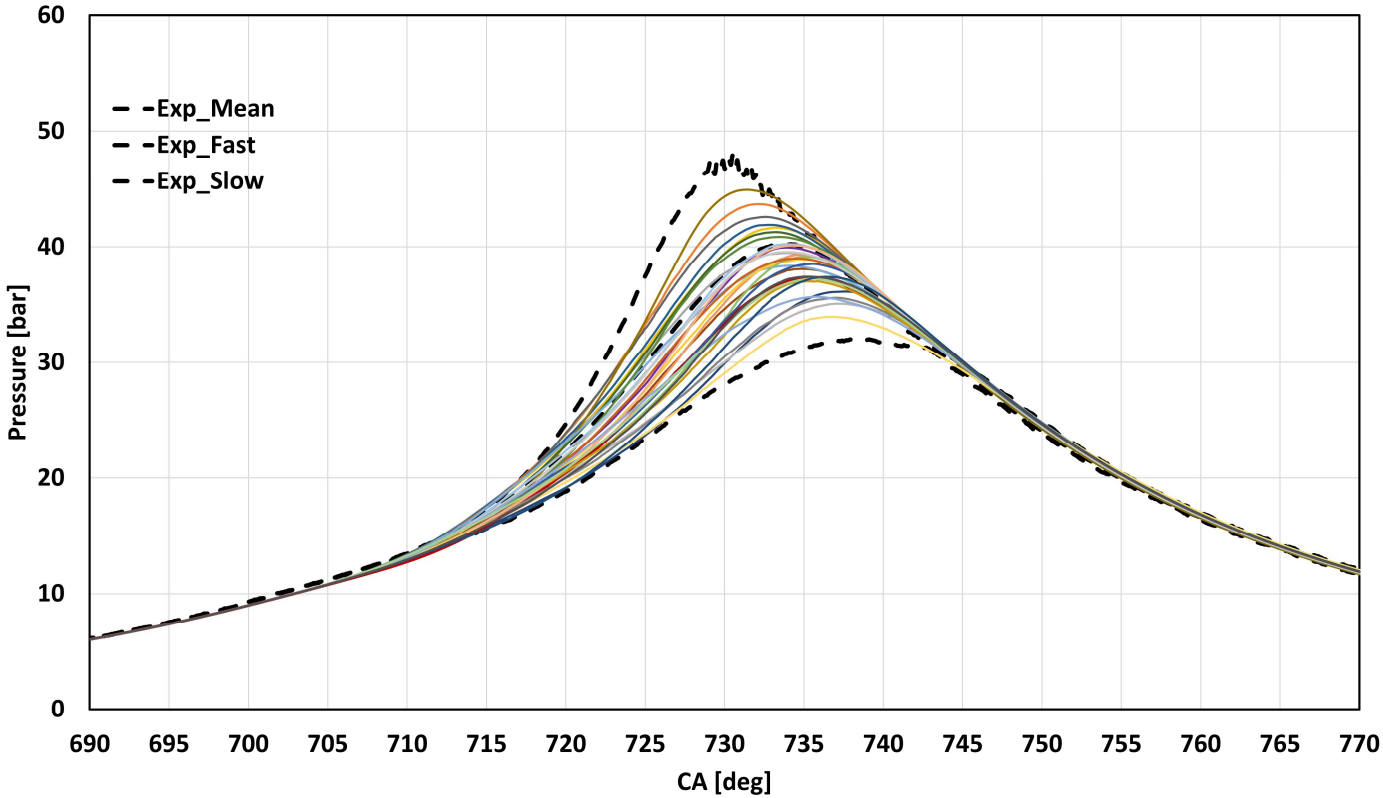

Figure 7.1 Comparison of in-cylinder pressure between LES and experimental data

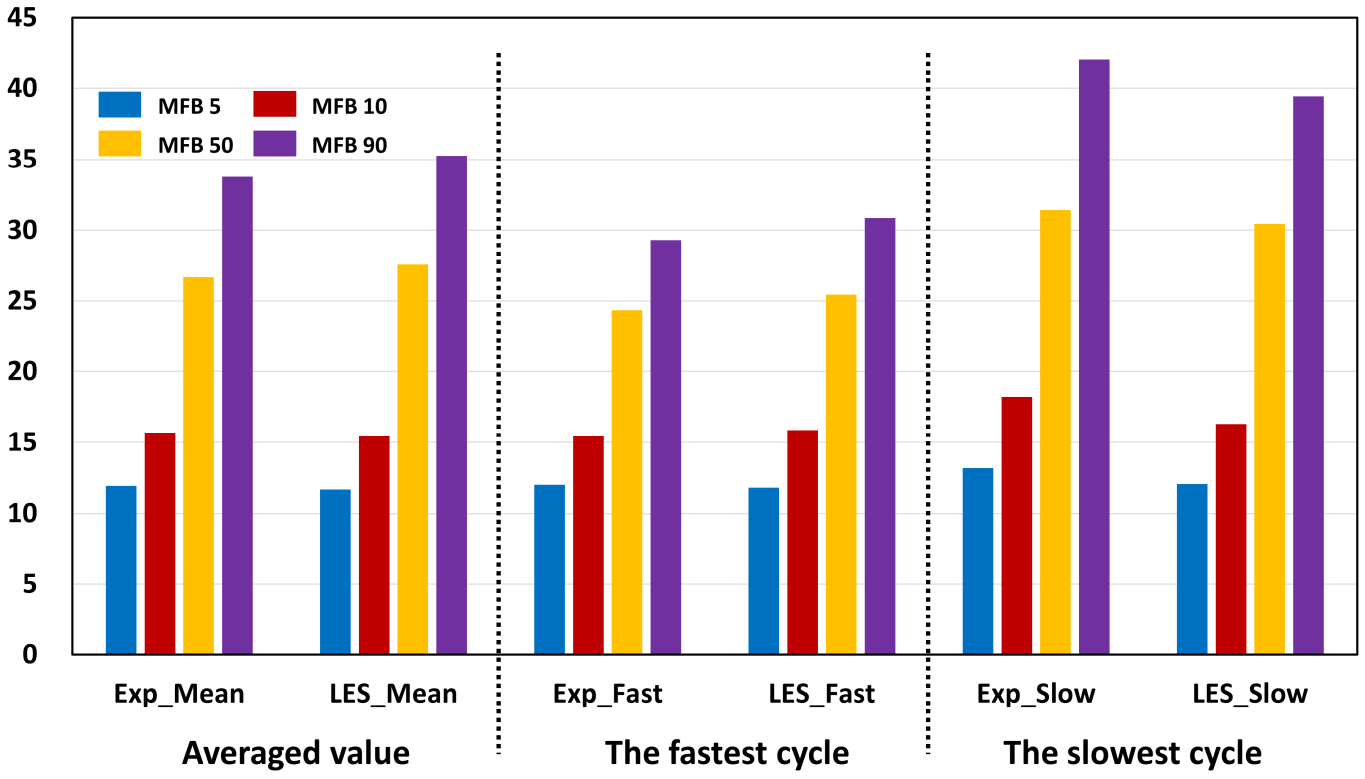

Figure 7.2 Comparison of MFB between LES and Experimental data

Table 7.1 COV of each burn duration

	Experiment	LES
MFB 5	5.00	5.18
MFB 10	5.89	5.35
MFB 50	6.41	5.68
MFB 90	7.36	5.97
Peak Pressure	7.69	6.63

7.2 Correlation between Combustion Phase and Peak Pressure

Flow variation at the early flame propagation stage is known as the dominant source of the CCV. First of all, a correlation coefficient technique is adopted to evaluate the effect of the early flame propagation deviation on the variation of final combustion. The correlation coefficient to analyze the correlation between the two parameters is defined as the following equation:

$$\rho_i = abs\left(\frac{cov(X,Y_j)}{\sqrt{var(X)\cdot var(Y)}}\right) \tag{7.2}$$

In the present research, to find the relationship between deviations, the deviation of the peak pressure and each stage of the combustion phase are defined as comparison factors. First, the relationship between the deviation of the peak pressure and the deviation of each combustion phase is illustrated in Figure 7.3. Naturally, the peak pressure is highly correlated with the MFB as the combustion progresses. However, it is difficult to analyze the source of the CCV because interaction between flame and flow accumulates over time from the time of ignition. For the MFB 50 and the MFB 90, the deviation of the peak pressure is very close to 88% and 96%, respectively, and for Figure 7.4, the relationship between the MFB 50 deviation and the MFB 90 deviation is very close at 90%. Therefore, it is easy to analyze the cause of the CCV because the MFB 50 can represent the overall combustion phase and is about 10 CA degree faster than the MFB90 as shown in Figure 7.2. Next, the MFB 5 is chosen as the factor representing the early flame propagation. In Figure 7.3, there is not much difference between the MFB 5 and the MFB 10 compared with the peak pressure deviation, 58% and 67%, respectively. And looking at

the relationship with the deviation of the MFB 50 in Figure 7.4, correlation coefficients of the MFB 5 and the MFB 10 with the MFB 50 are 70% and 80%, respectively, and the small discrepancy between the two are negligible. Furthermore, the MFB 5 is about 4CA degree faster than the MFB 10 as shown in Figure 7.2, making it more appropriate to analyze the effects of the early flame propagation. To sum up, it can be said that the MFB 50 represents the overall combustion phase, and the MFB 5 represents the early flame propagation. Therefore, the analysis will be conducted on the MFB 5 and the MFB 50 based.

In Figure 7.5, the correlation between the MFB 5 and the MFB 50 is shown to understand the effect of the early flame propagation on the overall combustion phase. The R square value of the trend line between the early flame propagation and the overall combustion phase is 0.37, and it means that the initial flame propagation does not absolutely determine the combustion phase. Therefore, in order to find the cause of the cyclic variation, it is necessary to analyze not only the flow analysis during the early flame propagation, but also all the combustion phase.

To further analyze the relationship between the early flame propagation and the overall combustion phase, the cycle numbers are listed as follows. First, 30 cycles are sorted in ascending order based on the overall combustion phase (MFB 50). The 30 cycles are divided into three group. The first ten cycles are classified as fast cycles, and the last ten cycles are categorized as slow cycles and others are classified as medium cycles. The 30 cycles are sorted again based on the MFB5 to find the relationship between the early phase and overall phase as shown in Figure 7.6. Generally, previous studies concluded that early flame propagation has a dominant effect on the overall combustion phase. However, it is noteworthy in the present study that the early flame propagation

does not have an absolute effect on the overall combustion phase. For example, the fastest cycle (fifth cycle) ended up being the medium cycle of combustion speed, and the fourth and the seventh cycles, which are intermediate combustion speed, changed to fast cycles. These special cases exist, but if slow cycles are looked at, to some extent the early flame propagation affects the entire combustion phase.

In the following section, the effect of turbulent flow on the CCV of combustion is analyzed with the verified LES results. Due to the characteristics of LES, turbulence can be divided into two main categories: the large scale turbulent flow and the small scale turbulent flow. The large scale turbulent flow is resolved and the small scale turbulent flows is simulated through the SGS model. Therefore, the analysis is carried out in terms of the large scale and the small scale turbulent flows.

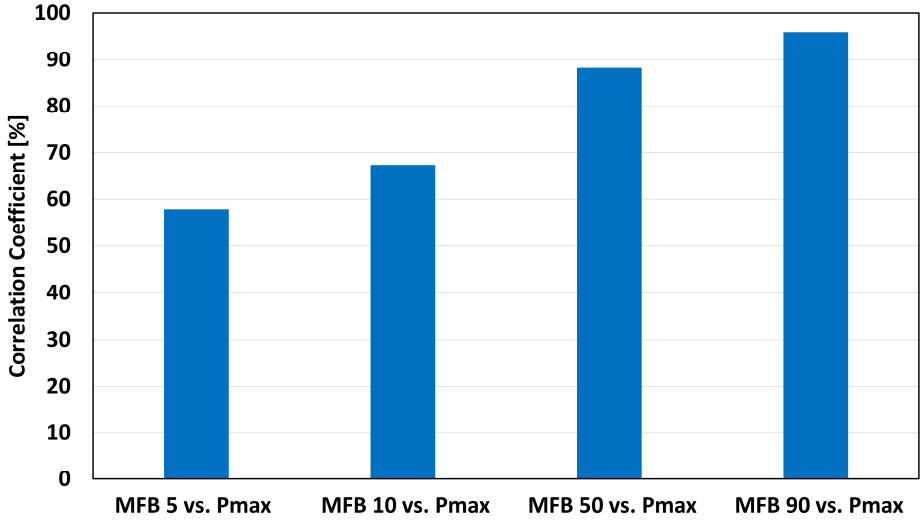

Figure 7.3 Correlation coefficient of COV: MFB5, MFB10, MFB50, MFB90 vs. peak pressure

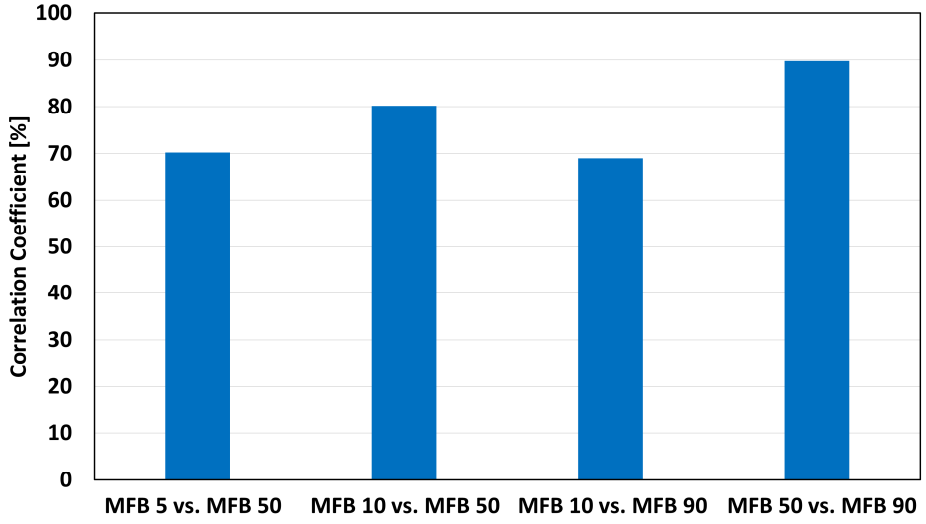

Figure 7.4 Correlation coefficient of COV between MFB rates

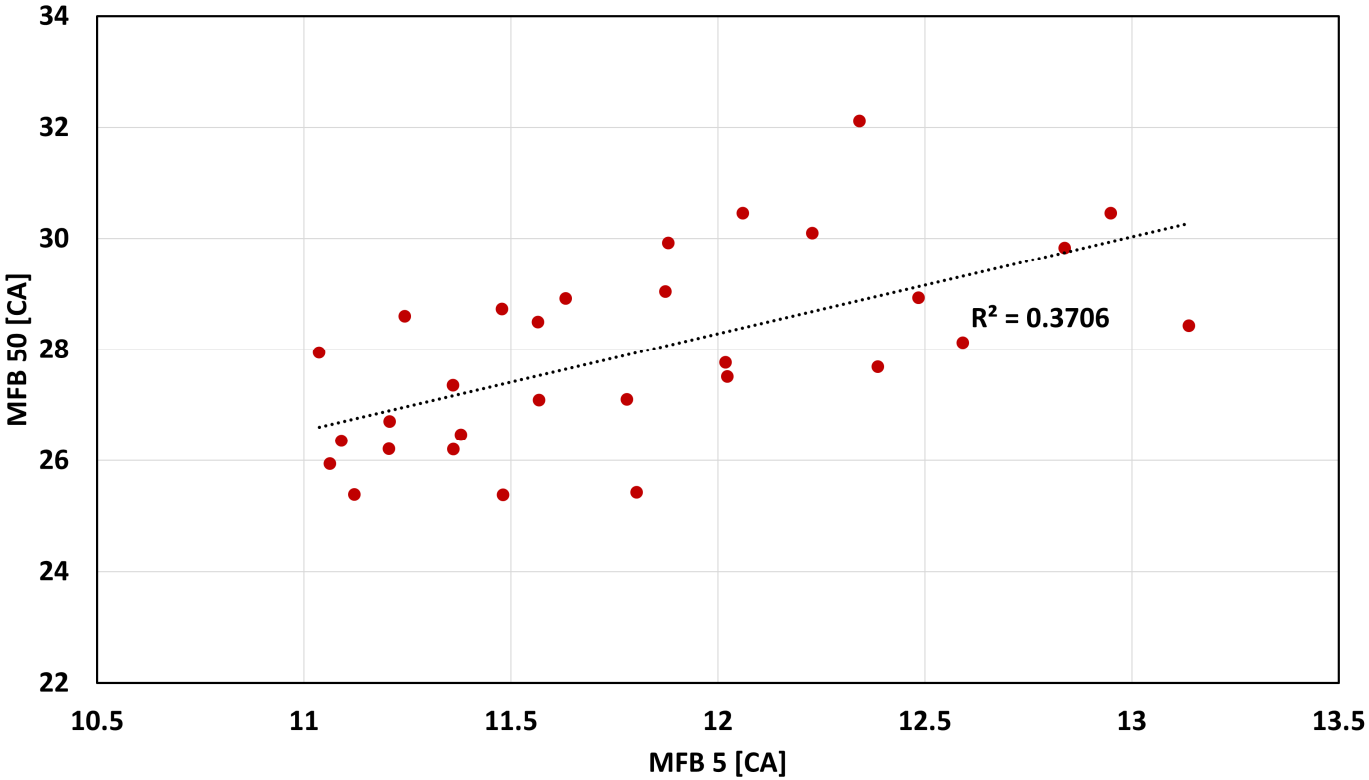

Figure 7.5 The correlation between MFB 5 and MFB 50

MFB5	MFB50
5	4
3	6
1	7
6	3
2	9
10	2
27	1
17	21
9	10
21	24
20	22
4	17
26	14
24	23
15	13
22	5
7	11
19	16
18	26
13	27
14	20
25	15
12	30
29	19
23	28
30	18
11	12
28	25
8	8
16	29

Figure 7.6 Cycles arranged in ascending order according to combustion speed in MFB5 and MFB50

7.3 Investigation of turbulent flow effect on CCV

7.3.1 Small Scale Turbulent Flow Effect on CCV

The small scale turbulent flow is represented as the SGS turbulent kinetic energy in LES. The SGS turbulent kinetic energy and the SGS turbulent velocity are in relation to $u'_{sgs} = \sqrt{\frac{2}{3}k_{sgs}}$ and effect on the turbulent flame propagation with the equation $S_T = S_L + b_1 u'_{sgs}$ described in chapter 4.3. Therefore, the small scale turbulent flow is an important factor that affects the flame propagation. Figure 7.7 illustrates the volume averaged of the in-cylinder SGS turbulent velocity in the fast cycles, the average value of the slow cycles, and mean of the total 30 LES cycles. During the intake stroke, there is no difference of the SGS turbulent velocity between the fast cycles and the slow cycles. By approximately 660CA, both the fast and slow cycle groups have nearly the same values, and from then on, it can be found that the SGS turbulent velocity of the fast cycle group has a little bit higher value than the slow cycle group. After ignition, the SGS turbulent velocity (mass-averaged) on the flame surface is shown in Figure 7.8. The difference of the SGS turbulent velocity between the averaged fast cycles and the averaged slow cycles before the ignition becomes larger as combustion progresses. Figure 7.9 shows the SGS turbulent velocity at the spark plug gap. As with the previous results, the average value of the fast cycles is higher than the average value of the slow cycles. Immediately after the ignition, a sharp decrease of the SGS turbulent velocity is observed, as the measured position is located in the behind of the flame surface. Therefore, the small scale turbulent flow can be considered as one of the causes of the cyclic variation of the flame propagation.

Figure 7.10 shows the correlation between the SGS turbulent velocity (mass-averaged) on the flame surface at 702 CA and the MFB 50 which represents the overall combustion phase. 702 CA time is the MFB 1 time after 3 degrees of ignition and represents the very early combustion phase. In general, the MFB 50 of the high SGS turbulence velocity cycle is short, but the R square value between the two values is 0.3. The result means that the small scale turbulent flow is one of the factors affecting combustion speed, but it does not have an absolute effect.

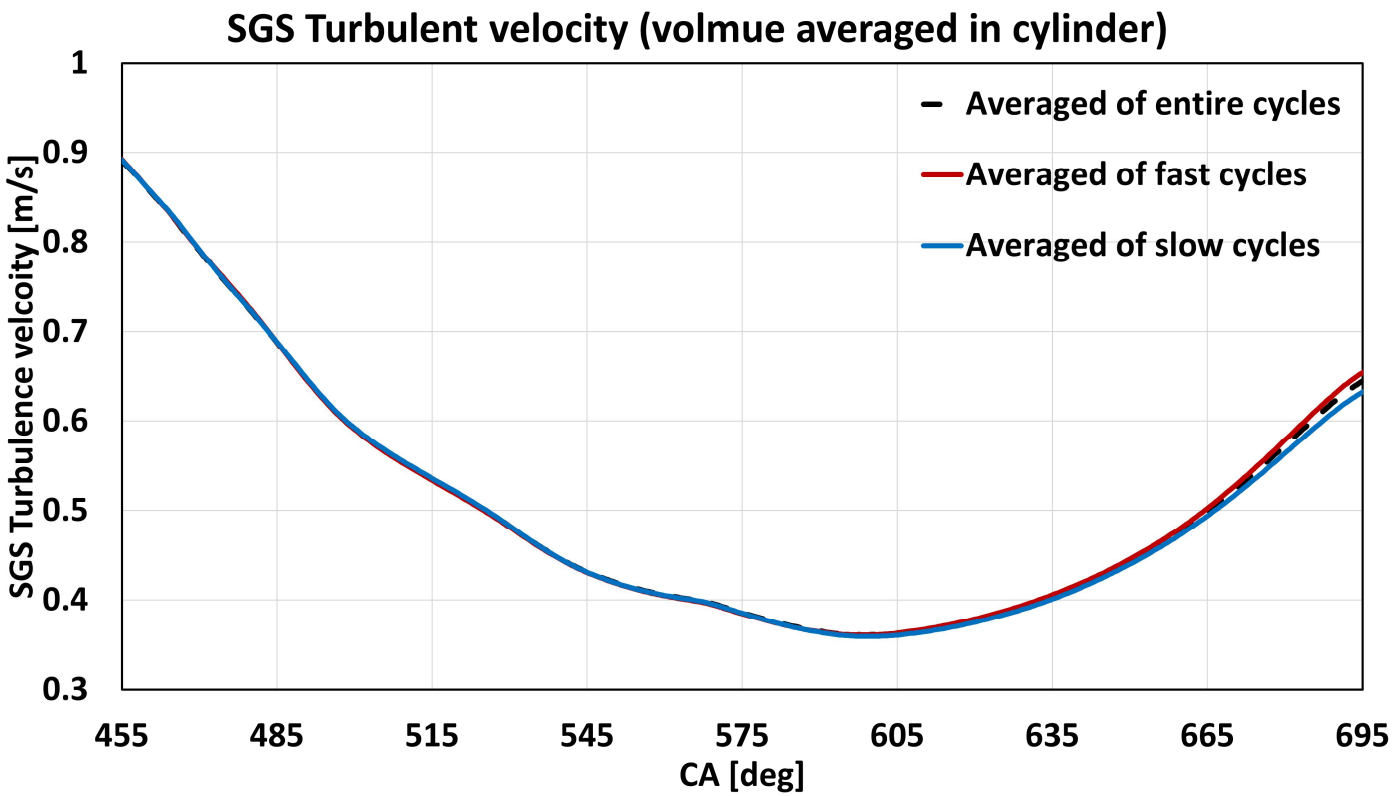

Figure 7.7 Comparison of SGS turbulent velocity before ignition. Black dotted line: Averaged value of entire cycles, Red solid line: Averaged value of fast cycles, Blue solid line: Averaged value of slow cycles

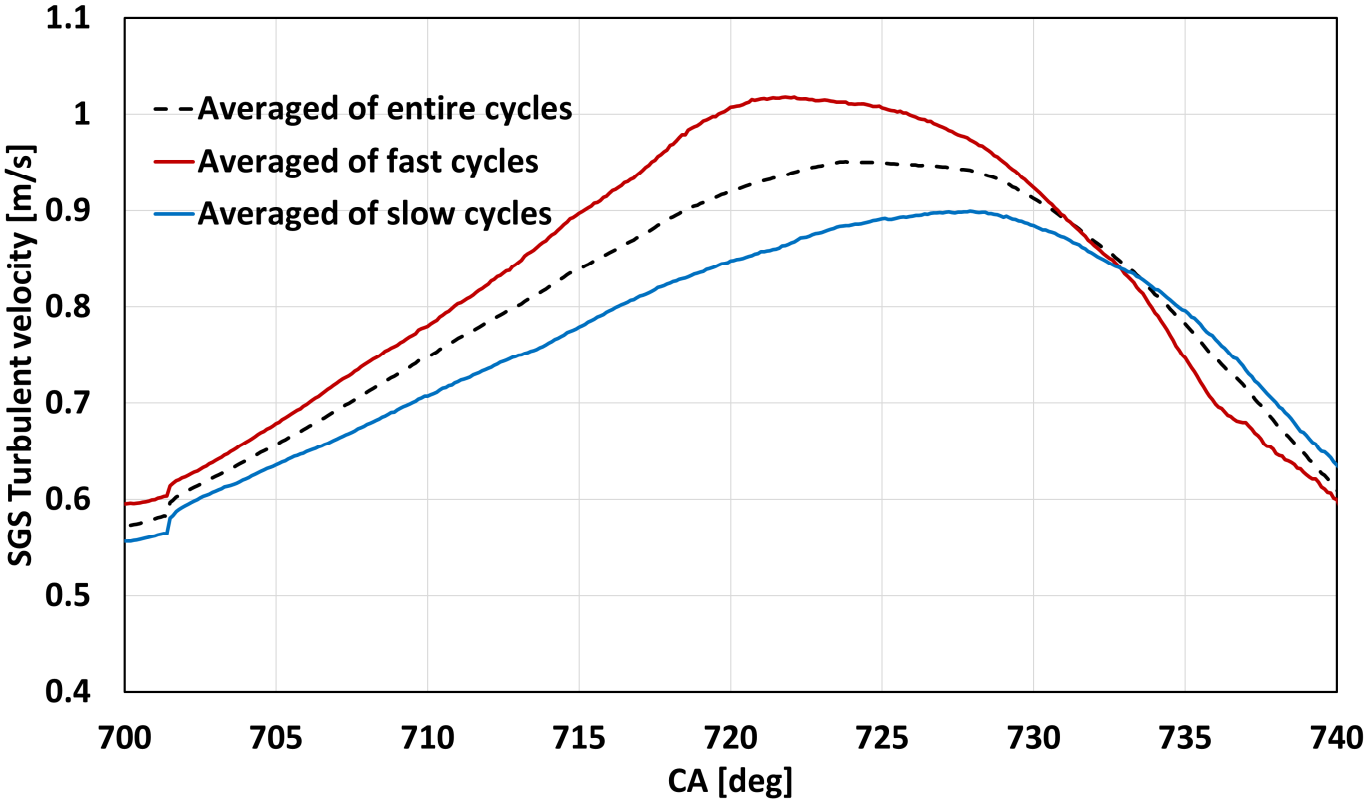

Figure 7.8 Comparison of SGS turbulent velocity on the flame surface after ignition. Black dotted line: Averaged value of entire cycles, Red solid line: Averaged value of fast cycles, Blue solid line: Averaged value of slow cycles

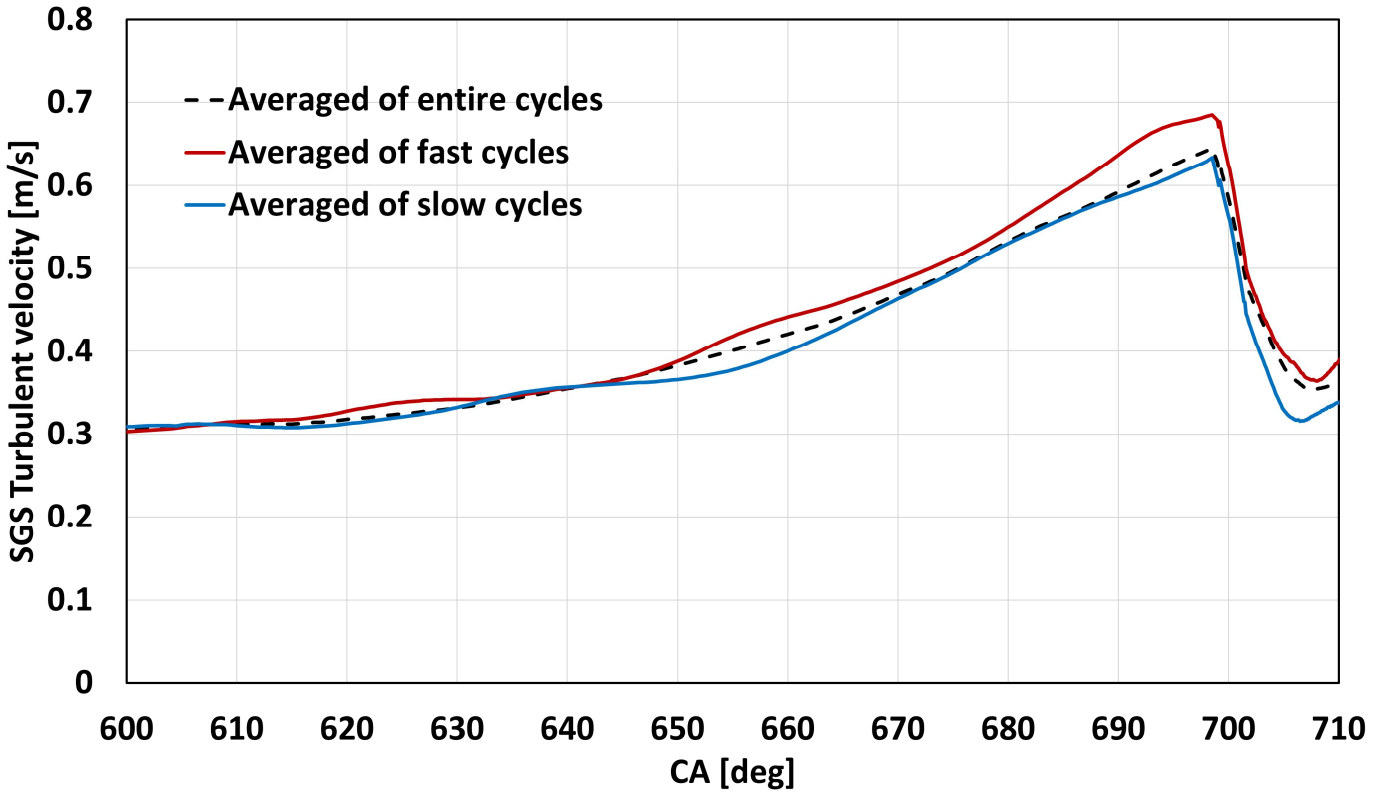

Figure 7.9 Comparison of SGS turbulent velocity at center of spark plug gap. Black dotted line: Averaged value of entire cycles, Red solid line: Averaged value of fast cycles, Blue solid line: Averaged value of slow cycles

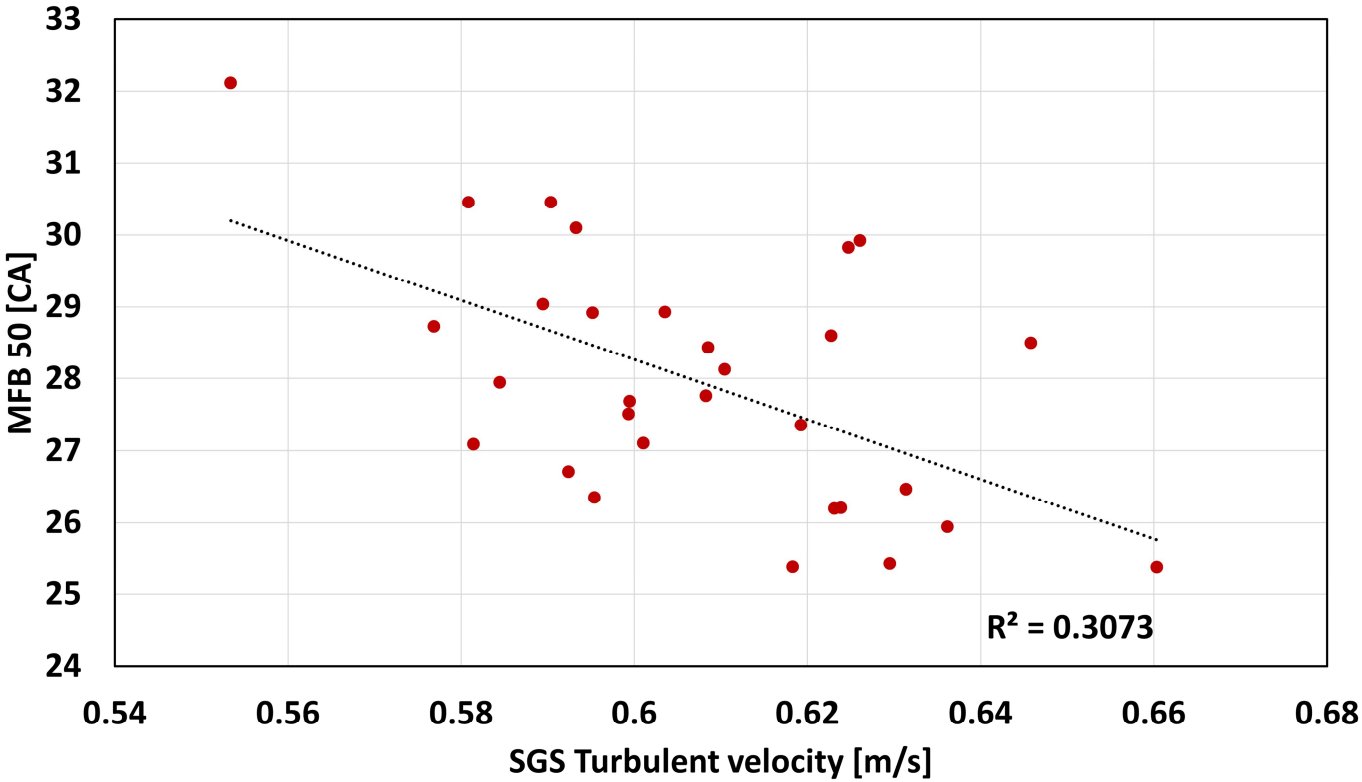

Figure 7.10 The correlation between SGS turbulent velocity and MFB 50

7.3.2 Large Scale Turbulent Flow Effect on CCV

The large scale turbulent flow is turbulent flow resolved by grid in LES, not represented by a single term, unlike the small scale turbulent flow. First, the representative large scale motions (tumble X, Y and swirl) in the combustion chamber are illustrated in Figures 7.11 – 7.13. The dotted line represents the averaged value of entire cycles, the red solid line indicates the mean value of the fast combustion cycles and the blue solid line means the mean value of the slow combustion cycles. Figure 7.11 shows the tumble Y ratio which is important factor in SI engines. During the intake process, both the tumble ratio of fast and slow cycles are irrelevant to the combustion phase as the both of the tumble ratio are smaller than the overall mean value. Subsequently, during the compression process, the tumble ratio of the fast cycles is greater than the slow cycles. However, it is interesting to note that the tumble ratio of both the fast and slow cycle groups becomes similar at the ignition time (21 CA bTDC). The difference of the tumble ratio between the fast and slow cycles decreases from about 660 CA as shown in Figure 7.7, at that time, the SGS turbulence velocity for the fast cycles begins to be higher than the slow cycles. Therefore, it can be seen that the energy of tumble is converted into turbulent flow during the compression process until the ignition time. In SI engines, the tumble X and the swirl are not intended flow motion, so very small values are observed throughout the cycle as shown in Figures 7.12 and 7.13.

Next, flow field is analyzed to evaluate the effect of the large scale turbulent flow in a local area. Four noticeable cycles are investigated in the present study as shown in Figure 7.6. The 5th cycle which is fast combustion in early stage but belongs to the medium combustion speed group on the basis

of the MFB 50. The 4th cycle that is initially propagated at the medium combustion speed but later in the fast combustion speed group. The 18th cycle which is initially propagated at the medium combustion speed but later in the slow combustion speed group. The combustion phase of 23rd cycle is slow at first but faster as combustion progresses and eventually belongs to the medium combustion phase group. The field analysis is carried out in four planes in Figure 7.14.

First, the reason why the early flame propagation of 5th cycle is fast and then slow down as combustion progresses is described. In Figure 7.15, the spatial velocity distributions near the spark plug at the ignition time are shown. The strong flow from right to left is shown in Figure 7.15 (a) and (b). Due to the strong flow, the flame propagates to the left side in the early phase as shown in Figure 7.16. At 703CA (Figure 7.16 (a)), the flame is observed to meet the vortex in the left side and propagates rapidly in the direction of rotation of the vortex (Figure 7.16 (b)). Similarly, Figure 7.17 (a) describes the flame in contact with the vortex on the left side of the spark plug again at 710 CA, but there is no vortex in the right side. As a result, the flame leans toward to the left side as shown in Figure 7.17 (b). In Figure 7.18, the early flame propagation is shown on the side view (Y=0mm). In the side view, it is also observed that the flame meets the vortex and propagates quickly. The initial flame propagation of the 5th cycle is fast because the flame meets the vortices early time and spreads rapidly. However, as in Figure 7.17, the flame is skewed to left side, showing an unbalanced flame propagation as shown in Figure 7.19. This is the reason why the combustion phase of the 5th cycle is rapid in the early stage but slows over time.

In Figure 7.20, the vector fields of the 4th cycle near the spark plug at the ignition time are shown. In the side view (Figure 7.20 (a)), two vortices

slightly away from the spark plug toward the intake valve are observed. As a result, it can be observed that the flame evenly propagates in the direction of the exhaust valve and the intake valve by meeting the two vortices as it moves out of the spark plug region as shown in Figure 7.21. In the front view (Figure 7.20 (b)), there are three vortices and the flow is seen from left to right. Therefore, the flame is initially propagated to the right, as shown in Figure 7.22 (a), but it meets the vortex on the left and begins to propagate rapidly to the left as shown in Figure 7.22 (b). As a result, the flame is propagated in balance from side to side (Figure 7.23 (a)), and the flame propagation is accelerated by the additional contact of the vortex (Figure 7.23 (b)). The balanced flame propagation is also identified in the top view of Figure 7.24. In the 4th cycle, the contact time with the vortex in the initial flame phase is about 4 CA slower than the 5th cycle, but it encounters more vortices as flame propagates. Thus the flame propagation in the 4th cycle, as opposed to the 5th cycle, is slow in the early stage, but becomes faster over time.

In the Figure 7.25, the velocity fields of the 18th cycle near the spark plug at the ignition time are shown. On the side view (Figure 7.25 (a)), the flow is directed downward due to the rapid flow observed in upper and right of the spark plug Therefore, the flame is also observed to propagate in the same direction of flow as shown in Figure 7.26 (a) and (b). At 705 CA, the flame begins to be affected by the vortex in the lower right of the Figure 7.26 (b). However, since the flow, as shown in Figure 7.25 (b), passes through the spark plug and flows strongly down the right side, it is observed that the flame propagates completely over the right side as shown in Figure 7.27. Despite the fact that the flame in the side view is affected by the vortex at an early time, the initial flame propagation is relatively slow due to the disproportionate flame propagation identified in the front view. Furthermore, as identified in Figure 7.28, the flame propagation becomes slower and slower because there is

no contact between the flame and a vortex during the flame propagation. In the Figure 7.29, the flame propagation is slower than the two cycles described earlier

Lastly, the flame propagation of the 23th cycle is analyzed. Figure 7.30 shows the vector fields near the spark plug at the ignition time. On the side view (Figure 7.30 (a)), there is a strong flow toward to the bottom on the right of spark plug. Thus, the early flame propagates to only under the spark plug as shown in Figure 7.31. In addition, on the front view (Figure 7.30 (b)), the flow moves rapidly from right to left of the spark plug. Therefore, the flame also propagates to the left as the flow motion as shown in Figure 7.32. For the two reasons, the 23th cycle has the very slow early flame propagation. As shown in Figure 7.33, the flame is not affected by a vortex up to 715 CA. However, after 718CA, the flame meets the vortices on the left and right side, accelerating the propagation relatively evenly. Therefore, flame propagation is identified to propagate evenly after 720 CA as shown in Figure 7.35

The relationship between the flow distribution and the flame propagation is investigated in detail in four analysis planes by using four cycles. The factors determining the rate of the early flame propagation are how uniform the flow distribution near spark plug at the ignition timing is and how quickly the flame contacts with the vortex. After that, the combustion phase depends on when, where, and how much the flame meets the vortices.

So far, the effect of the small scale and the large scale turbulent flow effect on the combustion CCV is investigated. It is identified that the small scale turbulent flow is related to the tumble motion. As a result, the deviation of the tumble ratio is one of the causes of the CCV, but its variation is modest. Next, the effect of local flow fields on the flame propagation is analyzed. The great effect of local vortices on the flame propagation is observed. Therefore,

in the present study, it is found that the local vortices are the main source of the combustion CCV. In the following section, the way to reduce the combustion CCV will be discussed.

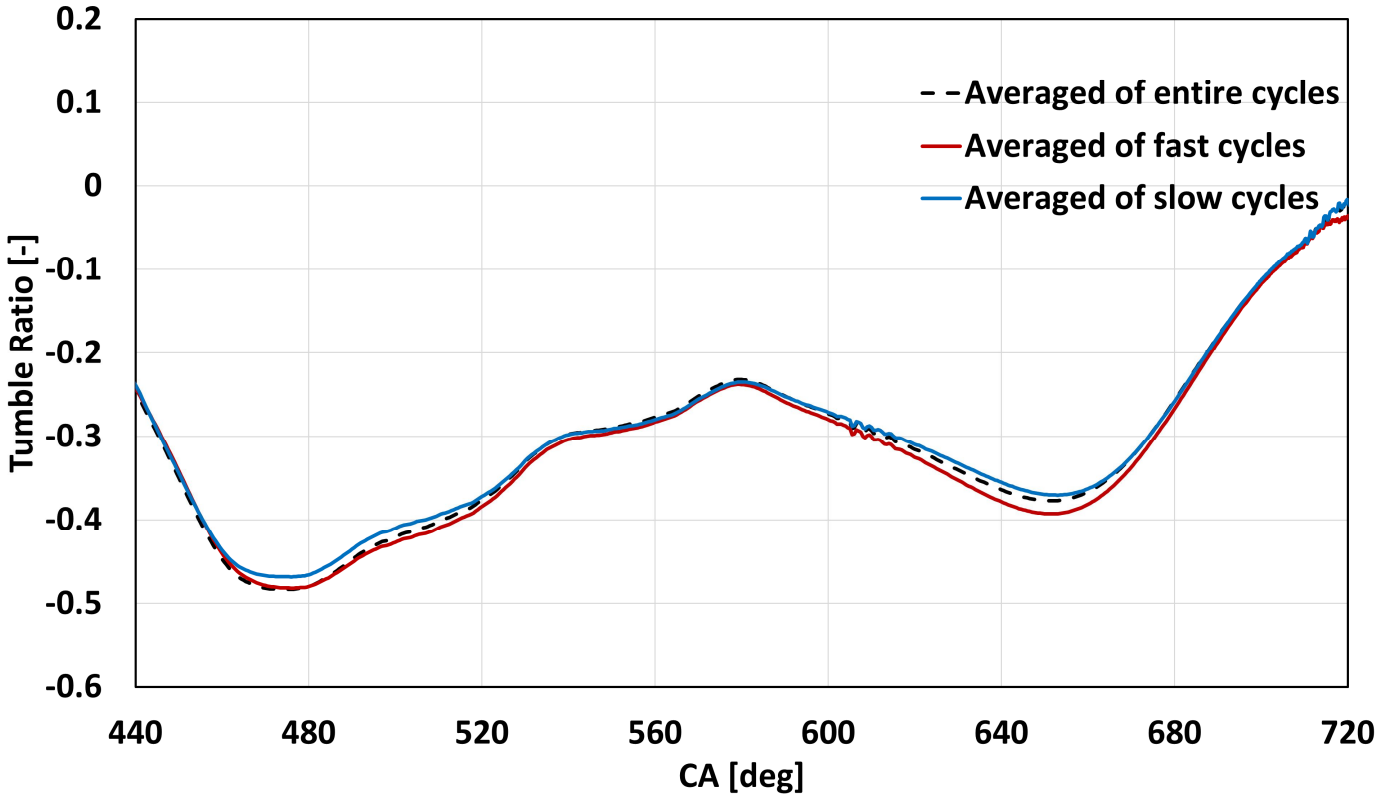

Figure 7.11 Comparison of tumble Y ratio. Black dotted line: Averaged value of entire cycles, Red solid line: Averaged value of fast cycles, Blue solid line: Averaged value of slow cycles

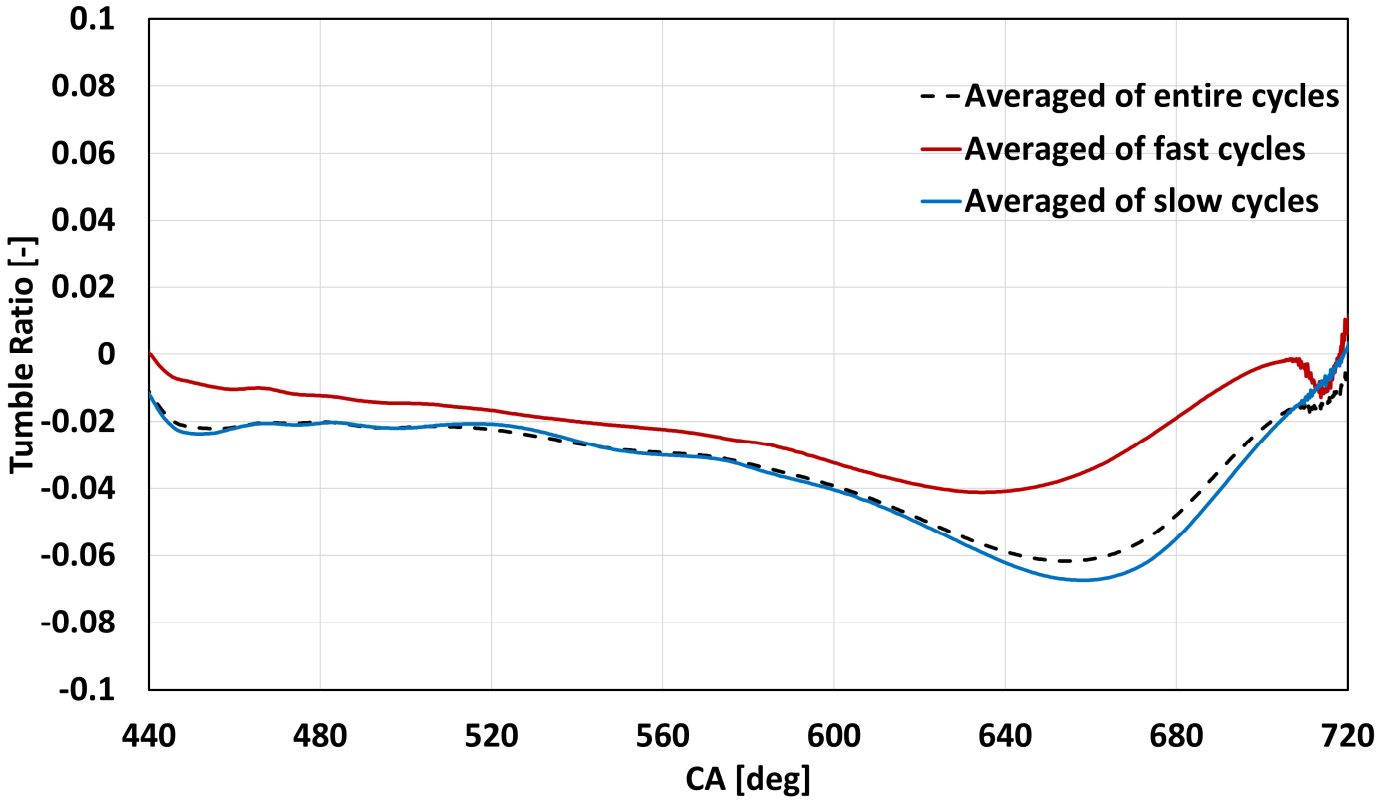

Figure 7.12 Comparison of tumble X ratio. Black dotted line: Averaged value of entire cycles, Red solid line: Averaged value of fast cycles, Blue solid line: Averaged value of slow cycles

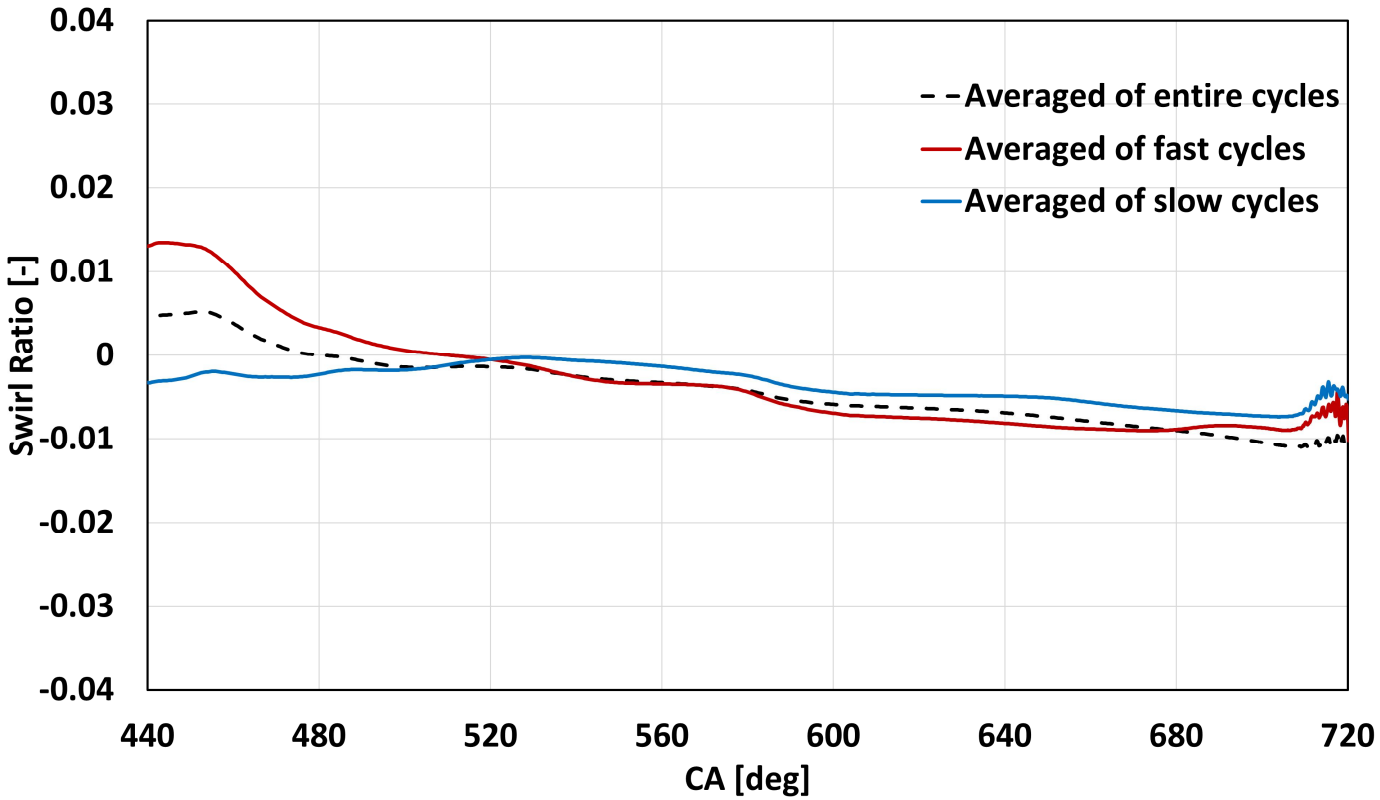

Figure 7.13 Comparison of swirl ratio. Black dotted line: Averaged value of entire cycles, Red solid line: Averaged value of fast cycles, Blue solid line: Averaged value of slow cycles

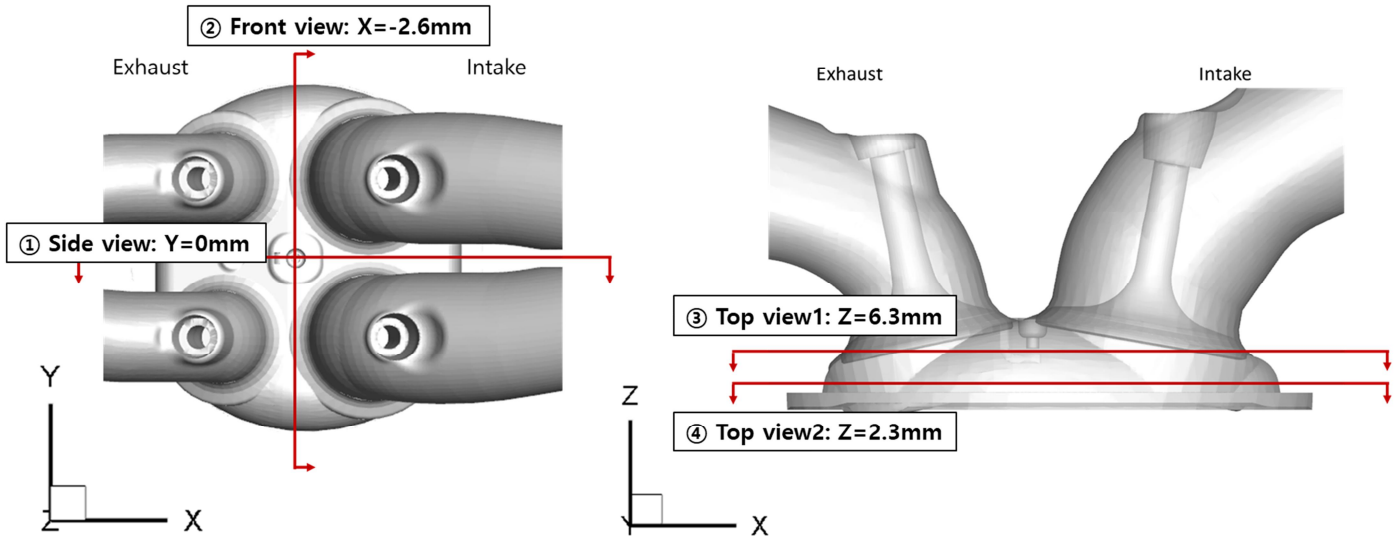

Figure 7.14 Analysis sections: ① Side view: Y=0mm, ② Front view: X=-2.6mm, ③ Top view1: Z=6.3mm, ④ Top view2: Z=2.3mm

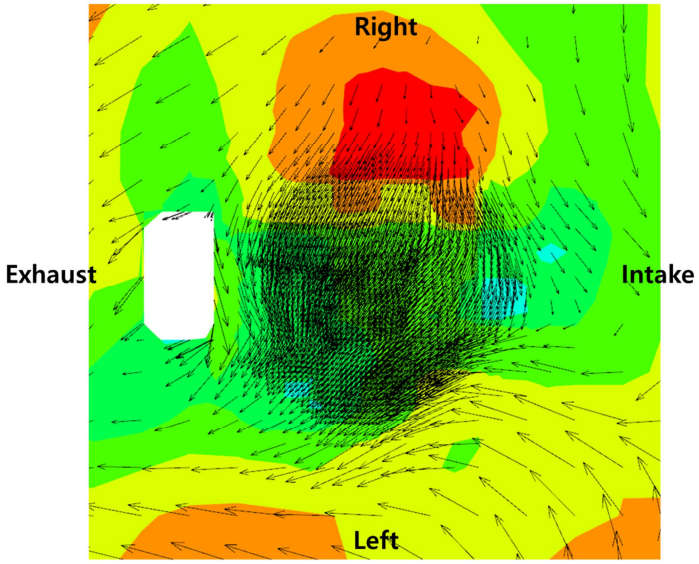

(a)

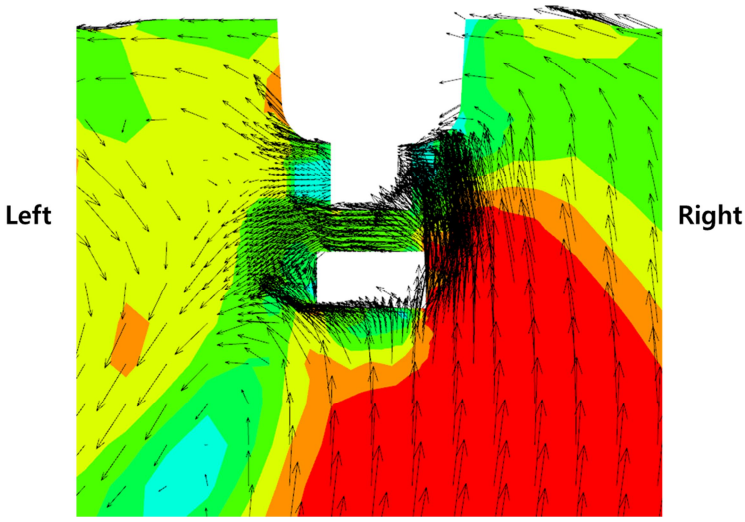

(b)

Figure 7.15 The vector field of 5th cycle at 699 CA. (a) Top view1 (Z=6.3mm), (b) Front view (X=-2.6mm)

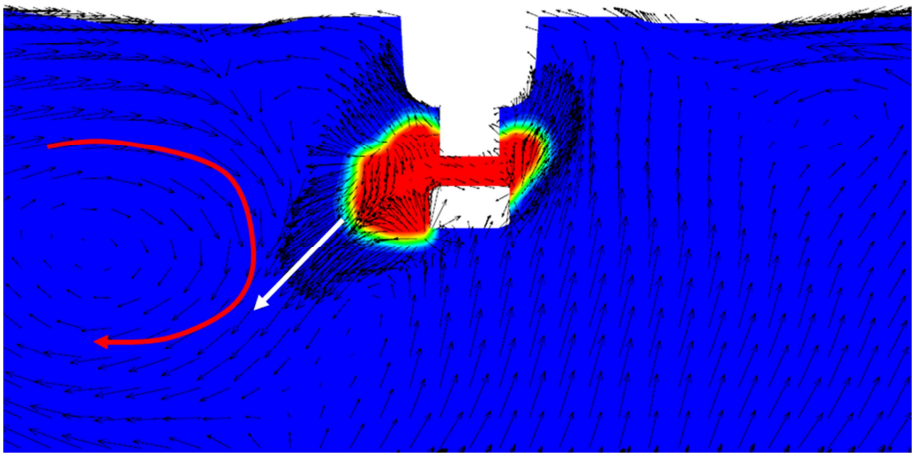

(a)

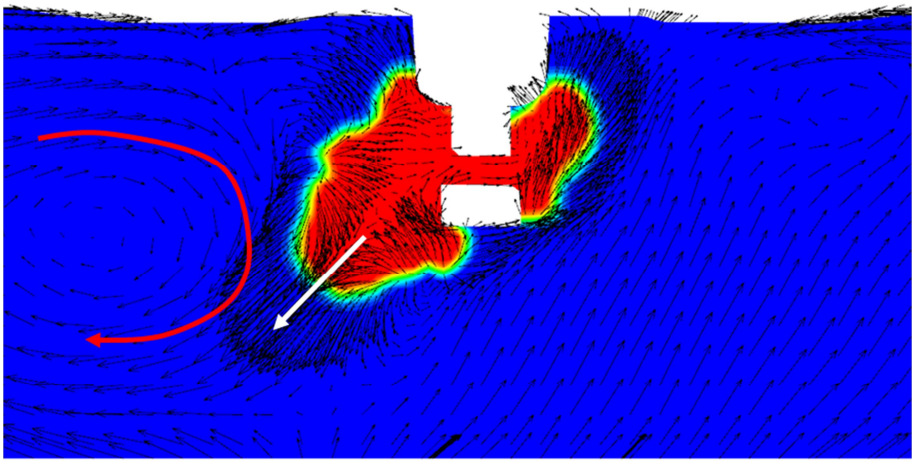

(b)

Figure 7.16 Progress variable and vector field of 5th cycle on front view (X=-2.6mm). (a) 703 CA, (b) 704 CA

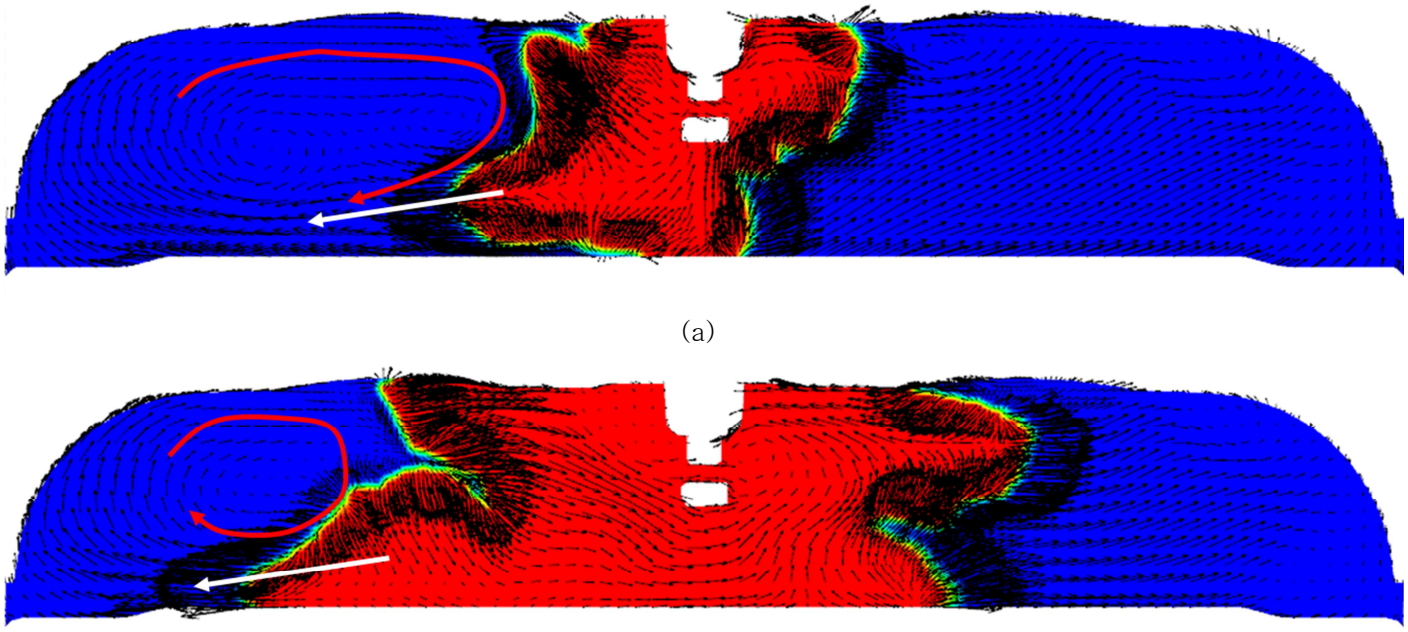

(a)

(b)

Figure 7.17 Progress variable and vector field of 5th cycle on front view (X=-2.6mm). (a) 710 CA, (b) 716 CA

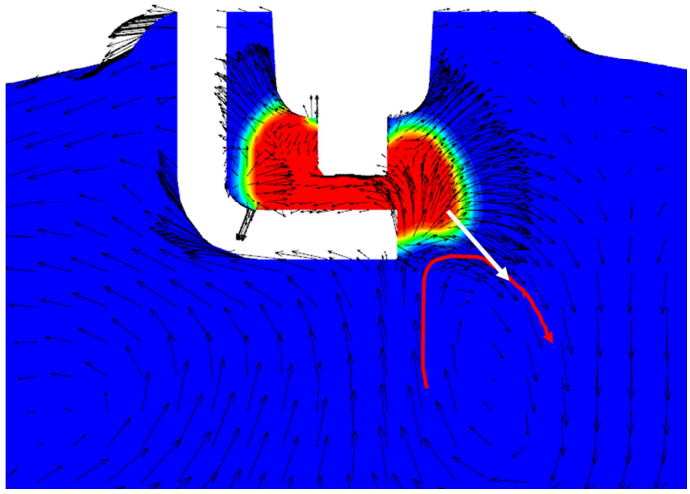

(a)

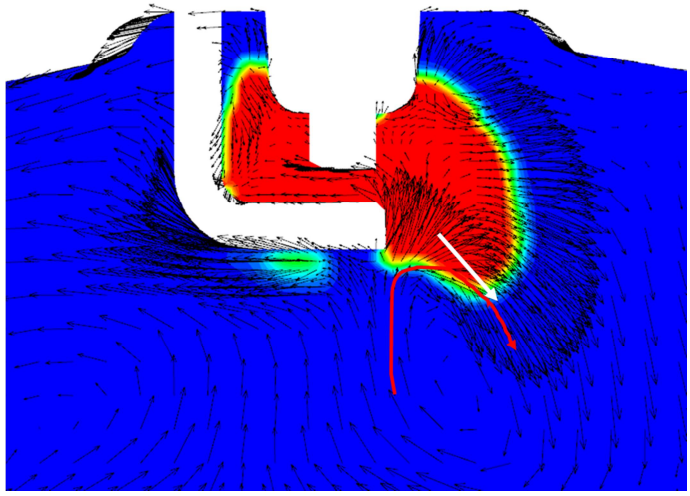

(b)

Figure 7.18 Progress variable and vector field of 5th cycle on side view (Y=0mm). (a) 703 CA, (b) 704 CA

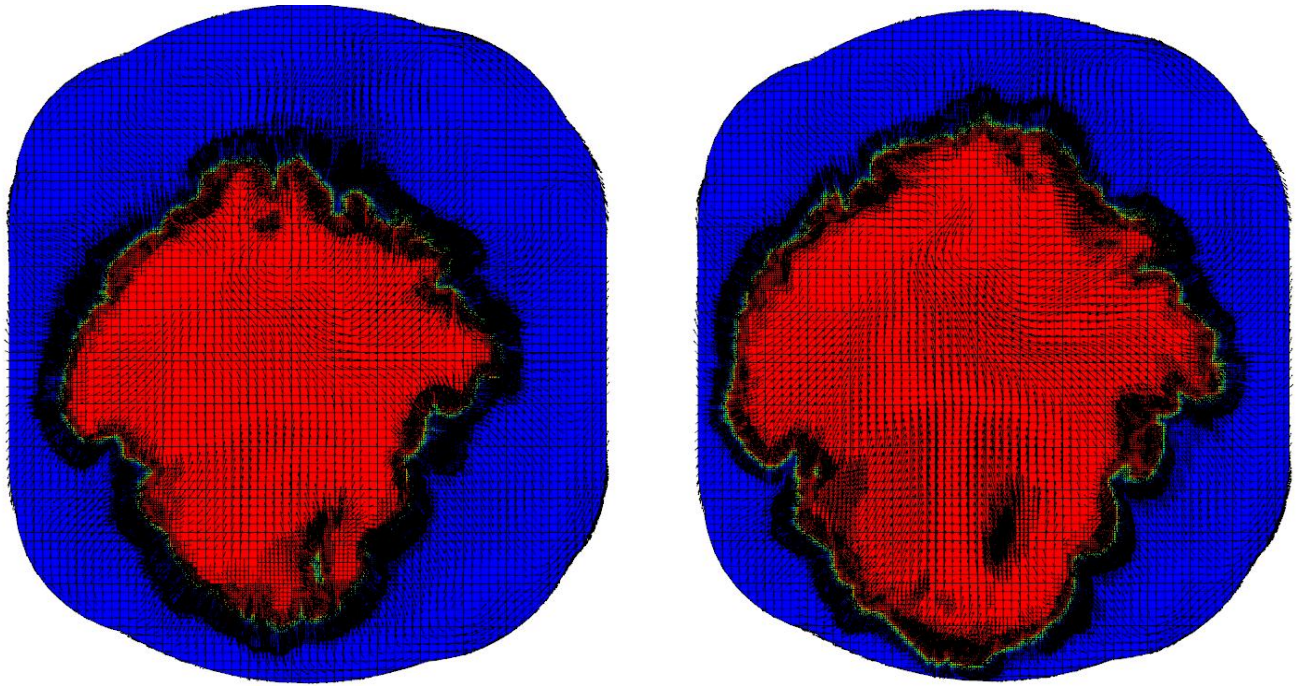

(a) (b)

Figure 7.19 Progress variable and vector field of 5th cycle on top view2 (X=2.3mm). (a) 720 CA, (b) 723 CA

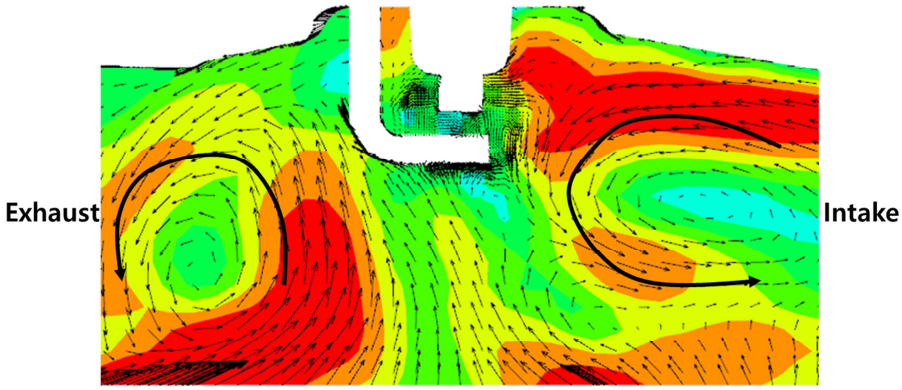

(a)

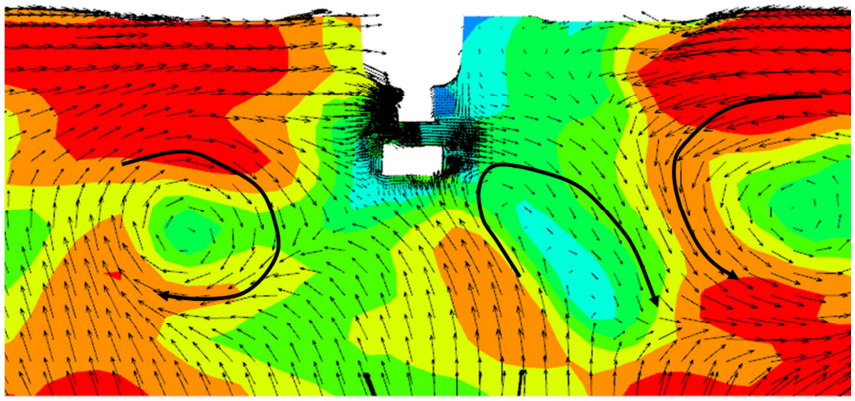

(b)

Figure 7.20 The vector field of 4th cycle at 699 CA. (a) Side view (Y=0mm), (b) Front view (X=-2.6mm)

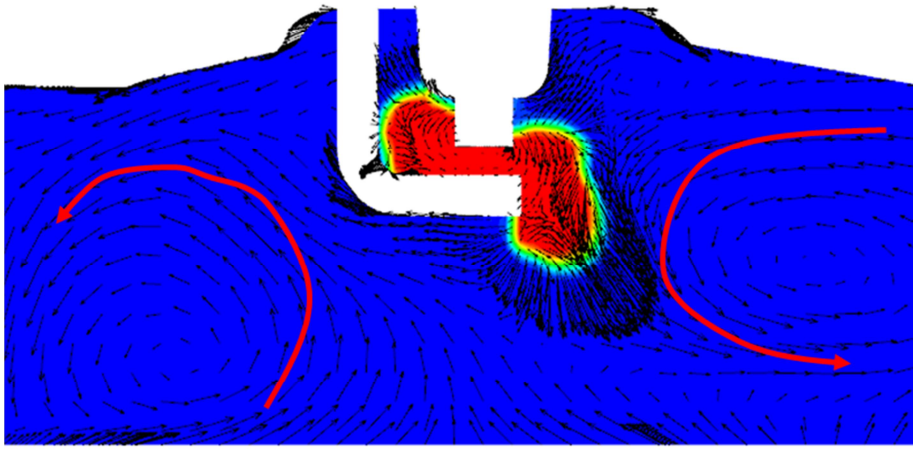

(a)

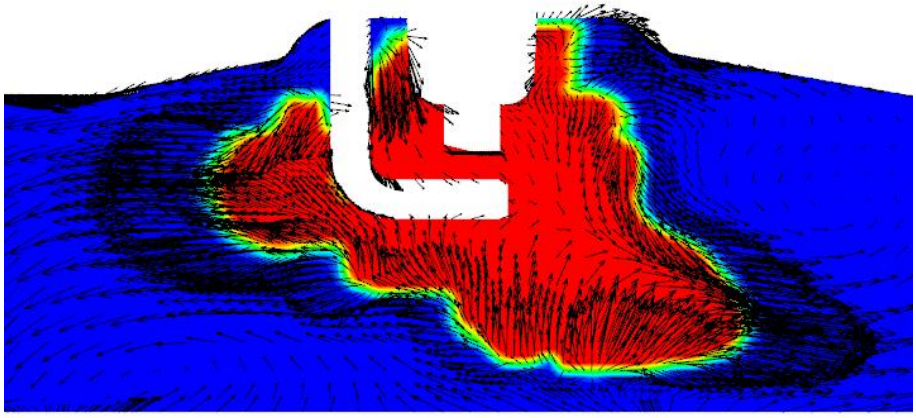

(b)

Figure 7.21 Progress variable and vector field of 4th cycle on side view (Y=0mm). (a) 705 CA, (b) 709 CA

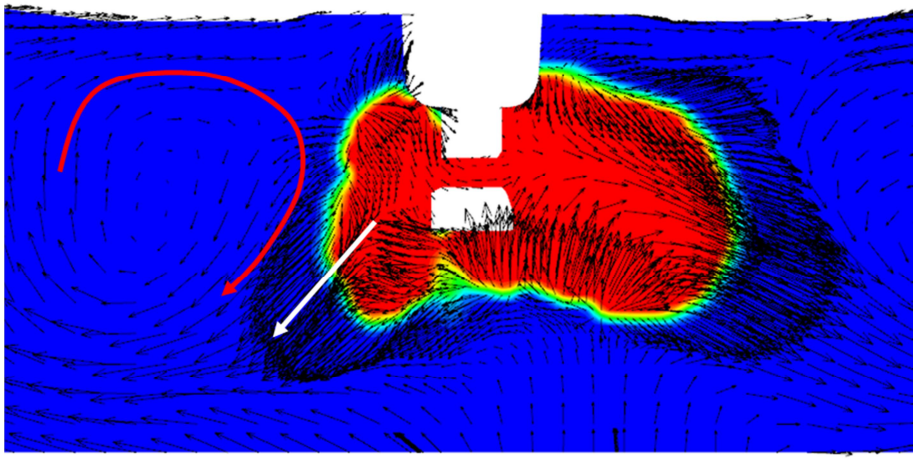

(a)

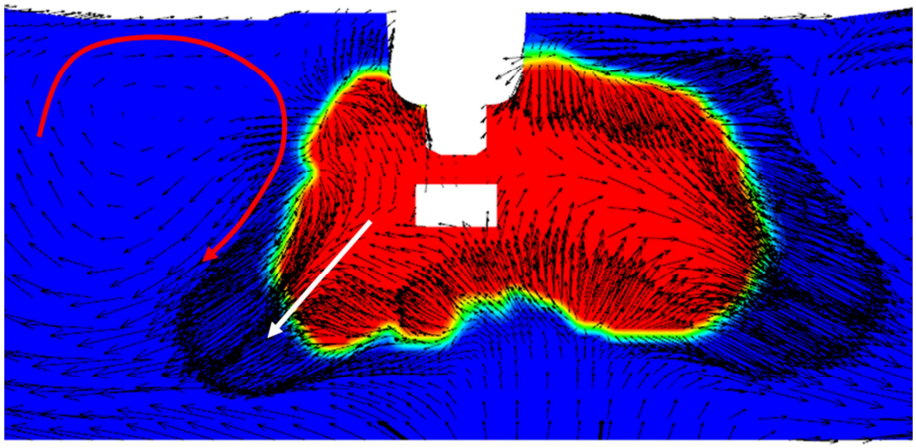

(b)

Figure 7.22 Progress variable and vector field of 4th cycle on front view (X=-2.6mm). (a) 707 CA, (b) 708 CA

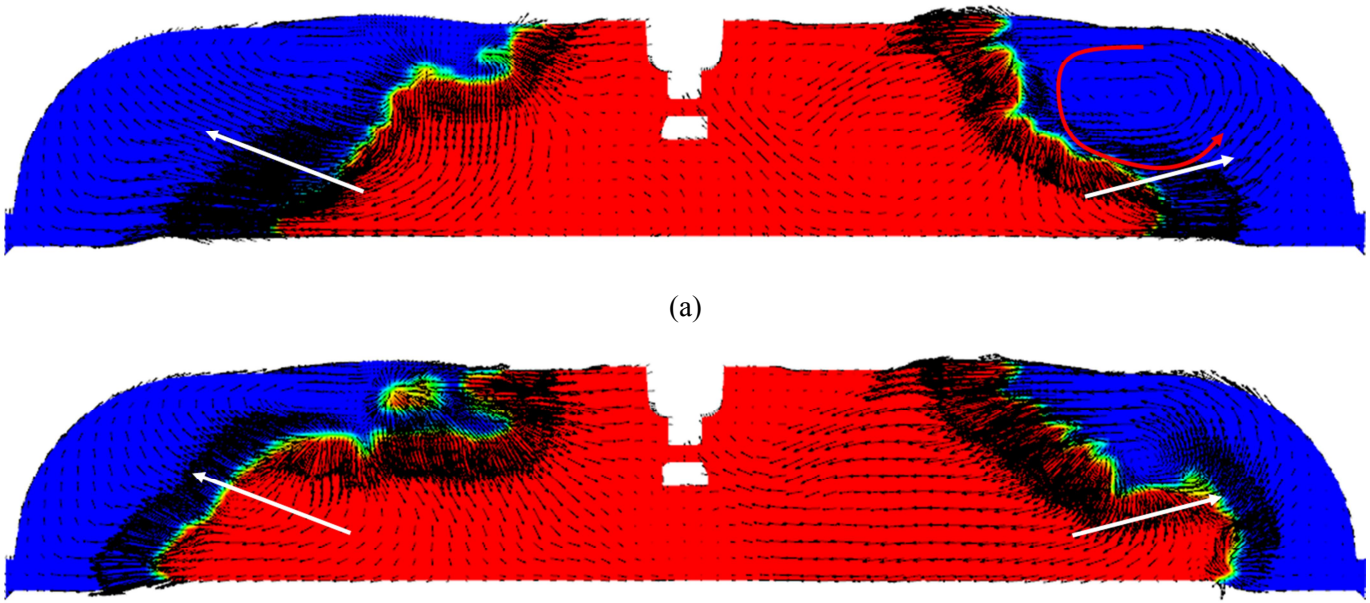

(a)

(b)

Figure 7.23 Progress variable and vector field of 4th cycle on front view (X=-2.6mm). (a) 717 CA, (b) 720 CA

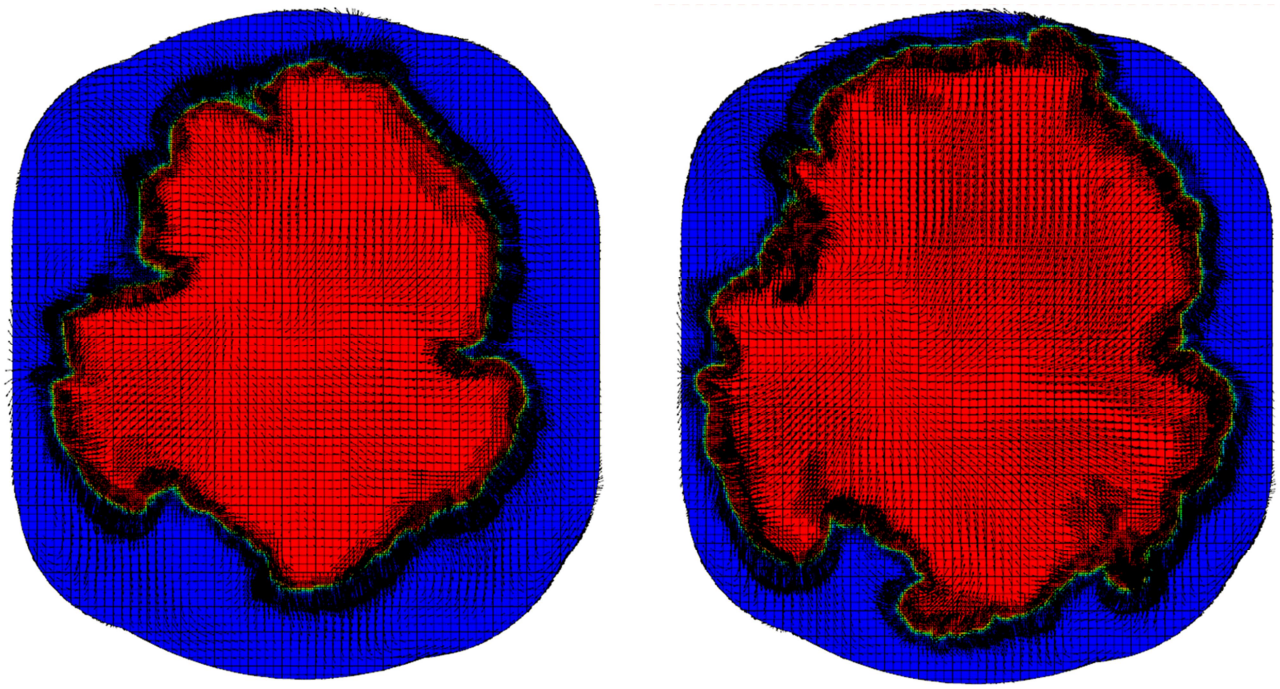

(a) (b)

Figure 7.24 Progress variable and vector field of 4th cycle on top view2 (X=2.3mm). (a) 720 CA, (b) 723 CA

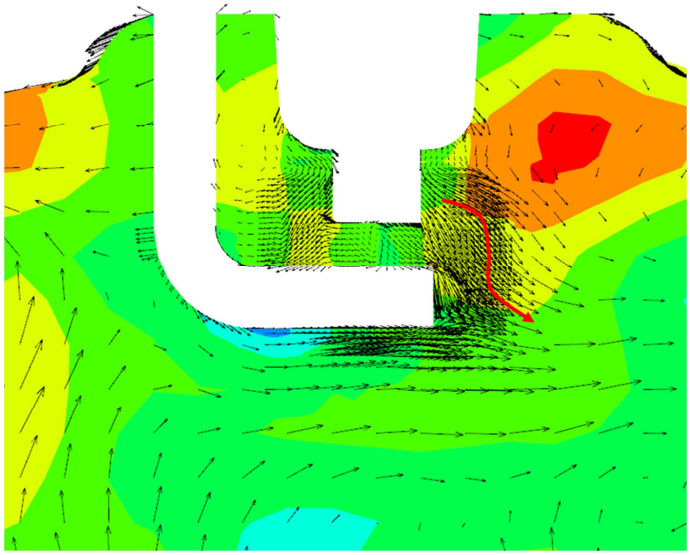

(a)

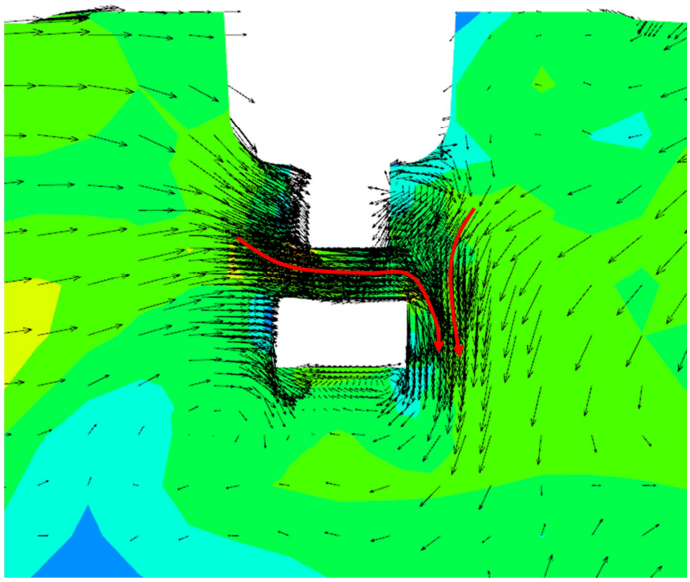

(b)

Figure 7.25 The vector field of 18th cycle at 699 CA. (a) Side view (Y=0mm), (b) Front view (X=-2.6mm)

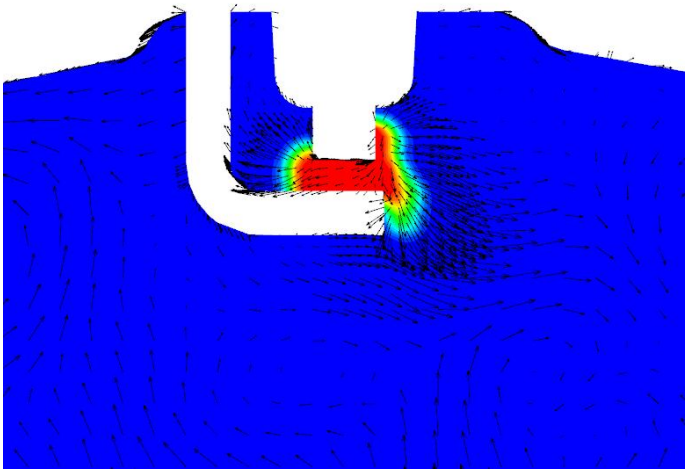

(a)

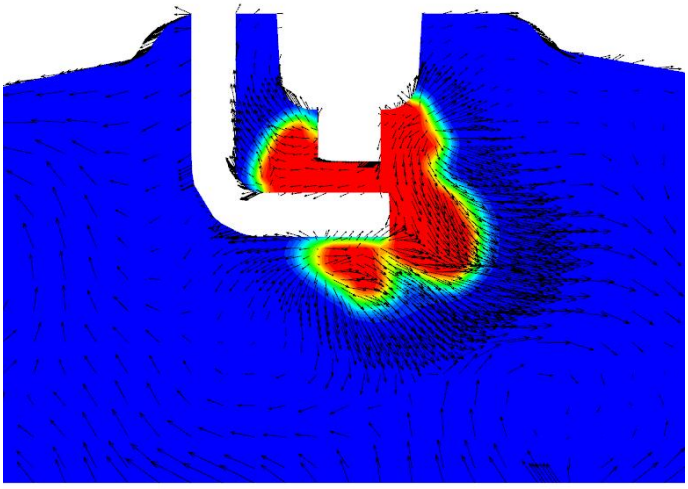

(b)

Figure 7.26 Progress variable and vector field of 18th cycle on side view (Y=0mm). (a) 703 CA, (b) 705 CA

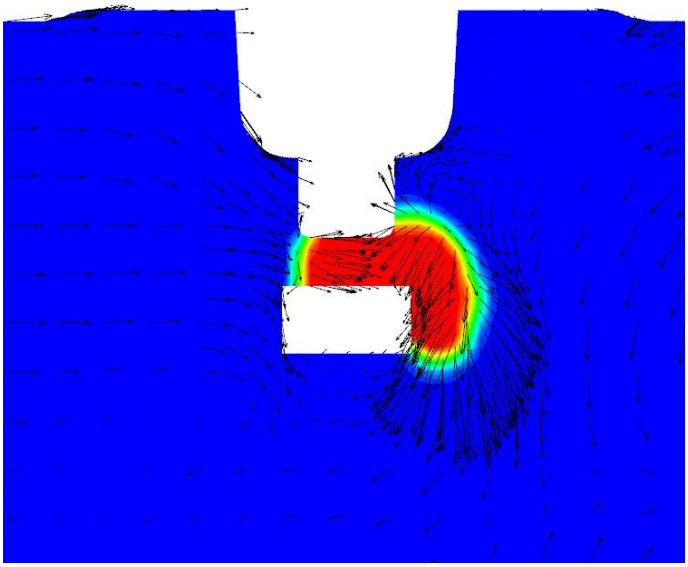

Figure 7.27 Progress variable and vector field of 18th cycle on front view (X=-2.6mm) at 702 CA.

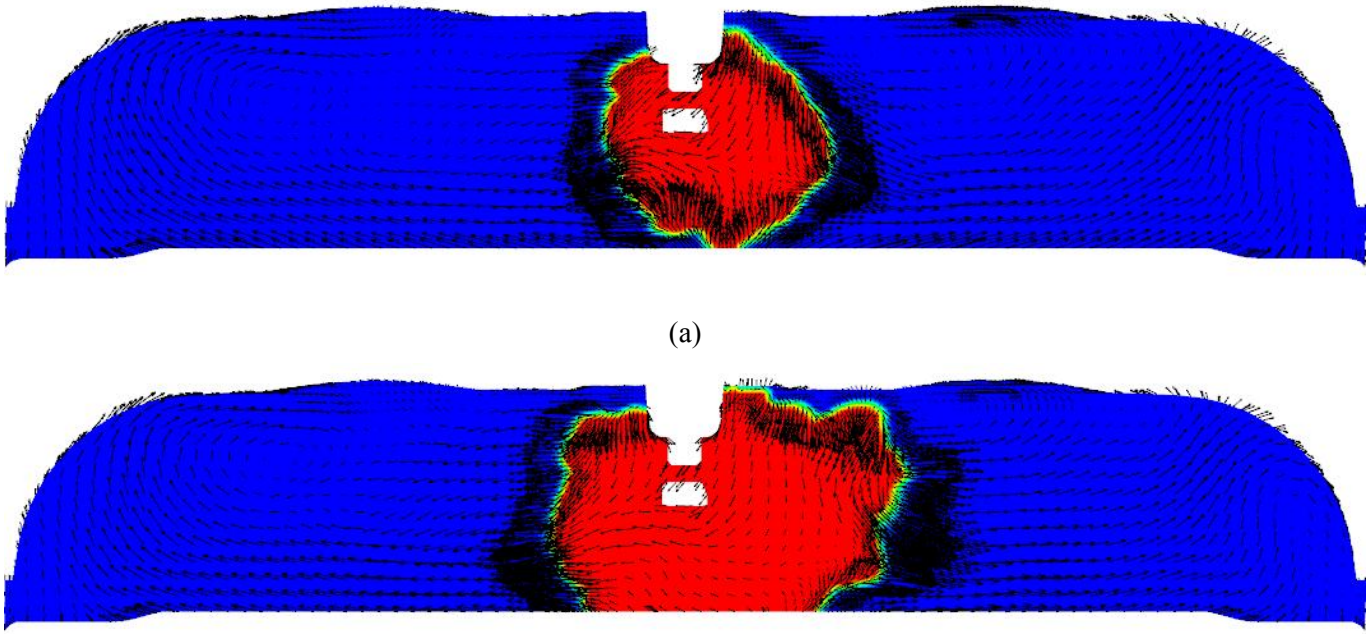

(a)

(b)

Figure 7.28 Progress variable and vector field of 18th cycle on front view (X=-2.6mm). (a) 709 CA, (b) 712 CA

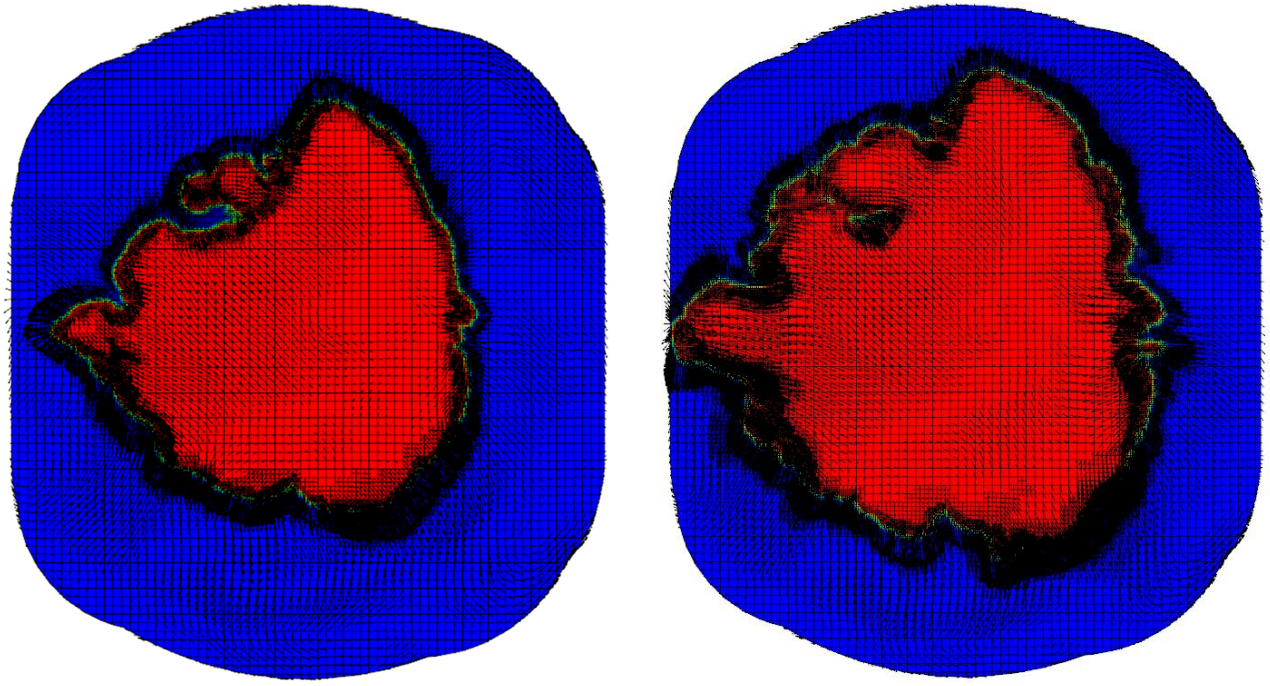

(a) (b)

Figure 7.29 Progress variable and vector field of 18th cycle on top view2 (X=2.3mm). (a) 720 CA, (b) 723 CA

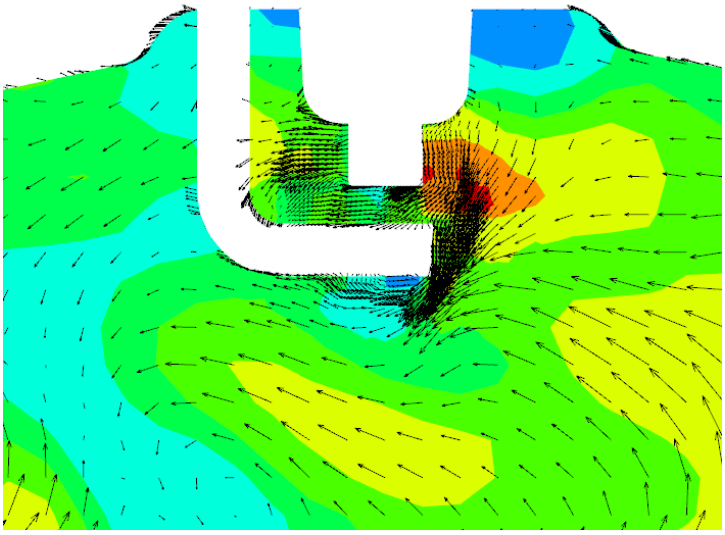

(a)

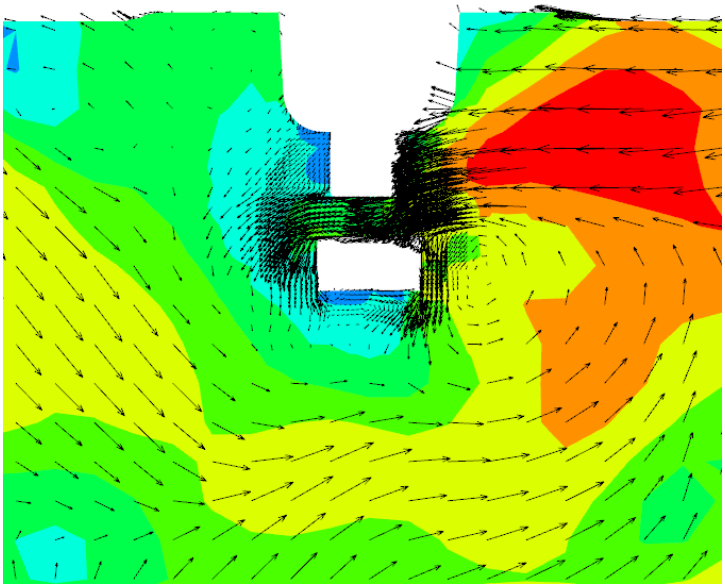

(b)

Figure 7.30 The vector field of 23th cycle at 699 CA. (a) Side view (Y=0mm), (b) Front view (X=-2.6mm)

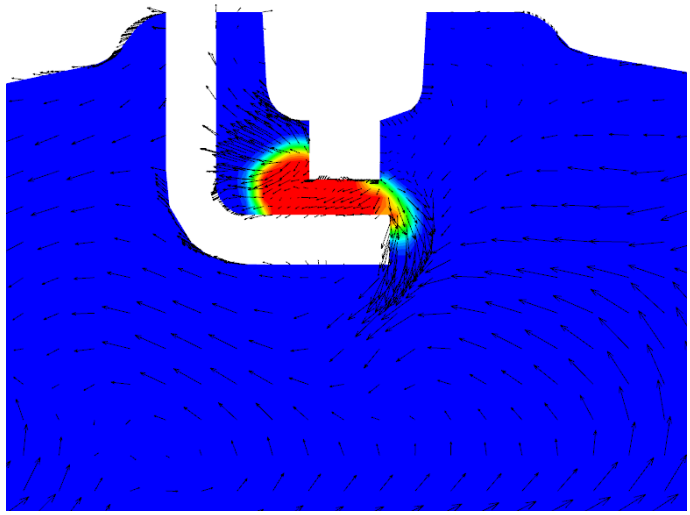

(a)

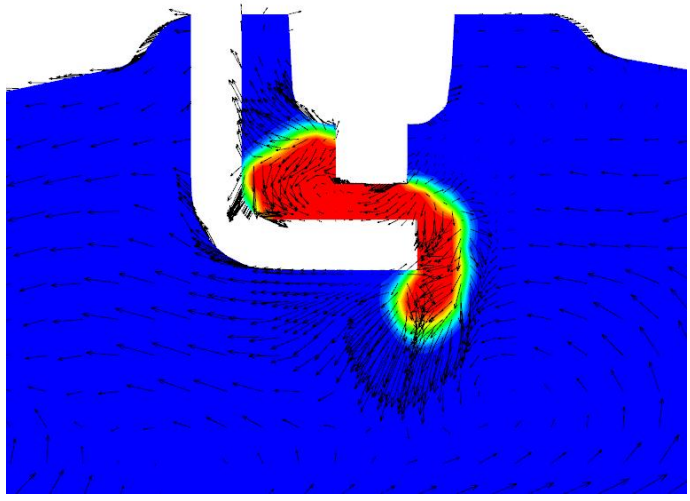

(b)

Figure 7.31 Progress variable and vector field of 23th cycle on side view (Y=0mm). (a) 703 CA, (b) 705 CA

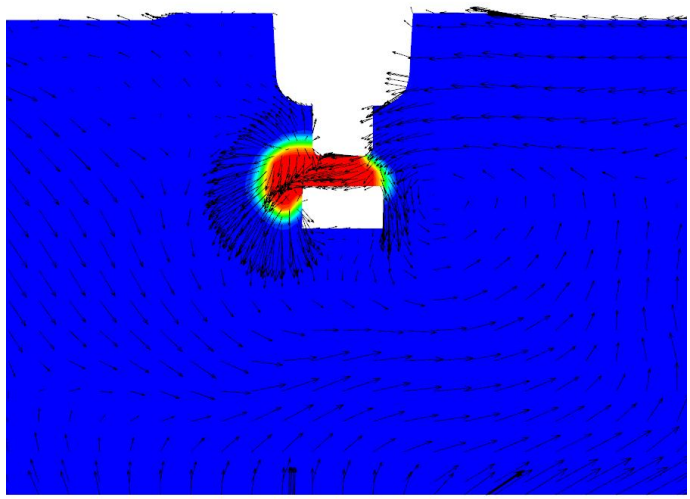

(a)

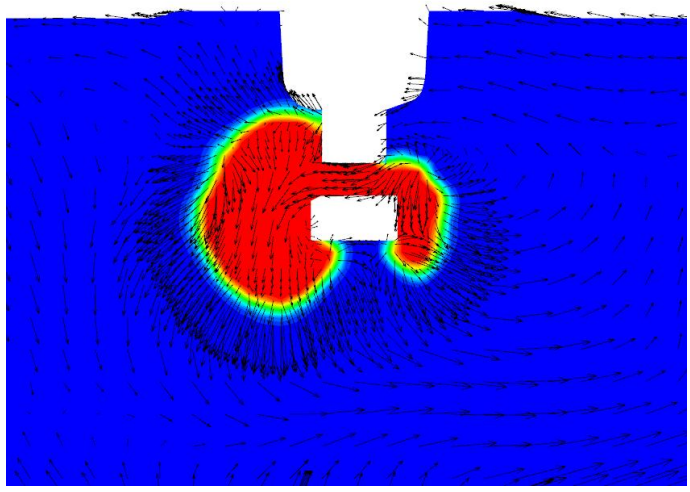

(b)

Figure 7.32 Progress variable and vector field of 23th cycle on front view (X=-2.3mm). (a) 702 CA, (b) 705 CA

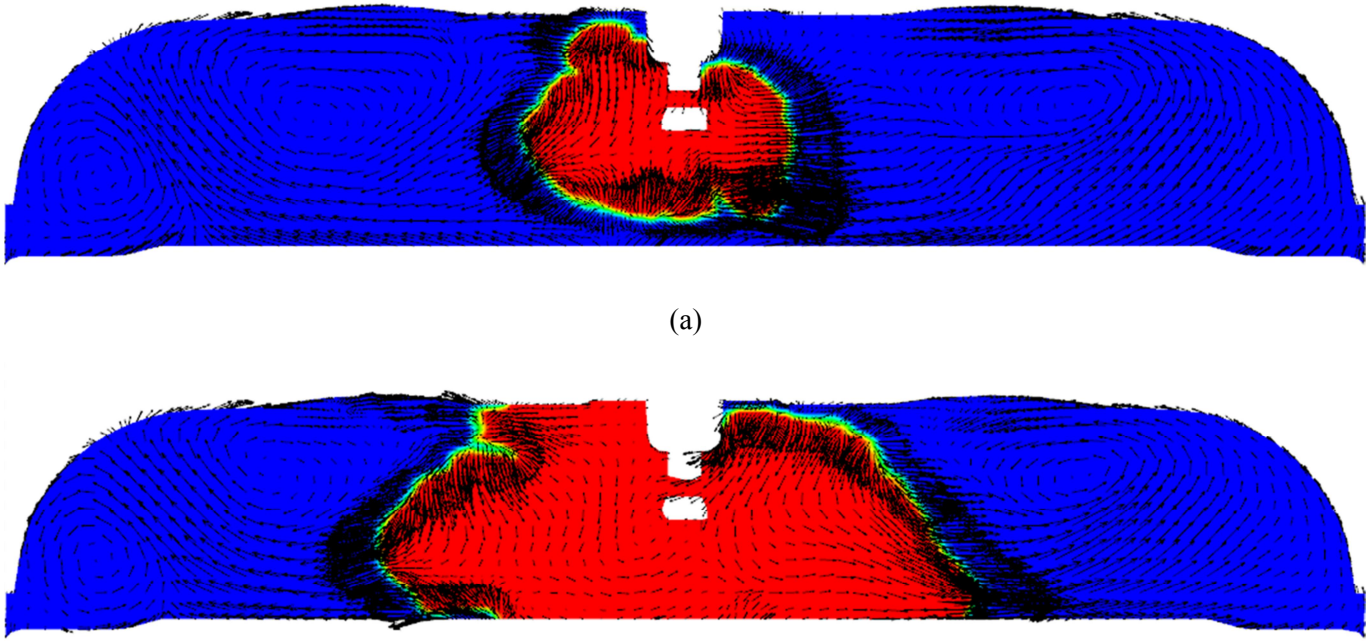

(a)

(b)

Figure 7.33 Progress variable and vector field of 23th cycle on front view (X=-2.6mm). (a) 709 CA, (b) 715 CA

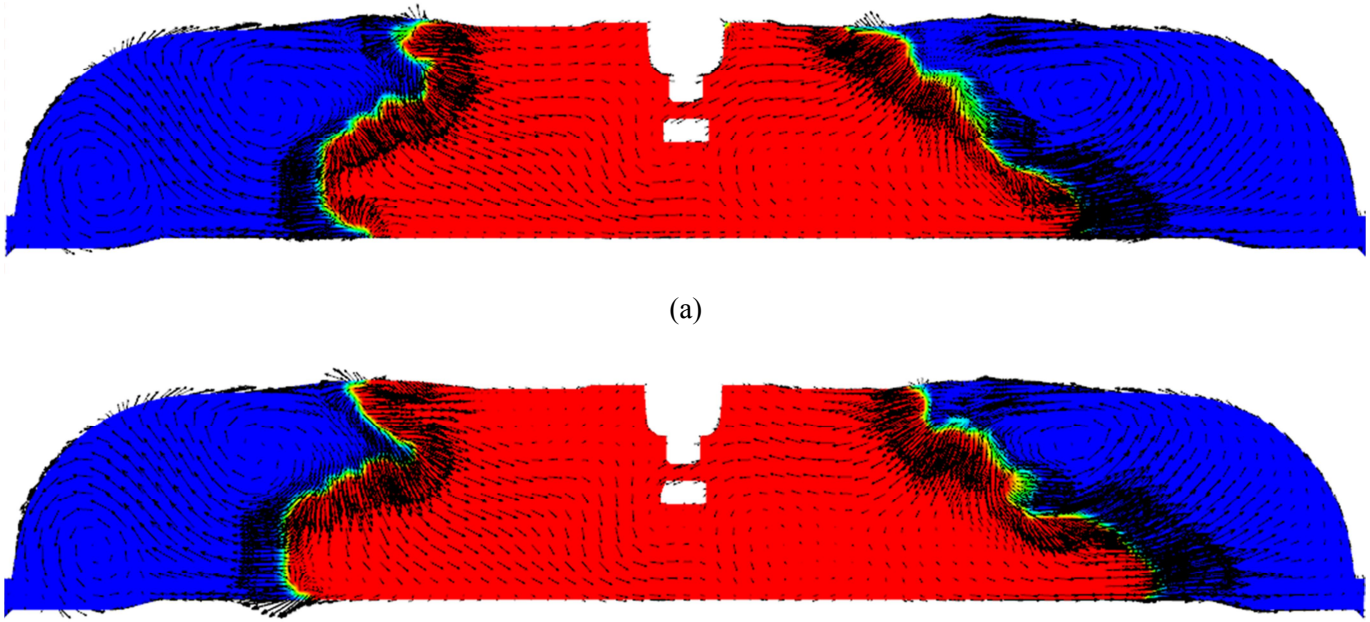

(a)

(b)

Figure 7.34 Progress variable and vector field of 23th cycle on front view (X=-2.6mm). (a) 718 CA, (b) 720 CA

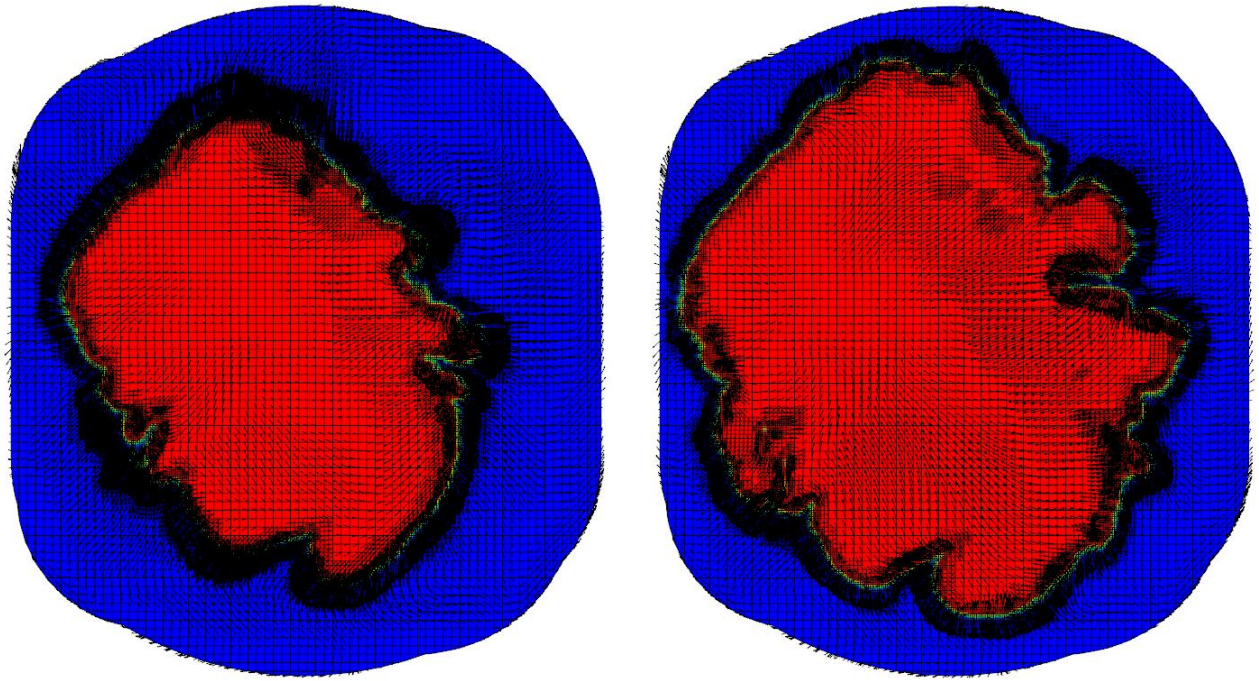

(a) (b)

Figure 7.35 Progress variable and vector field of 23th cycle on top view2 (X=2.3mm). (a) 720 CA, (b) 723 CA

7.4 Method for Reduction of CCV

7.4.1 Investigation of the Controllable Source of CCV

The factors affecting the CCV are the small scale turbulent flow and the local vortex which is the large scale turbulent flow. The way how to control the factors to reduce the CCV is investigated. It is generally known that the strong tumble flow can also lead to stronger turbulence. Therefore, at first, the controllability of the small scale turbulent flow and the tumble ratio is investigated. Next, the controllability of the local vortices is analyzed

Two cycles of the fastest and the slowest combustion phase are used to evaluate the controllability of turbulence flow: the 4th cycle is the fastest cycle, the 29th cycle is the slowest cycle as shown in Figure 7.6. In Figure 7.36, the SGS turbulent velocity distribution of the fastest and the slowest combustion cycle at the maximum intake valve lift timing is shown. There is no noticeable difference in the SGS turbulent velocity of two cycles from intake port to intake valve. There is also no noticeable difference in the vector field comparison similar to the comparison of the SGS turbulent velocity as shown in Figure 7.37.

The velocity field of two cycles during the compression process is analyzed. In Figures 7.38 and 7.39, the flow field is shown on the side view (Y=0mm) to investigate the tumble motion. Due to the flat piston shape, the tumble motion is not observed at 630 CA (Figure 7.38) and 660 CA (Figure 7.39). At 695 CA just before the ignition timing, the flow field of two cycles show randomness motion rather than the typical tumble motion as shown in Figure 7.40. Unlike the flow field observed in the side view, an organized flow

motion is found in the front view. A strong wall flow on the left and right side is identified in the both the fastest and the slowest combustion cycles during compression process as shown in Figure 7.41. In Figure 7.42, as compression progresses, a more organized wall flow is observed at 660 CA. As the wall flow in the fastest cycle is stronger than the wall flow in the slowest cycle as shown in Figure 7.42, the well-formed vortices can be observed in the fastest cycle just before ignition. In the front view, the importance of the wall flow to generate well-formed vortices is identified. Therefore, a new piston shape that can enhance the wall flow will be introduced and the result of reduced the CCV will be described in the following section.

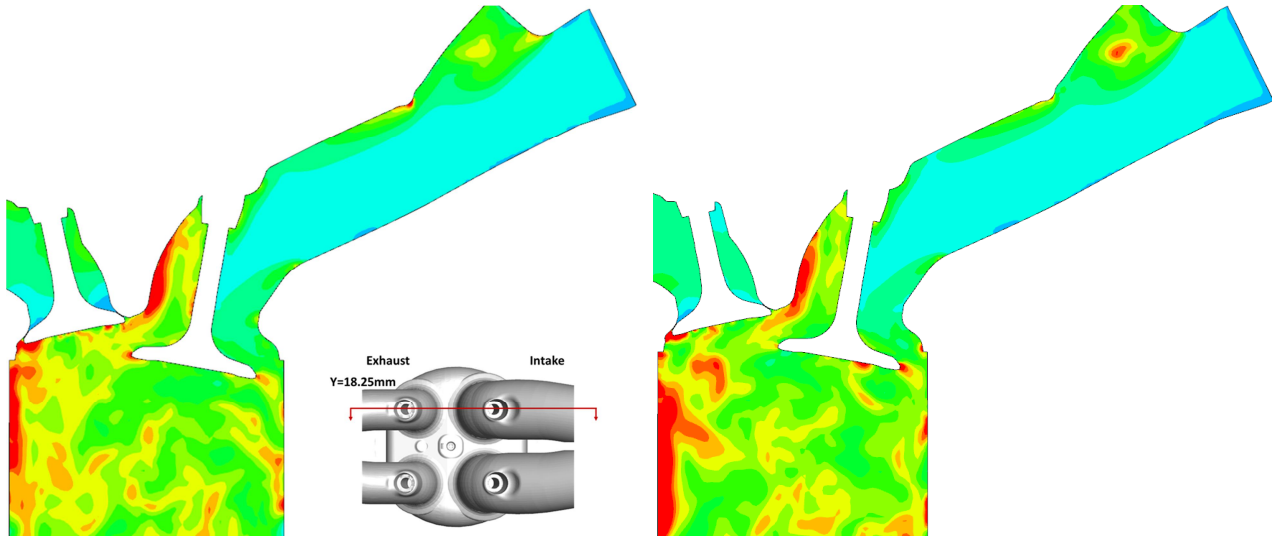

(a) (b)

Figure 7.36 The SGS turbulent velocity distribution of the fastest and the slowest combustion cycles on Y=18.25mm plane at the maximum intake valve lift timing (485 CA). (a) the fastest cycle (4th cycle), (b) the slowest cycle (29th cycle)

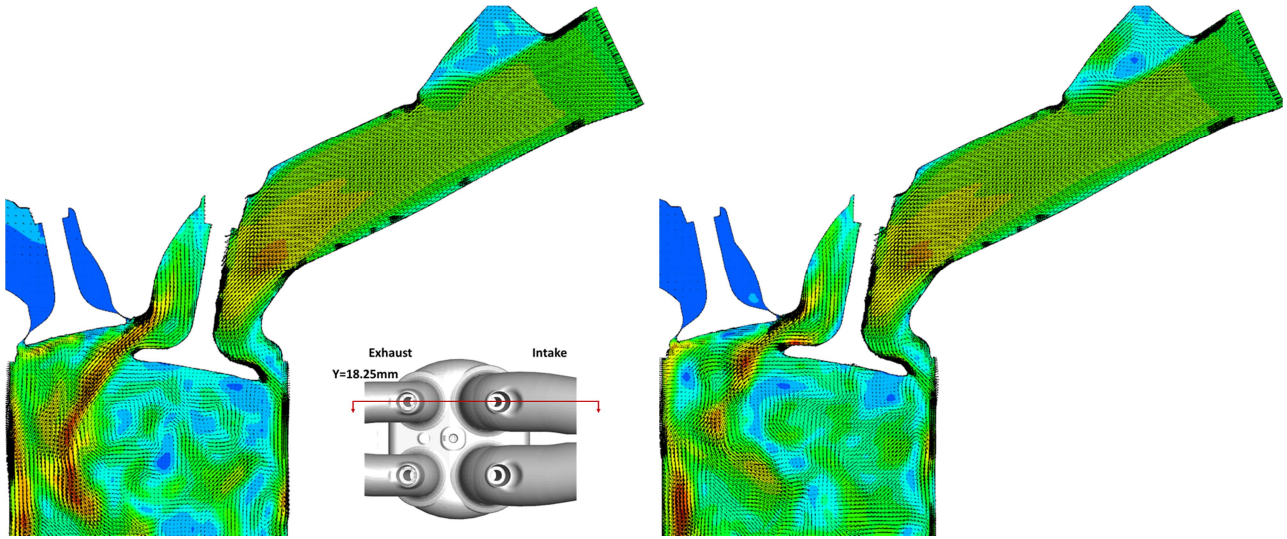

(a) (b)

Figure 7.37 The velocity distribution of the fastest and the slowest combustion cycles on Y=18.25mm plane at the maximum intake valve lift timing (485 CA). (a) the fastest cycle (4th cycle), (b) the slowest cycle (29th cycle)

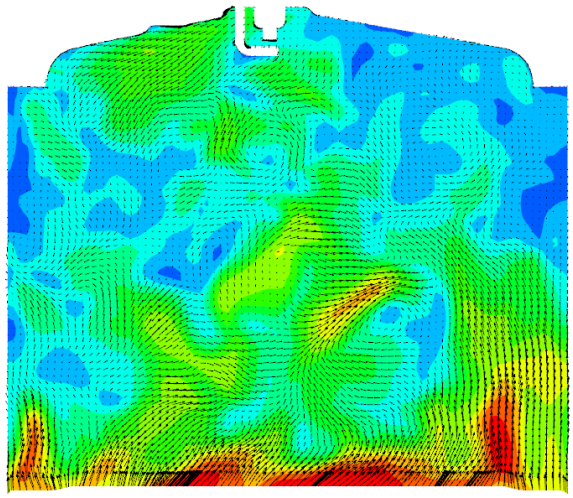

(a)

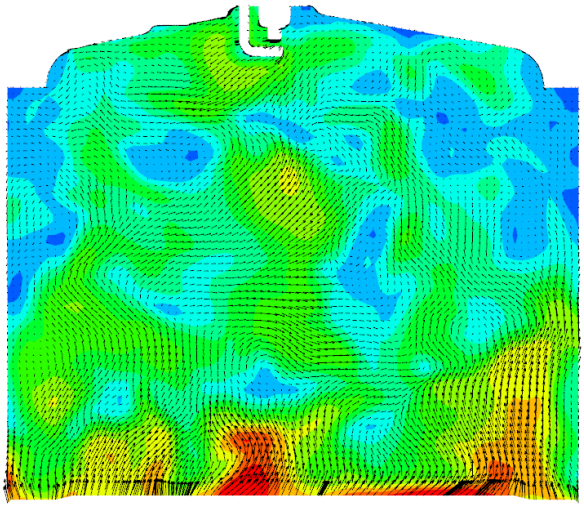

(b)

Figure 7.38 The velocity distribution of the fastest and the slowest combustion cycles on the side view (Y=0mm) at 630 CA. (a) the fastest cycle (4th cycle), (b) the slowest cycle (29th cycle)

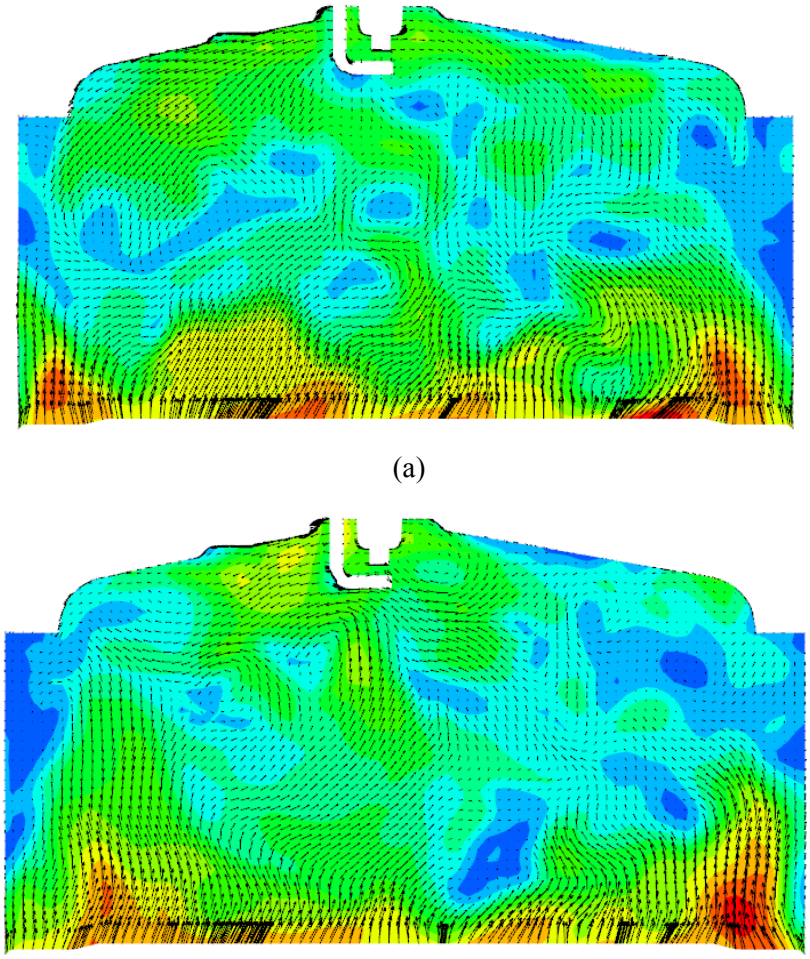

(a)

(b)

Figure 7.39 The velocity distribution of the fastest and the slowest combustion cycles on the side view (Y=0mm) at 660 CA. (a) the fastest cycle (4th cycle), (b) the slowest cycle (29th cycle)

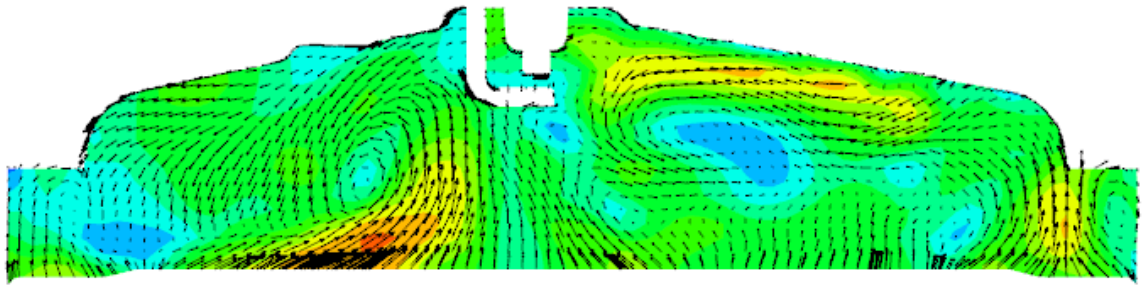

(a)

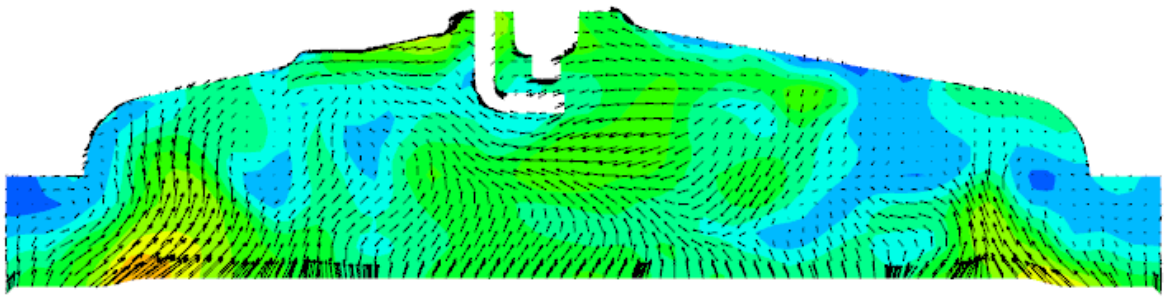

(b)

Figure 7.40 The velocity distribution of the fastest and the slowest combustion cycles on the side view (Y=0mm) at 695 CA. (a) the fastest cycle (4th cycle), (b) the slowest cycle (29th cycle)

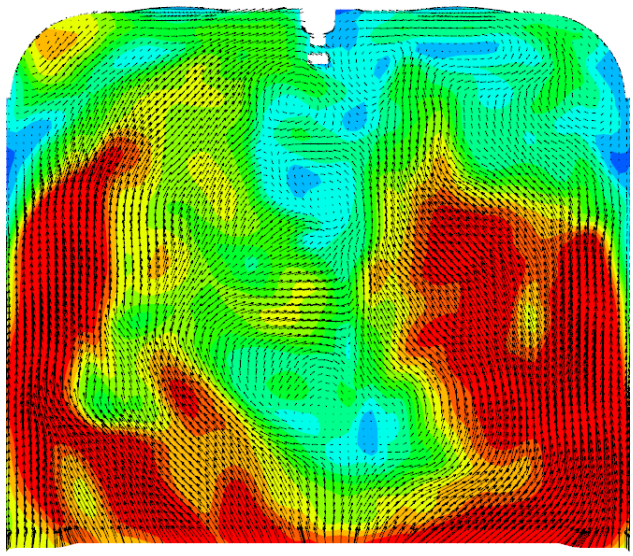

(a)

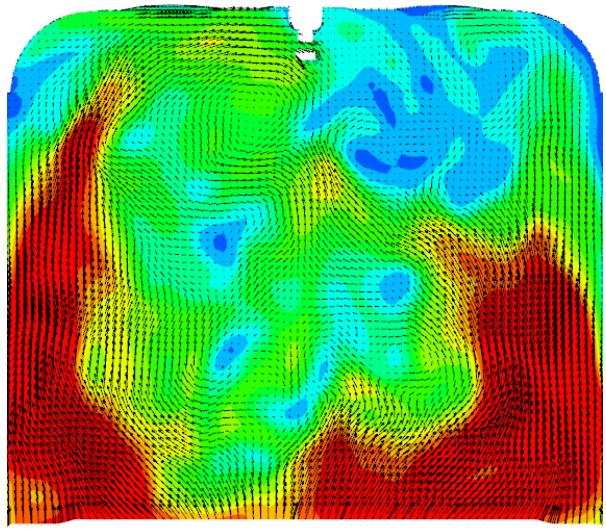

(b)

Figure 7.41 The velocity distribution of the fastest and the slowest combustion cycles on the front view (X=-2.6mm) at 630 CA. (a) the fastest cycle (4th cycle), (b) the slowest cycle (29th cycle)

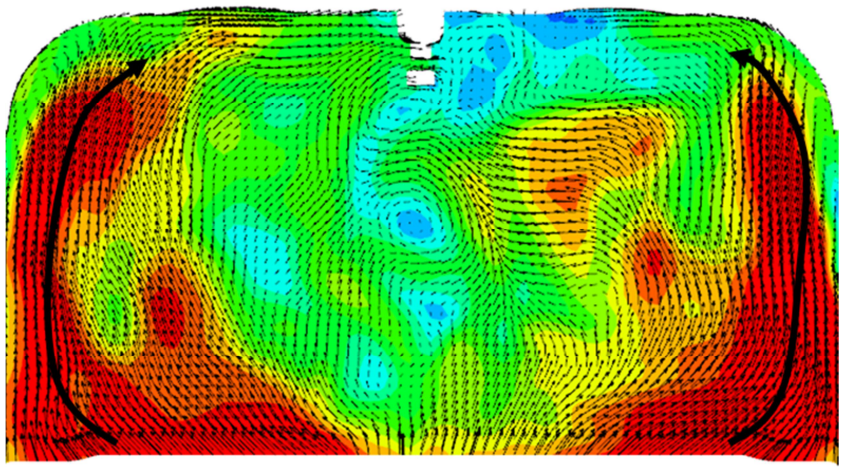

(a)

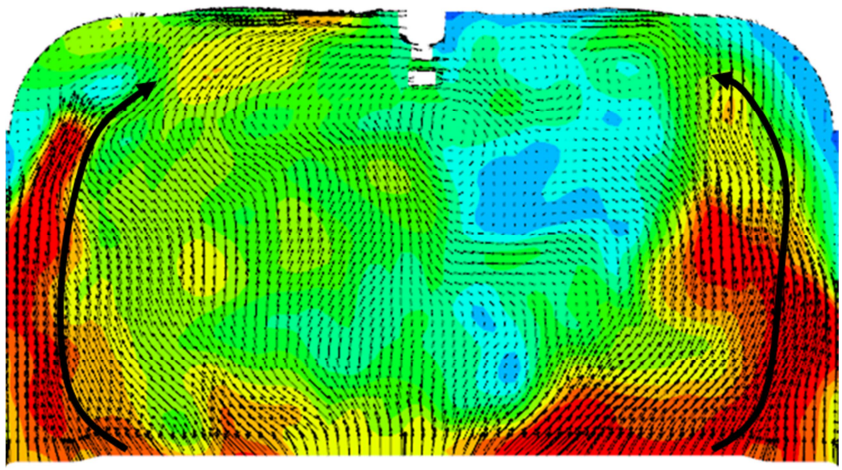

(b)

Figure 7.42 The velocity distribution of the fastest and the slowest combustion cycles on the front view (X=-2.6mm) at 660 CA. (a) the fastest cycle (4th cycle), (b) the slowest cycle (29th cycle)

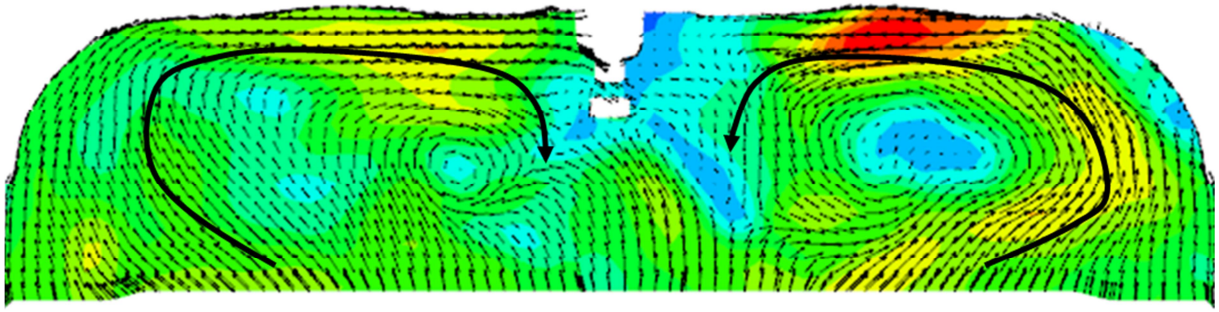

(a)

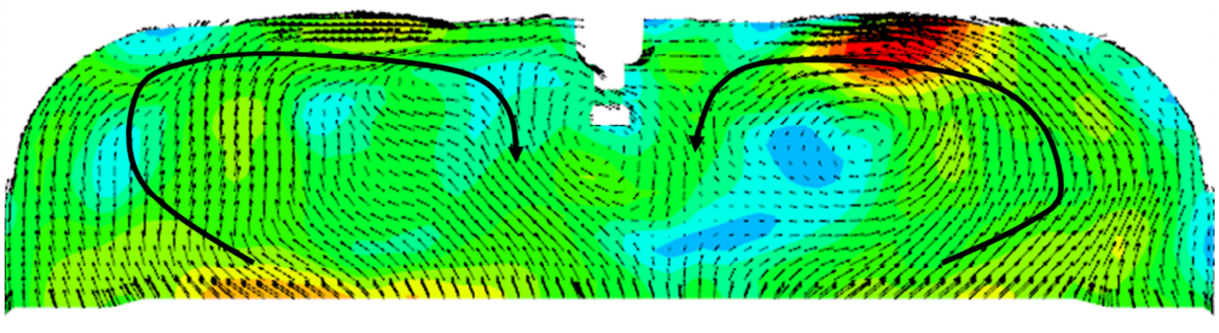

(b)

Figure 7.43 The velocity distribution of the fastest and the slowest combustion cycles on the front view (X=-2.6mm) at 695 CA. (a) the fastest cycle (4th cycle), (b) the slowest cycle (29th cycle)

7.4.2 Result of New Designed Piston

Figure 7.44 shows a new designed piston shape that enhances wall flow at the end of compression to make a vortex formation better. The width of the left and right sides is reduced by 2mm from 6.3mm to 4.3mm, and the height of the top of the piston is raised by 1mm to strengthen the wall flow. At first, the new designed piston is evaluated by using RANS approach. The numerical setup of RANS is identical to the numerical setup for LES introduced in chapter 6. except the turbulence model. Figure 7.45 shows the vector field of the base piston case and the new designed piston case on the front view (X=-2.6mm) at 695 CA. Vortices are observed in the both case. Due to the intended wall flow of the new piston case, the vortices of the new piston case is more distinctly generated than the base piston case.

The 14 LES cycles of the new piston case are conducted to compare the COV of peak pressure with base case. The numerical setup is the same as the base case described in chapter 6. The in-cylinder pressure curves of LES are compared with the experimental data in Figure 7.46. The range of pressure curves is narrower than the base case shown in Figure 7.1. Even though the sample of the new piston case is not enough, the trend of the reduced COV of peak pressure is observed in Figure 7.47. When the number of samples in the base case of LES is 14 cycles same as in the new case, the COV of peak pressure for the base case is 8.44% and the COV of the new case is 5.83%. Therefore, the enhanced vortices formation is effect for combustion CCV. However, the average combustion pressure is predicted to be somewhat lower than the experimental data. For quantitative comparison, the MFB values of the experiment, the base case and the new piston case are compared in Figure 7.48. Both the base and the new piston cases are well matched with the experimental

results up to the MFB 10. However, in the case of the new piston result, the MFB 90 value slows down as flame propagates.

The reason why the combustion of the new piston case slows down in the latter phase is identified in Figure 7.49. Figure 7.49 describes the vector field of the base and the new piston cases calculated by using RANS approach under the cold-flow condition at 715 CA when is the timing of the MFB 10. There is no flow separation in the base case, but the separations are identified on the left and right ends of the piston in the new piston case. Because of the unfavorable flow behavior, the flame propagation of the new piston case slows down in the latter phase. Because the new piston is designed only in terms of reducing the CCV, it results in the unintended consequence of slowed combustion speed. Nevertheless, it is identified that the formation of vortex by the enhanced wall flow plays an important role in reducing the combustion CCV. Furthermore, if the piston is well designed to form a flow that helps the combustion speed, both rapid combustion phase and the CCV reduction can be achieved.

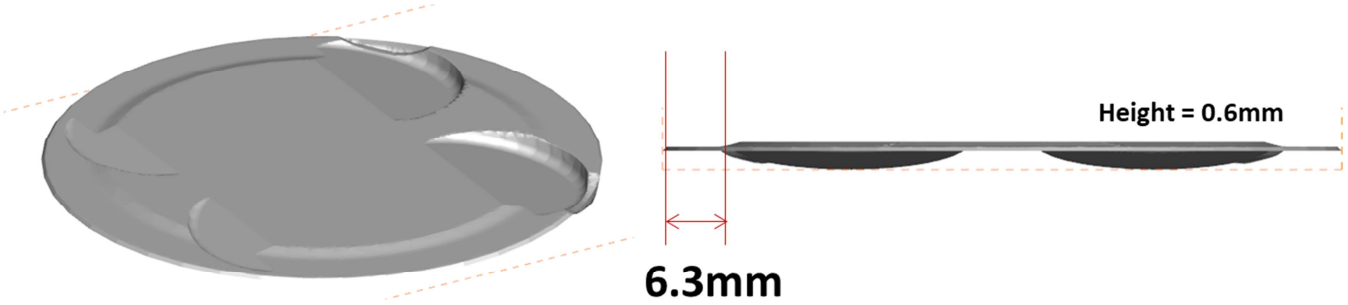

(a)

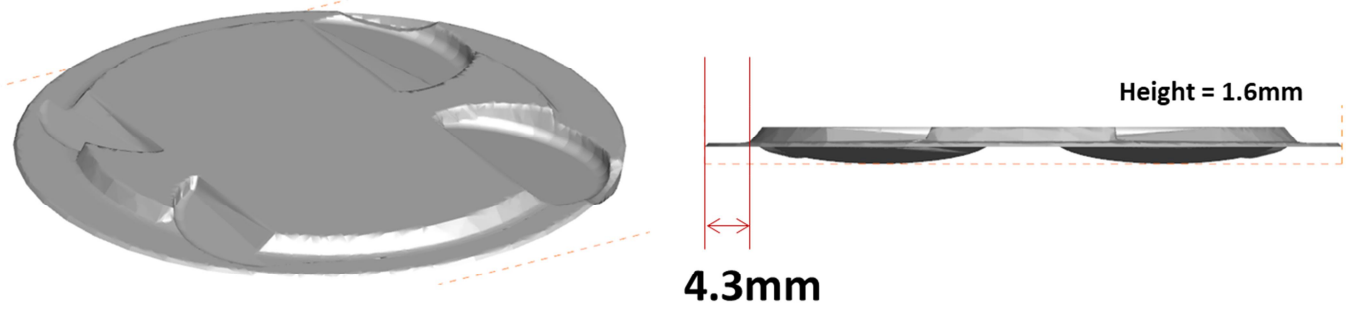

(b)

Figure 7.44 The base piston and new designed piston shape. (a) Base piston, (b) New piston

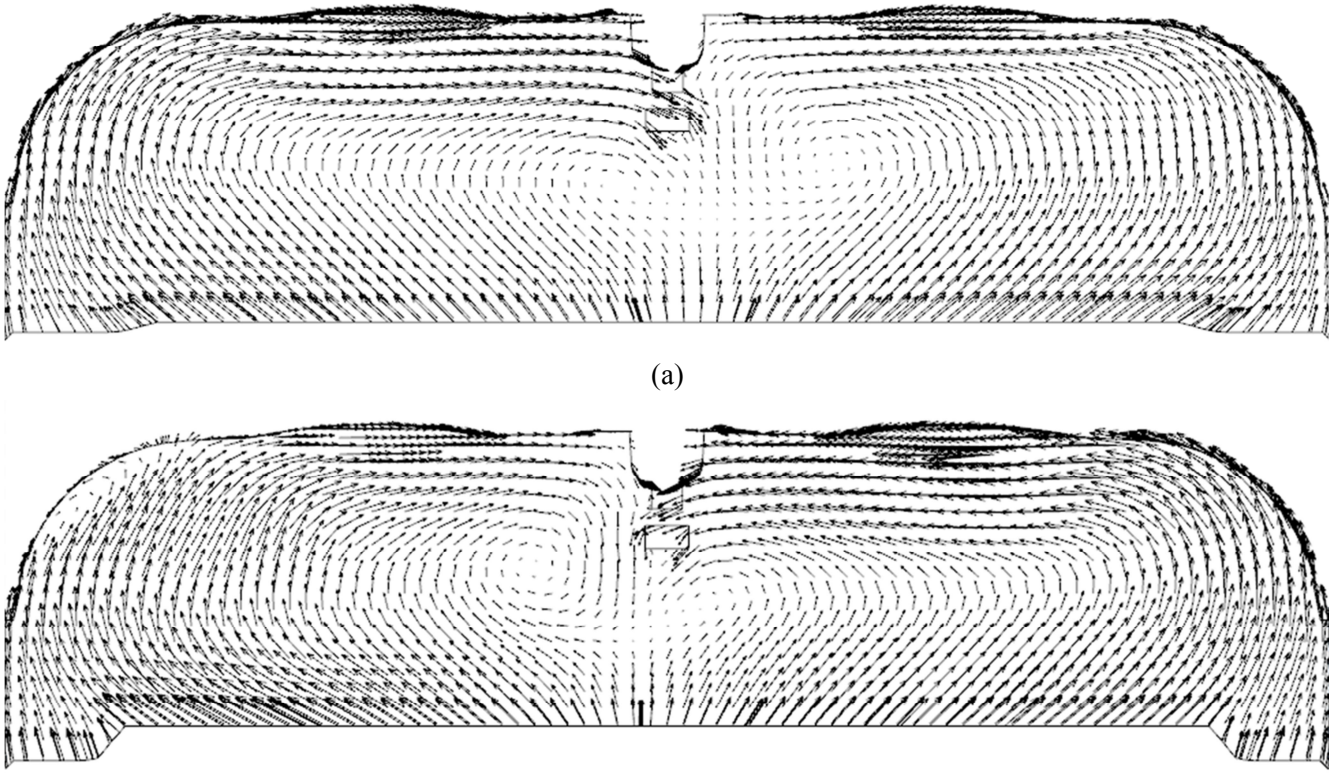

(a)

(b)

Figure 7.45 The vector field of the base piston case and the new piston case on the front view (X=-2.6mm) at 695 CA. (a) Base piston, (b) New piston

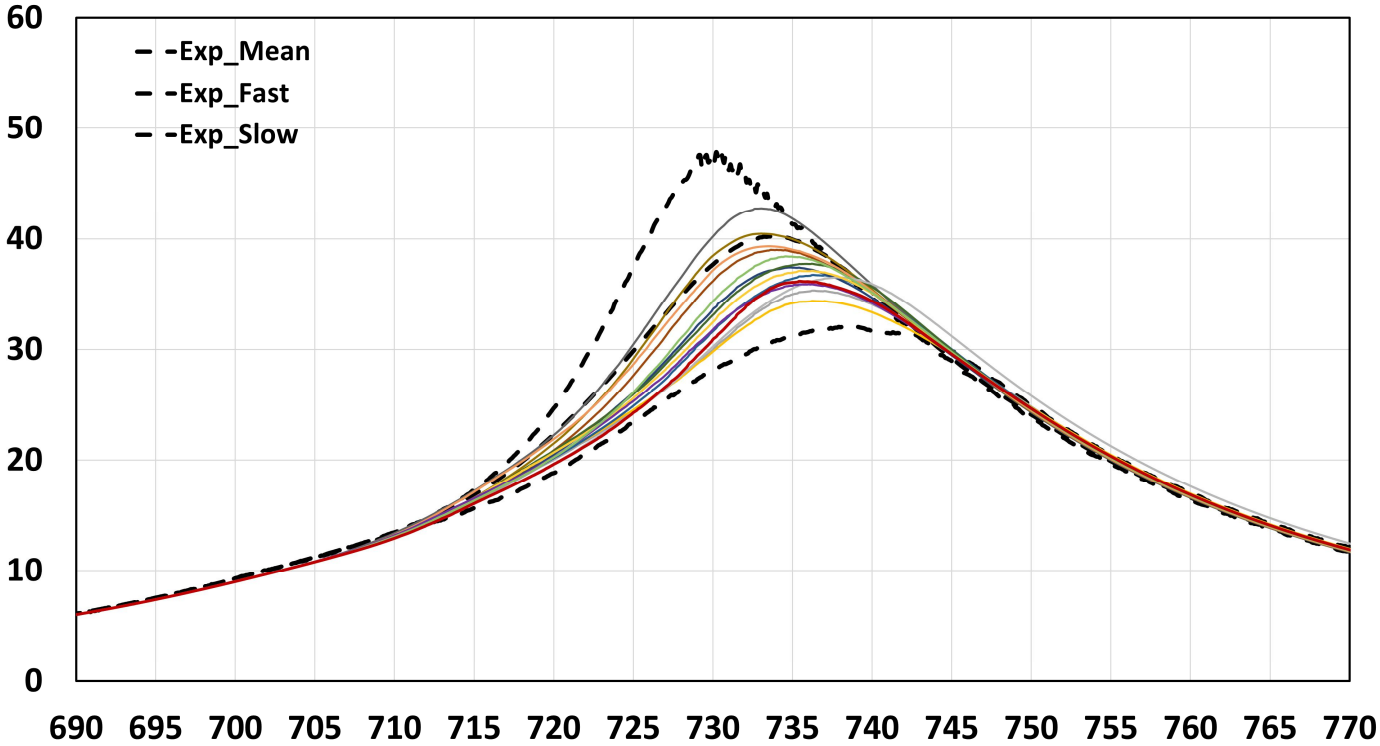

Figure 7.46 Comparison of in-cylinder pressure between LES (new piston) and experimental data

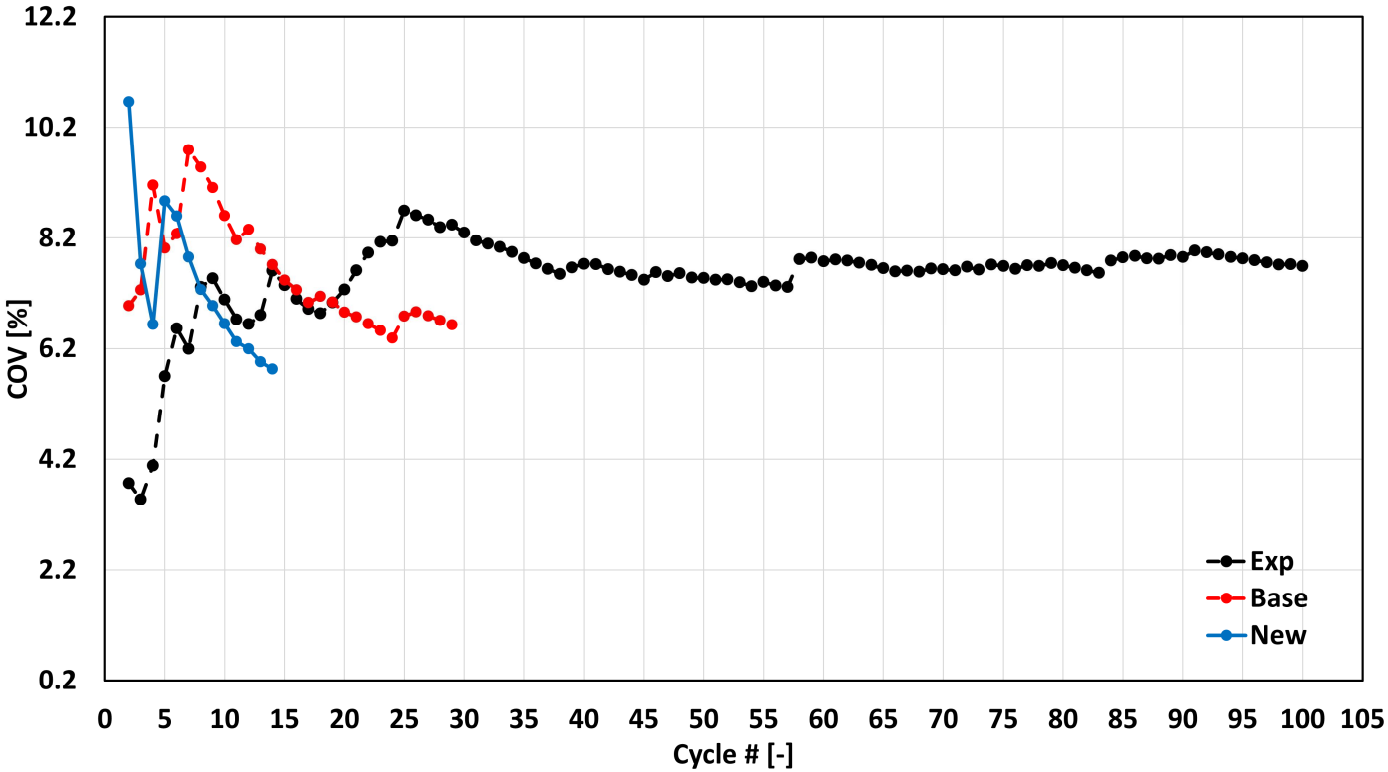

Figure 7.47 The cumulative COV of peak pressure. Black dotted line: experiments, red dotted line: base, blue solid line: new piston

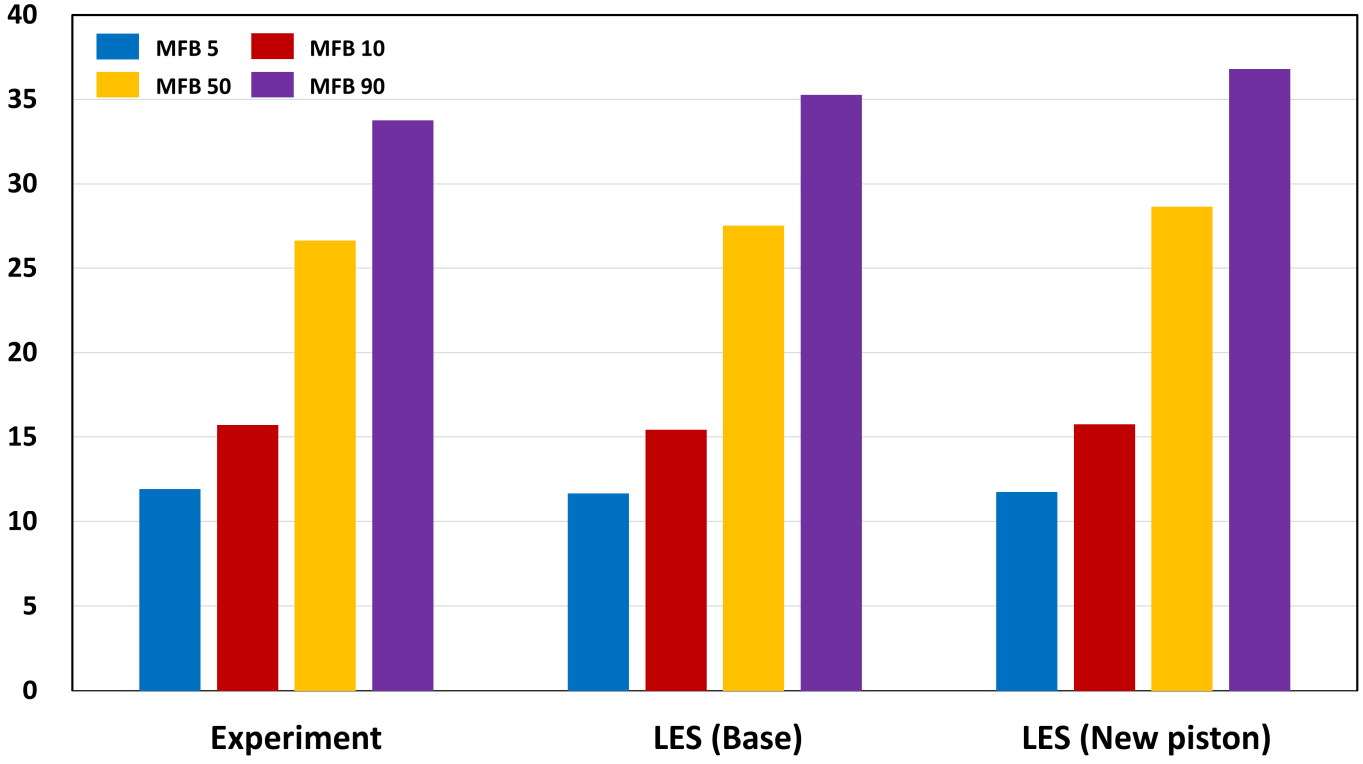

Figure 7.48 Comparison of MFB among experimental data, LES result of base case and LES result of new piston case

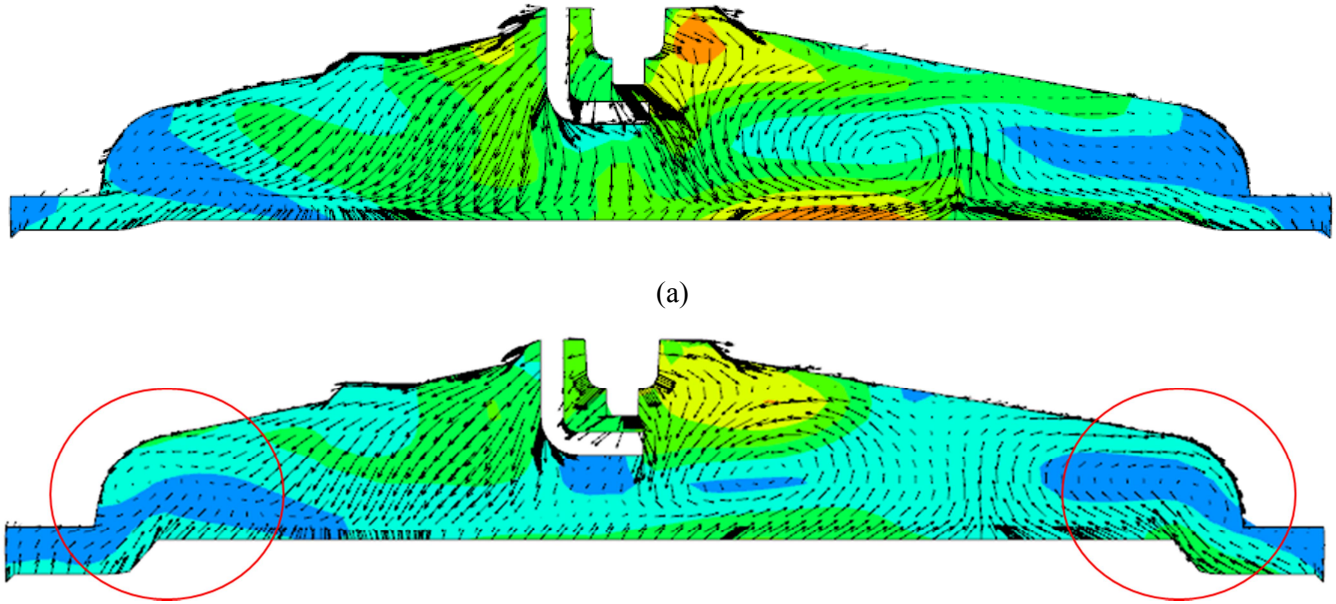

(a)

(b)

Figure 7.49 The comparison of vector field between base case and new piston case calculated by using RANS approach on the front view (X=-2.6mm) at 715 CA. (a) Base case and (b) New piston case

Chapter 8. Conclusions

In this study, the multi-cycle LES is conducted to reproduce the combustion CCV of the engine using the lagrangian ignition model reflecting the characteristics of LES. The investigation of the turbulent flow effect on the combustion CCV is conducted with the verified LES results. The main source of CCV is found and the guide to reduce the combustion CCV is provided.

First of all, the cold-flow engine simulation was conducted to evaluate the SGS turbulent model that could accurately simulate the in-cylinder flow motion. The PIV experimental data performed on the TCC-III single cylinder optical engine designed by University of Michigan and GM research center was used as validation data. Three SGS turbulent models were compared with the PIV data in terms of the velocity field in a combustion chamber. The most common used the static Smagorinsky model, the dynamic Smagorinsky and the 1-equation dynamic structure model with the transport equation for the SGS turbulent kinetic energy were compared. In terms of the prediction of velocity field, the dynamic Smagroinsky and the DSM were well matched with the PIV data. The LES quality index was used to assess the impact of the SGS turbulent model. The LES quality index can evaluate the contribution of the SGS model effect on the turbulent flow. Thanks to the superior concept of dynamically calculated model coefficient, the dynamic Smagorinsky and the DSM showed the proper contribution of the SGS model with 1mm of in-cylinder grid size, leading to reasonable computational cost. Although the accuracy of both the dynamic Smagorinsky model and the DSM was excellent, the DSM was adopted because of the numerical stability coming from the transport equation of the SGS turbulent kinetic energy and the theoretical advantages of the one-equation model.

To predict combustion phenomena, the G-equation combustion model was adopted. Pitsch [67] proposed the G-equation model for LES. The author derived the sub-filtered G-equation for the corrugated flamelets regime and the thin reaction flamelets regime based on the Peter's research [45]. The turbulent burning velocity for both the corrugated flamelets regime and the thin reaction flamelets regime is quite complicated with many model coefficients. The model coefficients are typically derived for RANS approach. Therefore, the adjustment of the model coefficient is necessary, but too many coefficients make it difficult to find proper values. Thus, it is important to identify which combustion regime belongs to under engine conditions to define the turbulent flame speed. Through RANS approach, it is verified that the target engine condition belongs to the corrugated flamelets regime. Therefore, the turbulent burning velocity is derived for the corrugated flamelets regime based on the Pitsch's work [67]. Finally, a very simple equation of the turbulent burning velocity with only one model coefficient is derived. The coefficient value is found with the validation of in-cylinder pressure against the experimental data.

The ignition model is developed for LES. At first, lagrangian particles are employed to predict the behavior of the ignition channel. The elongation of the ignition channel by turbulent flow can be reproduced. The secondary electric circuit model is used to calculate the spark energy, and it can predict the restrike and the end of ignition time. Immediately after the breakdown phase, the plasma channel at high temperature grows by the thermal expansion for a short time (~10μs). Generally, the thermal expansion is calculated using the 1D sub-cycle model, but it requires a lot of computational time, which is not suitable for multi-cycle LES. Therefore, in the present study, the empirical function is derived to predict the time, temperature and radius of the ignition channel after end of the arc phase. At first, the 1D simulation for the thermal expansion is conducted under various ambient temperature and pressure

conditions to build the database. Next, the empirical function is derived based on the database. After the thermal expansion, the channel grows by chemical reaction and flame propagation progresses. In the early stage, the flame is thin and unstable, so it is propagated by the laminar burning velocity. And over time, the flame is propagated by the turbulent burning velocity. The turbulent frame brush thickness term suitable for LES is introduced to predict the transition state between laminar flame propagation and turbulent flame propagation. Finally, when the channel is grown sufficiently, flame is propagated in the 3D field by the G-equation.

The multi-cycle engine simulation is performed using the SGS turbulent model, the combustion model and the developed ignition model. The accuracy of simulation is verified compared to the experimental data in terms of the in-cylinder pressure, the combustion phase and the COV of peak pressure. Next, the turbulent flow effect on the combustion CCV is investigated to find the source of the CCV. In this study, LES results are analyzed from two perspectives: the small scale turbulent flow and the large scale turbulent flow. In LES, the small scale turbulent flow is realized by the SGS turbulent velocity and the large scale turbulent flow is reflected in the velocity field. Before the ignition timing, the volume averaged SGS turbulent velocity in in-cylinder is analyzed. During the compression process, the SGS turbulent velocity of the fast combustion cycles increased than the SGS turbulent velocity of the slow cycles, and after ignition, the SGS turbulent velocity of the fast cycles around the flame surface continued to be greater. However, when the correlation between the SGS turbulent velocity and the MFB 50 is analyzed, it is found that the SGS turbulent velocity has an effect on the combustion speed but it is not absolute.

Next, the large scale turbulent flow effect on the combustion CCV is investigated. First of all, the tumble ratios, typical large scale turbulent flow, is analyzed. The negligible effect of the secondary tumble and swirl is observed. However, the conversion of the energy contained in the main tumble into the SGS turbulent velocity during the compression process is identified. To analyze the direct effect of the large scale turbulence flow on combustion, the representative four cycles of velocity field and the flame propagation are analyzed. It is turned out that he local vortex effect is an important factor for the combustion CCV. The velocity distribution and the SGS turbulent velocity field are investigated to find out the controllable factor to reduce the CCV. Finally, the possibility of reducing the combustion CCV is found by enhancing the wall flow to generate intended vortices.

The new piston is designed to strengthen the wall flow. RANS approach is used to evaluate the effect of the new piston shape before performing multi-cycle LES. Based on RANS result, the multi-cycle LES of the new piston shape is conducted and compared with the base case in terms of the combustion CCV. The new designed piston case results in the lower CCV than the base piston case. However, because of the unintended flow separation on the end of the piston, the combustion speed is slower than the base case. The drawback of the new piston can be easily improved by a design change. Finally, despite of the slow combustion speed, the new piston shape can reduce the combustion CCV.

This research includes study of the SGS turbulent model for the ICE, the combustion model, the ignition model and the effect of turbulent flow on the combustion CCV. From the results, the main source of the CCV and the possibility of the controllability are found. The new piston results show the

reduced CCV of combustion. Therefore, this study can contribute to provide the guide how to analyze and reduce the combustion CCV in SI engines.

Chapter 9. Bibliography

[1] Sources of Greenhouse Gas Emissions, United States Environmenatl Protection Agency (EPA). Available from: https://www.epa.gov/ghgemissions/sources-greenhouse-gas-emissions

[2] K. Min, Future IC Engine Technology: Toward Near Zero CO2 and Exhaust Emissions, china Engine Technology Summit, 2020.

[3] B. John, Heywood, Internal combustion engine fundamentals, Pub: McGraw Hill International Editions, (1988).

[4] X. Baby, A. Dupont, A. Ahmed, W. Deslandes, G. Charnay, M. Michard, A new methodology to analyze cycle-to-cycle aerodynamic variations, in, SAE Technical Paper, 2002.

[5] J. Bode, J. Schorr, C. Krüger, A. Dreizler, B. Böhm, Influence of three-dimensional in-cylinder flows on cycle-to-cycle variations in a fired stratified DISI engine measured by time-resolved dual-plane PIV, Proceedings of the Combustion Institute, 36 (2017) 3477-3485.

[6] T. Fujikawa, Y. Nomura, Y. Hattori, T. Kobayashi, M. Kanda, Analysis of cycle-by-cycle variation in a direct injection gasoline engine using a laser-induced fluorescence technique, International Journal of Engine Research, 4 (2003) 143-153.

[7] S. Hokimoto, T. Kuboyama, Y. Moriyoshi, M. Iida, T. Watanabe, Analyses of Cycle-to-Cycle Variation of Combustion and In-Cylinder Flow in a Port Injection Gasoline Engine Using PIV and PLIF Techniques, in: SAE Technical Paper Series, 2017.

[8] S. Fontanesi, A. D'Adamo, S. Paltrinieri, G. Cantore, C. Rutland, Assessment of the Potential of Proper Orthogonal Decomposition for the Analysis of Combustion CCV and Knock Tendency in a High Performance Engine, in: SAE Technical Paper Series, 2013.

[9] D. Goryntsev, A. Sadiki, M. Klein, J. Janicka, Large eddy simulation based analysis of the effects of cycle-to-cycle variations on air–fuel mixing in realistic DISI IC-engines, Proceedings of the Combustion Institute, 32 (2009) 2759-2766.

[10] M. Schmitt, R. Hu, Y.M. Wright, P. Soltic, K. Boulouchos, Multiple Cycle LES Simulations of a Direct Injection Natural Gas Engine, Flow, Turbulence and Combustion, 95 (2015) 645-668.

[11] N. Van Dam, C. Rutland, Understanding In-Cylinder Flow Variability Using Large-Eddy Simulations, Journal of engineering for gas turbines and power, 138 (2016).

[12] S. Pischinger, T. Korfer, Heading towards Higher Diesel Powertrain Efficiencies - Tailored Electrificatio and Hybridization, SIA Powertrain Conference, 2016.

[13] E. Zervas, Correlations between cycle-to-cycle variations and combustion parameters of a spark ignition engine, Applied Thermal Engineering, 24 (2004) 2073-2081.

[14] B. Huang, E. Hu, Z. Huang, J. Zheng, B. Liu, D. Jiang, Cycle-by-cycle variations in a spark ignition engine fueled with natural gas–hydrogen blends combined with EGR, International Journal of Hydrogen Energy, 34 (2009) 8405-8414.

[15] Y. Chen, Y. Wang, R. Raine, Correlation between cycle-by-cycle variation, burning rate, and knock: A statistical study from PFI and DISI engines, Fuel, 206 (2017) 210-218.

[16] D.C. Haworth, Large-eddy simulation of in-cylinder flows, Oil & Gas Science and Technology, 54 (1999) 175-185.

[17] L. Thobois, G. Rymer, T. Souleres, T. Poinsot, Large-eddy simulation in IC engine geometries, SAE Transactions, (2004) 1192-1209.

[18] B. Enaux, V. Granet, O. Vermorel, C. Lacour, L. Thobois, V. Dugué, T. Poinsot, Large Eddy Simulation of a Motored Single-Cylinder Piston Engine: Numerical Strategies and Validation, Flow, Turbulence and Combustion, 86 (2010) 153-177.

[19] C. Angelberger, X. Yang, T.-W. Kuo, Correlation of CCV Between In-Cylinder Swirl Ratio and Polar Velocity Profile in Valve Seat Region Using LES Under Motored Engine Condition, Oil & Gas Sciences and Technology – Revue d'IFP Energies nouvelles, 72 (2017).

[20] C. Chen, M.M. Ameen, H. Wei, C. Iyer, F. Ting, B. Vanderwege, S. Som, LES Analysis on Cycle-to-Cycle Variation of Combustion Process in a DISI Engine, in: SAE Technical Paper Series, 2019.

[21] A. d'Adamo, S. Breda, S. Fontanesi, G. Cantore, LES Modelling of Spark-Ignition Cycle-to-Cycle Variability on a Highly Downsized DISI Engine, SAE International Journal of Engines, 8 (2015) 2029-2041.

[22] S. Fontanesi, S. Paltrinieri, G. Cantore, LES Analysis of Cyclic Variability in a GDI Engine, in: SAE Technical Paper Series, 2014.

[23] V. Granet, O. Vermorel, C. Lacour, B. Enaux, V. Dugué, T. Poinsot, Large-Eddy Simulation and experimental study of cycle-to-cycle variations of stable and unstable operating points in a spark ignition engine, Combustion and flame, 159 (2012) 1562-1575.

[24] Y. Yu, D. Splitter, S. Kim, Predicting Cycle-to-cycle Variations in a Spark-ignition Engine using Multi-cycle Large Eddy Simulation, in, Oak Ridge National Lab.(ORNL), Oak Ridge, TN (United States), 2019.

[25] M. Ghaderi Masouleh, K. Keskinen, O. Kaario, H. Kahila, S. Karimkashi, V. Vuorinen, Modeling cycle-to-cycle variations in spark ignited combustion engines by scale-resolving simulations for different engine speeds, Applied Energy, 250 (2019) 801-820.

[26] S. Fontanesi, A. d'Adamo, C.J. Rutland, Large-Eddy simulation analysis of spark configuration effect on cycle-to-cycle variability of combustion and knock, International Journal of Engine Research, 16 (2015) 403-418.

[27] A. Robert, K. Truffin, N. Iafrate, S. Jay, O. Colin, C. Angelberger, Large-eddy simulation analysis of knock in a direct injection spark ignition engine, International Journal of Engine Research, 20 (2018) 765-776.

[28] C. Chen, P. Pal, M. Ameen, D. Feng, H. Wei, Large-eddy simulation study on cycle-to-cycle variation of knocking combustion in a spark-ignition engine, Applied Energy, 261 (2020).

[29] M.M. Ameen, M. Mirzaeian, F. Millo, S. Som, Numerical Prediction of Cyclic Variability in a Spark Ignition Engine Using a Parallel Large Eddy Simulation Approach, Journal of Energy Resources Technology, 140 (2018).

[30] S. Som, R. Scarcelli, J. Kodavasal, E. Pomraning, S. Wijeyakulasuriya, D.M. Probst, Predicting Cycle-to-Cycle Variation With Concurrent Cycles in a Gasoline Direct Injected Engine With Large Eddy Simulations, Journal of Energy Resources Technology, 142 (2020).

[31] O. Reynolds, Iv. on the dynamical theory of incompressible viscous fluids and the determination of the criterion, Philosophical transactions of the royal society of london.(a.), (1895) 123-164.

[32] J. Smagorinsky, General circulation experiments with the primitive equations: I. The basic experiment, Monthly weather review, 91 (1963) 99-164.

[33] J.W. Deardorff, A numerical study of three-dimensional turbulent channel flow at large Reynolds numbers, Journal of Fluid Mechanics, 41 (2006) 453-480.

[34] D. Lilly, On the application of the eddy viscosity concept in the inertial sub-range of turbulence. 1966, NCAR Manuscript.

[35] P.J. Mason, N.S. Callen, On the magnitude of the subgrid-scale eddy coefficient in large-eddy simulations of turbulent channel flow, Journal of Fluid Mechanics, 162 (2006).

[36] U. Piomelli, P. Moin, J.H. Ferziger, Model consistency in large eddy simulation of turbulent channel flows, Physics of Fluids, 31 (1988).

[37] A. Yoshizawa, Statistical theory for compressible turbulent shear flows, with the application to subgrid modeling, The Physics of fluids, 29 (1986) 2152-2164.

[38] M. Germano, U. Piomelli, P. Moin, W.H. Cabot, A dynamic subgrid□scale eddy viscosity model, Physics of Fluids A: Fluid Dynamics, 3 (1991) 1760-1765.

[39] A. Yoshizawa, A statistically-derived subgrid model for the large-eddy simulation of turbulence, Physics of Fluids, 25 (1982).

[40] A. Yoshizawa, K. Horiuti, A statistically-derived subgrid-scale kinetic energy model for the large-eddy simulation of turbulent flows, Journal of the Physical Society of Japan, 54 (1985) 2834-2839.

[41] R.H. Kraichnan, The structure of isotropic turbulence at very high Reynolds numbers, Journal of Fluid Mechanics, 5 (1959) 497-543.

[42] V.C. Wong, A proposed statistical□dynamic closure method for the linear or nonlinear subgrid□scale stresses, Physics of Fluids A: Fluid Dynamics, 4 (1992) 1080-1082.

[43] S. Ghosal, T.S. Lund, P. Moin, K. Akselvoll, A dynamic localization model for large-eddy simulation of turbulent flows, Journal of Fluid Mechanics, 286 (2006) 229-255.

[44] E. Pomraning, Development of large eddy simulation turbulence models, Uni-versity of Wisconsin-Madison, 2000, in, Ph. D. thesis.

[45] N. Peters, Turbulent combustion, in, IOP Publishing, 2001.

[46] D. Spalding, Mixing and chemical reaction in steady confined turbulent flames, in: Symposium (International) on Combustion, Vol. 13, Elsevier, 1971, pp. 649-657.

[47] B.F. Magnussen, B.H. Hjertager, On mathematical modeling of turbulent combustion with special emphasis on soot formation and combustion, in: Symposium (international) on Combustion, Vol. 16, Elsevier, 1977, pp. 719-729.

[48] D. Veynante, L. Vervisch, Turbulent combustion modeling, Progress in energy and combustion science, 28 (2002) 193-266.

[49] S. Pope, Computations of turbulent combustion: progress and challenges, in: Proc. Combust. Inst, Vol. 23, 1990, pp. 591-612.

[50] C. Dopazo, Recent developments in pdf methods, Turbulent reacting flows, (1994) 375-474.

[51] T. Hulek, R.P. Lindstedt, Joint Scalar-velocity pdf Modelling of Finite Rate Chemistry in a Scalar Mixing Layer, Combustion Science and Technology, 136 (1998) 303-331.

[52] S.B. Pope, A Monte Carlo Method for the PDF Equations of Turbulent Reactive Flow, Combustion Science and Technology, 25 (2008) 159-174.

[53] S.B. Pope, PDF methods for turbulent reactive flows, Progress in energy and combustion science, 11 (1985) 119-192.

[54] A.R. Kerstein, A Linear- Eddy Model of Turbulent Scalar Transport and Mixing, Combustion Science and Technology, 60 (1988) 391-421.

[55] A.R. Kerstein, Linear-eddy modelling of turbulent transport. Part 3. Mixing and differential molecular diffusion in round jets, Journal of Fluid Mechanics, 216 (2006) 411-435.

[56] A.R. Kerstein, Linear-eddy modelling of turbulent transport. Part 6. Microstructure of diffusive scalar mixing fields, Journal of Fluid Mechanics, 231 (2006) 361-394.

[57] A.R. Kerstein, Fractal Dimension of Turbulent Premixed Flames, Combustion Science and Technology, 60 (1988) 441-445.

[58] A.R. Kerstein, Linear-Eddy Modeling of Turbulent Transport. Part 4. Structure of Diffusion Flames, Combustion Science and Technology, 81 (1992) 75-96.

[59] P.A. McMurthy, S. Menon, A.R. Kerstein, A linear eddy sub-grid model for turbulent reacting flows: Application to hydrogen-air combustion, in: Symposium (International) on Combustion, Vol. 24, Elsevier, 1992, pp. 271-278.

[60] S. Menon, A.R. Kerstein, Stochastic simulation of the structure and propagation rate of turbulent premixed flames, in: Symposium (International) on Combustion, Vol. 24, Elsevier, 1992, pp. 443-450.

[61] K. Bray, J.B. Moss, A unified statistical model of the premixed turbulent flame, Acta Astronautica, 4 (1977) 291-319.

[62] K.C. BRAY, Recent developments in BML Model of premixed turbulent combustion, Turbulent reacting flows, (1994).

[63] P.A. Libby, F.A. Williams, Turbulent reacting flows, Academic press, 1994.

[64] J. Duclos, D. Veynante, T. Poinsot, A comparison of flamelet models for premixed turbulent combustion, Combustion and flame, 95 (1993) 101-117.

[65] F.E. Marble, J.E. Broadwell, The coherent flame model for turbulent chemical reactions, in, PURDUE UNIV LAFAYETTE IN PROJECT SQUIDHEADQUARTERS, 1977.

[66] H. Pitsch, A G-equation formulation for large-eddy simulation of premixed turbulent combustion, Annual Research Briefs, (2002) 3-14.

[67] H. Pitsch, A consistent level set formulation for large-eddy simulation of premixed turbulent combustion, Combustion and flame, 143 (2005) 587-598.

[68] S.B. Pope, Turbulent flows, in, IOP Publishing, 2001.

[69] Z. Warsi, Conservation form of the Navier-Stokes equations in general nonsteady coordinates, AIAA Journal, 19 (1981) 240-242.

[70] A. Leonard, Energy cascade in large-eddy simulations of turbulent fluid flows, Adv. Geophys. A, 18 (1974) 237-248.

[71] U. Piomelli, W.H. Cabot, P. Moin, S. Lee, Subgrid□scale backscatter in turbulent and transitional flows, Physics of Fluids A: Fluid Dynamics, 3 (1991) 1766-1771.

[72] J.W. Deardorff, A numerical study of three-dimensional turbulent channel flow at large Reynolds numbers, Journal of Fluid Mechanics, 41 (1970) 453-480.

[73] I. Ko, A. D'Adamo, S. Fontanesi, K. Min, Study of LES Quality Criteria in a Motored Internal Combustion Engine, in: SAE Technical Paper Series, 2017.

[74] I. Ko, K. Min, F. Rulli, A. D'Adamo, F. Berni, S. Fontanesi, Investigation of Sub-Grid Model Effect on the Accuracy of In-Cylinder LES of the TCC Engine under Motored Conditions, in: SAE Technical Paper Series, 2017.

[75] P. Schiffmann, S. Gupta, D. Reuss, V. Sick, X. Yang, T.W. Kuo, TCC-III Engine Benchmark for Large-Eddy Simulation of IC Engine Flows, Oil & Gas Science and Technology – Revue d'IFP Energies nouvelles, 71 (2015).

[76] P. Abraham, D. Reuss, V. Sick, High-Speed Particle Image Velocimetry Study of In-Cylinder Flows with Improved Dynamic Range, in, SAE International, 2013.

[77] F. di Mare, R. Knappstein, M. Baumann, Application of LES-quality criteria to internal combustion engine flows, Computers & Fluids, 89 (2014) 200-213.

[78] S.B. Pope, Ten questions concerning the large-eddy simulation of turbulent flows, New Journal of Physics, 6 (2004) 35-35.

[79] W.L. Nelson, Petroleum refinery engineering, McGraw-Hill, 2018.

[80] S. Yang, R.D. Reitz, C.O. Iyer, J. Yi, Improvements to combustion models for modeling spark-ignition engines using the G-equation and detailed chemical kinetics, SAE International Journal of Fuels and Lubricants, 1 (2009) 1009-1025.

[81] S. Yang, E. Pomraning, M. Jia, Simulations of gasoline engine combustion and emissions using a chemical-kinetics-based turbulent premixed combustion modeling approach, Proceedings of the Institution of Mechanical Engineers, Part D: Journal of Automobile Engineering, 231 (2017) 743-765.

[82] H.J. Curran, P. Gaffuri, W.J. Pitz, C.K. Westbrook, A comprehensive modeling study of iso-octane oxidation, Combustion and flame, 129 (2002) 253-280.

[83] C. Westbrook, H. Curran, W. Pitz, J. Griffiths, C. Mohamed, S. Wo, The effects of pressure, temperature, and concentration on the reactivity of alkanes: Experiments and modeling in a rapid compression machine, in: Symposium (international) on combustion, Vol. 27, Elsevier, 1998, pp. 371-378.

[84] M. Mehl, W. Pitz, M. Sjöberg, J.E. Dec, Detailed kinetic modeling of low-temperature heat release for PRF fuels in an HCCI engine, in, SAE Technical Paper, 2009.

[85] C.V. Naik, W.J. Pitz, C.K. Westbrook, M. Sjöberg, J.E. Dec, J. Orme, H.J. Curran, J.M. Simmie, Detailed chemical kinetic modeling of surrogate fuels for gasoline and application to an HCCI engine, SAE Transactions, (2005) 1381-1387.

[86] J.C.G. Andrae, Comprehensive chemical kinetic modeling of toluene reference fuels oxidation, Fuel, 107 (2013) 740-748.

[87] K. Lee, Y. Kim, K. Min, Development of a reduced chemical kinetic mechanism for a gasoline surrogate for gasoline HCCI combustion, Combustion Theory and Modelling, 15 (2010) 107-124.

[88] J.C.G. Andrae, R.A. Head, HCCI experiments with gasoline surrogate fuels modeled by a semidetailed chemical kinetic model, Combustion and flame, 156 (2009) 842-851.

[89] J.C.G. Andrae, A kinetic modeling study of self-ignition of low alkylbenzenes at engine-relevant conditions, Fuel Processing Technology, 92 (2011) 2030-2040.

[90] H.J. Curran, W. Pitz, C. Westbrook, G. Callahan, F. Dryer, Oxidation of automotive primary reference fuels at elevated pressures, in: Symposium (International) on Combustion, Vol. 27, Elsevier, 1998, pp. 379-387.

[91] M. Mehl, J.Y. Chen, W.J. Pitz, S.M. Sarathy, C.K. Westbrook, An Approach for Formulating Surrogates for Gasoline with Application

toward a Reduced Surrogate Mechanism for CFD Engine Modeling, Energy & Fuels, 25 (2011) 5215-5223.

[92] Ö.L. Gülder, Correlations of laminar combustion data for alternative SI engine fuels, in, SAE Technical Paper, 1984.

[93] M. Metghalchi, J.C. Keck, Burning velocities of mixtures of air with methanol, isooctane, and indolene at high pressure and temperature, Combustion and flame, 48 (1982) 191-210.

[94] S. Yang, R.D. Reitz, Integration of a continuous multi-component fuel evaporation model with an improved G-equation combustion and detailed chemical kinetics model with application to GDI engines, in, SAE Technical Paper, 2009.

[95] Z. Zhao, J.P. Conley, A. Kazakov, F.L. Dryer, Burning velocities of real gasoline fuel at 353 K and 500 K, SAE Transactions, (2003) 2624-2629.

[96] S. Jerzembeck, N. Peters, P. Pepiotdesjardins, H. Pitsch, Laminar burning velocities at high pressure for primary reference fuels and gasoline: Experimental and numerical investigation, Combustion and flame, 156 (2009) 292-301.

[97] O. Mannaa, M.S. Mansour, W.L. Roberts, S.H. Chung, Laminar burning velocities at elevated pressures for gasoline and gasoline surrogates associated with RON, Combustion and flame, 162 (2015) 2311-2321.

[98] L. Sileghem, V.A. Alekseev, J. Vancoillie, K.M. Van Geem, E.J.K. Nilsson, S. Verhelst, A.A. Konnov, Laminar burning velocity of gasoline and the gasoline surrogate components iso-octane, n-heptane and toluene, Fuel, 112 (2013) 355-365.

[99] Y.H. Liao, W.L. Roberts, Laminar Flame Speeds of Gasoline Surrogates Measured with the Flat Flame Method, Energy & Fuels, (2016).

[100] J. Kim, K. Min, Modeling laminar burning velocity of gasoline using an energy fraction-based mixing rule approach, Proceedings of the Institution of Mechanical Engineers, Part D: Journal of Automobile Engineering, 233 (2018) 1245-1258.

[101] F. Williams, The mathematics of combustion, SIAM, Philadelphia, 97 (1985).

[102] R. Maly, M. Vogel, Initiation and propagation of flame fronts in lean CH4-air mixtures by the three modes of the ignition spark, in: Symposium (international) on combustion, Vol. 17, Elsevier, 1979, pp. 821-831.

[103] L. Fan, G. Li, Z. Han, R.D. Reitz, Modeling Fuel Preparation and Stratified Combustion in a Gasoline Direct Injection Engine, SAE Transactions, 108 (1999) 105-119.

[104] J. Duclos, O. Colin, Arc and Kernel Tracking Ignition Model for 3D Spark Ignition Engine Calculations, 5th Int, in: Symp. on Diagnostics and Modeling of Combustion in Internal Combustion Engines, COMODIA, 2001.

[105] R.N. Dahms, M.C. Drake, T.D. Fansler, T.W. Kuo, N. Peters, Understanding ignition processes in spray-guided gasoline engines using high-speed imaging and the extended spark-ignition model SparkCIMM. Part A: Spark channel processes and the turbulent flame front propagation, Combustion and flame, 158 (2011) 2229-2244.

[106] R.N. Dahms, M.C. Drake, T.D. Fansler, T.W. Kuo, N. Peters, Understanding ignition processes in spray-guided gasoline engines using high-speed imaging and the extended spark-ignition model SparkCIMM, Combustion and flame, 158 (2011) 2245-2260.

[107] O. Colin, K. Truffin, A spark ignition model for large eddy simulation based on an FSD transport equation (ISSIM-LES), Proceedings of the Combustion Institute, 33 (2011) 3097-3104.

[108] J. Song, M. Sunwoo, A Modeling and Experimental Study of Initial Flame Kernel Development and Propagation in SI Engines, in, SAE International, 2000.

[109] S. Refael, E. Sher, A theoretical study of the ignition of a reactive medium by means of an electrical discharge, Combustion and flame, 59 (1985) 17-30.

[110] T. Lucchini, L. Cornolti, G. Montenegro, G. D'Errico, M. Fiocco, A. Teraji, T. Shiraishi, A Comprehensive Model to Predict the Initial Stage of Combustion in SI Engines, in: SAE Technical Paper Series, 2013.

[111] S. Falfari, G.M. Bianchi, Development of an Ignition Model for S.I. Engines Simulation, in, SAE International, 2007.

[112] J.D. Cobine, Gaseous conductors: theory and engineering applications, (1958).

[113] R. Herweg, R.R. Maly, A Fundamental Model for Flame Kernel Formation in S. I. Engines, SAE Transactions, 101 (1992) 1947-1976.

[114] A. D'Angola, G. Colonna, C. Gorse, M. Capitelli, Thermodynamic and transport properties in equilibrium air plasmas in a wide pressure and temperature range, The European Physical Journal D, 46 (2007) 129-150.

[115] J. Kim, R.W. Anderson, Spark Anemometry of Bulk Gas Velocity at the Plug Gap of a Firing Engine, SAE Transactions, 104 (1995) 2256-2266.

[116] S. Sayama, M. Kinoshita, Y. Mandokoro, T. Fuyuto, Spark ignition and early flame development of lean mixtures under high-velocity flow conditions: An experimental study, International Journal of Engine Research, 20 (2018) 236-246.

[117] J. Ewald, N. Peters, On unsteady premixed turbulent burning velocity prediction in internal combustion engines, Proceedings of the Combustion Institute, 31 (2007) 3051-3058.

[118] 조석원, Study on the Effect of Cylinder Wall Temperatures on Knock Characteristics in Spark-Ignited Engine, in: 가솔린 엔진에서 실린더 벽면 온도가 노킹 현상에 미치는 영향에 관한 연구, 서울 : 서울대학교 대학원, 서울, 2018.

국 문 초 록

현재 전 세계 대기오염 문제가 중요한 이슈로 떠오르고 많은 나라들이 이 문제를 해결하기 위해 노력하고 있다. 내연기관 차량의 배기 가스 배출량을 줄이기 위해 전 세계적으로 배출가스 규제가 강화되었다. 2014년부터 미국은 Tier 3 배기배출물 규정을 유럽연합은 EURO 6 규정을 채택하고 있다. 현재 연비 규제인 CO2도 매년 강력

하게 강화되고 있다. 강화된 CO2 규정을 충족시키기 위해, 고효율 엔진의 개발은 각 차량 제조사에 의해 활발하게 이루어지고 있다. 고효율 엔진 개발에서 핵심은 열효율 증가이다. 열효율을 높이기 위해 많은 기술이 개발되어 양산 엔진에 적용되고 있다. 그러나 현재 엔진 개발에 가장 큰 장애물로 연소 사이클 간 편차가 있다. 따라서 사이클 편차에 대한 연구도 활발히 진행되고 있다. 사이클 편차에 영향을 미치는 원인은 다양하고 복잡하기 때문에, 실험 연구를 통해 사이클 편차의 근본 원인에 대한 상세한 연구를 실시하기 어렵다. 따라서 대안으로 3D 시뮬레이션을 활용한 연구가 활발히 진행되고 있다.

본 연구에서는, 연소의 사이클 편차 현상을 Large-Eddy Simulation (LES) 유동 해석 방법을 이용하여 재현하고 사이클 편차의 원인에 대한 연구를 진행한다. 현재 LES를 이용한 엔진 시뮬레이션은 아직까지 미숙한 단계이다. 따라서 정확한 시뮬레이션을 위해 각 물리적 현상을 구현할 수 있는 모델을 구현해야 한다. 먼저, 3개의 sub-grid scale (SGS) 난류 모델을 단기통 광학 엔진의 (TCC-III) particle image velocimetry (PIV) 측정 결과로 평가하였다. PIV 데이터와 비교한 유동장 및 예측된 SGS 난류속도에 대한 분석을 바탕으로 본 연구에서는 dynamic structure model (DSM)이 채택되었다.

둘째로, G-equation 모델을 연소 모델로 선택하였다. G-equation 모델은 Pitsch[1]에 의해 LES 적용 가능 하도록 개발되었다. 이 모델은 corrugated flamelets regime과 thin reaction flamelets regime에서 사용될 수 있다. 연소 속도 모델은 두 연소 환경에 포함된 난류 연소를 모사하기 위해 상당히 복잡하다. 따라서 본 연구에서

는 RANS 를 이용하여 대상 엔진 작동 조건의 연소 환경을 찾아 내었고, 연소 환경은 corrugated flamelets regime에 속한 것을 확인하였다. 따라서 기존의 G-equation 연소 모델을 corrugated flamelets regime에 맞도록 변경 하였다.

셋째로, LES의 특성을 반영한 점화 모델이 개발되었다. Lagrangian 개념을 이용하여 점화 채널을 구현하고, 2차 전기 회로 모델을 이용하여 점화 에너지, 리스트라이크, 점화 시간 종료 등을 예측하였다. 본 연구에서 개발된 점화 모델의 주요 특징 중 하나는 아크 페이즈 중 열 팽창 현상을 구현을 위해 간단한 경험 함수를 이용한다는 것이다. 아크 페이즈 후, 점화 해널은 화학 반응에 성장하고 화염 전파가 진행된다. 난류 화염 두께는 층류 화염 전파와 난류 화염 전파 사이의 천이 상태를 예측하기 위해 도입되었다. 마지막으로 점화 채널이 충분히 커지면 G-equation 의해 3D 계산 영역에서 화염 전파가 구현된다.

마지막으로 30개의 LES 사이클을 수행하여 연소의 사이클 편차 원인을 분석하고 실험 데이터를 이용하여 시뮬레이션의 정확도를 검증하였다. 연소의 사이클 편차의 원인은 주로 작은 규모의 난류 유동과 큰 규모의 난류 유동에서 나온다. 난류 모델로 구현된 작은 규모의 난류 유동과 큰 규모의 난류 유동에 속한 텀블 값을 같이 분석하였다. 작은 규모의 난류 유동은 텀블 값과 관계가 있다는 사실을 파악 하였다. 큰 규모 난류 유동 측면에서는 국부적인 유동의 소용돌이가 화염 전파에 미치는 영향을 유동장을 상세히 분석하여 확인되었다. 특히 2차 텀블면에서 벽면 유동에 의해 생성되는 소용돌이가

연소의 사이클 편차에 미치는 중요한 요인임을 밝혀 내었다. 벽면 유동에 의한 소용돌이 형성을 강화하기 위해 새로운 피스톤 현상을 설계 하였다. 새로운 피스톤 형상의 결과는 베이스 피스톤보다 연소의 CCV가 줄어들었다. 본 연구는 향후 엔진 개발을 위해 연소 CCV의 원인을 조사하는 방법과 연소 CCV를 줄이는 방법에 대한 방법론을 제시한다.

주요어: 전기점화 엔진, LES, 전산유체역학, 사이클 편차, 점화모델, 난류모델

학 번: 2013-20641

공학박사학위논문

수치해석 기법을 이용한 가솔린 엔진에서 난류 유동이 연소의 사이클 편차에 미치는 영향에 대한 연구

The Effect of Turbulent Flow on the Combustion Cyclic Variation in a Spark Ignition Engine using Large-Eddy Simulation

2020 년 8 월

서울대학교 대학원

기계항공공학부

고 인 석

수치해석 기법을 이용한 가솔린 엔진에서 난류 유동이 연소의 사이클 편차에 미치는 영향에 대한 연구

The Effect of Turbulent Flow on the Cyclic Variation in a Spark Ignition Engine using Large-Eddy Simulation

지도교수 민 경 덕

이 논문을 공학박사 학위논문으로 제출함

2020 년 4 월

서울대학교 대학원

기계항공공학부

고 인 석

고인석의 공학박사 학위논문을 인준함

2020 년 6 월

위 원 장 : 송 한 호 (인)

부위원장 : 민 경 덕 (인)

위 원 : 도 형 록 (인)

위 원 : 이 복 직 (인)

위 원 : 최 회 명 (인)

Abstract

The Effect of Turbulent Flow on the Combustion Cyclic Variation in a Spark Ignition Engine using Large-Eddy Simulation

Insuk Ko

Department of Mechanical and Aerospace Engineering
The Graduate School
Seoul National University

At the present, the problem of worldwide air pollution has emerged as an important issue and many countries are trying to solve the problem. Emission regulations have been tightened around the world in an effort to reduce emissions from internal combustion engine (ICE) vehicles. From 2014, Tier 3 emissions standards in the United States (U.S.) and EURO6 regulations in the European Union (EU) are adopted. Currently, CO2 is also being strongly enforced annually. To meet the tightened CO2 regulations, the development of high efficiency engines is actively being carried out by each vehicle manufacturer. In the development of high efficiency engines, the key point is the increase in thermal efficiency. Many technologies have been developed to increase thermal efficiency and are being applied to mass-production engines. However, there is currently a cycle-to-cycle variation (CCV) of combustion as the biggest obstacle to engine

development. Therefore, research on the CCV is also being actively carried out. Because the causes that affect the cycle deviation are various and complex, it is difficult to conduct detailed research on the source of the CCV through experimental studies. Therefore, the 3D simulation is actively carried out as an alternative.

In the present study, the CCV phenomenon of combustion was reproduced using large-eddy simulation (LES) approach and the investigation on the source of CCV are conducted. Currently, the engine simulation using LES is immature. Therefore, it is necessary to consider each sub-model for accurate simulation. First, three Sub-grid scale (SGS) turbulence models were evaluated with particle image velocimetry (PIV) data from the single-cylinder transparent combustion chamber (TCC-III) engine. The dynamic structure model (DSM) was adopted for this study, based on the analysis of the flow field and the predicted SGS turbulent velocity compared to the PIV data.

Secondly, the G-equation was employed as a combustion model. The model can be used in the corrugated flamelets regime and the thin reaction flamelets regime. The turbulent burning velocity of the model is quite complicated to simulate the turbulent flame included in the two regimes. Therefore, in this study, the combustion regime of the target engine operating condition was found by using Reynolds averaged navier-stokes equation (RANS) approach and was identified to the corrugated flamelets regime. Thus, the G-equation was modified for the corrugated flamelets regime.

Thirdly, an ignition model reflecting the characteristics of LES was developed. The lagrangian particles were employed to realize the ignition channel and the secondary electric circuit model was implemented to predict the spark energy, restrikes phenomena and the end of ignition time. The one of the key features of the ignition model developed in this study is that a simplified empirical

function is implemented to realize the thermal diffusion during arc phase. After ignition phase, the channel grows by chemical reaction and the flame propagation progresses. The turbulent flame brush thickness term is introduced to predict the transition state between the laminar flame propagation and the turbulent flame propagation. Finally, when the channel is grown sufficiently, flame is propagated in the 3D field by the G-equation

Finally, 30 LES cycles were performed to identify the cause of the CCV and validated against the experimental data. The sources of the CCV are mainly from the small scale turbulent flow and the large scale turbulent flow. The small scale turbulent flow effect was investigated and the fact that the small scale turbulent flow is related to the tumble motion is identified. In terms of the large scale turbulent flow, the effect of the local vortex on the flame propagation was found through the detailed analysis of the flow field. In particular, the vortex produced by wall flow on the secondary tumble plane is an important factor. A new piston shape was designed to strengthen the vortex formation by wall flow. The result of new piston case shows the reduced combustion CCV than the base case. This research provides the guide how to investigate the sources of the combustion CCV and how to reduce the combustion CCV for the future engine development

Keywords: SI engine, LES, CFD (Computational Fluid Dynamics), CCV (Cycle-to-cycle variation), Ignition model, SGS model

Student Number: 2013-20641

Contents

List of Figures

List of Tables

Nomenclature

Acronyms

AKTIM	the arc and kernel tracking ignition model
ALE	arbitrary lagrangian-eulerian
AMR	adaptive mesh refinement
ASI	arbitrary sliding interface
BDC	bottom dead center
BEV	battery electric vehicle
BML	Bray-Moss-Libby
CA	crank angle
CARB	California air resources board
CCV	cycle-to-cycle variation
CFD	computational fluid dynamics
CFL	Courant-Friedrichs-Lewy
CFM	coherent flame model
COV	coefficient of covariation
CSD	circular standard deviation
DI	direct injection
DNS	direct numerical simulation
DPFI	dual-port fuel injection
DPIK	the discrete particle ignition kernel model
DSM	dynamic structure model
EBU	eddy-break-up
ECFM	the extended coherent flame model
EDM	eddy dissipation model
EGR	exhaust gas recirculation

EPA	environmental protection agency
FAS	fleet average system
FEV	hybrid electric vehicle
FSD	flame surface density
FTP	federal test procedure
HEV	hybrid electric vehicle
ICE	internal combustion engine
ISSIM-LES	the imposed stretch spark ignition model for LES
LCA	life cycle assessment
LEM	linear eddy model
LES	large-eddy simulation
MARS	monotone advection and reconstruction scheme
MFB	mass burned fraction
MUSCL	monotonic upstream-centered scheme for conservation laws
NA	naturally aspirated
NEDC	new European driving cycle
nIMEP	indicated mean effective pressure
NMOG	non-methane organic gas
PDF	probability density function
PISO	pressure implicit with splitting of operator
PIV	particle image velocimetry
PRF	primary reference fuel
RANS	Reynolds averaged navier-stokes equation
RCM	rapid compression machine
RED	real driving emissions
RMSd	root-mean-square deviation
rpm	revolution per minute
SGS	sub-grid scale
SI	spark ignition

SparkCIMM	the spark-channel ignition monitoring model
TCC	transparent combustion chamber
TRF	toluene reference fuel
U.S.	the United States
WLTC	worldwide harmonized light-duty vehicles test cycles

Chapter 1. Introduction

1.1 Background and Motivation

At the present, the problem of worldwide air pollution has emerged as an important issue and many countries are trying to solve the problem. There are lots of man-made air pollutant sources including power station, manufacturing facilities, waste incinerators, agriculture, food as well as transportation. In the transportation system, the internal combustion engine (ICE) equipped vehicles are considered to be a major source of air pollution. Therefore, emission regulations have been tightened around the world in an effort to reduce emissions from ICE vehicles.

In 1973, the United States (U.S.) firstly adopted Tier 0 standards for railroad locomotives and locomotive engines fueled by diesel and by other fuels. The emission regulations have become stricter and Tier 3 emissions standards from the U.S. Environmental Protection Agency (EPA) were adopted in March 2014 and have been enforced from 2017 to 2025. In European Union, the first EURO1 regulations were introduced in 1992, and currently EURO6 regulation has been effective. In 2009, Republic of Korea adopted California Air Resources Board (CARB)'s non-methane organic gas (NMOG) fleet average system (FAS) for gasoline-fueled vehicles. Currently, K-LEV III standards have been enforced. To assess the emission levels of vehicle engines and fuel economy in passenger cars, the New European Driving Cycle (NEDC) and the EPA Federal Test Procedure (FTP) were introduced in European Union and the U.S., respectively. From 2017, the NEDC was replaced with the worldwide harmonized light-duty vehicles test cycles (WLTC) for all types of vehicles. There is a difference between the driving mode and the driving conditions of the actual road. To evaluate these differences,

the real driving emissions (RDE) test has been introduced to reflect the real road conditions. As above, regulations on emissions are being tightened in countries around the world. According to the U.S. EPA, CO2 emissions from the transportation sector in the U.S. account for 28 percent of the total industrial sector in 2018 [1]. Therefore, the European Union regulates CO2 emissions, reducing by about 27% from 130g/km in 2015 to 95g/km by 2021 as shown in Figure 1.1 [2]. Furthermore, the regulations on CO2 emissions will be greatly tightened by 2030, down about 37.5 percent to 59g/km. In the U.S., the regulations on CO2 emissions reduction were eased to 89g/km by 2025, 102.5g/km by 2026. The U.S. had previously planned to impose very strict regulations on CO2 emissions of 89 g/km by 2025. However, in March 2020, the government announced eased the regulations to limit CO2 emissions to 102.5g/km by 2026, reflecting more practical difficulties. Republic of Korea has regulated the amount of CO2 emissions from 140g/km in 2015 to 97g/km in 2020, which is about 31% tightened. Due to the tightened CO2 regulations, many car manufacturers are putting a lot of effort into developing eco-friendly internal combustion engines to meet the future regulations.

In addition, there has been lots of effort to develop the alternative powertrains such as the battery electric vehicle (BEV), the fuel cell electric vehicle (FEV) and the hybrid electric vehicle (HEV). Thus, many outlooks have predicted that the market sharer of the ICE would be diminished. In the past, the tank-to-wheel emissions have been mainly dealt, but recently the importance of well-to-wheel emissions have emerged through the life cycle assessment (LCA). In Figure 1.2, the well-to-wheel CO2 emission from the BEV and the ICE obtained through the LCA is shown. Depending on the energy source, the CO2 emissions of the BEV are in a wide range of approximately 50 to 170g/km. The reason is that the well-to-tank CO2 emissions of the BEV is very dependent on the generation system of electricity. The CO2 emissions of the conventional ICEs such as natural gas, diesel

and gasoline are about 125-160g/km, which is higher than the BEV. However, if the ICEs are hybridized, the HEV's CO2 emissions are approximately 105 to 125g/km, which is equivalent to the BEV. The market share prediction in 2025 in major markets is shown in Figure 1.3. The market share of conventional ICEs is very small, but the increase in the HEVs is a noticeable. Since the HEVs are equipped with the ICE, the ICEs is still considered as the mainstream of the vehicle market. Therefore, continuous research on the ICE engines is needed.

The ICE converts the chemical energy of hydrocarbon fuel into the thermal energy by combustion, and thereby into the mechanical energy by the reciprocating piston movement, of which the latter efficiency is called thermal efficiency [3]. The increase of the thermal efficiency plays a key role to reduce CO2 emissions. Through the Otto cycle, theoretical maximum thermal efficiency can be obtained as equation (1.1). The thermal efficiency is a function of the compression ratio and the specific heat ratio. The higher the compression ratio and the lower the specific heat ratio, the greater the thermal efficiency. To lower the specific heat ratio, lowering the equivalence ratio is mainly adopted. However, the higher the compression ratio, the more vulnerable it becomes to knocking, and the lower the equivalence ratio, the lower the combustion stability. Therefore, many technologies are being introduced to overcome these problems. For instances, the downsized engine with the direct injection (DI) and the turbocharging system to achieve the utilization of the sweet spots and the high compression ratio and the burn engines, which reduce pumping loss and lowers the specific heat ratio to increase the thermal efficiency. The direction of the engine development is in line with the method of increasing the thermal efficiency in the Otto cycle, which is the theoretical thermal efficiency.

$$\eta = 1 - \frac{1}{r_c^{k-1}} \quad (1.1)$$

Where, η: thermal efficiency

r_c: compression ratio

k: specific heat ratio

There is a major obstacle which is a cycle-to-cycle variation (CCV) phenomena to the development of the spark ignition (SI) engine to improve efficiency using these latest technologies. Generally, engine studies develop using the average of several cycles as a representative value. However, the actual engine operation shows different behavior for each cycle, called the CCV as shown in Figure 1.4. As shown in Figure 1.4, combustion is a behavior within a large range, largely up and down, and the larger this range results in abnormal combustion and combustion instability. There are lots of causes of the CCV, coming from the external environment to inside the engine. For example, the external environments include conditions of ambient air, and internal sources of the CCV are revolution per minute (rpm) fluctuation, fuel injection, deviation of mechanical movement such as valves and pistons, etc. During the four strokes, the effects of each factors are intertwined, finally the combustion CCV occurs. Since the CCV is such a complex phenomenon, it is now considered an uncontrollable obstacle. However, many studies have begun in recent years, as a must-over for the future high-efficiency engine development. Experimental studies [4-7], especially using a optical engine to reproduce the CCV and find the causes of it, have been carried out but the limitations of information make it difficult to identify the causes and assess the impact of the factors. Therefore, a lot of research have been conducted using 3D simulation.

In the 3D simulation, information on the factors that are difficult to measure in the experiment can be obtained, visualized and quantified. One of the most widely used techniques in the 3D simulation is Reynolds averaged navier-stokes equation (RANS) approach. RANS is a technique that simulates turbulence using averaging method, and there is a limit to the implementation of chaotic behavior of flow from the outside, one of the causes of the CCV. There is another turbulence model, called the large-eddy simulation, as a method to overcome these limitations. In LES, the large scales of turbulence which are larger than a LES filter size can be resolved, and the small turbulence scales which are smaller than the LES filter size is modeled. Due to the characteristic of resolving the large scale turbulence, it is possible to reproduce the randomness behavior of flow that is difficult in RANS. Thanks to these characteristics, research on the CCV phenomenon in the ICE using LES has been actively carried out [8-11]. Currently, however, LES research in the ICE community is still in its early stages, and a model study is still underway to implement physical phenomena during the combustion process based on LES. Therefore, the present study analyzes the causes of the CCV with LES based physical models, especially for the ignition and the combustion processes.

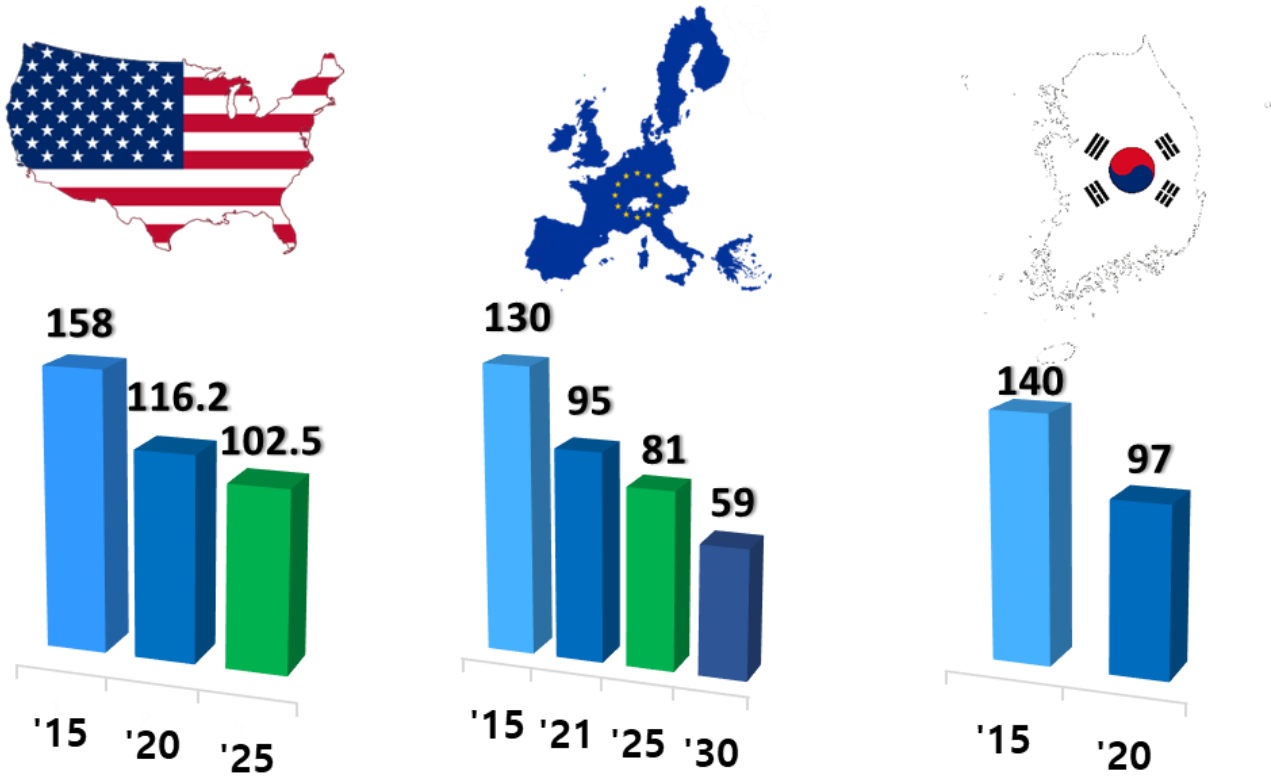

Figure 1.1 CO2 regulations in global markets [2]

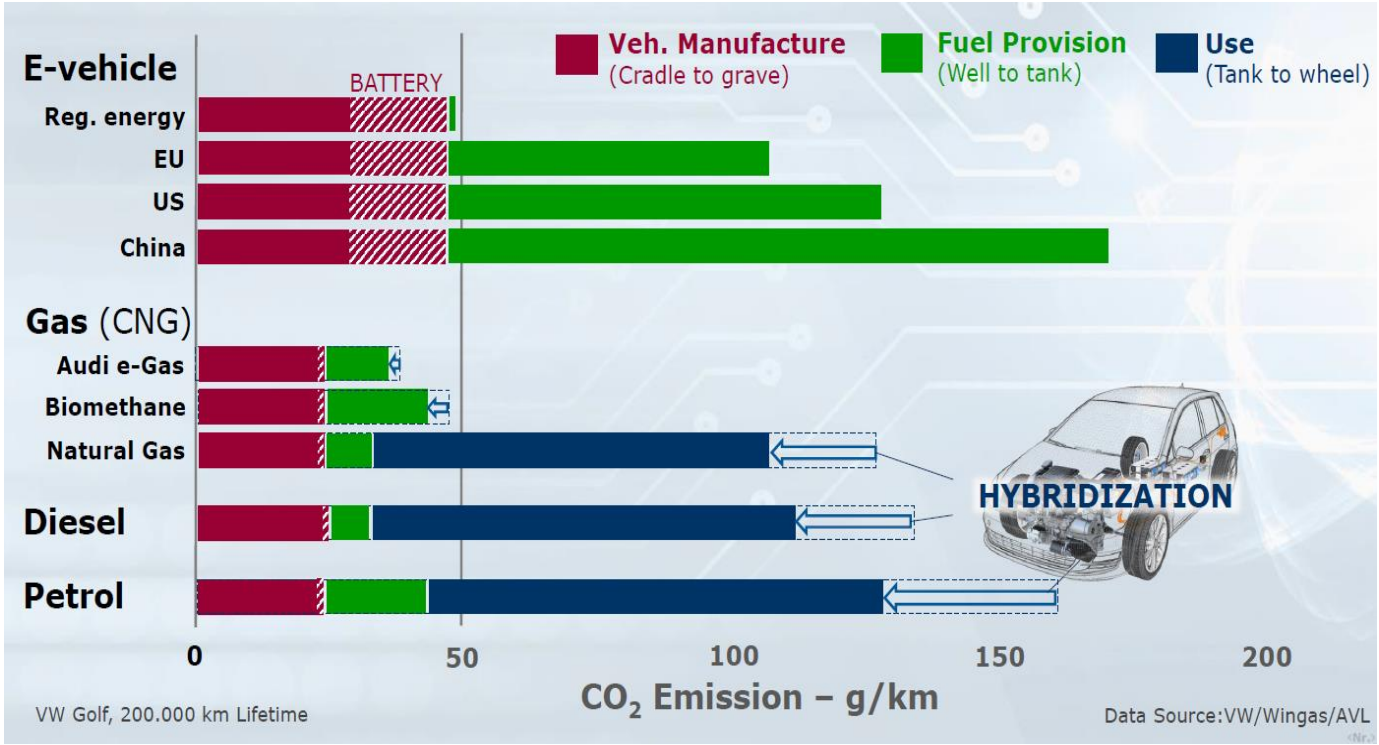

Figure 1.2 Life cycle assessment of CO2 emission from internal combustion engine vehicle and battery electric vehicle [2]

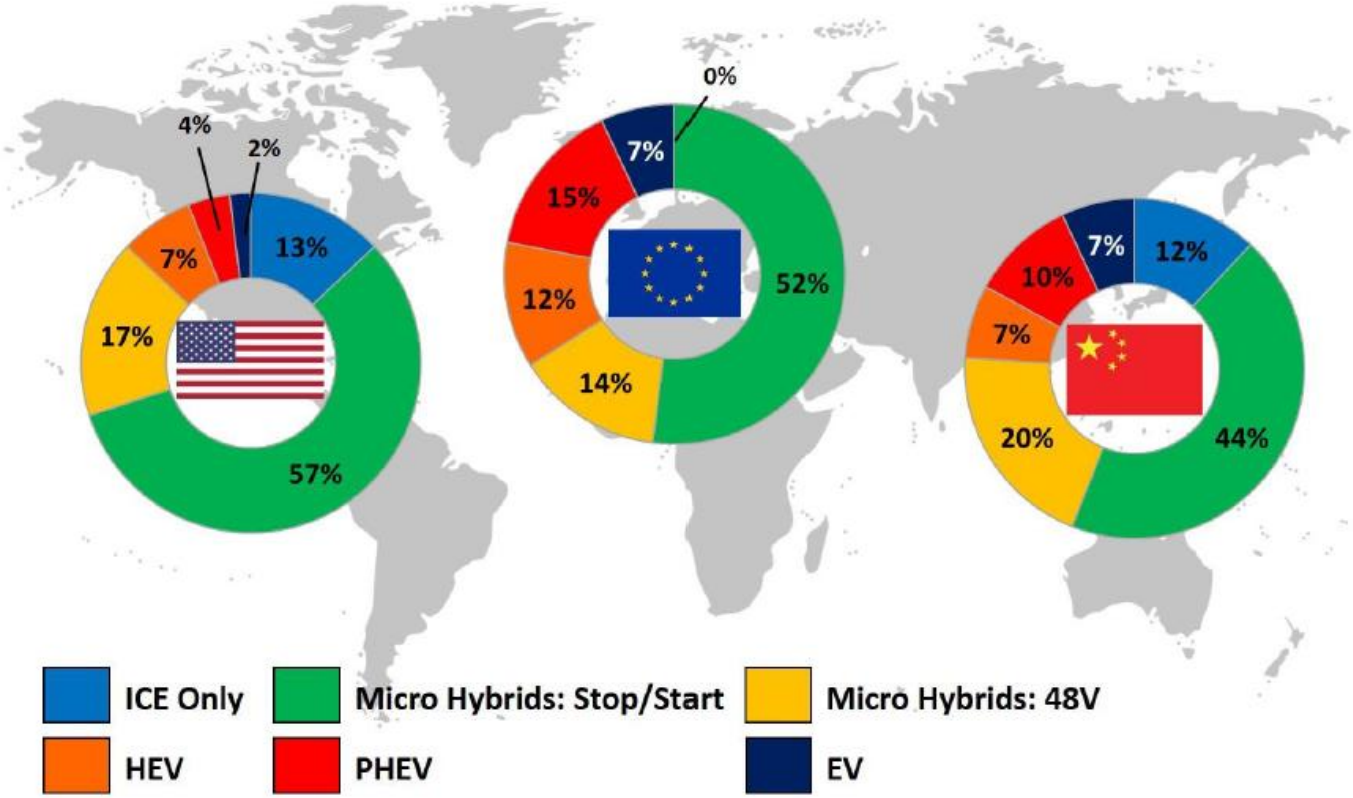

Figure 1.3 Outlook of future market share of powertrain types in 2025 [12]

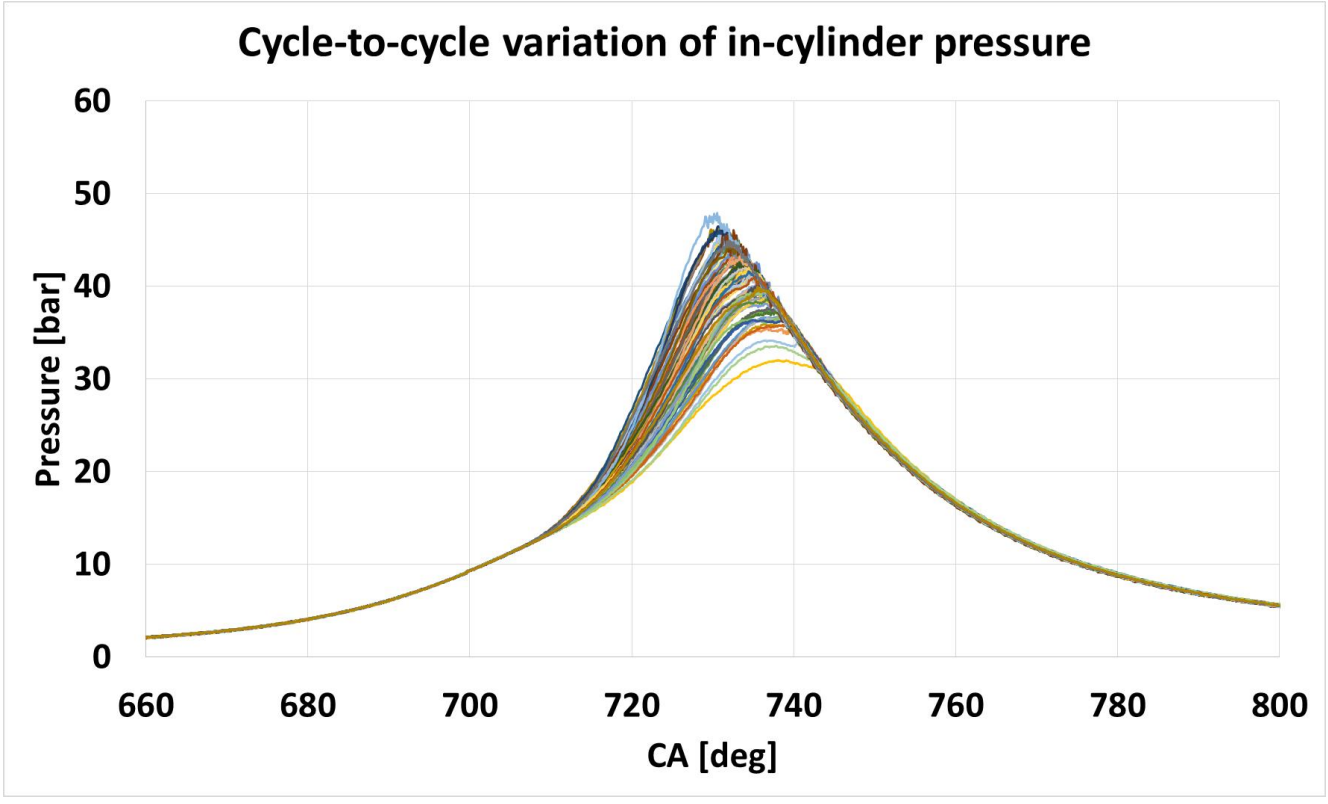

Figure 1.4 Cycle –to-cycle variation of in-cylinder pressure in a SI engine

1.2 Literature Review

1.2.1 Cycle-to-cycle variation in engine combustion

The combustion CCV in engines means different behavior in every cycle, not always reproducing the same combustion behavior, even under the same operating conditions. The combustion CCV is a major obstacle to the development of high-efficiency, high-performance engines, and many studies have been conducted recently. First of all, experimental studies have been conducted to analyze the combustion CCV using engine combustion deviations. Zervas [13] evaluated the coefficient of covariation (COV) of the beginning and the end of the combustion, and the mass fraction burnt (MFB) 50% to assess the combustion CCV. Huang et al. [14] investigated the exhaust gas recirculation (EGR) effect on the CCV in a SI engine fueled with natural gas-hydrogen blends. Chen et al. [15] conducted the statistical analysis to find correlations between combustion parameters, such as burning rate and knock, and COV of net indicated mean effective pressure (nIMEP) and peak pressure. However, in experimental studies, there is a lack of information on the correlation between factors affecting the CCV and difficulty in controlling the variables. Therefore, the 3D simulation research is drawing attention as an excellent method of study of the CCV research.

Among several turbulence modelling approaches in the 3D simulation, LES is widely used in an engine CCV research because of the advantage of being able to simulate the chaotic flow of the large turbulence. In the early stage of LES research in the ICE, studies on engine like geometries were conducted to verify the possibility of LES approach [16, 17]. Next, studies were conducted on the cyclic deviation of the flow in the engine through multi-cycle analysis under the cold flow condition using LES. Enaux et al. [18] evaluated a numerical strategy

including mesh movement and specific treatments of boundary conditions to realize the CCV in the ICE. Van Dam et al. [11] conducted multi-cycle LES of motored flow in an optical engine. The simulation result is compared against the particle image velocimetry (PIV) data. The author suggested that analysis of the circular standard deviation (CSD) is a promising method to identify critical points such as vortex centers or stagnation points which may be useful for engine designation. Angelberger et al. [19] found the correlation of CCV between the in-cylinder swirl ratio and the polar velocity profile in the valve seat region using LES and the PIV results. Early studies were mainly conducted to successfully simulate the flow CCV using LES and comparing it with the PIV results.

Next to the studies of the flow CCV, Goryntsev et al. [9] conducted a study on the flow CCV on the fuel-air mixing in a direct injection engine that is important for combustion. Several researches have been conducted to reproduce the combustion CCV in SI engines [10, 20-24]. Fontanesi et al. evaluated the boundary condition effect on the combustion CCV in a SI engine. The authors compared the CCV result of cycle-specific boundary condition from experiment and that of cycle constant boundary condition from the 1D simulation. It was found that the impact of the boundary condition on the CCV is modest. Gharderi et al. [25] conducted the study on the assumption that the rpm and the flow of ignition timing had a great effect on the combustion CCV and evaluated its influence. Fontanesi et al. [8] reproduce the combustion CCV and knock in a SI engine. Fontanesi et al. [26] assessed the effect of the spark plug location and direction on the combustion CCV and knock phenomena. Robert et al. [27] evaluate the effect of spark timing on the combustion CCV and knock with experimental data. Chen et al. [28] found the correlation between knock intensity and, combustion phase and peak pressure. In LES research on the CCV, multi-cycle simulation must be conducted, so high computational costs are required. There are some researches [29, 30] focusing on reduction of computational cost

using parallel perturbation methodology. This method implements the CCV by imposing perturbation at the initial conditions, allowing multiple cycles to be carried out simultaneously in parallel rather than consecutive cycle simulations. Researches on the CCV using LES have mainly shown the potential for the CCV reproduction and analyzed the causes of the CCV through statistical analysis. However, since research on LES-based physical models is still in its infancy, there is a limit to the lack of consideration for models.

1.2.2 Turbulence Modeling

Turbulent flow represents to irregular random flow movements depending on the time and the space of large and small eddies. Thanks to this movement of randomness, it is characterized by active transport and mixing of fluid compared to laminar flow. This is particularly important in combustion phenomenon, and a turbulence model that can be accurately predicted in computational fluid dynamics (CFD) is very important. There are three main ways to simulate turbulence in the CFD: Reynolds averaged navier-stokes equation, large-eddy simulation and direct numerical simulation (DNS) as shown in Figure 1.5. Characteristic of each methods is that RANS simulates all turbulence length scales through modeling [31] and the calculation is very fast, but the accuracy is relatively lower than other methods. DNS is the high fidelity method to resolve all turbulence length scales, as opposed to RANS. The disadvantage is that a grid size of simulation domain must be smaller than the Kolmogorov scale to resolve all turbulence scales, so it is the most accurate, but due to calculation cost, DNS is not applicable to engineering application. LES is a method that utilizes the advantages and complements the disadvantages of these two methods, LES predicts the turbulence length scales smaller than a certain size (filter) through a

sub-grid scale (SGS) model, and turbulence scales larger than the filter size are resolved. Thus, LES is an appropriate modeling approach that can reduce calculation time while simultaneously reproduce the randomness of turbulence flow. Because of these characteristics, the turbulence modeling method using LES is suitable for the CCV study of engines.

The turbulence model of LES is called the SGS model, and there are the zero-equation and the one-equation models. The first SGS model was introduced in 1963 by Smagorinsky [32]. The Smagorinsky model is a representative zero-equation model and adopts the eddy-viscosity hypothesis to predict the SGS turbulence viscosity. Fundamental studies using the Smagorinsky model have suggested model coefficients for various condition [33-37]. However, the model has a drawback to predict turbulence in strong transient condition because a constant value of the SGS model coefficient is used. There is a method of dynamically calculating the SGS model coefficient locally using double filters introduced by Germano to overcome the drawback of the Smagorinsky model [38]. This model uses dynamic coefficients, reflecting local characteristics so that non-steady flows can be better predicted than the conventional Smagorinsky model.

The one-equation model improves the accuracy of prediction of the SGS turbulence terms by adding a transport equation for the SGS kinetic energy. The transport equation has a SGS turbulent kinetic energy budget which is available for the formulation of the SHS models. Therefore, the use of the transport equation for the SGS turbulent kinetic energy makes it possible to use relatively coarser grids compared to the zero-equation model. The one-equation was derived by Yoshizawa [39] and by Yoshizawa and Horiuti [40], on the basis of the Kraichnan's direct-interaction approximation [41]. In 1992, Wong first introduced the dynamic modeling approach to the one-equation model [42]. The transportation equation is defined by the source and sink terms that require

dynamic model coefficient. Ghosal et al. [43] proposed the advanced dynamic one-equation model to calculate the dynamic model coefficient using a iterative method. However, there is a problem that the iterative solution do not always converge and scaling issues that the dynamic modeling approach depends on are not considered. To overcome the problem, the dynamic structure model (DSM) has been introduced by Pomraning [44]. This is the one-equation non-viscosity dynamic model which estimates the stress tensor directly instead of modeling the stress tensor with the SGS viscosity. The transportation equation for the SGS turbulent kinetic energy is added to give the energy flow of the SGS turbulent kinetic energy between the resolved and the sub-grid scales.

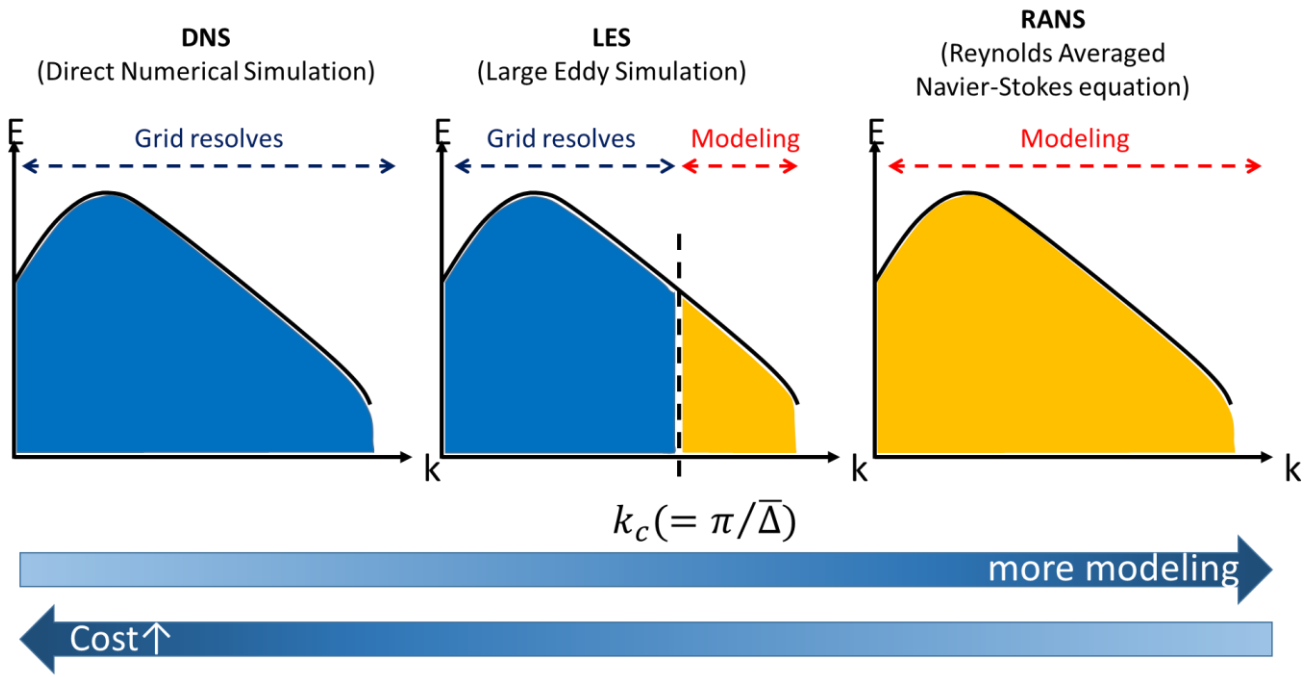

Figure 1.5 Three main ways to simulate turbulence in computational fluid dynamics: RANS, LES and DNS

1.2.3 Combustion Modeling

Combustion is a phenomenon in which flames are propagated in chemical reactions of fuel and air mixtures. In order to realize combustion with flow, an additional scalar reaction equation (equation. (1.2)) is needed to calculate chemical reactions and their source terms. In turbulent combustion, there is a closure problem to solve the scalar reaction equation, because chemical reactions which are complex non-linear function of chemical species are strongly coupled with turbulent fluid dynamics. Therefore, the main objective of turbulent combustion modelling is to close the problem with appropriate assumptions in order to reproduce turbulent combustion phenomenon [45].

$$\rho \frac{\partial \psi_i}{\partial t} + \rho v \cdot \nabla \psi_i = \nabla \cdot (\rho D_i \nabla \psi_i) + \omega_i \qquad (1.2)$$

Where ω_i: chemical source term.

Spalding [46] attempted to solve the closure problem of chemical source term. The author assumed that turbulent mixing is a cascade process from the integral length scales to the molecular scales and therefore the cascade process also controls chemical reactions. This model is called the Eddy-break-up (EBU) model. The turbulent mean reaction rate of products is related with the variance of the product mass fraction and the EBU model constant. Magnussen and Hjertager [47] have modified the EBU model by replacing the variance of the product mass fraction to the mean mass fraction of the deficient species, so called the Eddy dissipation model (EDM). The model requires at least three rates defined with the mean fuel mass fraction, the mean oxidizer mass fraction and the product mass fraction in order to calculate the mean chemical source term. The main idea of these two models is to replace the chemical time by the turbulent time scale. The

model is based on the fast chemistry limit without the influence of the chemical kinetics. The model constant for the EBU or the EDM must be tuned for a particular combustion condition. However, since the models assume the fast chemistry and the chemical equilibrium [48], the models overestimate the reaction rate in certain situations.

Another approach based on statistics was introduced by Pope [49]. The model adopts a probability density function (PDF) transport equation for the velocity and the reactive scalars formulated for one-point statistics. The early model uses only the joint pdf equation of velocity, viscous dissipation and reactive scalars which does not include scalar gradients and therefore it does not include information about the mixing time scale. Therefore, Dopazo [50] propose a transport equation for the joint statistic of velocity, velocity gradient, reactive scalars and their gradients. In addition to the closure of chemical source term, it describes the straining and rotation of scalar gradients, the properties are considered necessary in turbulent reacting flows. In the slow chemistry condition, Hulek and Lindstedt [51] showed a very good agreement with experimental data using the joint scalar-velocity approach. However, in the fast chemistry, molecular mixing and chemical reaction arise in thin layers where the molecular transport and the chemical source term balance each other. Therefore, the molecular mixing term and the chemical source term are closely related to each other. However, from a numerical point of view, the pdf transport equation is not attractive because its requirement of memory increase approximately exponentially with dimensionality in finite volume and finite-difference techniques. To overcome the memory problem, Monte-Carlo method which adopts the lagrangian algorithm was introduced [52, 53]. But this method is suffered from a statistical error with the small number of lagrangian particles.

The Linear Eddy Model (LEM) approach is also used to deal with a non-equilibrium chemistry in turbulent combustion. At first, it was developed for non-reacting flows by Kerstein [54-57] and was improved for reactive scalars by Kerstein [58]. This approach obtains an information of molecular mixing by simulating the molecular mixing on a one-dimensional domain. Two processes are conducted simultaneously to calculate the reactive scalars. In the first process, the evolution of the reactive scalar field is described in the one dimension. In the second process, a stochastic procedure of instantaneous, statistically independent "rearrangement events" is occurred. McMurtry et al. [59] applied the LEM to hydrogen-air combustion and Menon and Kerstein [60] used the LEM on the G-equation. However, there is a limitation on the LEM that the calculation of molecular mixing should be performed at the finest scales of turbulent flow in physical space, so that LES requires high computational cost.

The flamelet concept is widely used to reproduce the turbulent combustion phenomenon. The flamelets are defined as thin reactive-diffusive layers where are embedded in turbulent flow field. It assumes that the flame structure is infinitely thin and there is no intermediate temperature between unburnt mixture gas and burnt gas. The progress variable is introduced to separate unburnt mixture and burnt gas in a mixture field. The Bray-Moss-Libby (BML) model is one of the popular method in the flamlets approach [61]. This model adopts the progress variable as a scalar quantity which is normalized by temperature or product mass fraction. The transport equation for the progress variable is adopted instead of the reactive scalar transport equation. There is also closure problem in chemical source term. The chemical source term is modeled by the mean chemical reaction rate which is related to the un-stretched laminar burning velocity, a stretch factor and the crossing length scale which needs to be modeled [62, 63].

Alternative approach for the chemical source term is the Coherent flame model (CFM) which defines the chemical source term with the flame surface density. In the CFM, there is an additional transport equation for the flame surface density [64, 65]. Formulations of the CFM are discussed by Duclos [64].

More recently, the level-set approach using the non-reacting scalar G rather than the progress variable is widely adopted for premixed combustion. This model is called the G-equation. Since the G-equation adopts the non-reacting scalar G, there is no need to consider the complications related with closure problem of chemical source term. Because of this advantage, the present study adopts the G-equation model as a combustion model. So far, most combustion models have been developed as RANS base. In contrast to RANS approach which is modelling all turbulent scales, LES resolve the turbulent scales larger than the filter size and the smaller turbulence scales are modeled. Therefore, the existing combustion models have been re-developed to fit the characteristics of LES [66, 67]. The detailed information of the G-equation for LES will be described in Chapter 4.

1.3 Research Objective

Research on the CCV is essential in the development of high efficiency engines. LES approach has been spotlighted as a useful way to investigate the CCV. Therefore, nowadays a lot of researches using LES are actively underway, but it is still immature. Sub-models, such as spray model, ignition model, combustion model and etc., considering the characteristics of LES have been developed, but there are still lots of rooms to be developed in order to improve the accuracy of LES simulation on engine research. Apart from the accuracy of sub-models, many studies are currently underway to find the causes of the CCV, but so far there are lack of researches on how each causes is generated and how it affects the CCV. Therefore, this study consists of two main parts: development of highly accurate models, and analysis of the causes of the CCV and suggestion how to reduce the CCV. The detailed objectives are as followed:

1. Selection of the SGS turbulent model

    - LES with three SGS models are performed to evaluate the SGS model effect on in-cylinder flow under motored condition.

2. Development of ignition mode

    - The lagrangian ignition model for LES is developed.

3. Investigation of cycle-to-cycle variation

    - The cycle-to-cycle variation is reproduced using LES.

    - Root of the cycle-to-cycle variation is investigated.

4. Suggestion to reduce the CCV
    - Provision of a guide on how to reduce the CCV using LES simulation of new designed hardware with reduced the CCV.

1.4 Structure of the Thesis

The present study consists of eight main chapter. In chapter 2, the evaluation of the SGS model effect under motored condition is described. The results of three SGS models are compared with PIV data, and finally one model is selected. In chapter 3, the modeling of gasoline surrogate fuel is introduced. In chapter 4, the flamelets regime in engine condition is investigated. A level-set method for the corrugated flamelets regime is described. In chapter 5, the lagrangian concept of ignition model for LES is introduced. At first, the model concept is described and the detailed description for each sub-model is illustrated. In chapter 6, the experimental and the numerical configuration for the target engine are introduced. In chapter 7, the multi-cycle LES simulation is performed and the CCV phenomenon is reproduced and validated against the measured data from the single-cylinder port fuel injection engine experiment. Investigation of source of the CCV is conducted to find the controllable cause. The way to reduce the CCV is introduced. Finally, the study closes with a summary and conclusions in chapter 8.

Chapter 2. Sub-grid Scale Turbulence Model

In this section, the theory of turbulent flow is described. From the point of LES, the SGS turbulence model and the grid size are very important factor to realize turbulence flow. Therefore, three SGS turbulence models are introduced and LES quality assessment to select the SGS turbulence model is introduced.

2.1 The Fundamentals of Turbulent Flow

2.1.1 The Energy Cascade

Turbulent flow is an unpredictable flow which is called the stochastic flow. The stochastic behavior of turbulent flow enhances the transport and mixes fluid much more effective than laminar flow. In the Pope' text book [68], the stochastic behavior is caused by 'eddy' which contains turbulence energy. Turbulent flow is composed of various size of eddies and the large eddy can contain the smaller eddies. Each eddies has a characteristic length ℓ, velocity $u(\ell)$ and timescale $\tau(\ell) \equiv \ell/u(\ell)$. In Figure 2.1, eddy sizes and ranges at high Reynolds number are shown [68]. $\mathcal{L}$ is the flow scale, ℓ_0 is the length scale of the largest eddy size which is comparable to the flow scale. ℓ_{EI} is the demarcation between the anisotropic large eddies in the energy-containing range and the isotropic small eddies in the universal equilibrium range, and it is estimated with $\ell_{EI} = \frac{1}{6}\ell_o$. ℓ_{DI} (with $\ell_{DI} = 60\eta$) is the demarcation between the inertial subrange and dissipation range in the universal equilibrium range. η is the characteristic length scale of the smallest turbulent motions, called the Kolmogorov length scale. The Kolmogorov scale is defined from dissipation (ε) and viscosity (ν):

$$\eta \equiv \left(\frac{\nu^3}{\varepsilon}\right)^{1/4} \tag{2.1.1}$$

$$\tau_\eta \equiv \left(\frac{\nu}{\varepsilon}\right)^{1/2} \tag{2.1.2}$$

$$u_\eta \equiv (\nu\varepsilon)^{1/4} \tag{2.1.3}$$

The larger eddies are unstable and break up to the smaller eddies with transferring their energy. This process is continued until the eddy motion is stable and molecular viscosity is effective to dissipate the kinetic energy. This process is called the energy cascade and its schematic diagram is shown in Figure 2.2. The energy-containing range contains most of the energy and it is transferred to the smaller scales by the transfer rate $\mathcal{T}(\ell)$. The transfer rate is independent of ℓ in the inertial subrange as below.

$$\mathcal{T}_{EI} \equiv \mathcal{T}_{(\ell_{EI})} \equiv \mathcal{T}_{(\ell)} \equiv \mathcal{T}_{DI} \equiv \mathcal{T}_{(\ell_{DI})} \equiv \varepsilon \tag{2.1.4}$$

Hence, the energy is transferred from the large scales to the small scales by the constant rate of the dissipation rate ε.

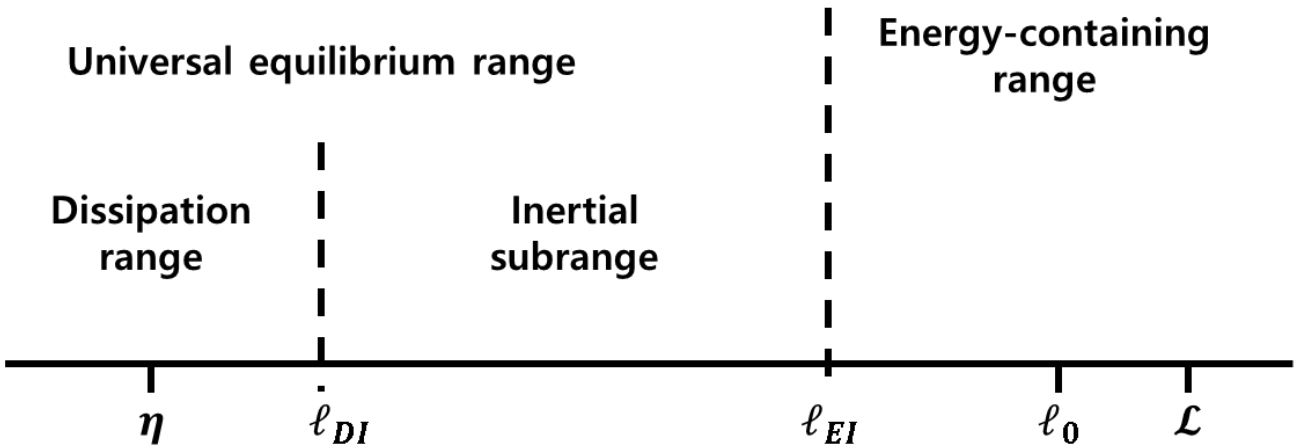

Figure 2.1 Eddy sizes at very high Reynolds number, showing the various length scales and ranges [68]

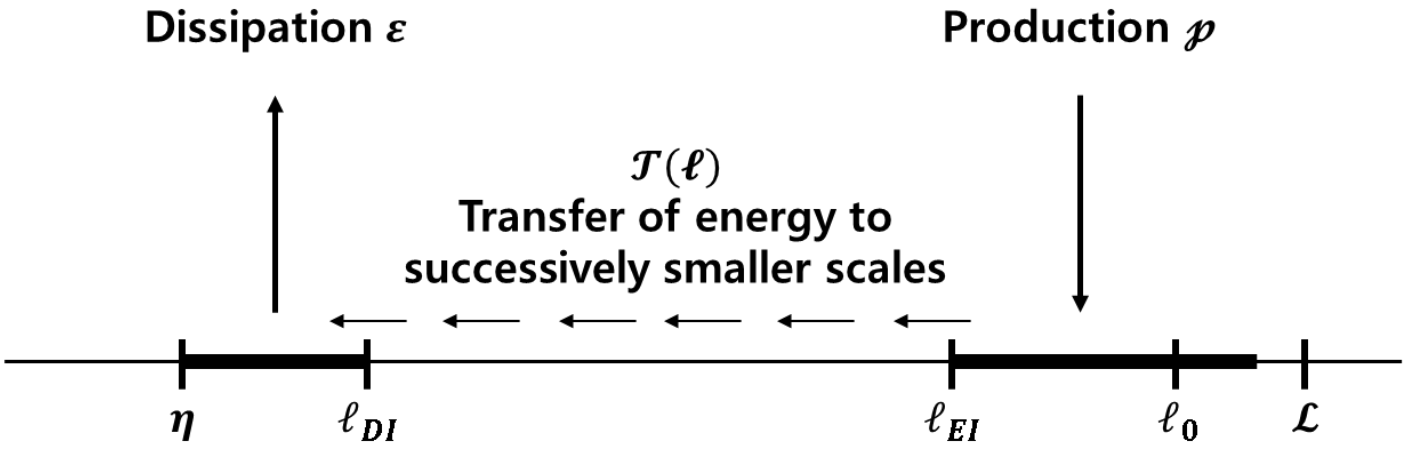

Figure 2.2 A Schematic diagram of the energy cascade at very high Reynolds number [68]

2.1.2 The Energy Spectrum

Turbulent flow is composed of different scales of eddy and the turbulent kinetic energy is distributed among the different scales [68]. In the Kolmogorov hypothesis, the turbulent kinetic energy among different eddy scales can be described as below Figure 2.3. The turbulent length scale ℓ (characteristic eddy size) is transformed to wave length κ domain. The energy spectrum function $E(\kappa)$ is formed from the dissipation rate ε and wave length κ as below.

$$E(\kappa) = C\varepsilon^{2/3}\kappa^{-5/3} \tag{2.1.5}$$

The region of $E(\kappa)\sim\kappa^2$ is at the low wave lengths (large turbulent lengths) which have most of turbulent kinetic energy and $E(\kappa)\sim\kappa^{-5/3}$ is in the inertial subrange. Because, in LES, a filter size determines the resolved turbulent length scale, it is very important to understand the energy cascade and the energy spectrum. Following section derives the governing equation of LES and highlights the importance of a grid size for the LES filter.

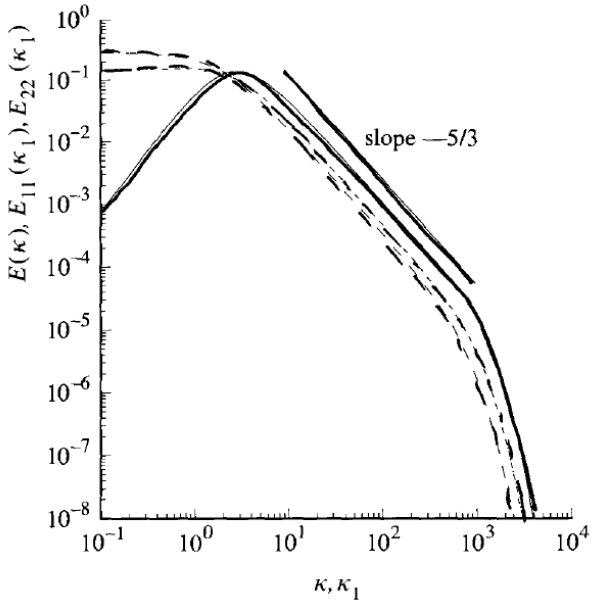

Figure 2.3 Comparison of spectra in isotropic turbulence at $R_\lambda = 500$ [68]

2.2 Sub-grid Scale Turbulence Model

The governing equations of mass and momentum conservation are described as equations (2.2.1) and (2.2.2) [69]

$$\frac{\partial \rho}{\partial t} + \frac{\partial (\rho u_i)}{\partial x_i} = \dot{m} \tag{2.2.1}$$

$$\frac{\partial (\rho u_i)}{\partial t} + \frac{\partial}{\partial x_i}\left(\rho u_j u_i - \tau_{ij}\right) = -\frac{\partial P}{\partial x_i} + \dot{M}_\iota \tag{2.2.2}$$

Where, t: time

ρ: density

x_i: Cartesian coordinate (i= 1, 2, 3)

u_i: velocity component

P: pressure

τ_{ij}: stress tensor

$\dot{m}$: mass source term

$\dot{M}_\iota$: momentum source term

In LES approach, the flow field is decomposed into a resolved (filtered) part and a SGS part by the LES filter as equation (2.2.3).

$$u_i = \bar{u}_i + \acute{u}_\iota \tag{2.2.3}$$

Where, u_i: velocity

$\bar{u}_i$: resolved (filtered) velocity

$\acute{u}_i$: sub-grid scale velocity

The resolved part is defined as a spatial average of the actual velocity field. Unlike RANS, LES filter has below properties.

$$\bar{\bar{u}}_i \neq \bar{u}_i \tag{2.2.4}$$

$$\bar{\acute{u}}_i \neq 0 \tag{2.2.5}$$

The filtered momentum equation is derived as equation (2.2.6). $\bar{}$ is used to denote the grid filter and $\tilde{}$ indicates the Favere-averaged term.

$$\frac{\partial \bar{\rho}\widetilde{u_i}}{\partial t} + \frac{\partial \bar{\rho}\widetilde{u_i}\widetilde{u_j}}{\partial x_j} = -\frac{\partial \bar{P}}{\partial x_i} + v\frac{\partial^2 \overline{u_i}}{\partial x_j \partial x_j} - \frac{\partial \tau_{ij}}{\partial x_j} \tag{2.2.6}$$

Where, v: kinematic viscosity

and

$$\widetilde{u_i} \equiv \frac{\overline{\rho u_i}}{\bar{\rho}} \tag{2.2.7}$$

$$\tau_{ij} = L_{ij} + C_{ij} + R_{ij} \tag{2.2.8}$$

Where,

$$L_{ij} = \overline{\bar{u}_i \bar{u}_j} - \bar{u}_i\,\bar{u}_j \tag{2.2.9}$$

$$C_{ij} = \overline{\bar{u}_i \acute{u}_j} + \overline{\acute{u}_i \bar{u}_j} \tag{2.2.10}$$

$$R_{ij} = \overline{\acute{u}_\iota \acute{u}_J} \tag{2.2.11}$$

L_{ij}, C_{ij} and R_{ij} are called the Leonard stresses, the sub-grid cross stresses and the sub-grid Reynolds stresses [70] respectively. Sub-grid scale stress tensor (Equation (2.2.8)) can be simplified to equation (2.2.12)

$$\tau_{ij} = \overline{u_\iota u_J} - \overline{u}_\iota \, \overline{u}_J \tag{2.2.12}$$

Because equation (2.2.12) cannot be calculated from the resolved field, it is necessary to model the sub-grid scale stress tensor. There are two approaches to model the sub-grid scale stress tensor: zero-equation and one-equation. In this study, two kinds of zero-equation and one-equation models are assessed with PIV results. Before discussion of results, LES models are briefly introduced.

2.2.1 Zero-equation Model

2.2.1.1 Smagorinsky Model

In 1963, Smagorinsky proposed a SGS model based on the assumption of eddy-viscosity[32]. The Smagorinsky model is the simplest and widely used. It is derived from a local equilibrium assumption that production and dissipation of the SGS turbulent kinetic energy are equal. The sub-grid stress tensor is derived as equation (2.2.13).

$$\tau_{ij} - \frac{1}{3}\tau_{kk}\delta_{ij} = -v_t \overline{S_{\iota J}} \tag{2.2.13}$$

Where, δ_{ij}: kronecker delta

v_t: sub-grid turbulent viscosity

S_{ij}: strain rate tensor

$$\overline{S_{ij}} = \frac{1}{2}\left(\frac{\partial \overline{u_i}}{\partial x_j} + \frac{\partial \overline{u_j}}{\partial x_i}\right) \quad (2.2.14)$$

$$v_t = 2C_s\Delta^2\left\|\overline{S_{ij}}\right\| \quad (2.2.15)$$

Where, C_s: model coefficient for sub-grid turbulent viscosity

Δ: filter size

$\left\|\overline{S_{ij}}\right\|$: Frobenius norm of the strain rate tensor

It is important to note that a priori knowledge for the flow field to determine the constant model coefficient for sub-grid turbulent viscosity. In addition, for a complex flow system such as in-cylinder flow, it may suffer from some severe drawbacks such as wall-bounded flow, flow involving a laminar/turbulent transition region, back scattering and excessive damping of large scale fluctuation in the presence of mean shear [71, 72].

2.2.1.2 Dynamic Smagorinsky Model

Germano et al. [38] suggested a dynamic version of Smagorinsky model which dynamically calculates model coefficient as a function of space and time from the resolved field. This approach assumes that different scales of resolved and sub-grid scale are mathematically identified. The advantage of dynamic model is that it doesn't require a priori knowledge of the flow to set the model coefficient.

Two different size of LES filters are used to calculate model coefficient. One is the 'test' filter and the other is called the 'grid' filter. The typical size of the test filter is twice that of the grid filter. The grid filtered stress tensor is given as equation (2.2.16) and the double (grid and test) filtered stress tensor is shown in equation (2.2.17). $\widehat{\ }$ denotes the test filter.

$$\tau_{ij} = \overline{u_i u_j} - \overline{u}_i \, \overline{u}_j \tag{2.2.16}$$

$$T_{ij} = \widehat{\overline{u_i u_j}} - \widehat{\overline{u}}_i \widehat{\overline{u}}_j \tag{2.2.17}$$

The Germano identity relates the test filtered stress tensor and the grid filtered stress tensor as equation (2.2.18).

$$L_{ij} = T_{ij} - \widehat{\tau_{ij}} = \left(\widehat{\overline{u_i u_j}} - \widehat{\overline{u}}_i \widehat{\overline{u}}_j\right) - \left(\widehat{\overline{u_i u_j}} - \widehat{\overline{u_i}}\,\widehat{\overline{u_j}}\right) = \widehat{\overline{u_i}}\,\widehat{\overline{u_j}} - \widehat{\overline{u}}_i \widehat{\overline{u}}_j \tag{2.2.18}$$

where L_{ij}, is the Leonard stress term. The test filtered Smagorinsky equation is shown in equation (2.2.19). In the dynamic Smagorinsky model, the Leonard stress term is derived by subtracting equation (2.2.13) from equation (2.2.19) as equation (2.2.20).

$$T_{ij} - \frac{1}{3} T_{kk} \delta_{ij} = -2 C_s \hat{\Delta}^2 \left\|\widehat{S_{ij}}\right\| \widehat{S_{ij}} \tag{2.2.19}$$

$$L_{ij} - \frac{1}{3} L_{kk} \delta_{ij} = C_s M_{ij} \tag{2.2.20}$$

Where,

$$M_{ij} = -2\left(\hat{\Delta}^2 \left\|\widehat{S_{ij}}\right\| \widehat{S_{ij}} - \Delta^2 \widehat{\left\|\overline{S_{ij}}\right\| \overline{S_{ij}}}\right) \tag{2.2.21}$$

Finally, the dynamic model coefficient is obtained as equation (2.2.22).

$$C_s = \frac{L_{ij} M_{ij}}{M_{ij} M_{ij}} \tag{2.2.22}$$

2.2.2 One-equation and Non-viscosity Model

2.2.2.1 Dynamic Structure Model

Above two models adopt the eddy-viscosity hypothesis. However, Liu et al. show little correlation between the eddy-viscosity assumption and the actual sub-grid stress tensor. To overcome the problem, there is an attempt to estimate the sub-grid stress tensor directly. The DSM also adopts 'test' and 'grid' stress tensors as equation (2.2.23) and (2.2.24)

$$\tau_{ij} = c_{ij}k \tag{2.2.23}$$

$$T_{ij} = c_{ij}K \tag{2.2.24}$$

Where, τ_{ij}: 'grid' filtered stress tensor

T_{ij}: 'test' filtered stress tensor

k: sub-grid scale turbulent kinetic energy of 'grid' filter

K: sub-grid scale turbulent kinetic energy of 'test' filter

c_{ij}: tensor coefficient

Where the SGS turbulent kinetic energy with the 'grid' and the 'test' filters are shown as equation (2.2.25) and (2.2.26).

$$k \equiv \frac{1}{2}(\overline{u_\iota u_\iota} - \overline{u}_\iota\,\overline{u}_\iota) \tag{2.2.25}$$

$$K \equiv \frac{1}{2}(\widehat{\overline{u_\iota u_\iota}} - \widehat{\overline{u}}_\iota\widehat{\overline{u}}_\iota) \tag{2.2.26}$$

Because this model doesn't employ the eddy-viscosity hypothesis, the sub-grid stress tensor can be obtained from a tensor coefficient. The tensor coefficient is derived as equation (2.2.27) by using the Germano identity.

$$L_{ij} = T_{ij} - \widehat{\tau_{ij}} = Kc_{ij} - \widehat{kc_{ij}} \tag{2.2.27}$$

Inserting equation (2.2.23) and (2.2.24) into equation (2.2.27), then the tensor coefficient has a relation with the Leonard stresses and the SGS turbulent kinetic energy as equation (2.2.28).

$$c_{ij}(K - k) = L_{ij} \tag{2.2.28}$$

Substituting the SGS turbulent kinetic energy (equations (2.2.25) and (2.2.26)) into equation (2.2.28), gives the tensor coefficient as equation (2.2.29).

$$c_{ij} = 2\frac{L_{ij}}{L_{kk}} \tag{2.2.29}$$

Finally, the SGS stress tensor is obtained as equation (2.2.30).

$$\tau_{ij} = 2k\frac{L_{ij}}{L_{kk}} \tag{2.2.30}$$

The DSM adopts a transport equation for the SGS turbulent kinetic energy and it is called one-equation model. The transport equation of the SGS turbulent kinetic energy is described as equation (2.2.31) [37, 60]

$$\frac{\partial(\bar{\rho}k)}{\partial t} + \frac{\partial(\bar{\rho}\,\overline{u_j}k)}{\partial x_j} = -\bar{\rho}\tau_{ij}\frac{\partial \overline{u_j}}{\partial x_j} - \bar{\rho}\varepsilon + \frac{\partial}{\partial x_j}\left(\bar{\rho}\,\overline{u_j}v_t\frac{\partial k}{\partial x_j}\right) \tag{2.2.31}$$

with the dissipation rate and the sub-grid turbulent viscosity as equation (2.2.32) and (2.2.33), respectively.

$$\varepsilon = C_1 \frac{k^{3/2}}{\Delta} \tag{2.2.32}$$

$$v_t = C_2 \Delta \sqrt{k} \tag{2.2.33}$$

Where, C_1: model coefficient for dissipation rate

C_2: model coefficient for sub-grid turbulent viscosity.

By adding the transport equation for the SGS turbulent kinetic energy, a kinetic energy budget serves that the information of the SGS turbulent kinetic energy is transferred to neighbors and it improves the numerical stability. Therefore, the accuracy of the SGS model is improved with coarser grids than the zero-equation models.

2.3 Evaluation of Turbulence Models

In the previous section, three SGS models were introduced. Three SGS models were evaluated with PIV results in the author's previous publications [73, 74]. The target engine is a single cylinder engine with transparent combustion chamber (TCC-III) which was designed for LES research by University of Michigan and GM Global R&D center [75, 76]. It consists of two valve head and a simple combustion chamber of pancake shape. Each intake and exhaust port is connected to a plenum. The schematic of the TCC-III engine is shown in Figure 2.4 [75]. The pressure signals were measured at inlet of intake plenum, outlet of exhaust plenum, intake port, exhaust port and in-cylinder every 0.5 crank angle (CA) degrees as shown in Figure 2.4 with a red dots. Detailed engine specifications are listed in Table 2.1. PIV measurements were conducted on four different section planes as shown in Figure 2.5. A monochrome high-speed camera (Vision Research, Phantom v1610) was used to record images measured every 5 CA degrees. Silicon-oil droplets (1μm) were used as seeding parcels and a ND:YLF laser (Darwin Duo, Quantronix) was used to illuminate the parcels. A DaVis 9.x which is a commercial PIV post-processing code made of LaVision was adopted to generate vector field from recorded images. A detailed information of the TCC-III engine and the PIV setup can be found in [75].

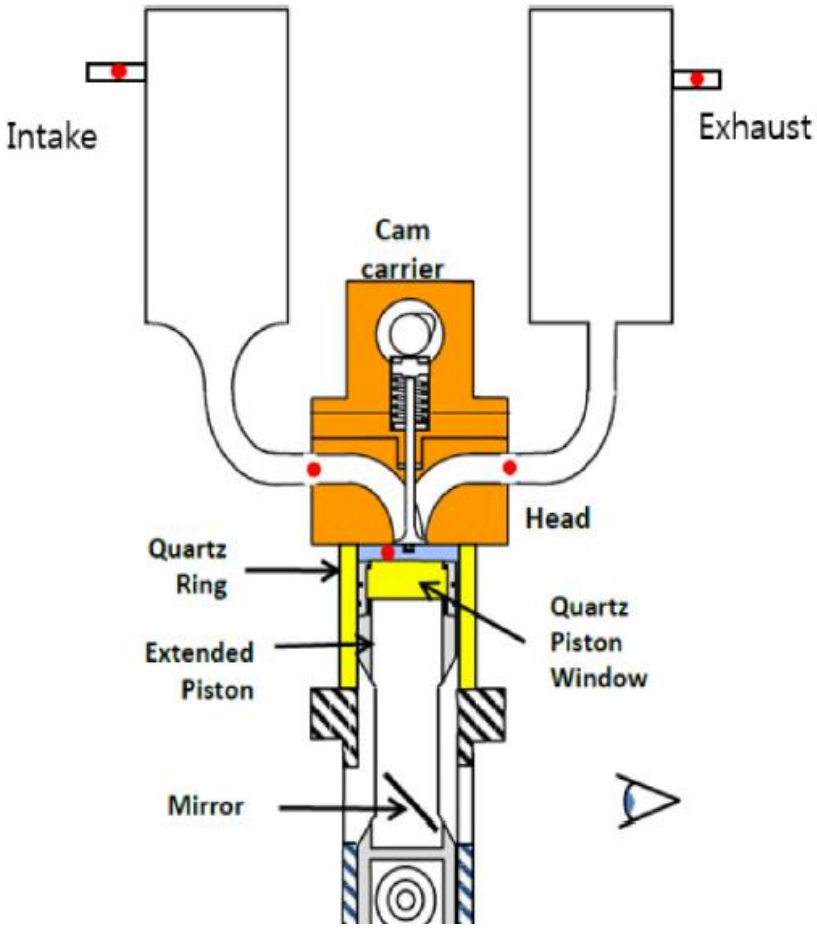

Figure 2.4 The schematic of TCC-III engine. The pressure signals are measured at red dots [75].

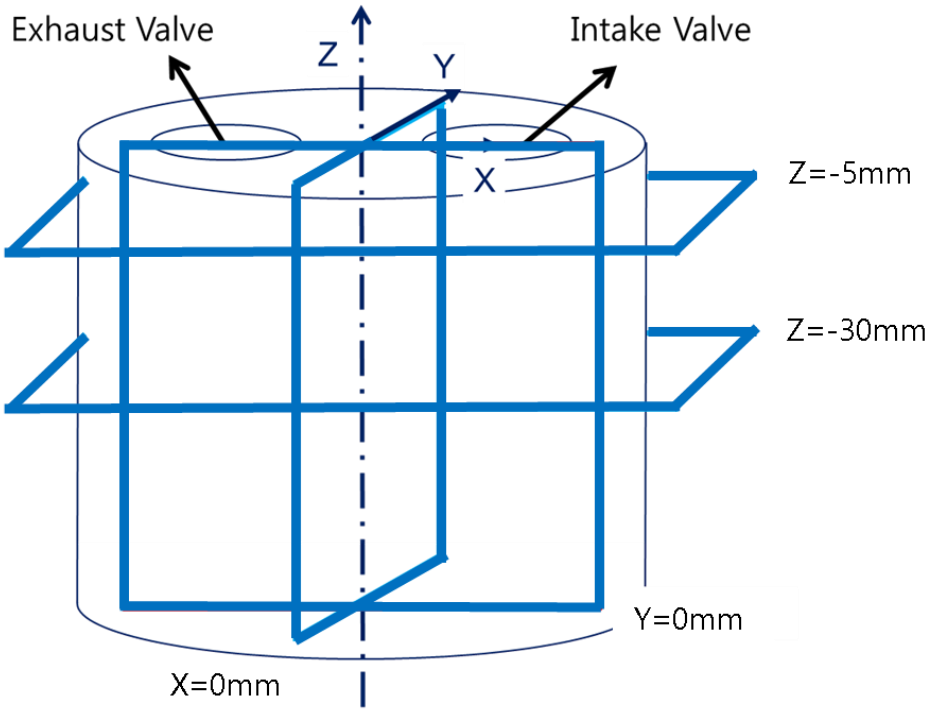

Figure 2.5 PIV measurement planes [75]

Table 2.1 The TCC-III engine specification

Parameter	Specification
Engine	TCC-III engine
Displacement Volume	570 cc
Bore	92 mm
Stroke	86 mm
Compression Ratio	10.0
Engine Speed	1300 RPM
Intake Pressure	0.4 bar

2.3.1 Numerical Configuration

The assessment of the SGS models was performed using STAR-CD v4.22 licensed by Siemens PLM. The numerical domain was meshed using trim method as Figure 2.6. To save the computational cost, a grid size of the intake and exhaust plenums was 6mm and that of the ports was 1.5mm. A mean grid size of the in-cylinder was 1mm. The high velocity gradient regions such as near the valve regions and the spark plug region were meshed with 0.4mm and 0.6mm, respectively. A single layer of prismatic cells aligned to the walls was used to construct mesh of near-wall regions. The total number of cells was approximately 1.15 million at bottom dead center (BDC) with 1 million cells of the intake and exhaust plenums. The arbitrary lagrangian-eulerian (ALE) formation and the arbitrary sliding interface (ASI) were adopted to deal with moving-boundary and mesh motion. The pressure implicit with splitting of operator (PISO) algorithm, which is optimized for transient flow, was employed for temporal discretization. The monotone advection and reconstruction scheme (MARS) was used for spatial discretization. The standard wall function was adopted for near-wall treatment.

Time-dependent pressure and boundary conditions were adopted for inlet and outlet condition. At first, pressure signals were measured at the inlet of plenum, the outlet of plenum, the intake, the exhaust and the in-cylinder as shown in Figure 2.4 [75]. The 1D (GT-power) simulation was conducted to obtain intake pressure and temperature, exhaust pressure and temperature and wall temperatures [75]. As shown in Figure 2.7, the discrepancy between the pressure of the inlet and the outlet in the experiment and the simulation was negligible. Therefore, the implementation of boundary conditions obtained from GT-power is reasonable choice.

To evaluate the SGS model effects, the vector fields were compared with the PIV result. Basically, the simulations and the PIV result were compared with the analysis of vector field and root-mean-square deviation (RMSd) of velocity vector. The definition of RMSd is as equation (2.3.1).

$$u' = \sqrt{\frac{1}{n-1}\sum_{i=1}^{n}(u_i - \langle u \rangle)^2} \tag{2.3.1}$$

Where, u': root-mean-square deviation of velocity

u_i: instantaneous velocity

$\langle \quad \rangle$: ensemble or phase average

n: total number of cycle

In addition, the alignment parameter and the LES quality index was used to assess the SGS models quantitatively. The alignment parameter is a very simple and effective method to quantify the local derivation of the simulated vector field with respect to the PIV vector field, which is assumed as a reference. The definition is formulated as equation (2.3.2).

$$\frac{\vec{A}\cdot\vec{B}}{\|\vec{A}\|\|\vec{B}\|} = \frac{\|\vec{A}\|\|\vec{B}\|\cos(\alpha)}{\|\vec{A}\|\|\vec{B}\|} = \cos(\alpha) \quad \in \quad [-1,1] \tag{2.3.2}$$

Where, $\vec{A}$: reference vector

$\vec{B}$: comparable target vector

α: angle between reference and comparable target vectors

If the parameter equals 1, it means that direction of the PIV (reference) vector field and the LES vector (comparable target) field is exactly aligned. While if the parameter equals -1, their vector has totally opposite direction. The value of 0 indicates that they have orthogonal direction.

Finally, the LES quality index was used to evaluate the level of resolved flow field. As mentioned before, the grid size determines the resolved flow field and the contribution of the SGS model. Therefore, the LES quality index is very useful tool to determine the grid size and the SGS model. The LES quality index, M, is defined as equation (2.3.10) [77, 78].

$$M = \frac{k_{res}}{k_{res}+k_{sgs}} \tag{2.3.10}$$

Where, $\langle \quad \rangle$ indicates the ensemble or phase average.

$$k_{res} = \frac{1}{2}(\langle \overline{u_i} - \langle \overline{u_i} \rangle \rangle^2) \tag{2.3.11}$$

$$k_{sgs} \equiv \frac{1}{2}(\overline{u_i u_i} - \overline{u_i}\,\overline{u_i}) \tag{2.3.12}$$

The index provides two aspects of significant information. It indicates whether the grid size is sufficient to resolve turbulence flow. The high value of index means that almost turbulence flow is resolved and only small turbulence scale is modeled by the SGS model. However, even though the grid size is small enough to resolve turbulent flow, the SGS models sometimes cannot predict turbulent flow field properly. Then, the index indicates low value regardless of grid resolution. So, the index also provides whether the SGS turbulent flow is adequately predicted by SGS models.

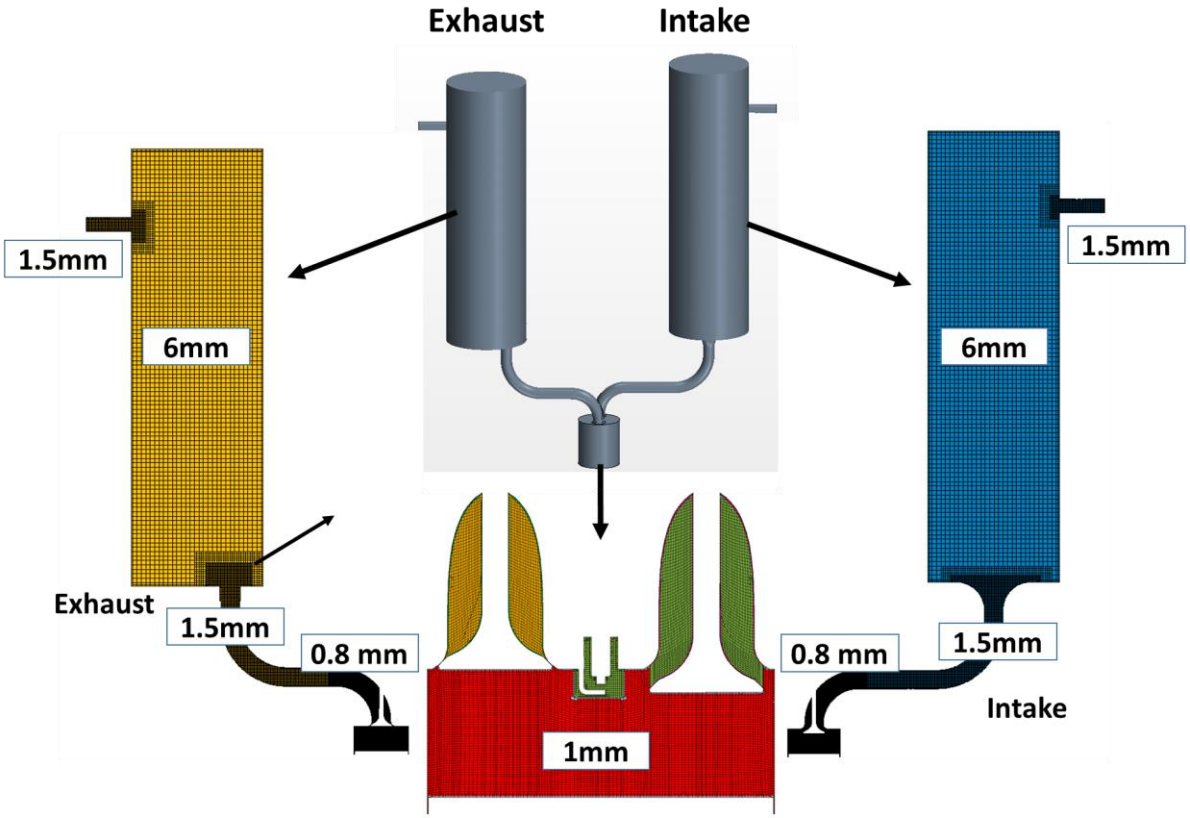

Figure 2.6 The computational domain of the TCC-III engine [73]

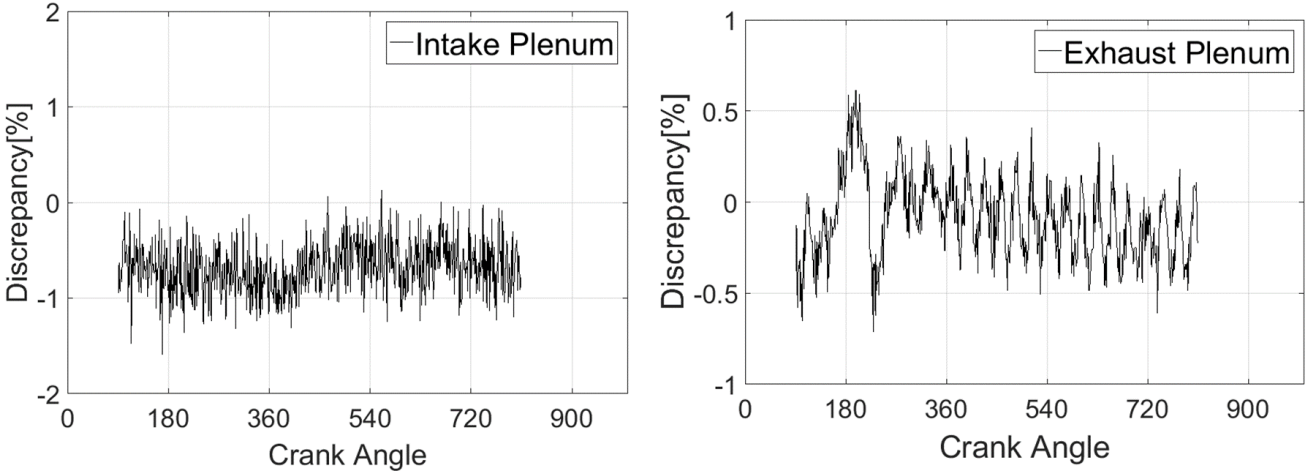

Figure 2.7 The discrepancies of pressure between experiment data and GT-power data [73]

2.3.2 Comparison of Sub-grid Scale Model

The comparison of the SGS model with the PIV result was mainly conducted under following condition. The engine operation speed was 1,300 rpm under about 0.4 bar of intake pressure. To obtain a stable initial condition, one cycle was performed using RANS approach for each SGS model case and it was used as an initial condition of LES cycle. The three sets of 51 consecutive LES cycles were conducted. The first cycle of each LES case was discarded to remove the unstable transition state between RANS and LES cycle. Figures 2.8 and 2.9 show the peak pressure and trapped mass for the 52 cycles including RANS cycle. The peak pressure results show convergence in 51 LES cycles, but in terms of trapped mass, the first cycle of LES is slightly deviated from the 51 cycle average. Therefore, the first cycle of three LES cases was discarded to remove the unstable cycle. Finally, three sets of effective 51 LES cycles were obtained. The measurement plane is Y=0mm section plane shown in Figure 2.5. The vector fields were evaluated at four different crank angle positions. The chosen crank angles represent significant engine events:

- Middle of exhaust stroke at 245 CA
- Middle of intake stroke at 475 CA
- BDC, 540CA
- Middle of compression stroke at 630CA

Figure 2.10 shows the vector fields of LES and the PIV results at four different CA on Y=0mm section plane. At 245 CA, the dynamic Smagorinsky model and the DSM cases are well matched with PIV data. However, the static Smagorinsky model case shows that a wall flow near left liner is relatively

stronger than the PIV and other LES results. At 540 CA and 630 CA, there is no significant difference between LES results. At 475 CA, an intake jet flow is observed in the PIV and LES results. All of the SGS model cases are well matched with the PIV data. Figure 2.11 shows the RMSd field of velocity for three LES cases and the PIV data. The LES cases slightly underestimate the magnitude of the RMSd velocity compared with the PIV data. The estimation of turbulent flow in LES can be divided into two types: large scale turbulent flow resolved by grid and small scale turbulent flow predicted by the SGS model. Thus, while only the large scale turbulent flow is reflected in the RMSd velocity field in LES, both the large and small scale turbulent flow are contained in the RMSd velocity field in PIV. This is why LES results underestimate the RMSd velocity field of the PIV. Except for this discrepancy between LES cases and the PIV data, there is no noticeable difference between LES results at 245 CA, 540 CA and 630 CA. However, there is noticeable difference among LES results at 475 CA. While the static Smagorinsky result predicts the wider and longer shape of intake jet flow than the PIV data, the dynamic Smagorinsky and the DSM cases are well matched with the PIV data. The results of alignment parameter are shown in Figure 2.12. At 245 CA, vector fields of the dynamic Smagorinsky model and the DSM cases are well aligned with the PIV result. However, the wide region of discrepancy is shown in the static Smagorinsky model case. At 475 CA, two discrepancy regions can be found in three SGS model cases. Because the intake jet flow of LES slightly leans to the left compared to the PIV counterpart, two regions of very poor alignment appear. The parameter values are spatial averaged and presented in Table 2.2. The spatial averaged value of alignment parameter for the dynamic Smagorinsky model and the DSM case show a good agreement with the PIV data.

In terms of the LES quality, the DSM case has the very high contribution of resolved part on turbulent flow field and the dynamic Smagorinsky model case also show high quality as shown in Figure 2.13. The remarkable point is that the

dynamic Smagorinsky model case predicts abnormally the high SGS turbulent kinetic energy in the high velocity gradient region near the valve at 245 CA. On the contrary, the DSM case can predict the reasonable SGS turbulent kinetic energy relative to the surrounding field. Except near the valve region, the level of grid resolution is enough to predict flow field for both the dynamic Smagorinsky model and the DSM case as Table 2.3 which summarizes the spatial averaged value of the LES quality index. In terms of the accuracy of flow field and prediction of the SGS turbulent kinetic energy, the dynamic Smagorinsky model and the DSM are superior model than the static Smagorinsky model. Furthermore, the DSM model was adopted in this study in consideration of the theoretical advantages of calculating the transport equation of the SGS turbulent kinetic energy.

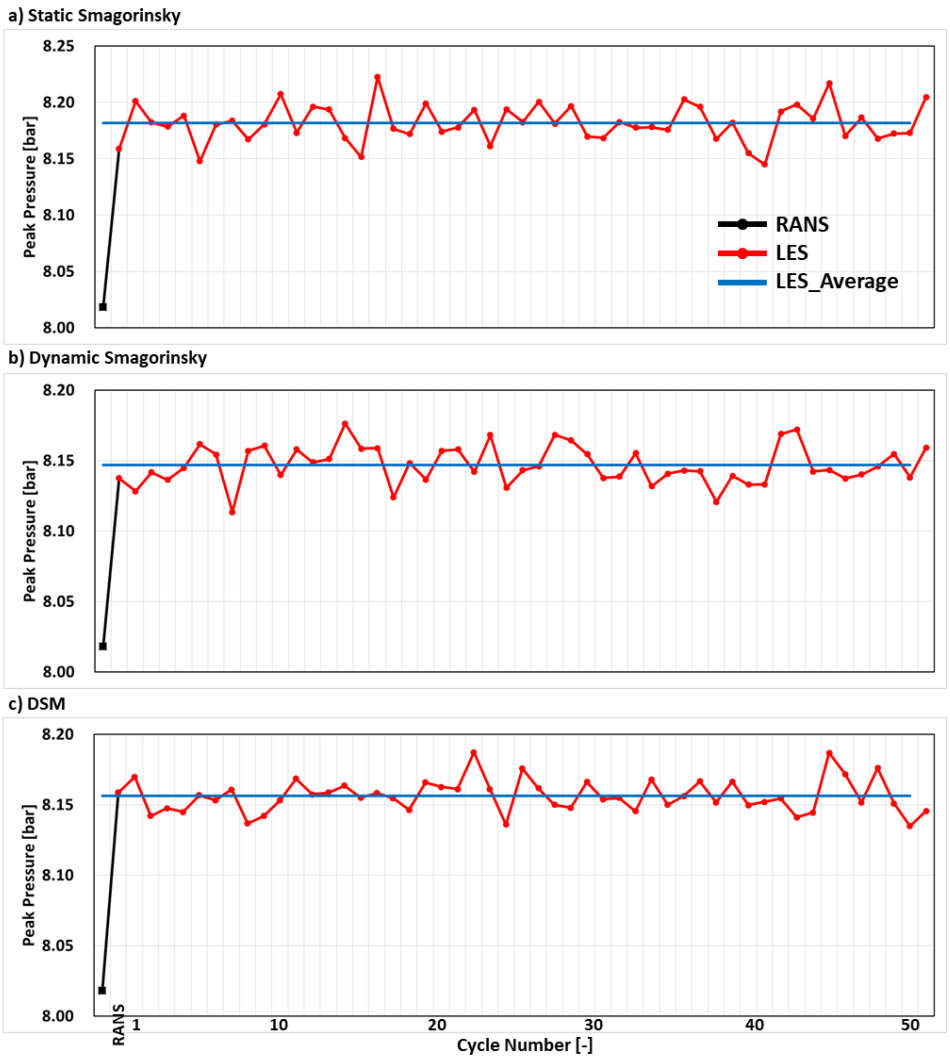

Figure 2.8 Peak pressure for the 52 cycles. The black circle identifies the discarded LES cycle for a) Static Smagorinsky, b) Dynamic Smagorinsky, c) DSM [74]

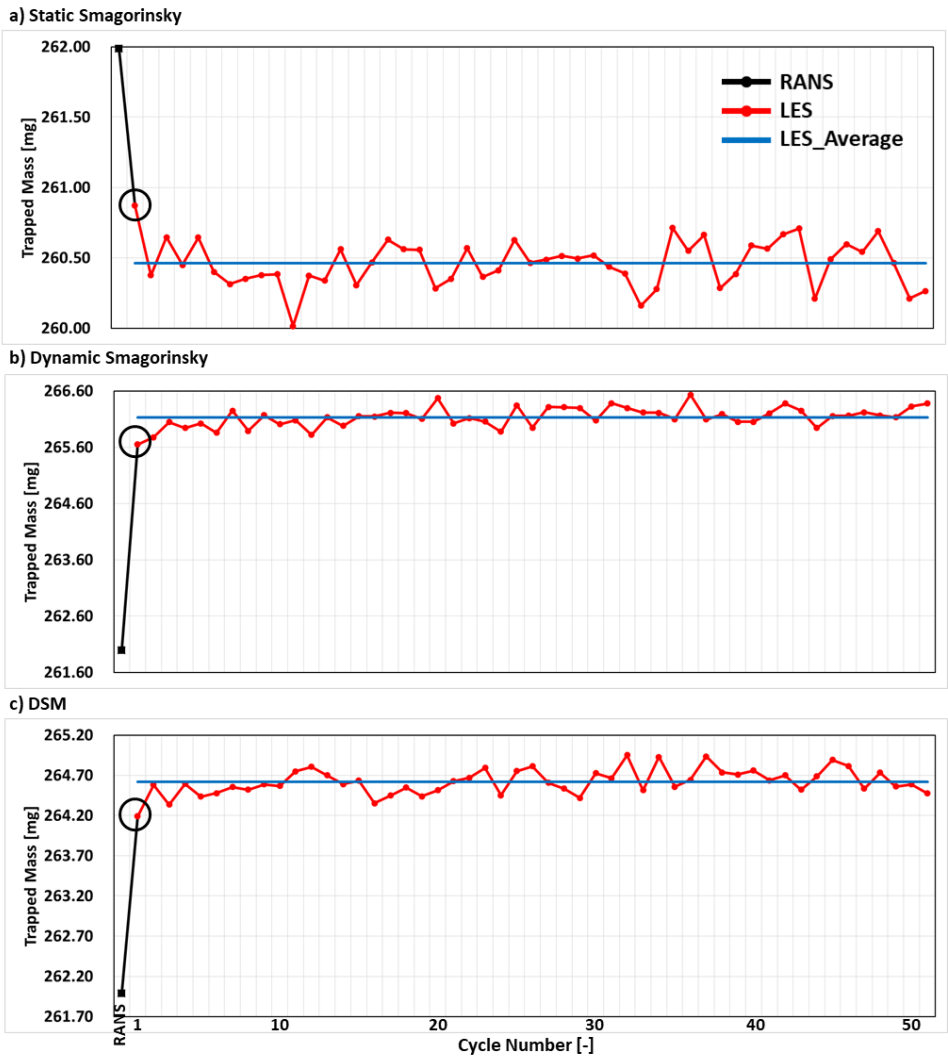

Figure 2.9 Trapped mass for the 52 cycles. The black circle identifies the discarded LES cycle for a) Static Smagorinsky, b) Dynamic Smagorinsky, c) DSM [74]

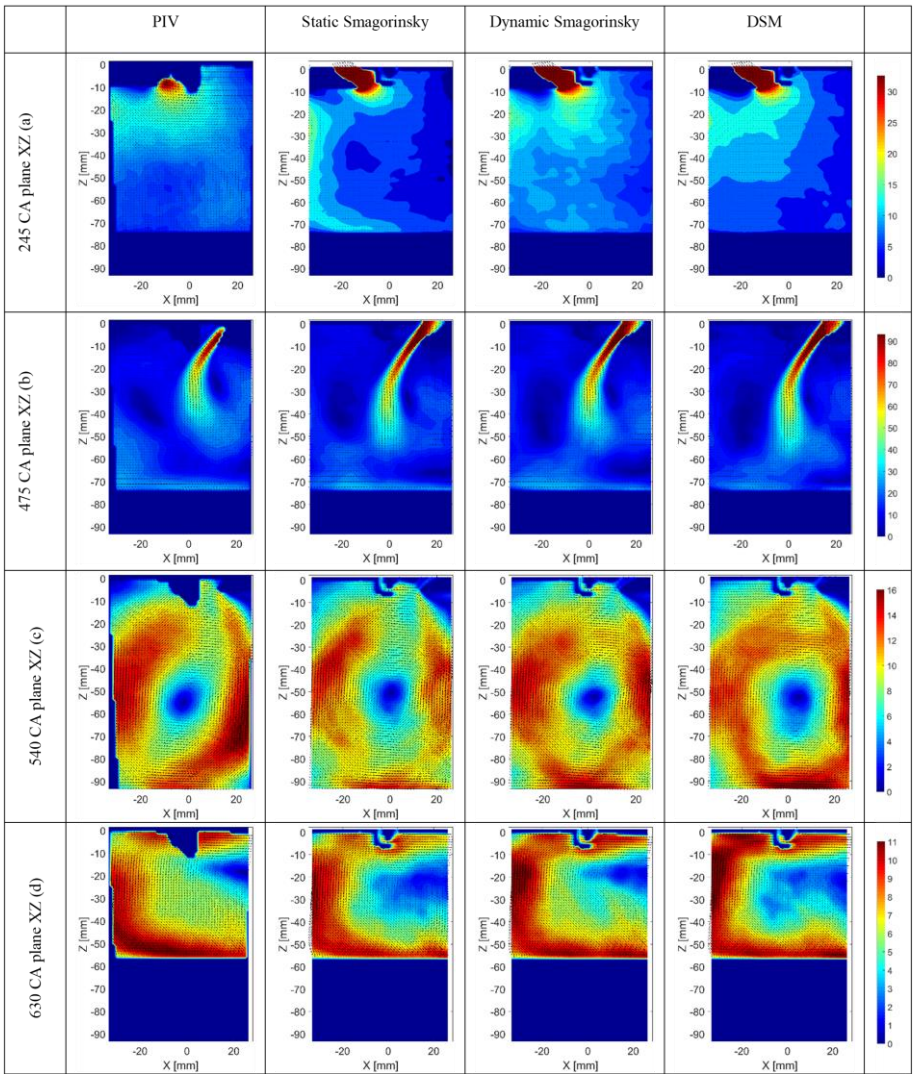

Figure 2.10 Averaged velocity field of PIV, static Smagorinsky, dynamic Smagorinsky and DSM cases at four different CA positions on section plane Y=0mm [74]

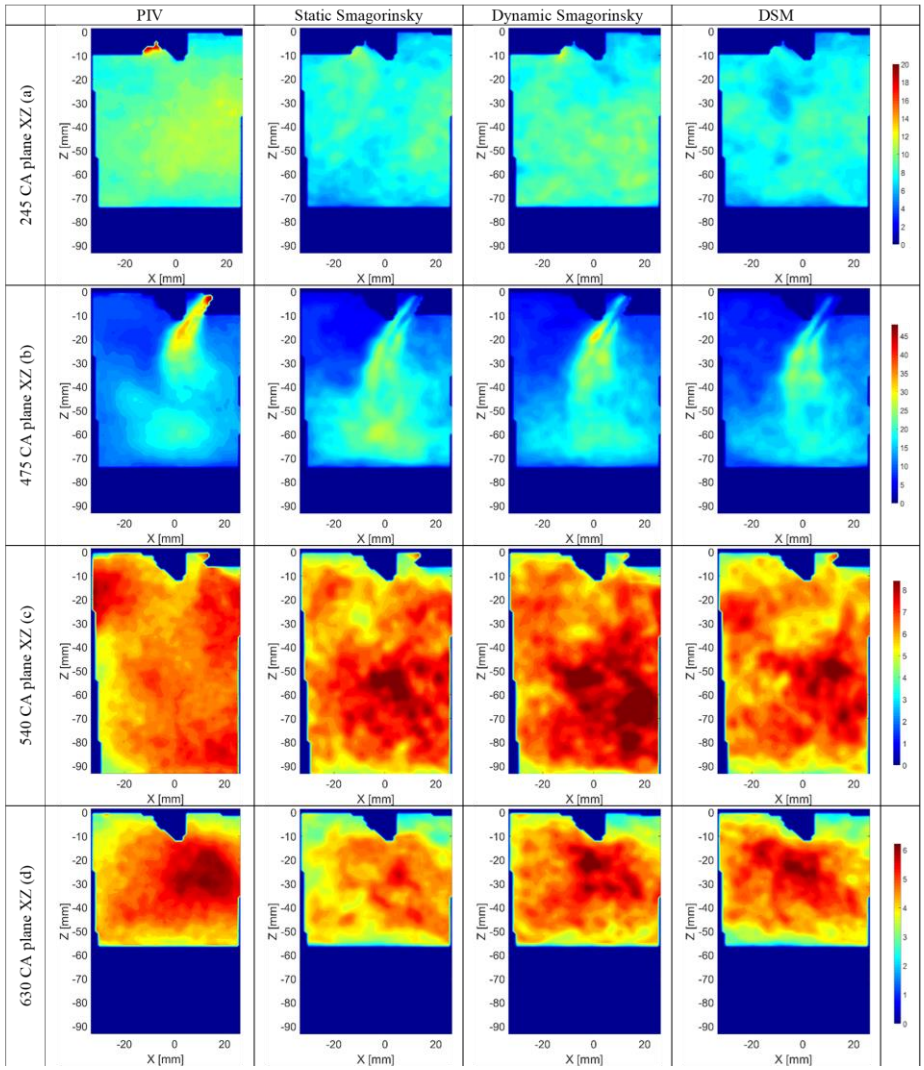

Figure 2.11 RMSd velocity field of PIV, static Smagorinsky, dynamic Smagorinsky and DSM cases at four different CA positions on section plane Y=0mm [74]

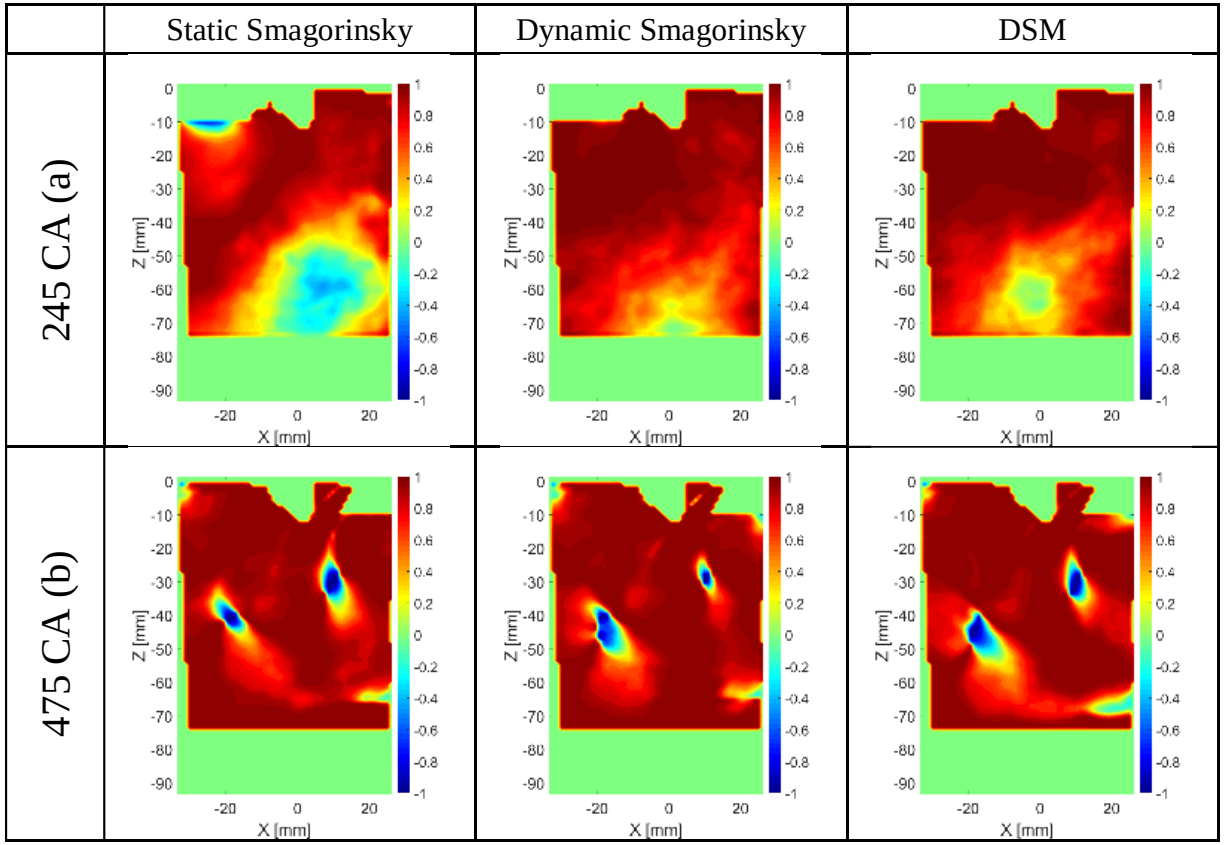

Figure 2.12 Alignment parameter representation on section plane Y=0mm at (a) 245 CA and (b) 475CA [74]

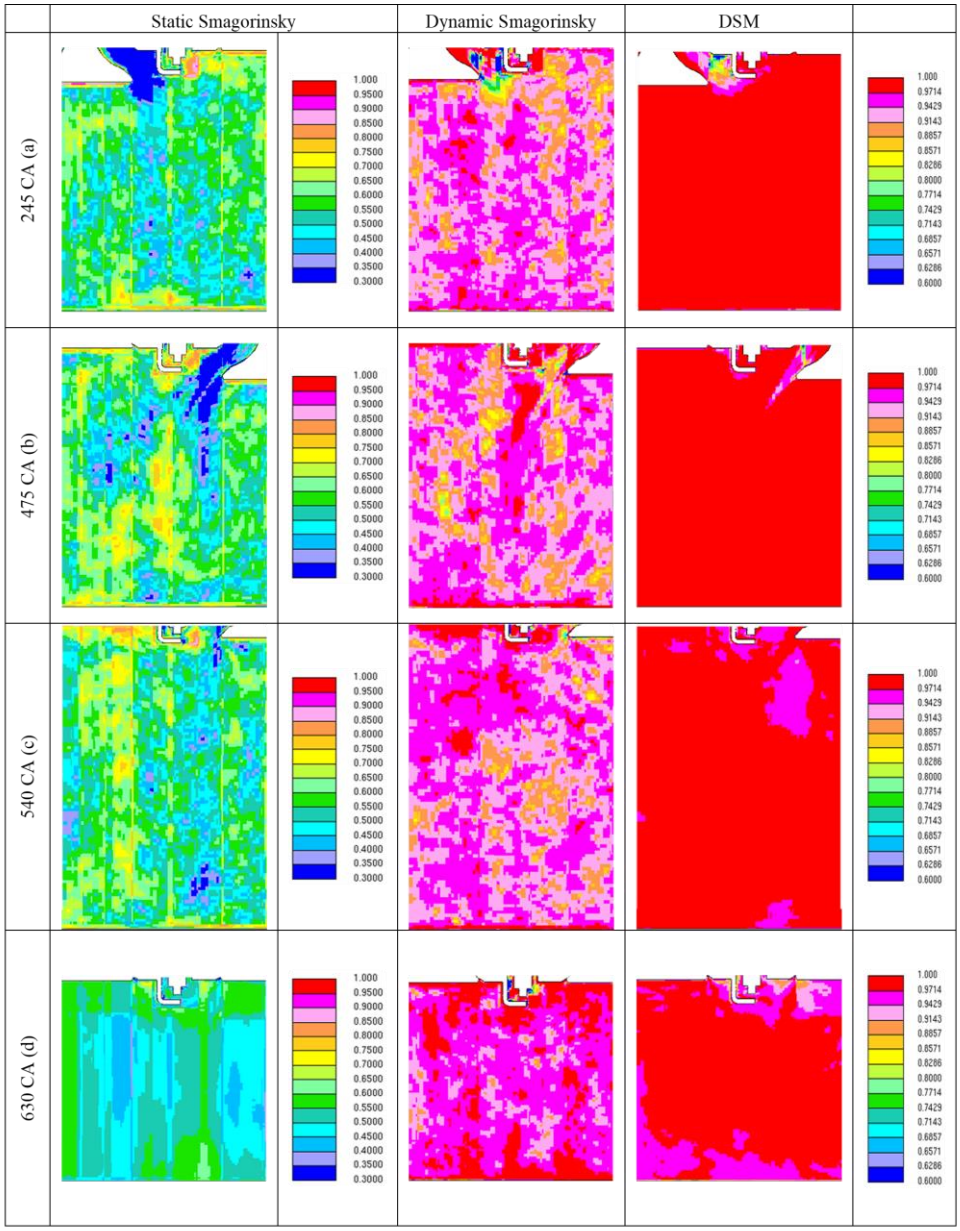

Figure 2.13 LES quality result of static Smagorinsky, dynamic Smagorinsky and DSM at four different CA positions on section plane Y=0mm [74]

Table 2.2 The spatial averaged value of alignment parameter at Y=0mm plane [74]

	Static Smagorinsky	Dynamic Smagorinsky	DSM
245 CA	0.5344	0.9383	0.9388
475 CA	0.4968	0.9265	0.9146
540 CA	0.5688	0.9329	0.9482
630 CA	0.6129	0.9511	0.9528

Table 2.3 The spatial averaged value of LES quality index at Y=0mm plane [74]

	Static Smagorinsky	Dynamic Smagorinsky	DSM
245 CA	0.611	0.831	0.808
475 CA	0.869	0.876	0.839
540 CA	0.956	0.962	0.939
630 CA	0.948	0.982	0.967

Chapter 3. Modeling of Gasoline Surrogate Fuel

Real gasoline consists of hundreds of hydrocarbon species which vary in the number of carbon atoms and various chemical families: paraffins, naphthenes, olefins and aromatics. And the composition of fuel depends on the crude oil origin and the refinery system [79]. There are many attempts to make surrogate fuels to predict real gasoline properties. A surrogate fuel which realizes many aspects of gasoline properties needs many amount of chemical species and reactions and extremely high computational cost to solve reactions. The important properties of gasoline are flame propagation, auto-ignition, distillation and emissions. However, it is very inefficient to use the surrogate fuel to predict all of gasoline properties for the 3D simulation. Considering computational cost, the surrogate fuel should be aimed to target properties. In this study, the engine operates with dual-port fuel injection (DPFI) system and emissions are not considered. Therefore, the target properties are flame propagation and auto-ignition.

In this chapter, the gasoline surrogate fuel is formulated by following steps. At first, the literature review for target properties are conducted. Next, the surrogate fuel and its mechanism are chosen for auto-ignition property of domestic gasoline fuel based on the literature review.

3.1 Literature Review

In SI engines, the combustion process starts from the electrical spark discharge. Then, the electrical energy transfers to the air-fuel mixtures in the spark channel and starts the flame propagation with turbulent flame speed. The turbulent flame speed is related to the laminar burning velocity and flow structures. So, the laminar burning velocity is a key feature of the surrogate fuel. As the flame

propagates with the turbulent flame speed, the temperature of burned gas and on flame region elevates to the flame temperature. Since the laminar burning velocity can be formulated by semi-empirical correlation, it will be discussed in Chapter 4. The flame temperature is related to the lower heating value. The low heating value of gasoline is around 42.8 MJ/kg. The primary reference fuel (PRF), a mixture of iso-octane and n-heptane, is a representative chemical species to formulate the surrogate fuel [80, 81].

3.2 Determination of Surrogate Component

In the previous section, the major chemical properties for the present study were introduced. The laminar burning velocity can be obtained by semi-empirical correlation. The toluene reference fuel (TRF) can mimic the lower heating value of gasoline and other chemical properties. Therefore, the TRF which consists of n-heptane, iso-octane and toluene meets the chemical property used in this study. In addition to the surrogate component, the selection of reaction mechanism and surrogate composition is important to predict the flame temperature.

There are several researches for development of detailed chemical mechanism. Detailed mechanisms of iso-octane [82] and PRF [83] developed by Lawrence Livermore National Laboratory were widely used. And Mehl et al. [84] introduced a detailed mechanism of PRF focused on a low-temperature heat release for an HCCI engine. Naik et al. [85] also developed a detailed mechanism of surrogate fuel which consists of iso-octane, n-heptane, 1-pentene, toluene and methyl-cyclohexane for an HCCI engine. However, even though these mechanisms have high accuracy and meet many aspects of fuel properties, they have too many reactions and species to apply on 3D simulation. Therefore, reduced mechanism has been developed as an alternative chemical mechanism.

Andrae [86] developed reduced mechanism of the TRF focusing on the ignition delay and the laminar burning velocity for gasoline at engine-relevant conditions. This mechanism is relatively heavy for the reduced mechanism due to prediction of two properties: the ignition delay and the laminar burning velocity. Lee et al. [87] conducted a rapid compression machine (RCM) experiment to obtain engine-relevant conditions and developed the reduced mechanism of the TRF focusing on the ignition delay time of Korean domestic gasoline with the RCM data. They validated iso-octane, n-heptane and toluene with experimental and detailed mechanism data, respectively. Even though the mechanism was built to predict ignition delay time, the mechanism was also composed to meet the properties of Korean gasoline as shown in Table 3.1. In their work, the selected composition of TRF is 54% iso-octane, 22% n-heptane and 24% toluene by liquid volume fraction. The properties of surrogate fuel are listed in Table 3.2 and good agreement with Korean gasoline. Therefore, the TRF mechanism of the introduced composition ratio (54% iso-octane, 22% n-heptane and 24% toluene by liquid volume fraction) is adopted in this study.

Table 3.1 The properties of Korean gasoline

Item	Value
ON(RON)	92
Density (g/cm3 at 15°C)	0.733
Vapor pressure (37.8°C, kPa)	55
Lead content (g/L)	Below 0.013
Surfer content (ppm)	19
Aromatic compound content (Vol %)	19.7
Benzene content (Vol %)	0.4
Olefin content (Vol %)	14.5
Oxygen content (wt %)	2.05
Methanol content (wt %)	Below 0.1

Table 3.2 The properties of TRF surrogate fuel

Item	Value
RON	87
MON	82
Density (g/cm3 at 15°C)	730.4
Lower heating value (MJ/kg)	44.03

Chapter 4. Combustion Model for LES

In SI engines, it is well known that the turbulent flame propagation is a comprehensive phenomenon which is affected by the thermo-chemical reaction of the air-fuel mixture and turbulent flow [45]. The laminar burning velocity is a pure propagation speed of chemical reactions. Therefore, it is a fuel property. Many researches have been conducted to measure the laminar burning velocity of pure hydrocarbons and develop the chemical mechanisms. Turbulence also affects the flame propagation by a convection, a kinematic interaction between turbulent eddies and the laminar flame, and an increase of scalar mixing. Therefore, the laminar burning velocity and the interaction between chemical reaction and turbulent flow are key role to predict the turbulent flame propagation.

In this chapter, the combustion model is described. At first, the laminar burning velocity is introduced based on literature review. Secondly, the G-equation model considering the characteristic of LES is described. Finally, the turbulent burning velocity for LES is illustrated.

4.1 The Laminar Burning Velocity

4.1.1 Literature Review

The laminar burning velocity is a fuel property as discussed in section 3.1.1. Many chemical mechanisms have been proposed to predict the laminar burning velocity of the gasoline surrogate fuel: detailed or semi-detailed mechanisms [88-90] and reduced mechanism [91]. However, these mechanisms have too many species and reactions to apply on the 3D engine simulation due to enormous

computational cost. Therefore, empirical (or semi) empirical correlation of the laminar burning velocity has been proposed [92]. The simplest and widely used form of empirical correlation is a function of the unstretched laminar burning velocity, temperature, pressure and residual gas fraction as equation (4.1.1).

$$s_L = s_{L,0}(T/T_0)^{\alpha}(P/P_0)^{\beta}(1-\gamma Y_{dil}) \quad (4.1.1)$$

Where, s_L: laminar burning velocity

$s_{L,0}$: unstreched laminar burning velocity

T_0: reference temperature

P_0: reference pressure

α: coefficient of temperature dependency

β: coefficient of pressure dependency

γ: coefficient of residual gas effect

Y_{dil}: residual gas fraction

The formulation of the unstreched laminar burning velocity and coefficients of temperature, pressure and residual gas dependency were based on the experimental or numerical researches [92-94].

Gulder [92] proposed a semi-empirical correlation of various pure hydrocarbons and binary mixtures. However, they were verified at low temperature (less than 600 K). Metgalchi and Keck [93] also developed correlation for methanol, iso-octane and indolene at high pressure and temperature. But, a single hydrocarbon has a limitation that it cannot satisfy the wide range of

engine operation conditions. Yang and Reitz [94] suggested an empirical correlation of various the PRF mixtures based on the experimental data and integrated the correlation with the G-equation combustion model for an engine simulation. However, its limitation is also that the correlation is based on the PRF. There are two experimental [95] and numerical [96] researches about the validation between the laminar flame speed of the PRF and real gasoline. While the PRF shows good agreement with real gasoline in their works, there is still a deviation with real gasoline under stoichiometric and rich mixtures.

To overcome the limitation of the PRF, many works with additional hydrocarbon (toluene), the TRF, have been conducted. Mannaa et al. [97] conducted experimental study on the laminar burning velocity of the PRF, the TRF and the real gasoline under various RON. In their work, the laminar burning velocity of TRF shows better agreement with gasoline result. Sileghem et al. [98] investigated the TRF mechanism to compare with the laminar flame speed of gasoline. The authors obtained the composition of a mixture of iso-octane, n-heptane and toluene by a mixing rule. Liao and Roberts [99] measured the laminar burning velocity of various compositions of the TRF with the flat flame method. The TRF results retains the satisfactory agreement and it is found that the deviation among various compositions of the TRF is negligible. Kim and Min [100] developed a new correlation using an energy fraction-based mixing rule approach. The correlations were derived for each surrogate fuel component with consideration for the effect of temperature, pressure and diluent. Because of mixing rule, the correlation can consider the various composition of the TRF. In this paper, the composition of the TRF is already determined to predict the auto-ignition phenomena. Therefore, the correlation for the laminar burning velocity is obtained by the mixing rule approach. The detailed process for the correlation is described in following section.

4.1.2 The Correlation for the Laminar Flame Speed

As aforementioned, the TRF which is composed of 54% iso-octane, 22% n-heptane and 24% toluene by liquid volume fraction is adopted as the gasoline surrogate fuel in this study. The correlation of the laminar burning velocity for the surrogate fuel is determined by mixing-rule approach[100]. In general, the mixing rule is described as equation (4.1.2).

$$s_{L,blend} = \sum_{i=1}^{n} \alpha_i s_{L,i} \tag{4.1.2}$$

Where, $s_{L,blend}$: the laminar burning velocity of surrogate fuel

$s_{L,i}$: the laminar burning velocity of each component

i: ith fuel component

α_i: blending factor of ith fuel component

The energy fraction-based mixing rule is used to calculate blend factor as equation (4.1.3).

$$\alpha_i = \frac{\Delta H_{c,i} x_i}{\sum_{i=1}^{n} \Delta H_{c,i} x_i} \tag{4.1.3}$$

Where, $\Delta H_{c,i}$: the heat of combustion

x_i: the mole fraction

Then, the correlation of the laminar burning velocity for each component follows the basic form as equation (4.1.1) and residual gas effect is neglected. The reference temperature and pressure are 600 K and 5 bar, respectively. An algebraic

equation is introduced to reproduce the unstretched laminar burning velocity of each component as equation (4.1.4)

$$s_{L,0,i} = a_i\left[1 - exp\{b_i(\phi - \phi_m)\} - exp\{\{-\xi(\phi - \phi_m)\}\} + \xi(\phi - \phi_t)^2\right] \quad (4.1.4)$$

Where, ϕ: equivalence ratio

$a_i,\ b_i,\ \phi_m,\ \phi_t,\ \xi$: model constants

The model constants are listed in Table 4.1.

The coefficients of temperature and pressure dependency are function of equivalence ratio. The coefficients are curve-fitted with a fifth-order polynomial as equations (4.1.5) and (4.1.6), respectively, and the temperature range is divided into low and high temperature regime.

$$\alpha(\phi) = \sum_{j=0}^{5} A_j \phi \quad (4.1.5)$$

$$\beta(\phi) = \sum_{j=0}^{5} B_j \phi \quad (4.1.6)$$

Where, A_j: coefficients of temperature dependency

B_j: coefficients of pressure dependency

The coefficients for polynomial equation are listed in Table 4.2 and 4.3.

Finally, the laminar burning velocity of the surrogate fuel with consideration of residual gas effect is obtained with determined component ratio of the TRF as equation (4.1.7).

$$s_L = \sum_{i=1}^{n} \alpha_i s_{L,i}\,(1 - \gamma Y_{dil}) \quad (4.1.7)$$

The laminar burning velocity under various conditions is verified against the measurement data from various literatures as Figures 4.1-4.3. The component of gasoline varies according to the crude oil origin and the refining process. In European Union, the aromatic content of commercial gasoline is limited under 35% of volume fraction. While, in South Korea, the content of aromatic is regulated that it does not exceed 22% of volume fraction. Thus, the laminar burning velocity of Korean gasoline may be faster than literature sources. Considering the difference, it is found that the laminar burning velocity of the surrogate fuel is well matched with that of real gasoline.

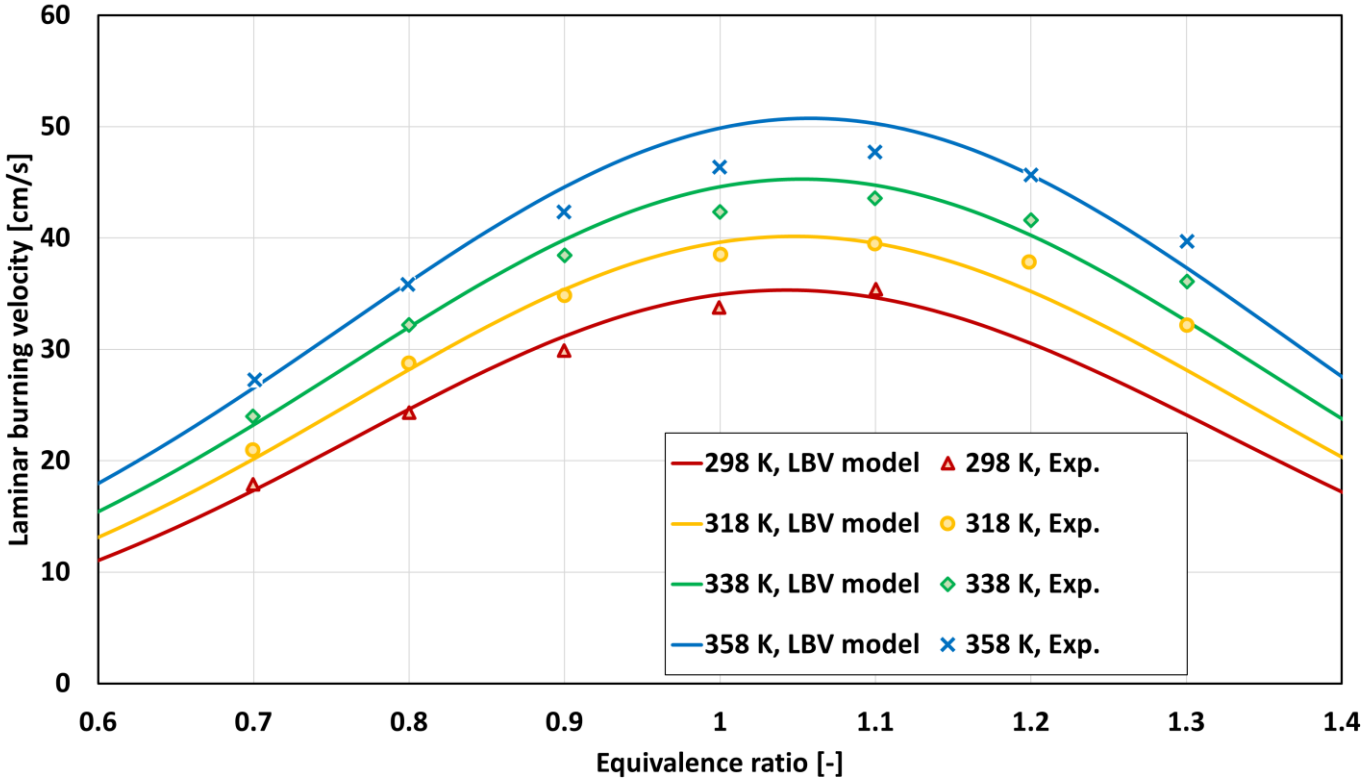

Figure 4.1 Validation of LBV model of this study (line) against the measurement data from literature source (symbol): Sileghem et al. @ p=1atm [98]

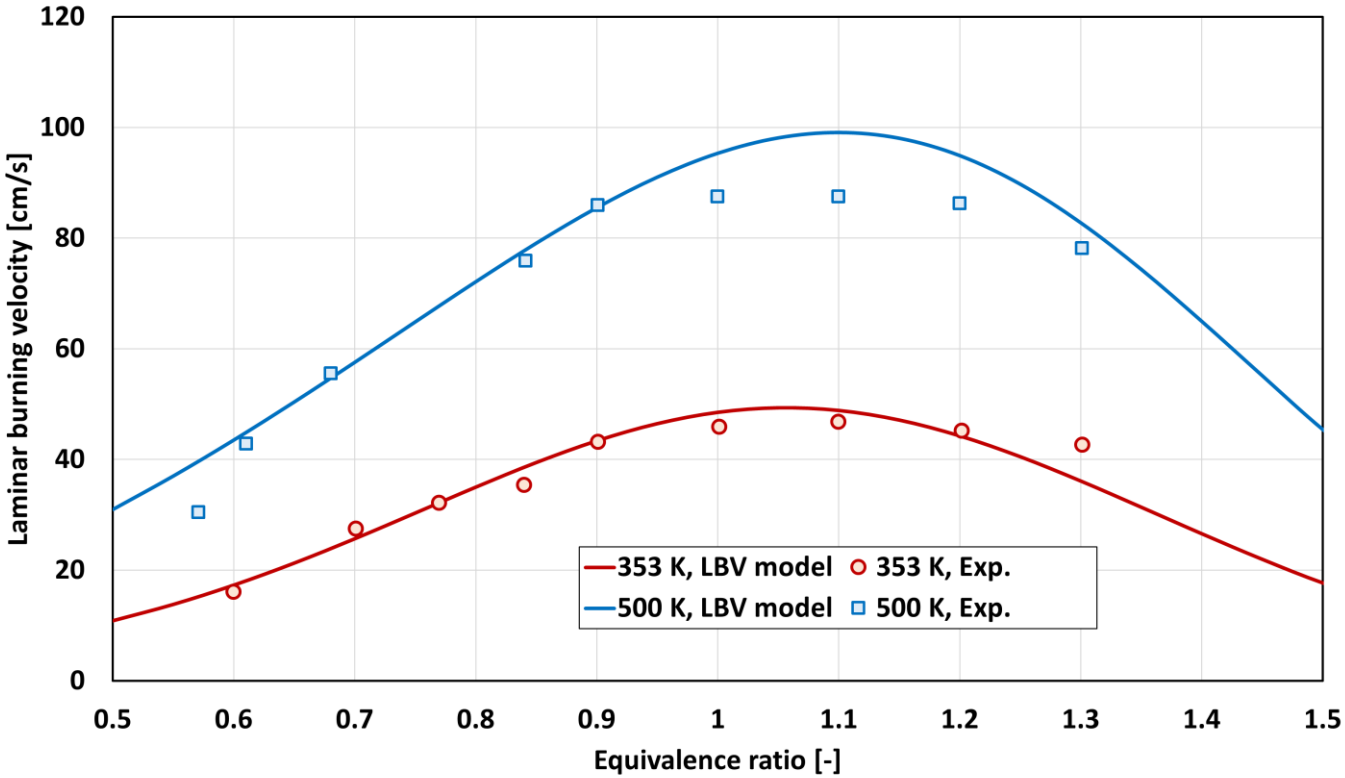

Figure 4.2 Validation of LBV model of this study (line) against the measurement data from literature source (symbol): Zhao et al. @ p=1 bar [95]

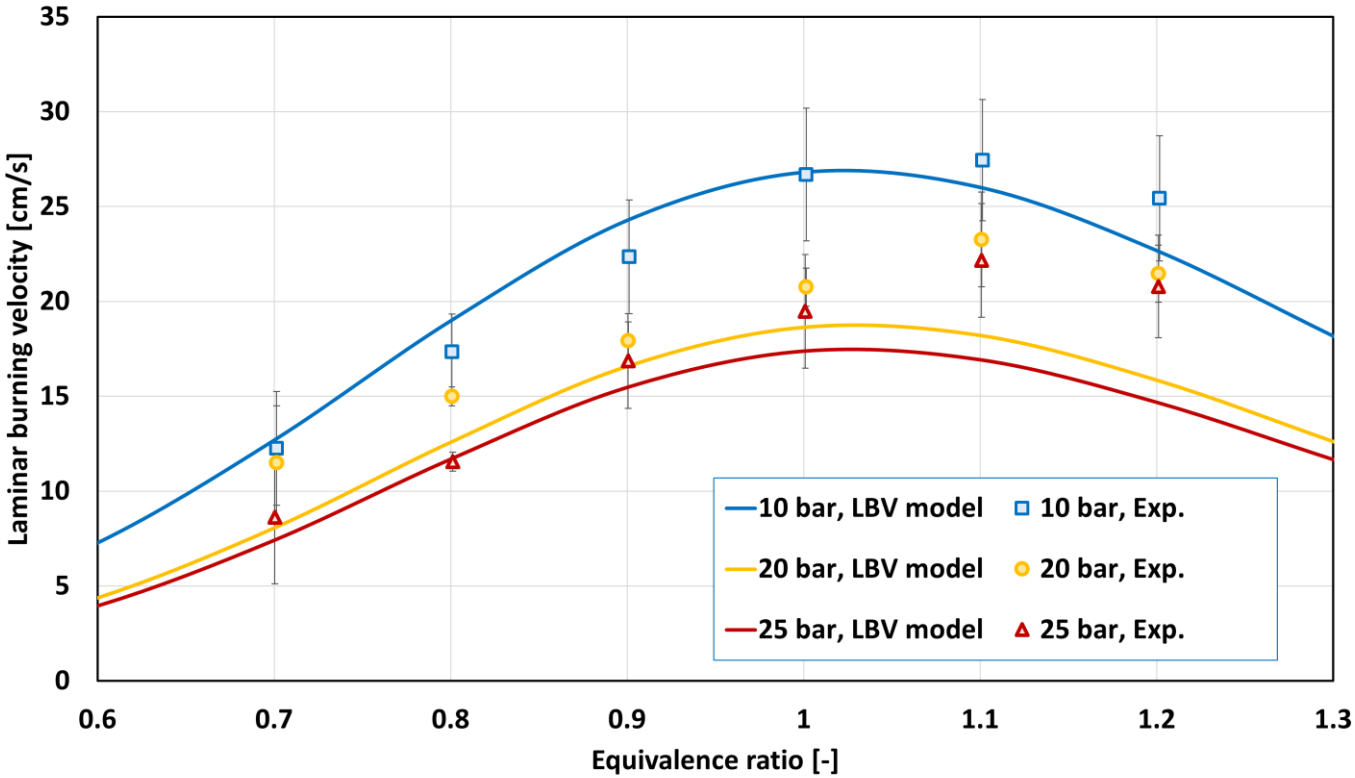

Figure 4.3 Validation of LBV model of this study (line) against the measurement data from literature source (symbol): Jerzembeck et al. @ T_u=373K [96]

Table 4.1 The model constants for laminar burning velocity

	iso-octane	n-heptane	Toluene
a_i	2.25	2.5	2.35
b_i	1.95	1.9	2
ϕ_m	1.1		
ϕ_t	1.5 (if ϕ>1.5, otherwise 0)		
ξ	9		

Table 4.2 Coefficients for fitting temperature dependence, $\alpha_i(\phi) = \sum_{j=0}^{5} A_{i,j}\phi^i$

$\alpha_i(\phi)$	$A_{i,0}$	$A_{i,1}$	$A_{i,2}$	$A_{i,3}$	$A_{i,4}$	$A_{i,5}$
High temperature regime (600-900 K)						
iso-octane	-2.564	40.879	-94.888	92.663	-40.318	6.488
n-heptane	6.253	-3.876	-8.627	13.795	-6.094	0.818
toluene	1.450	16.212	-40.638	37.634	-14.632	1.892
Low temperature regime (400-600 K)						
iso-octane	-0.610	29.461	-75.525	78.128	-35.367	5.856
n-heptane	2.368	14.331	-45.612	50.307	-23.321	3.901
toluene	0.105	24.815	-63.708	64.374	-28.146	4.469

Table 4.3 Coefficients for fitting pressure dependence, $\boldsymbol{\beta}_i(\phi) = \sum_{j=0}^{5} B_{i,j}\phi^i$

$\beta_i(\phi)$	$\mathbf{B}_{i,0}$	$\mathbf{B}_{i,1}$	$\mathbf{B}_{i,2}$	$\mathbf{B}_{i,3}$	$\mathbf{B}_{i,4}$	$\mathbf{B}_{i,5}$
iso-octane	-1.299	0.601	5.019	-8.817	5.203	-1.024
n-heptane	-0.954	-1.319	8.365	-11.400	6.147	-1.161
toluene	0.135	-6.040	16.668	-18.303	8.776	-1.527

4.2 G-equation Model for LES

The flame propagation is occurred with an interaction of transport processes and chemical reaction within the flame front. In the flamelet models, these processes are expressed by the flame front as a thin flame sheet propagating with the laminar burning velocity. Williams [101] first introduced a level set approach, so called the G-equation, based on the flamelet model to reproduce the behavior of the flame front. The flame front is defined by the iso-surface of non-reacting scalar G. The scalar G is defined that the flame front position is at $G = G_0$, the unburned region is in $G < G_0$ and the burned region is in $G > G_0$. Peters [45] developed the formulation based on the Reynolds-averaged approach for the corrugated flamelets and the thin reaction zone regimes. Pitsch [67] proposed the spatially filtered G-equation for LES. For the sake of brevity, the derivation procedure is briefly introduced in this study and the detailed information is referred to the original publication [67]. Prior to using the filtered g-equation model proposed by Pitsch, the combustion regime of the target engine was investigated as shown in Figure 4.4. RANS approach was used to simulate the combustion in the SI engine under the operating condition of the target engine described in the chapter 6. The numerical setup is shown in Table 4.4. According to the result, the combustion regime of the target engine condition is under the corrugated flamelets regime. Therefore, the filtered G equation for the corrugated flamelets is derived as equation (4.2.1).

$$\frac{\partial \check{G}}{\partial t} + \hat{v} \cdot \nabla \check{G} = -\widehat{S_L \boldsymbol{n}} \cdot \nabla \check{G} \qquad (4.2.1)$$

Where, $\widehat{G}$: the filtered flame front location

$\hat{V}$:the filtered velocity

S_L:the flame propagation term for the corrugated flamelets regime

n:the normal vector of the filtered flame front position

The flame propagation term for the corrugated flamelets regime $\widehat{s_L \boldsymbol{n}}$ can be modeled by the filtered laminar burning velocity $\widehat{s_L}$ and the sub-filter turbulent burning velocity s_T as equation (4.2.2).

$$\widehat{S_L \boldsymbol{n}} = \left(\widehat{S_L} + S_T\right)\boldsymbol{n} \tag{4.2.2}$$

The sub-filter turbulent burning velocity is described in the next section.

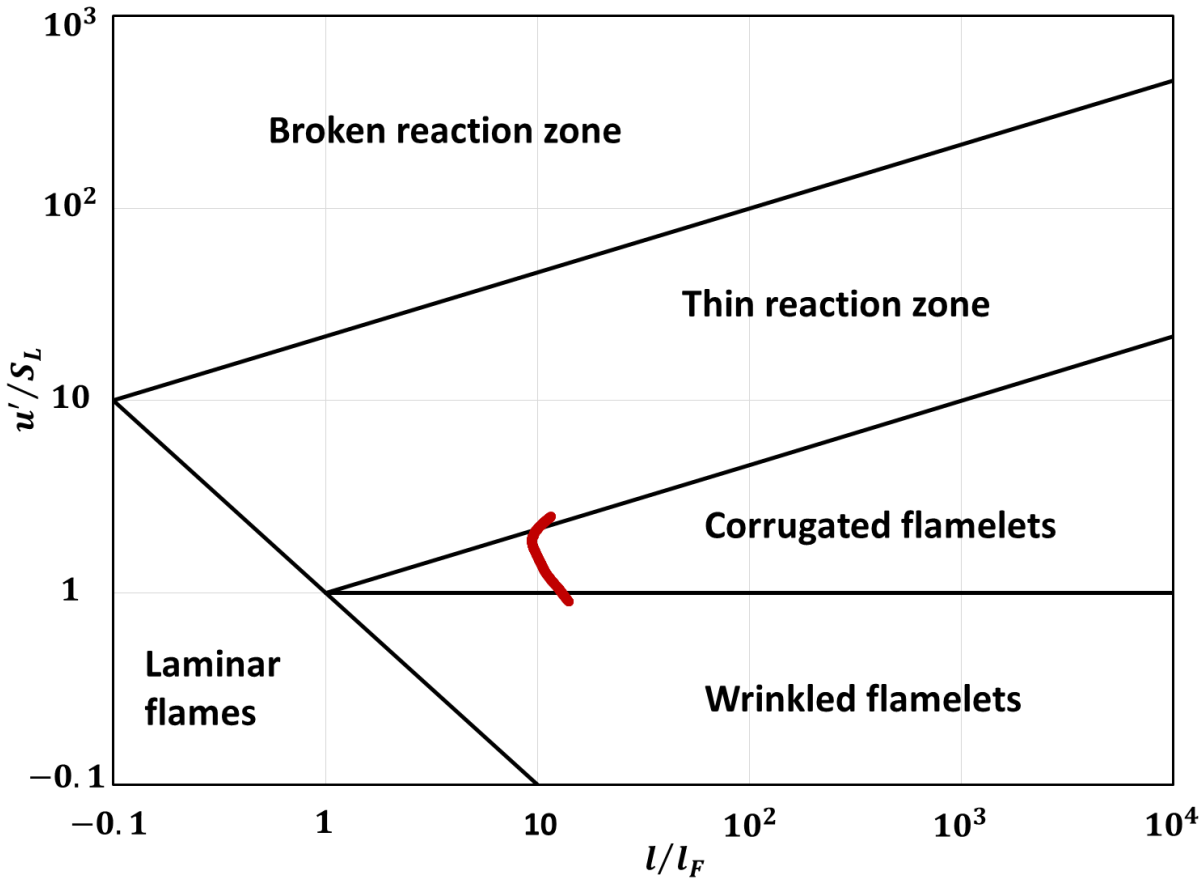

Figure 4.4 Regime diagram for premixed turbulent combustion

Table 4.4 The numerical setup of RANS approach

Parameter	Specification
Turbulent model	k-epsilon / RNG
Combustion model	G-equation (Level-set)
Ignition model	Single flame kernel model
Wall model	Standard wall function
Heat transfer model	GruMo-UniMORE
Fuel	TRF surrogate fuel

4.3 Sub-filter Turbulent Burning Velocity

The sub-filter turbulent burning velocity is derived from the sub-filter flame front fluctuations l [67]. For the sake of brevity, the derivation procedure is briefly introduced in this study and the detailed derivation procedure is described in the original publication [67]. The sub-filter flame front fluctuation is determined by the distance of the instantaneous to the filtered flame front as equation (4.3.1) and is schematically shown in Figure 4.5.

$$l = |\mathbf{l}| \text{ with } \mathbf{l} = x_f - \widehat{x_f} \tag{4.3.1}$$

A transport equation for the sub-filter flame front fluctuation is derived by the difference of the displacement speed between the instantaneous flame front and the filtered flame front as equation (4.3.2).

$$\frac{dl}{dt} = \frac{dx_f}{dt} - \widehat{\frac{dx_f}{dt}} \tag{4.3.2}$$

The equation (4.3.2) can be described with the kinematic restoration term and the scalar dissipation term as equation (4.3.3).

$$\frac{dl}{dt} = v - \hat{v} + S_L n - \widehat{S_L n} \tag{4.3.3}$$

The length scale of the sub-filter flame front fluctuation can be derived by multiplying equation (4.3.3) with $\mathbf{l}$ and applying the filtering operation as equation (4.3.4).

$$\widehat{\frac{dl^2}{dt}} = 2\widehat{l \cdot v'} + 2l \cdot \widehat{(S_L \boldsymbol{n})}' \tag{4.3.4}$$

The first term on the right-hand side means the production of flame front wrinkling due to turbulence. The second term describes the flame surface dissipation due to the flame propagation. The production term can be defined as equation (4.3.5).

$$\mathbf{l}\cdot\widehat{\dot{u}} = C_1 C_s \Delta u'_\Delta \tag{4.3.5}$$

Where, c_1: model coefficient

c_s: Smagorinsky constant

Δ: filter size

u'_Δ: SGS velocity

The flame surface dissipation term can be modeled as equation (4.3.6).

$$\mathbf{l}\cdot\widehat{(s_L\boldsymbol{n})}' = -c_2 c_s \Delta s_T \tag{4.3.6}$$

Substituting equation (4.3.5) and (4.3.6) into equation (4.3.4), and assuming that production term equals dissipation terms, equation (4.3.7) can be obtained.

$$S_T = \frac{c_1}{c_2} u'_\Delta \tag{4.3.7}$$

The constants for the equation can be replaced as equation (4.3.8).

$$\frac{c_1}{c_2} = b_1 \tag{4.3.8}$$

Where, b_1 the model constant

Finally, the sub-filter turbulent burning velocity can be written as equation (4.3.9).

$$\frac{S_T}{S_L} = b_1 \frac{u'_\Delta}{S_L} \tag{4.3.9}$$

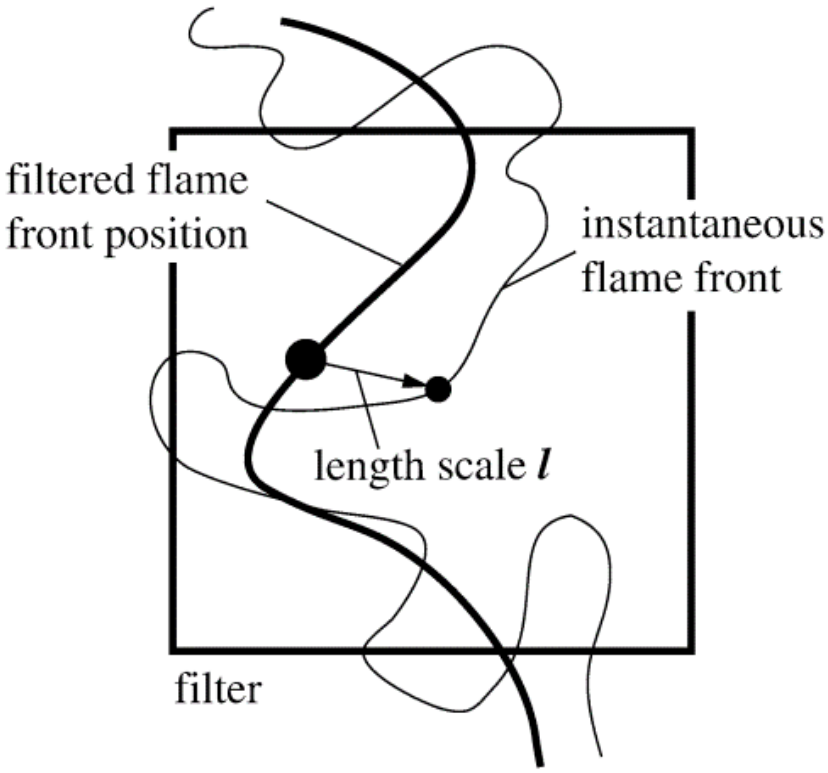

Figure 4.5 Instantaneous and filtered flame front position [67]

Chapter 5. Lagrangian Ignition Model

5.1 Literature Review

The spark ignition process is a very complicated phenomenon in which many different physical processes, such as electric circuit, chemical reaction and interaction of ignition channel and turbulent flow, take place within a short time. The spark ignition process is divided into three phases as shown in Figure 5.1 [102]: the breakdown phase, the arc phase and the glow discharge phase. During the breakdown phase, the voltage rapidly increases up to ~10kV and the current is about 200 A. The spark channel with a diameter of about 40μm and a temperature of about 60,000K is generated. The gas molecules in the channel are fully dissociated and ionized. The duration of the breakdown phase is very short, from 1 to 10 ns. As soon as the breakdown phase is over, the arc phase follows. The arc phase is characterized by very low voltage (<100V) due to voltage drop and high current. And small portion of gases are ionized, but dissociation is quite high in the central region of channel. The spark channel expands due to heat conduction and mass diffusion. Due to the heat loss to anode, cathode and surrounding gases, the temperature is decreases to 6,000K. The arc phase lasts in μs. The voltage increases to 300 to 500V and the current decreases to less than 200mA, moving over to the glow discharge phase. The characteristic of glow discharge phase is very similar with the arc phase. Due to the larger heat loss than the arc phase, the temperature of spark channel is about 3,000K. Due to the long duration (~ms) of glow discharge phase, most of the spark energy is transferred to the surrounding gases during this phase. The detailed characteristics of spark ignition process depends on the spark ignition system and surrounding gas condition. In the 3D simulation for the ICE, the spark ignition process is very

complicated and short duration. Therefore, most ignition models have been modeled by simplifying physical phenomena after the breakdown phase. The description of typical ignition models is followed.

The discrete particle ignition kernel model (DPIK) that was first developed by Fan et al. [103], is a spark ignition model that considers only one single flame kernel. The lagrangian particles are adopted to reflect the local condition at the flame surface of spherical single flame kernel. The particles expand in the radial direction by turbulent velocity and laminar flame speed. In this model, the breakdown, the spark-channel and the deflection of the spark-channel are not taken into account. Therefore, there is a limitation that the ignition simulation in the DPIK model cannot reflect the spark channel elongation by flow field.

Duclos et al. [104] proposed the arc and kernel tracking ignition model (AKTIM). The secondary electric circuit model is adopted to simulate the electrical energy for the spark ignition. To reflect the flow effect on the flame kernel, a set of lagrangian particles are generated between the electrodes. Unlike the DPIK, each of particles represents the gravity center of the flame kernel. The flame kernel propagation takes place as soon as an ignition spot has been formed. However, the model does not take into account the thermal expansion, mainly occurred during the arc phase.

The spark-channel ignition monitoring model (SparkCIMM), derived by Dahms et al. [105, 106], simulates the spark ignition process for a wide range of conditions. The model describes the spark channel dynamics using lagrangian particles. A set of lagrangian particles represents the spark channel like the AKTIM. The flamelet equations are adopted to evaluate the local ignitibility. If the kernels meet the criteria of ignitibility, quasi-spherical flame kernels are launched at the position of the spark channel and the kernels grow by chemical reactions. When the surface of the flame kernels can be resolved on the

computational grid, the particle tracking model is deactivated and the level-set approach is used to simulate the transportation of the mean turbulent flame front. This model reflects the local characteristics of spark channel, but it is a quite complicated and developed for RANS approach.

These introduced ignition models generally successfully realize ignition phenomena in RANS approach. In LES, however, the way to define turbulence is different from RANS, so it is difficult to use the introduced ignition model directly in LES approach. The imposed stretch spark ignition model for LES (ISSIM-LES) is suggested by Colin et al. [107]. This model is based on the same electrical circuit description as the AKTIM [104] and allows multi-ignition description without any ad hoc adaptation since the different ignitions are directly controlled by the flame surface density (FSD) equation, which is modified during early flame ignition. However, this model is suitable for the extended coherent flame model (ECFM) combustion model and requires a suitable LES ignition model for the G-equation.

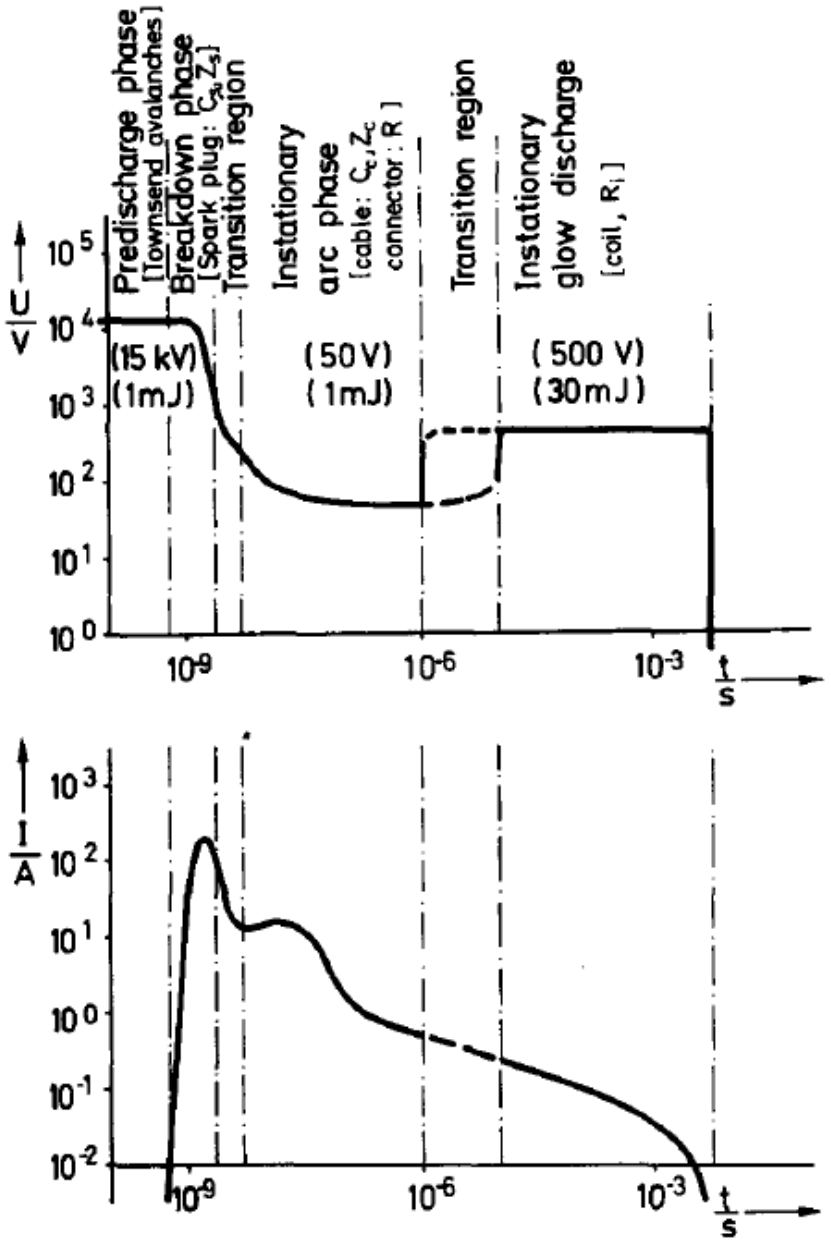

Figure 5.1 Schematic diagram of voltage and current of typical ignition system as functions of discharge time [102]

5.2 Modeling of Ignition

In the present study, lagrangian concept of ignition model is adopted to predict the initial stage of the combustion process in a spark-ignition engine. The spark-channel is initially represented by a set of lagrangian particles that are initially placed along a line between the two electrodes. Particles are convected by mean and turbulent flow and flame kernel grows simultaneously. Specific sub-models are implement to reproduce the ignition phenomenon. The sub-models are:

1. Initialization of particles (spark channel): A set of lagrangian parcels represents the spark channel.

2. Channel elongation: Particles are convected by mean and turbulent flow.

3. Electric circuit: The electrical energy is calculated by the secondary electric circuit model.

4. Plasma channel expansion: After the breakdown phase, the spark channel grows by the thermal diffusion.

5. Spark channel development: The ignition channel is developed by chemical reactions.

6. Restrike: Restrike is reproduced by the secondary electric circuit model.

7. Transition between the ignition model and the flame propagation.

5.2.1 Initialization of Particles

Among the three characteristic stages of ignition in SI engines, namely the breakdown, the arc and the glow discharge, only the last two are modeled because of the very short duration (~ns) of the breakdown phase. At ignition timing, the set of lagrangian particles are generated along the spark-gap centerline. In this study, ten particles are generated and a particle is added if the distance between neighboring two particles exceed 0.2 mm. The initial temperature and the diameter of the particles are estimated the following equations (5.2.1) and (5.2.2) [108, 109]. The breakdown temperature, T_{bd}, is 60,000 K suggested by Refael et al. [109] and the plasma channel specific heat ratio, *k*, is equal to 1.66. The breakdown energy is computed by the electrical circuit model and it will be explained further in detail.

$$T_i = \left[\frac{1}{k}\left(\frac{T_{bd}}{T_u} - 1\right) + 1\right] T_u \tag{5.2.1}$$

$$d_i = 2\left[\frac{k-1}{k}\frac{E_{bd}}{p d_{gap}\left(1-\frac{T_u}{T_i}\right)\pi}\right]^{1/2} \tag{5.2.2}$$

Where, T_u: unburned temperature

. T_{bd}: breakdown temperature

k: plasma channel specific heat ratio

E_{bd}: breakdown energy

d_{gap}: length of spark plug gap

5.2.2 Channel elongation

The motion of the spark channel, including the turbulent stretch and wrinkle effect, is modeled by the following convection equation solved for each representative lagrangian particle, p. The indices (p) and (cell) refer to the particle and to the computational grid cell value, respectively. The SGS turbulent velocity is denoted by u'_{SGS}. $x_{p,cell}$ is the local distance vector between the particle location and the corresponding grid cell center. $\widetilde{\ }$ indicates the sub-filtered value and $\overrightarrow{\ }$ denotes the vector. The rand-operator provides a random number between [-1, 1] to reflect the SGS turbulent velocity effect.

$$\widetilde{\overrightarrow{u_p}} = \widetilde{\overrightarrow{u_{cell}}} + \nabla\widetilde{\overrightarrow{u_{cell}}} \cdot \Delta\overrightarrow{x_{p,cell}} + \left(\widetilde{u'_{sgs}} + \nabla\widetilde{u'_{sgs}} \cdot \Delta\overrightarrow{x_{p,cell}}\right) \cdot sign(rand) \tag{5.2.3}$$

5.2.3 Electric circuit model

The energy transferred from the electrical circuit to the gas phase might affect significantly the flame kernel development. For this reason, the effects of electrical circuit on the flame kernel growth process need to be taken into account. Generally, the electric system of the spark plug is composed by the primary and the secondary circuit [104, 110], as illustrated in Figure 5.2.

The energy is sufficiently stored in the primary inductance before ignition timing. Therefore, only the secondary electric circuit is modeled in detail. In fact, the known amount of energy stored in the primary circuit at spark time is transferred to the secondary circuit as shown in equation (5.2.4).

$$E'_S = C_{eff} E_p \tag{5.2.4}$$

Where, E_S': initial secondary electric circuit energy for the breakdown phase

E_p: primary electric circuit energy

C_{eff}: transmission coefficient

Here, the transmission coefficient models the secondary inductance dissipation during the energy transfer from the primary to the secondary circuit and 0.6 was estimated by Duclos et al. [104]. Due to the very short duration of the breakdown phase, the breakdown phase effect is considered only as an initial condition of arc phase. The breakdown energy is calculated by equation (5.2.5) [111].

$$E_{bd} = \frac{V_{bd}^2}{C_{bd}^2 d_{gap}} \tag{5.2.5}$$

Where, E_{bd}: breakdown energy

V_{bd}: breakdown voltage [kV]

C_{bd}: breakdown constant [kV]

d_{gap}: inter-electrode distance [mm]

The breakdown voltage is computed as follows

$$V_{bd} = \mathrm{a} + \mathrm{b}\frac{p}{T_u} + c\frac{p}{T_u} d_{gap} \tag{5.2.6}$$

as reported in [111], the coefficient values of equation (5.2.6) are the following: a = 4.3 kV , b = 136 (kV·K)/bar and c = 324 (kV·K)/(bar·mm).

Consequently, the secondary circuit energy, E_s, at the beginning of the arc phase is obtained from equations (5.2.4) and (5.2.5) as

$$E_s = E_S' - E_{bd} \tag{5.2.7}$$

The time variation of secondary circuit energy is calculated as equation (5.2.5)

$$\frac{dE_S(t)}{dt} = -R_S i_S^2(t) - V_{IE}(t) i_S(t) \tag{5.2.8}$$

Where, R_S: Resistance of secondary electric circuit

i_S: current of secondary electric circuit

V_{IE}: voltage between the electrodes

The current of secondary electric circuit and the voltage between the electrodes are time-dependent parameters computed at each time-step as

$$i_S(t) = \sqrt{\frac{2E_S(t)}{L_S}} \tag{5.2.9}$$

$$V_{IE}(t) = V_{cf} + V_{af} + V_{gc}(t) \tag{5.2.10}$$

Where, L_S: impedance of the secondary electric circuit

V_{cf}: cathode voltage fall, 252 [V] [112]

V_{af}: anode voltage fall, 8.45 [V] [112]

V_{gc}: gas-column voltage fall [V]

The gas-column voltage fall is obtained as below equation.

$$V_{gc}(t) = a_{gc} l_{spk}(t) i_S^{b_{gc}}(t) p^{c_{gc}} \quad (5.2.11)$$

with the spark channel length (l_{spk}) in mm, the pressure (p) in bar and the coefficients (a_{gc} = 6.31, b_{gc}=-0.75 and c_{gc} = 0.51) for the glow discharge phase.

The spark discharging energy from the secondary electric circuit to the mixture gas is estimated as following equation (5.2.12) [104].

$$\dot{Q}_{spk} = \eta_{eff} V_{gc}(t) i_S(t) \quad (5.2.12)$$

During the spark discharge, there is heat loss to the electrodes. Therefore, the efficiency of the energy transfer process from the electrical circuit to the mixture gases is estimated as following equation (5.2.13) [110, 113].

$$\eta_{eff} = \eta_0 + \frac{(\eta_\infty - \eta_0) U^3}{A + U^3} \quad (5.2.13)$$

Where, η_0: energy transfer efficiency under quiescent mixture condition, η_0=8

η_∞: energy transfer efficiency under high velocity flow condition, η_∞=30

A: constant coefficient, 700 [m^3/s^3] for the glow discharge phase

U: average velocity at which channel is located

The spark discharge is maintained until the secondary circuit energy (E_s) reaches 0.

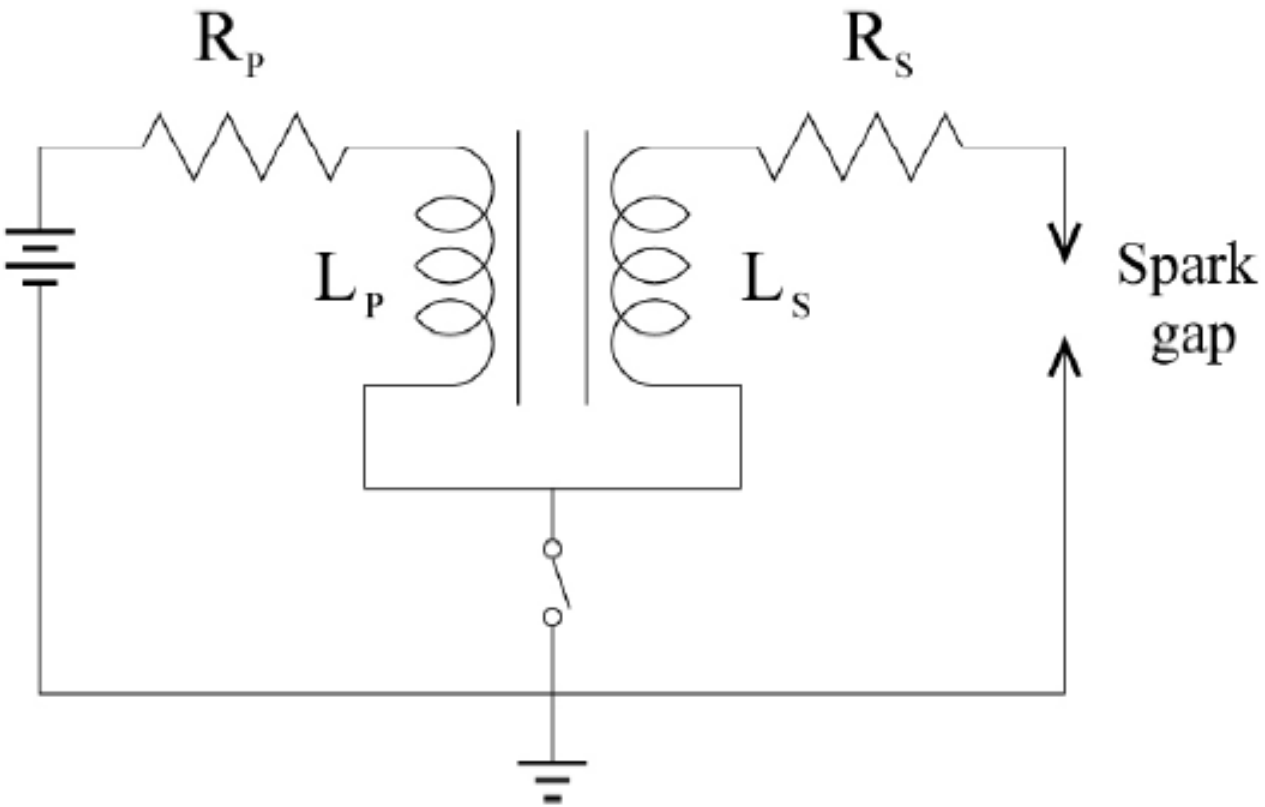

Figure 5.2 Schematic of primary and secondary electric circuit [110]

5.2.4 Plasma channel expansion.

After the breakdown phase, the initial temperature and the radius of the spark channel are obtained by equations (5.2.1) and (5.2.2). Although slightly different depending on the ambient temperature and pressure, the initial temperature and radius are about 40,000K and 0.2mm. When the temperature is high, generally $T_p > 3T_{ad}$, the heat conduction from the hot plasma channel to the unburnt mixture is important and expansion due to chemical reactions and heat transfer from the electric circuit is neglected [110]. Until the channel temperature remains higher than $3T_{ad}$, the plasma channel temperature is computed by solving the heat conduction equation as below equation (5.2.14) [113].

$$\frac{\partial T_{pl}}{\partial t} = \alpha \cdot \nabla^2 T_{pl} + \frac{\dot{Q}_{spk}}{\rho_{pl} \cdot c_{p,pl} \cdot V_{pl}} \tag{5.2.14}$$

Where, T_{pl}: plasma channel temperature

α: plasma thermal diffusivity

$\dot{Q}_{spk}$: spark discharging energy

ρ_{pl}: density under plasma

$c_{p,pl}$: specific heat under plasma

V_{pl}: volume of plasma channel

A sub-cycling procedure (Δt < 0.1 ns) between CFD iterations is used to solve equation (5.2.14). The domain is discretized on a 1D, axisymmetric grid representing the mixture gas region that surrounds the spark electrodes. The grid height is set to be equal to the distance between the electrodes, while the radial

length of the computational domain is set to 10 mm, which is sufficiently longer than the maximum diameter of the plasma channel that is reached during arc phase. The grid size is 10 μm and the following initial and boundary conditions are imposed at spark time:

$$t = t_0 : T_{pl} = T_i \; if 0 < r < r_i ; \; T_{pl} = T_u \; if \; r < r_i ; \;\; r = r_\infty : T_{pl} = T_u$$

At each time-step, the channel radius r_{ch} is identified at the location where the plasma temperature equals to the adiabatic flame temperature in the 1D domain.

The properties such as thermal diffusivity α, heat capacity $C_{p,pl}$ and density $\rho_{p,pl}$ need to be known. During the thermal expansion, the plasma temperature is very high, and dissociation of molecules and atom ionization play a very important role. These phenomena are considered by assuming chemical equilibrium and neglecting fuel contribution. In this way, the thermodynamic and transport properties functions provided by D'Angola et al. [114] are employed to calculate heat conduction equation. The heat conduction equation is solved until the temperature is below three times of adiabatic temperature ($T_{pl} < 3T_{ad}$).

Figure 5.3 shows the spatial distribution of temperature in the plasma channel calculated by 1D axisymmetric simulation. The ambient temperature is 700 K and the ambient pressure is 10 bar. Over time, the mean temperature of plasma channel decreases and the plasma channel widens to radial direction. At each given time, the r at the point where the plasma temperature $T_{pl}(r)$ equals the adiabatic temperature is the radius of the plasma channel. After about 10 μs, the mean temperature of the plasma channel is less than three times the adiabatic temperature, growth by chemical reactions is dominant rather than growth by the thermal expansion, hence the thermal expansion model is deactivated.

The plasma thermal expansion is actually a very short time (~10ms), but because of the very short time step and the small grid size of the sub-model, the required CPU time is very large. Furthermore, the plasma channel expansion model is only effected by the ambient temperature and pressure. Therefore, in this study, the required time and the radius of the ignition channel after the plasma channel expansion is calculated in advance and the database is built at the wide range of temperature (600 – 800K) and pressure (6 – 26 bar) conditions as shown in Figure5.5. Finally, the channel radius is derived from a time-based correlation function to predict the radius after the plasma thermal expansion (Arc phase).

The time when the plasma temperature is less than three times of adiabatic temperature is obtained as equation (5.2.15).

$$\mathrm{t} = t_{ref}\left(\frac{P}{P_0}\right)^{\alpha}\left(\frac{T}{T_0}\right)^{\beta} \qquad (5.2.15)$$

Where, $\alpha(P) = -6.3644e^{-5}P^2 + 3.6235e^{-2}P + 8.0157e^{-1}$

$\beta = -2$

$t_{ref=1.1939e^{-2}}\ [ms]$

At that time, the radius is obtained by below equation (5.2.16).

$$\mathrm{r} = r_{ref}\left(\frac{P}{P_0}\right)^{\alpha}\left(\frac{T}{T_0}\right)^{\beta} \qquad (5.2.16)$$

Where, $\alpha(P) = -1.0914e^{-5}P^3 + 1.8395e^{-4}P^2 + 1.1632e^{-2}P - 3.8142e^{-2}$

$\beta(T) = -1.0860e^{-3}\mathrm{T} - 5.6300e^{-2}$

$r_{ref} = 3.4232e^{-3}$ [m]

$T_0 = 700$ [K]

$P_0 = 10$ [bar]

The channel temperature is approximated by three times the adiabatic temperature.

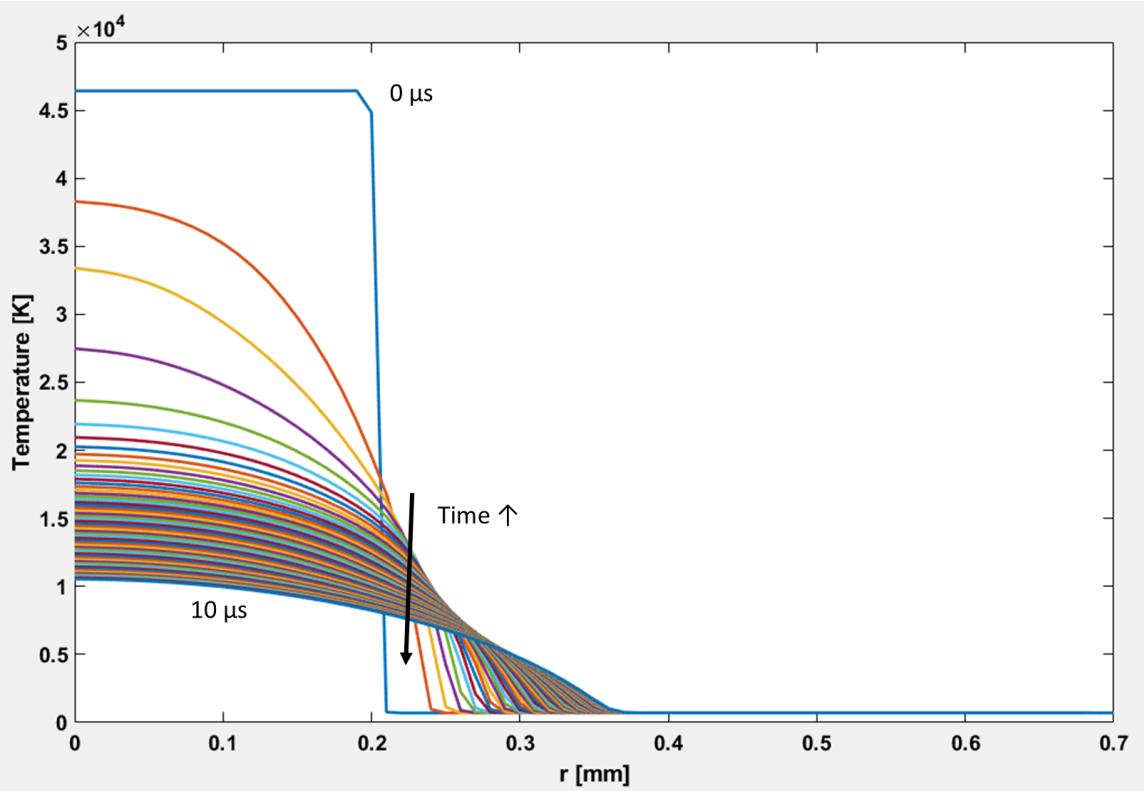

Figure 5.3 The spatial distribution of temperature in the plasma channel calculated by 1D axisymmetric simulation. The ambient temperature is 700 K and the ambient pressure is 10 bar.

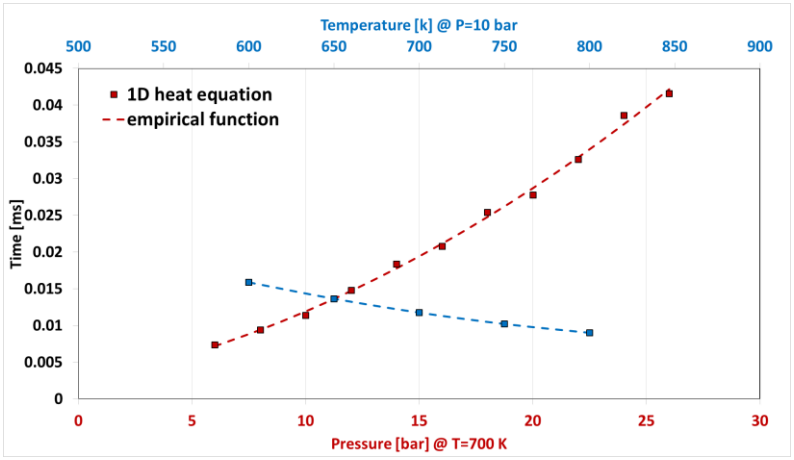

(a)

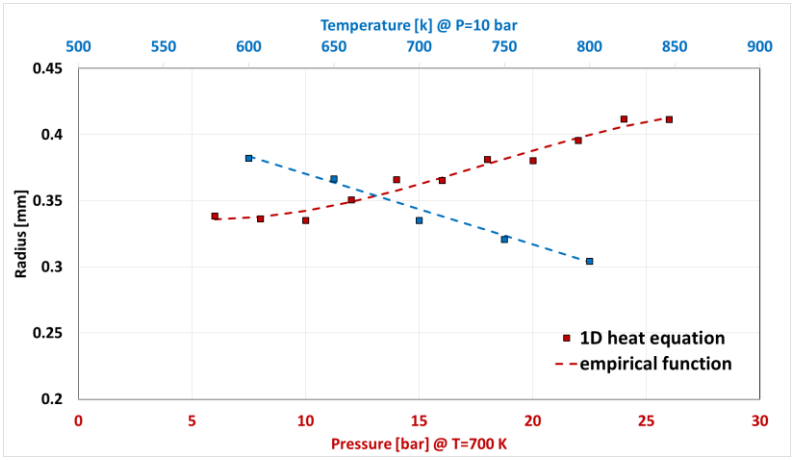

(b)

Figure 5.4 The required time for thermal expansion (arc phase) and the channel radius after thermal expansion. Dots represent the result of 1D heat conduction equation and solid lines indicate the result of empirical function. (a) The required time for thermal expansion, (b) the channel radius after thermal expansion.

5.2.5 Ignition channel development

After the plasma channel expansion, the ignition channel is developed by chemical reactions. The ignition channel is generated in a cylinder shape between the anode and the cathode of spark plug. Each lagrangian particles represents the channel location and interacts between the ignition channel and the 3D domain. The sum of the distances between particles means the length of the ignition channel. The particles are stretched by mean and turbulent flow as described in equation (5.2.1). At the same time, the ignition channel grows by chemical reactions. In this model, the properties of ignition channel are assumed uniform, thus the averaged properties in each particles represent the ignition properties.

The radius of ignition channel is calculated following

$$r_{ch} = \sqrt{\frac{m_{ch}}{\rho_{ch}\pi l_{ch}}} \tag{5.2.17}$$

Where, r_{ch}: ignition channel radius

m_{ch}: ignition channel mass

ρ_{ch}: density in the ignition channel

l_{ch}: ignition channel length

And the density in the ignition channel is obtained by equation (5.2.18)

$$\rho_{ch} = \frac{P}{R_b \cdot T_{ch}} \tag{5.2.18}$$

Where, R_b: specific gas constant of burned gas

T_{ch}: ignition channel temperature

The temperature is calculated from the following channel temperature equation:

$$\frac{d}{dt}T_{ch} = -\frac{\dot{m}_{ch}}{m_{ch}}(T_{ch} - T_{ad}) + \frac{\eta_{eff}}{m_{ch}C_p} + \frac{1}{\rho_{ch}C_p}\frac{dp}{dt} \quad (5.2.19)$$

The mass consumption rate of the ignition channel is calculated by equation (5.2.20),

$$\frac{d}{dt}m_{ch} = \dot{m}_{ch} = 2\pi r_{ch} l \rho_u S_T \quad (5.2.20)$$

The detailed description of the turbulent burning velocity is in chapter 5.2.7.

5.2.6 Restrike

The restrike is the phenomenon that when the spark channel length increase by interaction with flow, the spark channel is cut off and reformulated between the electrodes. There are two way to model the restrike. First, experimental research [115] shows that the gas-column voltage increase as the spark channel increase. If the voltage becomes greater than the breakdown voltage, the restrike occurs [110]. Secondly, if the spark channel length becomes longer than a threshold value, then the restrike occurs [105, 116]. The threshold value is determined by the experimental observation. The first way is applicable if the detailed information of spark system is provided. Otherwise, if the information is not provided sufficiently, then the second way may be an alternative. In this study, the first method is adopted with the general information of spark system from literature [14]. In this model, when the restrike occurs, the existing particles

representing the spark channel remain without the spark energy from the spark system and a new set of particles is created between the electrodes.

5.2.7 Transition between ignition and flame propagation

When the ignition channel grows by chemical reactions shortly after the plasma expansion, the flame is very thin and unstable, taking time to form a fully turbulent flame brush thickness. For modeling purposes, a one-dimensional steady planar flame is assumed. Then, the turbulent flame brush thickness is obtained as following equation (5.2.21).

$$\ell_{f,t} = b_2 \ell [1 - exp(-C_s/\tau)]^{1/2} \tag{5.2.21}$$

The detailed description is in [45]. The original equation of the turbulent flame brush thickness is derived for RANS approach. In RANS approach, the turbulent flame brush thickness is larger than grid size and takes a long time to fully develop, as the modelling term represents all length scales of turbulence. However, in LES, the turbulence scales less than the grid size (filter size) is modelled and others are resolved. Therefore, the turbulent flame thickness is smaller than the grid size and it requires a shorter time than RANS to be fully developed.

According to the equation (5.2.21), the fully developed turbulent flame brush thickness is expressed as $b_2 l$ with $b_2 = 2.0$ and l is the integral length scale [117]. Then, the normalized turbulent flame brush thickness is introduced as

$$\ell^* \equiv \ell_{f,t}/(b_2 \ell) \tag{5.2.22}$$

$$\ell^* = [1 - exp(-C_s/\tau)]^{1/2} \tag{5.2.23}$$

In the corrugated flamelets regime, the turbulent burning velocity is assumed to be independent on Damkohler number at high Damkohler number and a fully developed flame is shown in equation (5.2.24).

$$\sigma_t = b_1 v^{'} / S_L \tag{5.2.24}$$

It assumes that only small scale turbulent eddies smaller or equal to the flame brush thickness in the inertial range of the energy cascade shown in Figure 2.1 are able to effect on the flame surface. The small scale turbulent eddies are represented by the SGS turbulent length. Therefore, using a relationship of equation (5.2.25) [68], a scaling of the SGS turbulence velocity down to a given turbulent velocity scale, whose the turbulent length scale is smaller than the LES filter, in the inertial range of the turbulent energy spectrum is shown in equation (5.2.26).

$$v' \sim v_0' (l/l_0)^{1/3} \tag{5.2.25}$$

Where, v': turbulent velocity of a given eddy size l

v_0': turbulent velocity of a given eddy size l_0

$$v' = \left(l/\ell_{f,talg}\right)^{1/3} v_{\mathrm{sgs}}^{'} \tag{5.2.26}$$

Where, v': turbulent velocity of a given eddy size

$v_{\mathrm{sgs}}^{'}$: SGS turbulent velocity

l: turbulent length scale smaller than the LES filter (grid size)

$\ell_{f,talg}$: fully developed flame brush thickness resolved by grid size

Finally, the turbulent burning velocity is derived by equation (5.2.27).

$$\frac{s_T}{s_L} = b_1 \frac{u'_\Delta}{s_L} \ell^* \tag{5.2.27}$$

Here, l^* reproduce the transition state between the laminar flame propagation and the fully turbulent flame propagation. In this study, when the $(l^*)^{1/3}$ reaches 0.5, then the lagrangian ignition model is deactivated and the level-set approach is used to numerically transport the turbulent flame front.

Chapter 6. Experimental and Numerical Setup

6.1 Experimental Setup

A 0.5 L single cylinder engine equipped with the DPFI and a naturally aspirated (NA) system was used [118]. The detailed engine specifications and operating conditions are shown in table 6.1. The length of bore and stroke was 81 mm and 97 mm, respectively. The compression ratio was directly measured and it was 11.91. The engine was operated at 1500 rpm and the load was nIMEP 5.4 bar.

The schematic diagram of the engine testing system is shown in Figure 6.1. A Kistler 6056A piezoelectric pressure sensor was mounted flush in the cylinder head. AVL IndiMicro IFEM amplifier was used to amplify the in-cylinder pressure signal. A Kistler 4045A2 absolute pressure sensor was implemented in to the intake manifold to measure the intake pressure and the signal was amplified by a Kistler 4603 piezo-resistive amplifier. AVL IndiModule acquired the in-cylinder and intake pressure signals and analyzed the characteristics of combustion. Air, oil and coolant temperature were controlled by external control system. Oil pressure was controlled by an oil pump system with inverter and was supplied into the engines. A flow meter, OVAL CA001, was used to obtain fuel flow rate. Horiba MEXA-110λ and ETAS ES631.1 were used to monitor the air-fuel ratio during operation to obtain the stoichiometric condition. A Horiba MEXA-7100DEGR exhaust gas analyzer was used not only to measure emissions but also to validate the air-fuel ratio.

The K-type thermocouples were implemented to measure the head, piston and liner surface temperature [118]. The measuring points are shown in Figure

6.2. A special linkage system was developed for the reciprocating piston moving motion. The measured boundary temperatures are listed in Table 6.2 and they were used for the boundary condition of the 3D simulation.

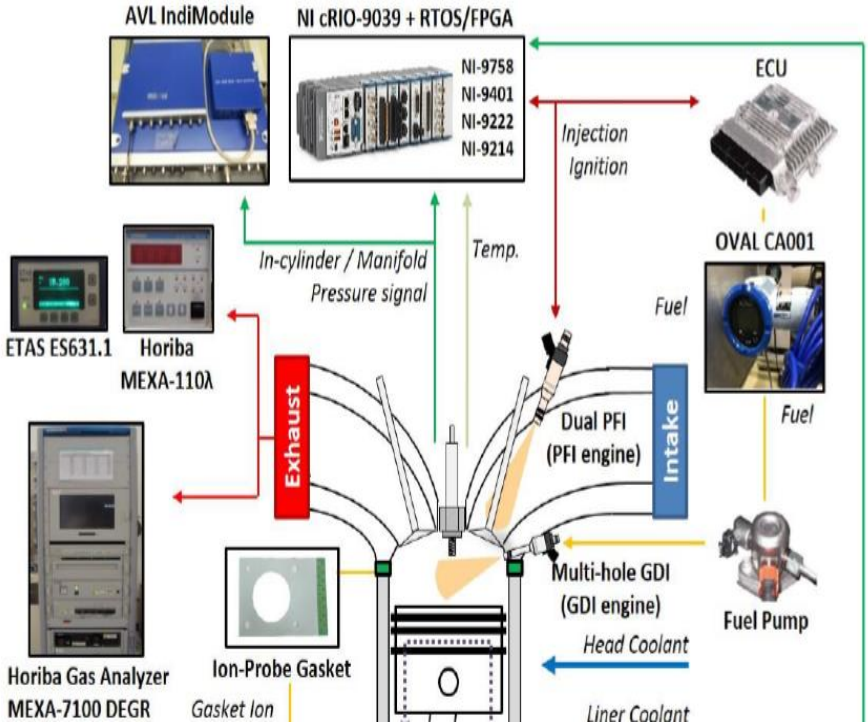

Figure 6.1 Schematic diagram of experimental system [118]

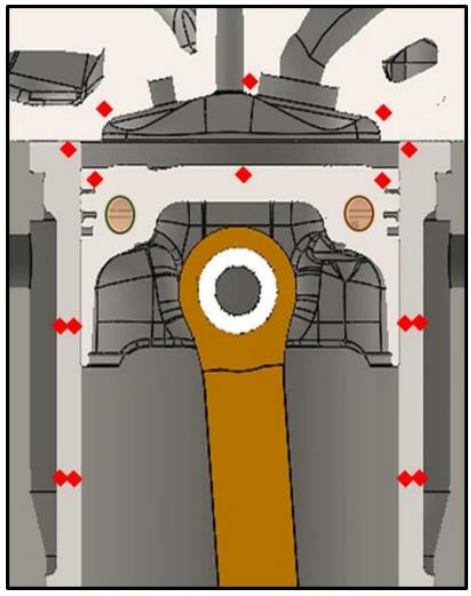

(a)

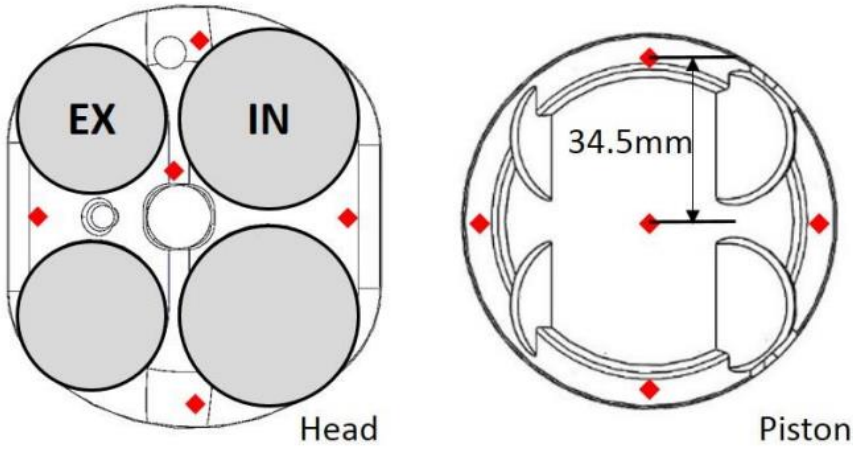

(b)

Figure 6.2 Temperature measurement points on the liner, head and piston. (a) Side view of combustion chamber, (b) Head and piston [118]

Table 6.1 Engine specification

Parameter		Specification
Engine		Single-cylinder N/A dual CVVT
Displacement volume [cc]		499.8
Stroke [mm]		97
Bore [mm]		81
Compression ratio		11.91
RPM [rev/min]		1500
Load		nIMEP 5.4 bar
Spark timing		21CA bTDC
Injection timing		540 CA bTDC
Valve timing (@ 0.1mm)	EVO	68 CA bBDC
	EVC	1 CA aTDC
	IVO	10 CA aTDC
	IVC	67CA aBDC
Maximum valve lift [mm]		10

Table 6.2 The measured Wall boundary temperature

Region	Temperature [K]	Region	Temperature [K]
Liner	393	Intake valve	403
Piston	453	Exhaust valve	513
Head	403	Intake port	373
		Exhaust port	473

6.2 Numerical Setup

In the present study, the CONVERGE v2.4.27 solver is used to calculate the mass, momentum and enthalpy equations of LES. And the ignition model is coupled to the CONVERGE solver by using user defined function. The grid size in the intake port and the cylinder consists of grid of 1 mm, and the exhaust port is 2 mm. The valve sheet is 0.5mm and the region around the spark plug is 0.125mm. Thanks to the adaptive mesh refinement (AMR) function, which is an advantage of CONVERGE, the region with large velocity gradient is refined to 0.5mm and the region around the flame surface is 0.25mm. Therefore, the grid size is refined to suit the transient characteristics of the engine, enabling efficient calculation.

The PISO algorithm and 2nd order monotonic upstream-centered scheme for conservation laws (MUSCL) scheme are employed as the Temporal and spatial discretization scheme. SOR scheme is applied to momentum, mass, energy and SGS turbulent kinetic energy equations. The time step is determined by the Courant-Friedrichs-Lewy (CFL) number. Basically the number of CFL 1 is the criterion for the determination of the time step. During the valve opening and closing time, the CFL number of 0.5 is used to calculate the time step due to very fast flow near valves. The DSM is adopted for the SGS turbulent model and the G-equation is employed as a combustion model. The turbulent burning velocity model for the corrugated flamlets regime is used. The ignition model, developed in this study, is adopted to realize the ignition phenomena. Werner and Wengle model is used for near wall treatment and GruMo-UniMORE model is employed to calculate wall heat transfer. The TRF surrogate fuel is adopted to mimic the domestic gasoline fuel. The described sub-models used for simulation are listed in Table 6.3. As a boundary condition, the intake pressure was obtained directly

from the experiment (Figure 6.3) and the exhaust pressure was calculated by GT-power (Figure 6.4). Wall temperature conditions were measured as shown in Table 6.3.

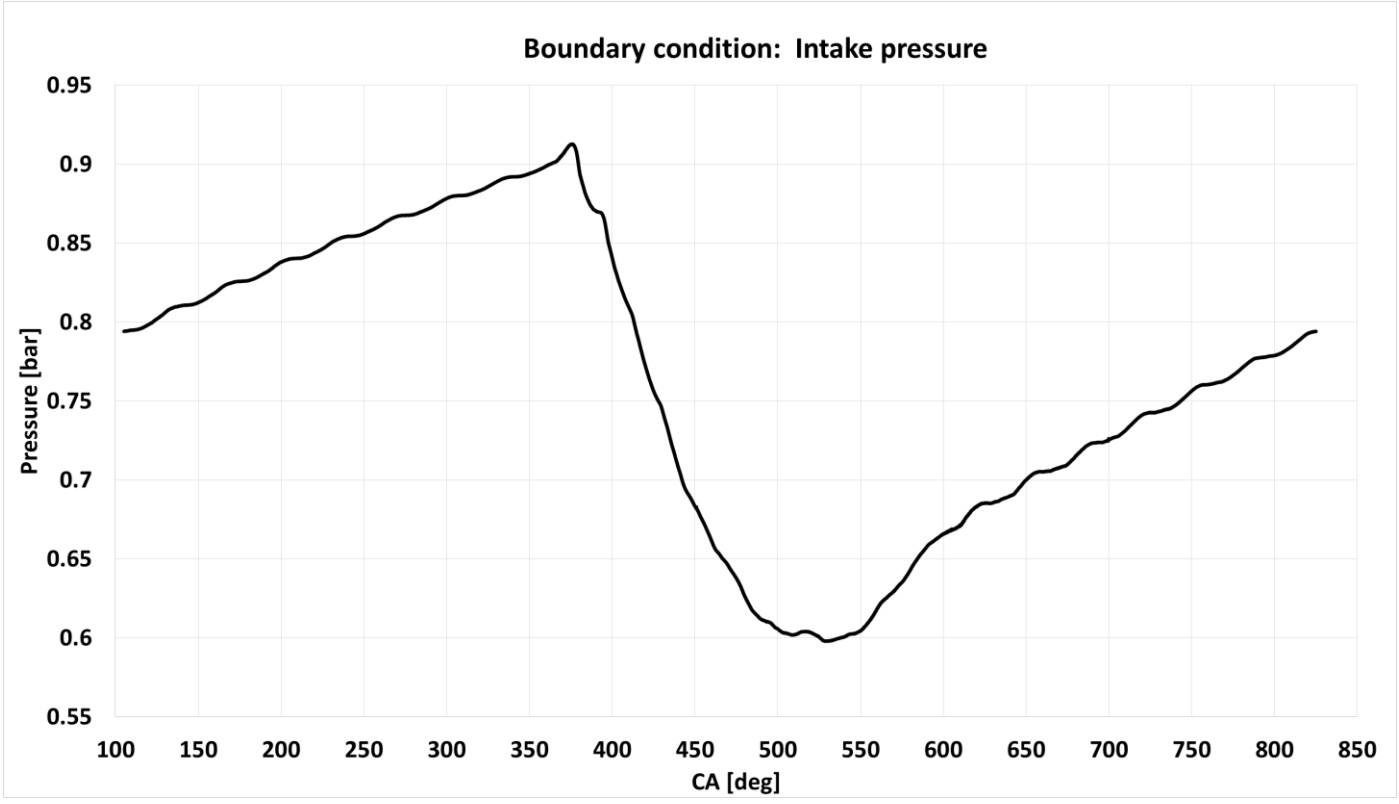

Figure 6.3 Boundary condition of intake pressure measured by experiment

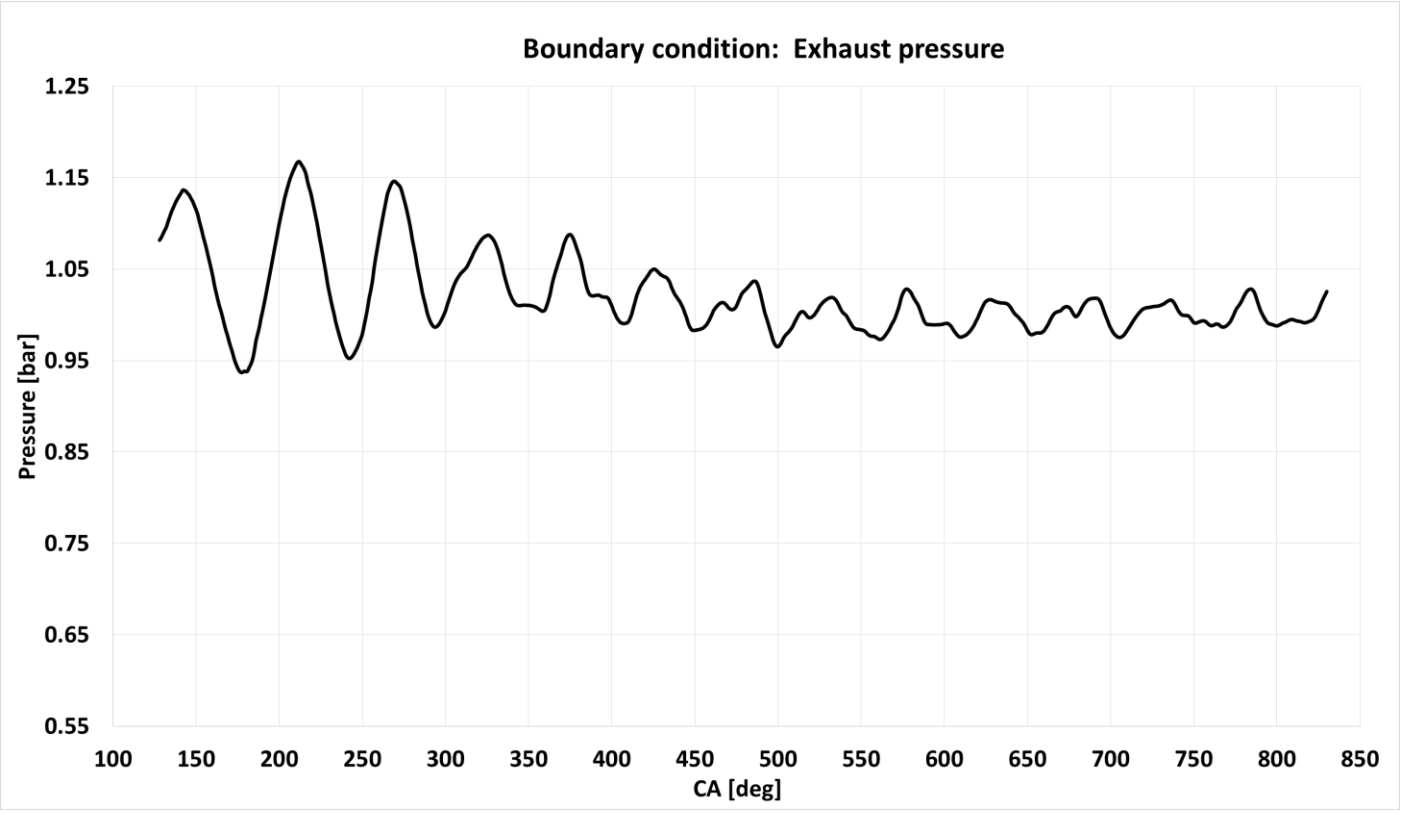

Figure 6.4 Boundary condition of exhaust pressure calculated by GT-power

Table 6.3 Adopted sub-models for simulation

Parameter	Specification
SGS turbulent model	DSM
Combustion model	G-equation (Level-set)
Turbulent burning velocity model	$S_T = b_1 u'_\Delta$ (b_1=3.4) Corrugated flamelets regime
Ignition model	In-house model
Heat transfer model	GruMo-UniMORE
Fuel	TRF surrogate fuel

Chapter 7. Simulation Results of Combustion CCV

In this chapter, the results of the 30 LES cycles are verified using in-cylinder pressure data from experimental data. In addition, the reproduced CCV phenomenon are analyzed in detail to evaluate the factors affecting the CCV. Finally, the most important factor to reduce the CCV is investigated and a guide on how to reduce the CCV is provided with an example of a re-designed piston case.

7.1 Validation of Simulation Results

As the first step of verification, the range of in-cylinder pressure predicted in LES is compared to the in-cylinder pressure range measured in the experiment. In Figure 7.1, the dotted line means the fastest and the slowest value of the experiment and the average value of 100 cycles, while the solid line represents the individual cycles of LES. The in-cylinder pressure of LES cycles fall within the range of cycle deviation of the experiment results, but the range of cyclic variation of LES cycles is slightly narrower than the cyclic variation of experiments. For reasons, the prediction of the cycle deviation of LES may be somewhat underestimated compared to the experiment, as there are many factors affecting the cycle deviation in the actual engine operation, but only the deviation of turbulence flow is considered in LES. And another possibility is that the number of cycles in LES is 30 cycles, less than the 100 cycles in the experiment. Therefore, discrepancy can occur due to differences in the number of samples. Given the differences between experiments and LES, the LES results are well matched with the experimental data in both terms of the combustion accuracy and the cycle-to-cycle variability.

Next, in Figure 7.2, the accuracy of LES for combustion phase is compared with the experimental data with the comparison of the MFB indicating the combustion phase. As noted in the previous comparison of pressure curves, the averaged value is very well simulated, but for the fastest and the slowest cycles, LES predicts slightly slower and faster, respectively.

In general, the CCV of the engine combustion is defined using the deviation of IMEP and peak pressure. IMEP is important parameter in terms of engine efficiency and performance, reflecting all four-stroke in addition to combustion, and peak pressure represents the characteristics of combustion because of variations caused by combustion phenomenon. Therefore, in the present study, the CCV of engine combustion is defined by the deviation of peak pressure for the analysis of the CCV occurring in the combustion phase.

The cycle-to-cycle variation is mainly defined using the COV. The COV is defined in the following equation:

$$\mathrm{COV} = \frac{\sigma}{\mu} \qquad (7.1)$$

Where, σ: standard deviation

μ: mean value

Table 7.1 shows the COVs of each combustion phase and peak pressure measured in LES and in the experiment. In the MFB 5, which indicates the early flame propagation, LES predicts slightly higher deviations, but as flame propagated, LES finally predicts slightly lower deviations of the peak pressure. There are two reasons for the slight discrepancy between the experiment and LES. One is that the sample of LES is smaller than the experiment and, unlike the experiment in LES, only the variation due to the flow is considered. As a result,

although slight difference exists, the CCV of LES has a good agreement with the CCV phenomenon found in the experiment.

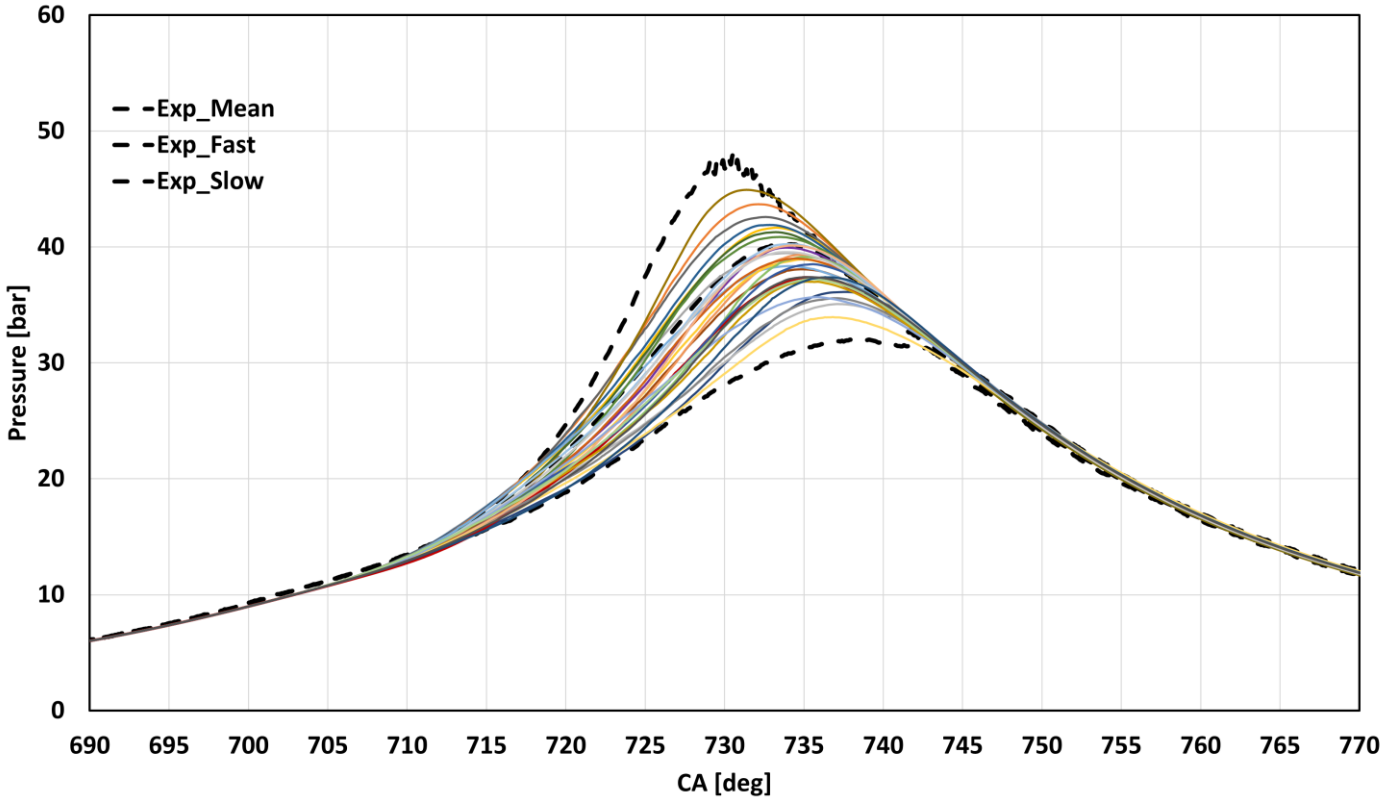

Figure 7.1 Comparison of in-cylinder pressure between LES and experimental data

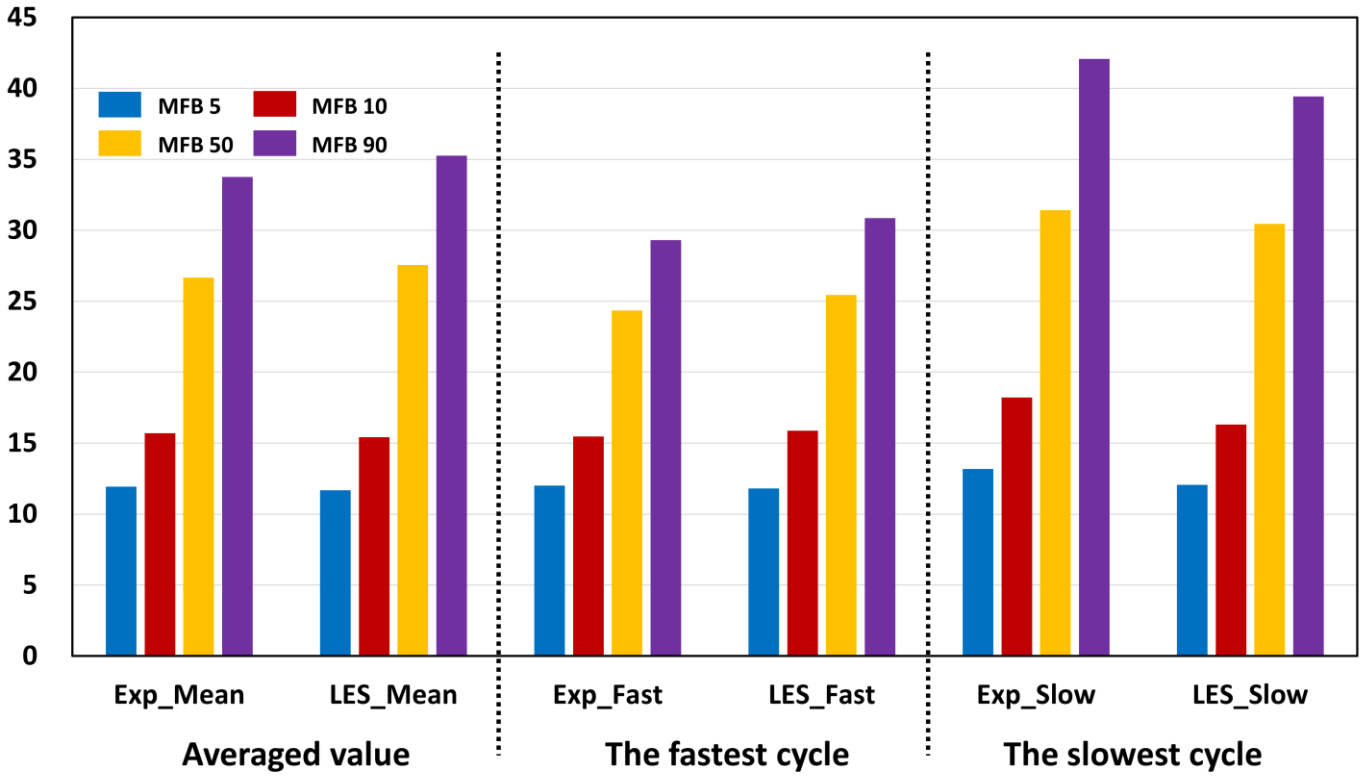

Figure 7.2 Comparison of MFB between LES and Experimental data

Table 7.1 COV of each burn duration

	Experiment	LES
MFB 5	5.00	5.18
MFB 10	5.89	5.35
MFB 50	6.41	5.68
MFB 90	7.36	5.97
Peak Pressure	7.69	6.63

7.2 Correlation between Combustion Phase and Peak Pressure

Flow variation at the early flame propagation stage is known as the dominant source of the CCV. First of all, a correlation coefficient technique is adopted to evaluate the effect of the early flame propagation deviation on the variation of final combustion. The correlation coefficient to analyze the correlation between the two parameters is defined as the following equation:

$$\rho_i = abs\left(\frac{cov(X,Y_j)}{\sqrt{var(X)\cdot var(Y)}}\right) \tag{7.2}$$

In the present research, to find the relationship between deviations, the deviation of the peak pressure and each stage of the combustion phase are defined as comparison factors. First, the relationship between the deviation of the peak pressure and the deviation of each combustion phase is illustrated in Figure 7.3. Naturally, the peak pressure is highly correlated with the MFB as the combustion progresses. However, it is difficult to analyze the source of the CCV because interaction between flame and flow accumulates over time from the time of ignition. For the MFB 50 and the MFB 90, the deviation of the peak pressure is very close to 88% and 96%, respectively, and for Figure 7.4, the relationship between the MFB 50 deviation and the MFB 90 deviation is very close at 90%. Therefore, it is easy to analyze the cause of the CCV because the MFB 50 can represent the overall combustion phase and is about 10 CA degree faster than the MFB90 as shown in Figure 7.2. Next, the MFB 5 is chosen as the factor representing the early flame propagation. In Figure 7.3, there is not much difference between the MFB 5 and the MFB 10 compared with the peak pressure deviation, 58% and 67%, respectively. And looking at the relationship with the

deviation of the MFB 50 in Figure 7.4, correlation coefficients of the MFB 5 and the MFB 10 with the MFB 50 are 70% and 80%, respectively, and the small discrepancy between the two are negligible. Furthermore, the MFB 5 is about 4CA degree faster than the MFB 10 as shown in Figure 7.2, making it more appropriate to analyze the effects of the early flame propagation. To sum up, it can be said that the MFB 50 represents the overall combustion phase, and the MFB 5 represents the early flame propagation. Therefore, the analysis will be conducted on the MFB 5 and the MFB 50 based.

In Figure 7.5, the correlation between the MFB 5 and the MFB 50 is shown to understand the effect of the early flame propagation on the overall combustion phase. The R square value of the trend line between the early flame propagation and the overall combustion phase is 0.37, and it means that the initial flame propagation does not absolutely determine the combustion phase. Therefore, in order to find the cause of the cyclic variation, it is necessary to analyze not only the flow analysis during the early flame propagation, but also all the combustion phase.

To further analyze the relationship between the early flame propagation and the overall combustion phase, the cycle numbers are listed as follows. First, 30 cycles are sorted in ascending order based on the overall combustion phase (MFB 50). The 30 cycles are divided into three group. The first ten cycles are classified as fast cycles, and the last ten cycles are categorized as slow cycles and others are classified as medium cycles. The 30 cycles are sorted again based on the MFB5 to find the relationship between the early phase and overall phase as shown in Figure 7.6. Generally, previous studies concluded that early flame propagation has a dominant effect on the overall combustion phase. However, it is noteworthy in the present study that the early flame propagation does not have an absolute effect on the overall combustion phase. For example, the fastest cycle (fifth cycle) ended

up being the medium cycle of combustion speed, and the fourth and the seventh cycles, which are intermediate combustion speed, changed to fast cycles. These special cases exist, but if slow cycles are looked at, to some extent the early flame propagation affects the entire combustion phase.

In the following section, the effect of turbulent flow on the CCV of combustion is analyzed with the verified LES results. Due to the characteristics of LES, turbulence can be divided into two main categories: the large scale turbulent flow and the small scale turbulent flow. The large scale turbulent flow is resolved and the small scale turbulent flows is simulated through the SGS model. Therefore, the analysis is carried out in terms of the large scale and the small scale turbulent flows.

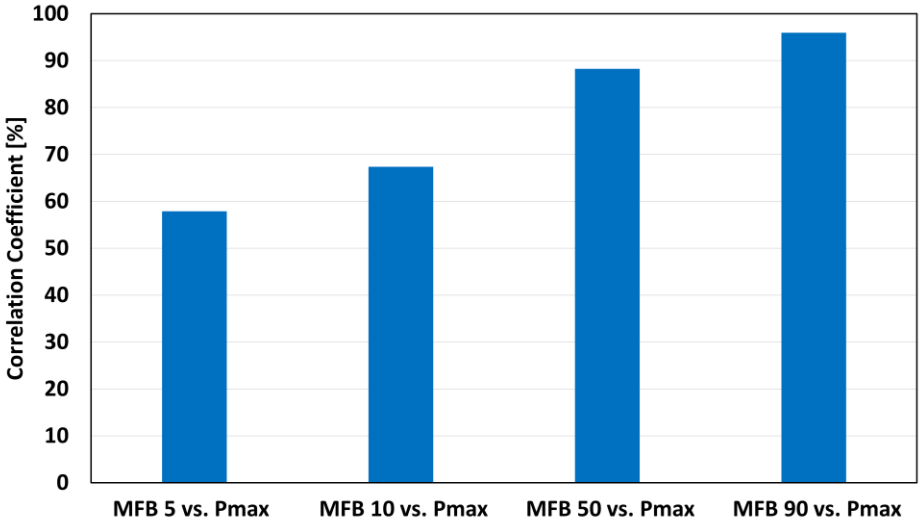

Figure 7.3 Correlation coefficient of COV: MFB5, MFB10, MFB50, MFB90 vs. peak pressure

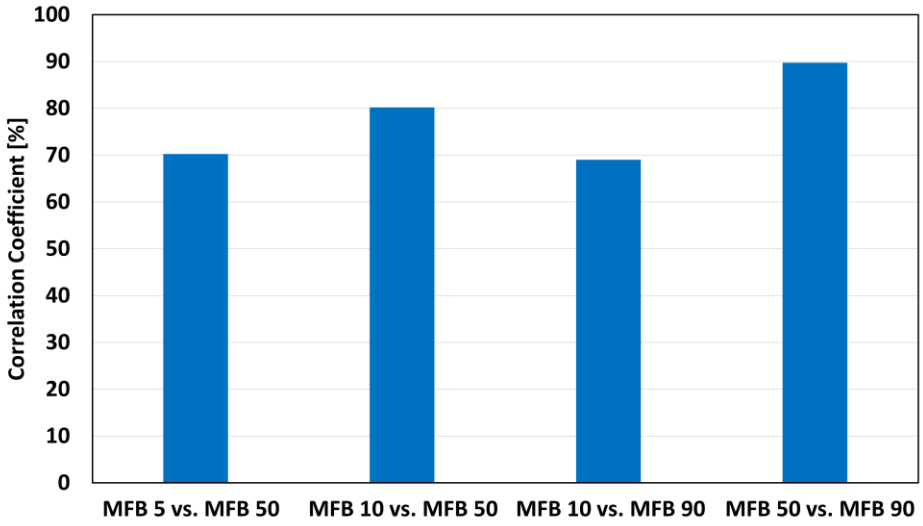

Figure 7.4 Correlation coefficient of COV between MFB rates

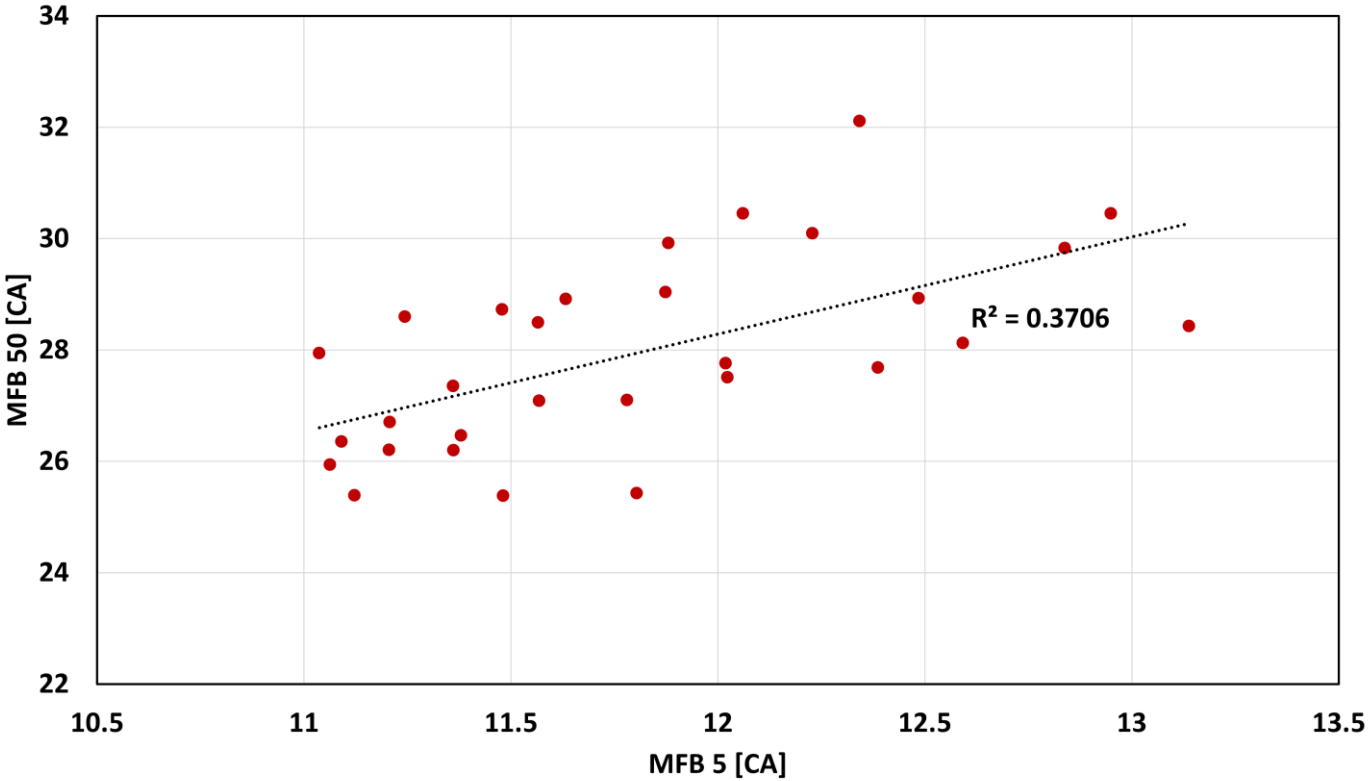

Figure 7.5 The correlation between MFB 5 and MFB 50

MFB5	MFB50
5	4
3	6
1	7
6	3
2	9
10	2
27	1
17	21
9	10
21	24
20	22
4	17
26	14
24	23
15	13
22	5
7	11
19	16
18	26
13	27
14	20
25	15
12	30
29	19
23	28
30	18
11	12
28	25
8	8
16	29

Figure 7.6 Cycles arranged in ascending order according to combustion speed in MFB5 and MFB50

7.3 Investigation of turbulent flow effect on CCV

7.3.1 Small Scale Turbulent Flow Effect on CCV

The small scale turbulent flow is represented as the SGS turbulent kinetic energy in LES. The SGS turbulent kinetic energy and the SGS turbulent velocity are in relation to $u'_{sgs} = \sqrt{\frac{2}{3}k_{sgs}}$ and effect on the turbulent flame propagation with the equation $S_T = S_L + b_1 u'_{sgs}$ described in chapter 4.3. Therefore, the small scale turbulent flow is an important factor that affects the flame propagation. Figure 7.7 illustrates the volume averaged of the in-cylinder SGS turbulent velocity in the fast cycles, the average value of the slow cycles, and mean of the total 30 LES cycles. During the intake stroke, there is no difference of the SGS turbulent velocity between the fast cycles and the slow cycles. By approximately 660CA, both the fast and slow cycle groups have nearly the same values, and from then on, it can be found that the SGS turbulent velocity of the fast cycle group has a little bit higher value than the slow cycle group. After ignition, the SGS turbulent velocity (mass-averaged) on the flame surface is shown in Figure 7.8. The difference of the SGS turbulent velocity between the averaged fast cycles and the averaged slow cycles before the ignition becomes larger as combustion progresses. Figure 7.9 shows the SGS turbulent velocity at the spark plug gap. As with the previous results, the average value of the fast cycles is higher than the average value of the slow cycles. Immediately after the ignition, a sharp decrease of the SGS turbulent velocity is observed, as the measured position is located in the behind of the flame surface. Therefore, the small scale turbulent flow can be considered as one of the causes of the cyclic variation of the flame propagation.

Figure 7.10 shows the correlation between the SGS turbulent velocity (mass-averaged) on the flame surface at 702 CA and the MFB 50 which represents the overall combustion phase. 702 CA time is the MFB 1 time after 3 degrees of ignition and represents the very early combustion phase. In general, the MFB 50 of the high SGS turbulence velocity cycle is short, but the R square value between the two values is 0.3. The result means that the small scale turbulent flow is one of the factors affecting combustion speed, but it does not have an absolute effect.

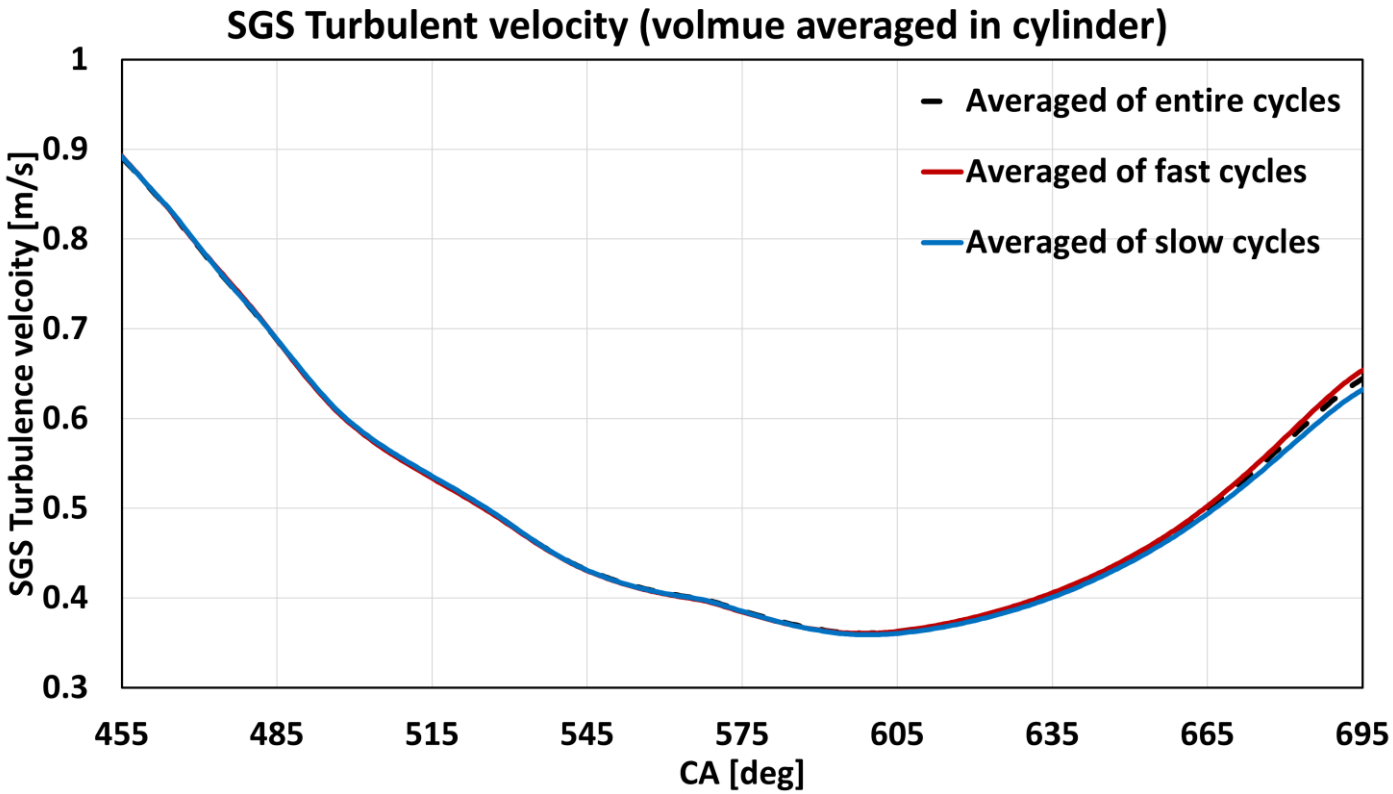

Figure 7.7 Comparison of SGS turbulent velocity before ignition. Black dotted line: Averaged value of entire cycles, Red solid line: Averaged value of fast cycles, Blue solid line: Averaged value of slow cycles

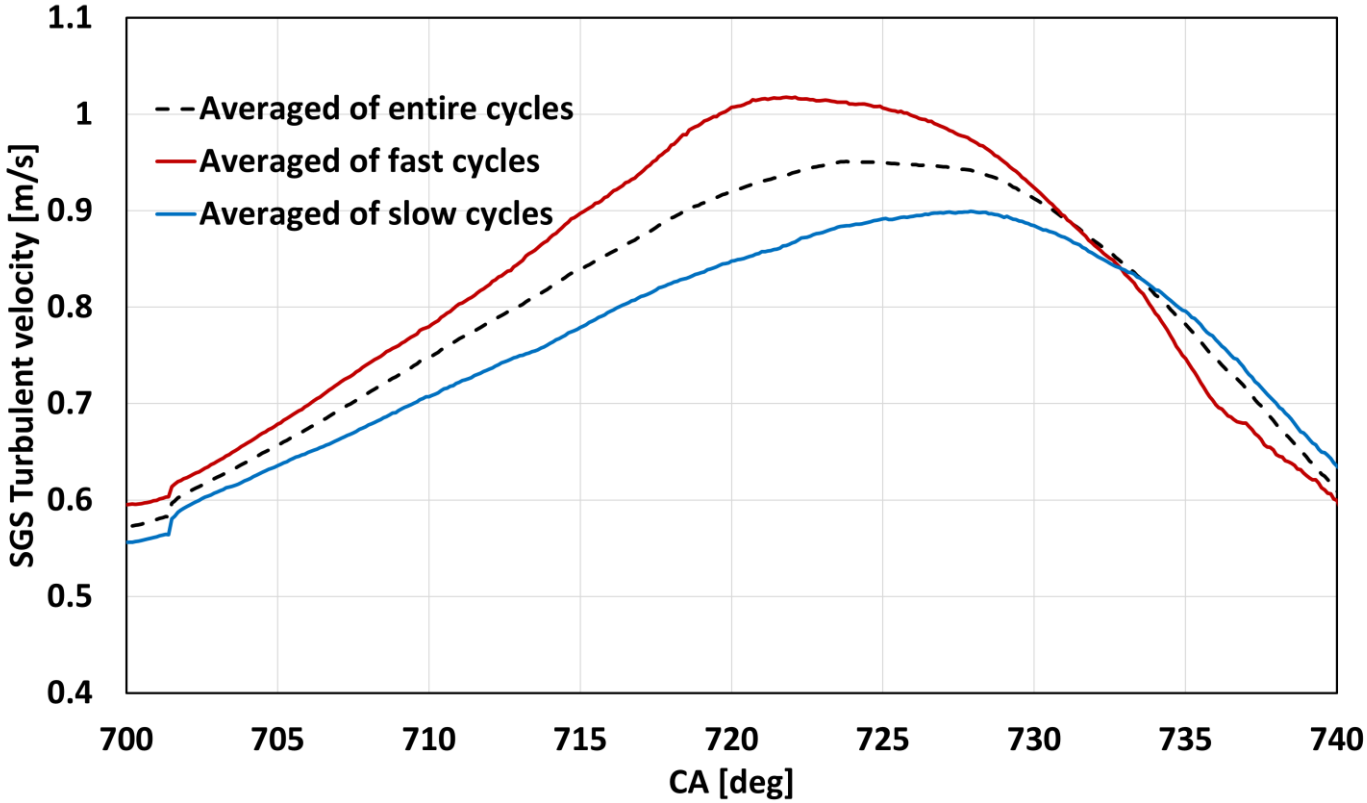

Figure 7.8 Comparison of SGS turbulent velocity on the flame surface after ignition. Black dotted line: Averaged value of entire cycles, Red solid line: Averaged value of fast cycles, Blue solid line: Averaged value of slow cycles

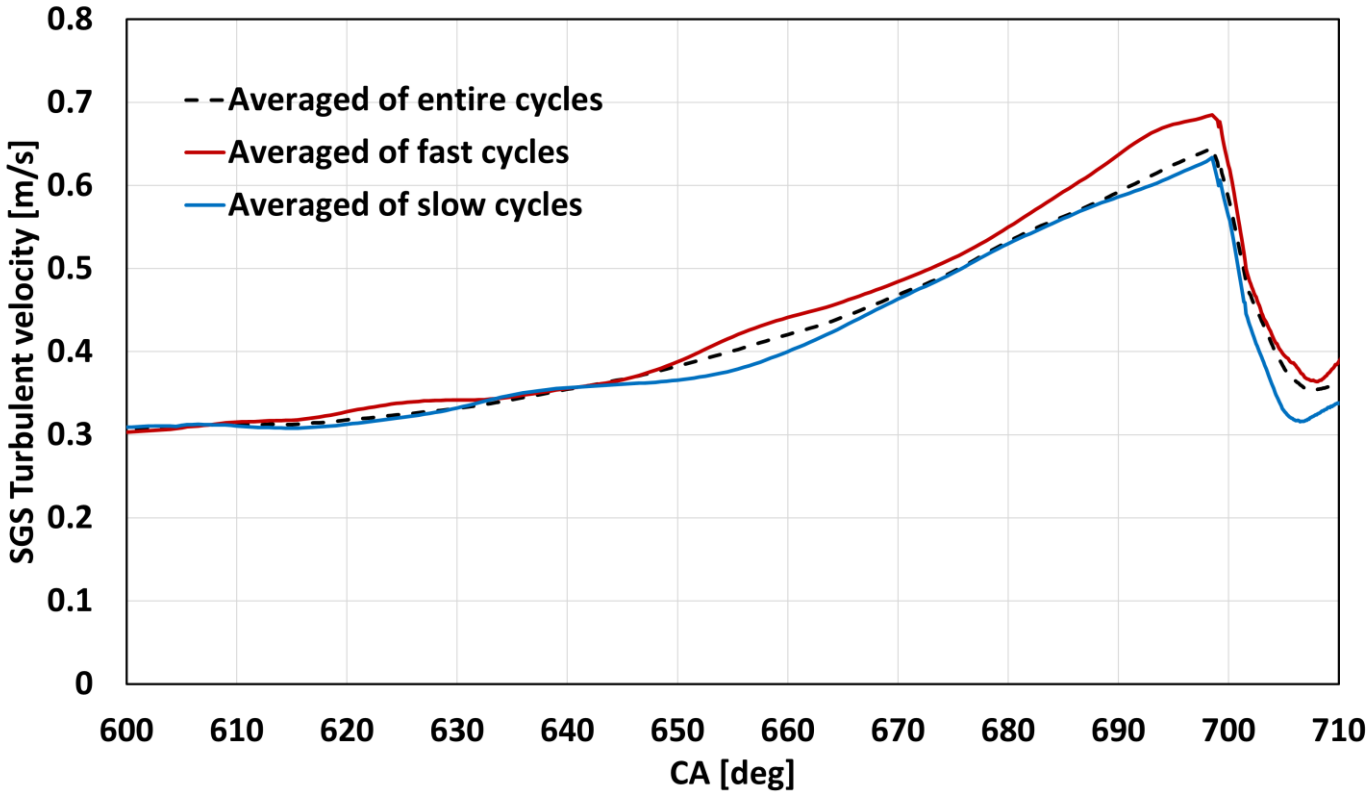

Figure 7.9 Comparison of SGS turbulent velocity at center of spark plug gap. Black dotted line: Averaged value of entire cycles, Red solid line: Averaged value of fast cycles, Blue solid line: Averaged value of slow cycles

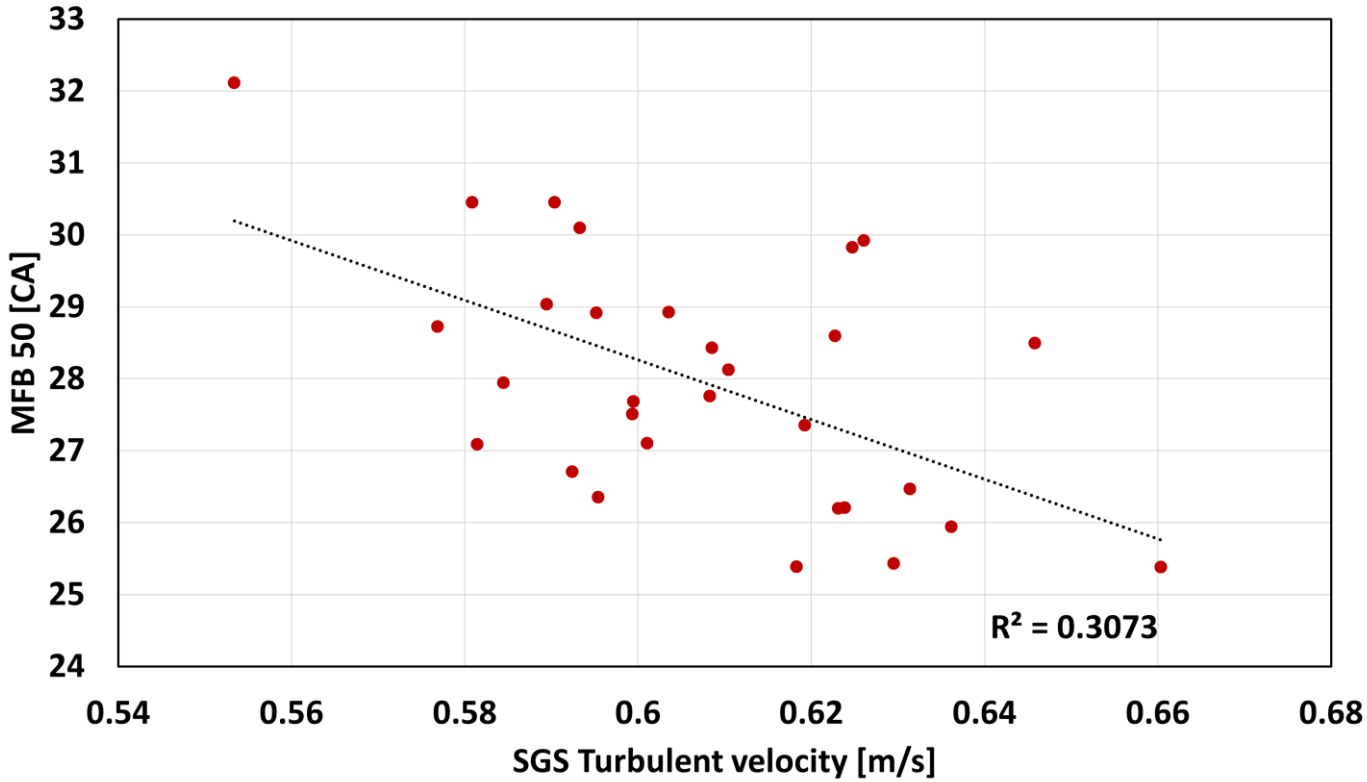

Figure 7.10 The correlation between SGS turbulent velocity and MFB 50

7.3.2 Large Scale Turbulent Flow Effect on CCV

The large scale turbulent flow is turbulent flow resolved by grid in LES, not represented by a single term, unlike the small scale turbulent flow. First, the representative large scale motions (tumble X, Y and swirl) in the combustion chamber are illustrated in Figures 7.11 – 7.13. The dotted line represents the averaged value of entire cycles, the red solid line indicates the mean value of the fast combustion cycles and the blue solid line means the mean value of the slow combustion cycles. Figure 7.11 shows the tumble Y ratio which is important factor in SI engines. During the intake process, both the tumble ratio of fast and slow cycles are irrelevant to the combustion phase as the both of the tumble ratio are smaller than the overall mean value. Subsequently, during the compression process, the tumble ratio of the fast cycles is greater than the slow cycles. However, it is interesting to note that the tumble ratio of both the fast and slow cycle groups becomes similar at the ignition time (21 CA bTDC). The difference of the tumble ratio between the fast and slow cycles decreases from about 660 CA as shown in Figure 7.7, at that time, the SGS turbulence velocity for the fast cycles begins to be higher than the slow cycles. Therefore, it can be seen that the energy of tumble is converted into turbulent flow during the compression process until the ignition time. In SI engines, the tumble X and the swirl are not intended flow motion, so very small values are observed throughout the cycle as shown in Figures 7.12 and 7.13.

Next, flow field is analyzed to evaluate the effect of the large scale turbulent flow in a local area. Four noticeable cycles are investigated in the present study as shown in Figure 7.6. The 5th cycle which is fast combustion in early stage but belongs to the medium combustion speed group on the basis of the MFB 50. The 4th cycle that is initially propagated at the medium combustion speed but later in

the fast combustion speed group. The 18th cycle which is initially propagated at the medium combustion speed but later in the slow combustion speed group. The combustion phase of 23rd cycle is slow at first but faster as combustion progresses and eventually belongs to the medium combustion phase group. The field analysis is carried out in four planes in Figure 7.14.

First, the reason why the early flame propagation of 5th cycle is fast and then slow down as combustion progresses is described. In Figure 7.15, the spatial velocity distributions near the spark plug at the ignition time are shown. The strong flow from right to left is shown in Figure 7.15 (a) and (b). Due to the strong flow, the flame propagates to the left side in the early phase as shown in Figure 7.16. At 703CA (Figure 7.16 (a)), the flame is observed to meet the vortex in the left side and propagates rapidly in the direction of rotation of the vortex (Figure 7.16 (b)). Similarly, Figure 7.17 (a) describes the flame in contact with the vortex on the left side of the spark plug again at 710 CA, but there is no vortex in the right side. As a result, the flame leans toward to the left side as shown in Figure 7.17 (b). In Figure 7.18, the early flame propagation is shown on the side view (Y=0mm). In the side view, it is also observed that the flame meets the vortex and propagates quickly. The initial flame propagation of the 5th cycle is fast because the flame meets the vortices early time and spreads rapidly. However, as in Figure 7.17, the flame is skewed to left side, showing an unbalanced flame propagation as shown in Figure 7.19. This is the reason why the combustion phase of the 5th cycle is rapid in the early stage but slows over time.

In Figure 7.20, the vector fields of the 4th cycle near the spark plug at the ignition time are shown. In the side view (Figure 7.20 (a)), two vortices slightly away from the spark plug toward the intake valve are observed. As a result, it can be observed that the flame evenly propagates in the direction of the exhaust valve and the intake valve by meeting the two vortices as it moves out of the spark plug

region as shown in Figure 7.21. In the front view (Figure 7.20 (b)), there are three vortices and the flow is seen from left to right. Therefore, the flame is initially propagated to the right, as shown in Figure 7.22 (a), but it meets the vortex on the left and begins to propagate rapidly to the left as shown in Figure 7.22 (b). As a result, the flame is propagated in balance from side to side (Figure 7.23 (a)), and the flame propagation is accelerated by the additional contact of the vortex (Figure 7.23 (b)). The balanced flame propagation is also identified in the top view of Figure 7.24. In the 4th cycle, the contact time with the vortex in the initial flame phase is about 4 CA slower than the 5th cycle, but it encounters more vortices as flame propagates. Thus the flame propagation in the 4th cycle, as opposed to the 5th cycle, is slow in the early stage, but becomes faster over time.

In the Figure 7.25, the velocity fields of the 18th cycle near the spark plug at the ignition time are shown. On the side view (Figure 7.25 (a)), the flow is directed downward due to the rapid flow observed in upper and right of the spark plug Therefore, the flame is also observed to propagate in the same direction of flow as shown in Figure 7.26 (a) and (b). At 705 CA, the flame begins to be affected by the vortex in the lower right of the Figure 7.26 (b). However, since the flow, as shown in Figure 7.25 (b), passes through the spark plug and flows strongly down the right side, it is observed that the flame propagates completely over the right side as shown in Figure 7.27. Despite the fact that the flame in the side view is affected by the vortex at an early time, the initial flame propagation is relatively slow due to the disproportionate flame propagation identified in the front view. Furthermore, as identified in Figure 7.28, the flame propagation becomes slower and slower because there is no contact between the flame and a vortex during the flame propagation. In the Figure 7.29, the flame propagation is slower than the two cycles described earlier

Lastly, the flame propagation of the 23th cycle is analyzed. Figure 7.30 shows the vector fields near the spark plug at the ignition time. On the side view (Figure 7.30 (a)), there is a strong flow toward to the bottom on the right of spark plug. Thus, the early flame propagates to only under the spark plug as shown in Figure 7.31. In addition, on the front view (Figure 7.30 (b)), the flow moves rapidly from right to left of the spark plug. Therefore, the flame also propagates to the left as the flow motion as shown in Figure 7.32. For the two reasons, the 23th cycle has the very slow early flame propagation. As shown in Figure 7.33, the flame is not affected by a vortex up to 715 CA. However, after 718CA, the flame meets the vortices on the left and right side, accelerating the propagation relatively evenly. Therefore, flame propagation is identified to propagate evenly after 720 CA as shown in Figure 7.35

The relationship between the flow distribution and the flame propagation is investigated in detail in four analysis planes by using four cycles. The factors determining the rate of the early flame propagation are how uniform the flow distribution near spark plug at the ignition timing is and how quickly the flame contacts with the vortex. After that, the combustion phase depends on when, where, and how much the flame meets the vortices.

So far, the effect of the small scale and the large scale turbulent flow effect on the combustion CCV is investigated. It is identified that the small scale turbulent flow is related to the tumble motion. As a result, the deviation of the tumble ratio is one of the causes of the CCV, but its variation is modest. Next, the effect of local flow fields on the flame propagation is analyzed. The great effect of local vortices on the flame propagation is observed. Therefore, in the present study, it is found that the local vortices are the main source of the combustion CCV. In the following section, the way to reduce the combustion CCV will be discussed.

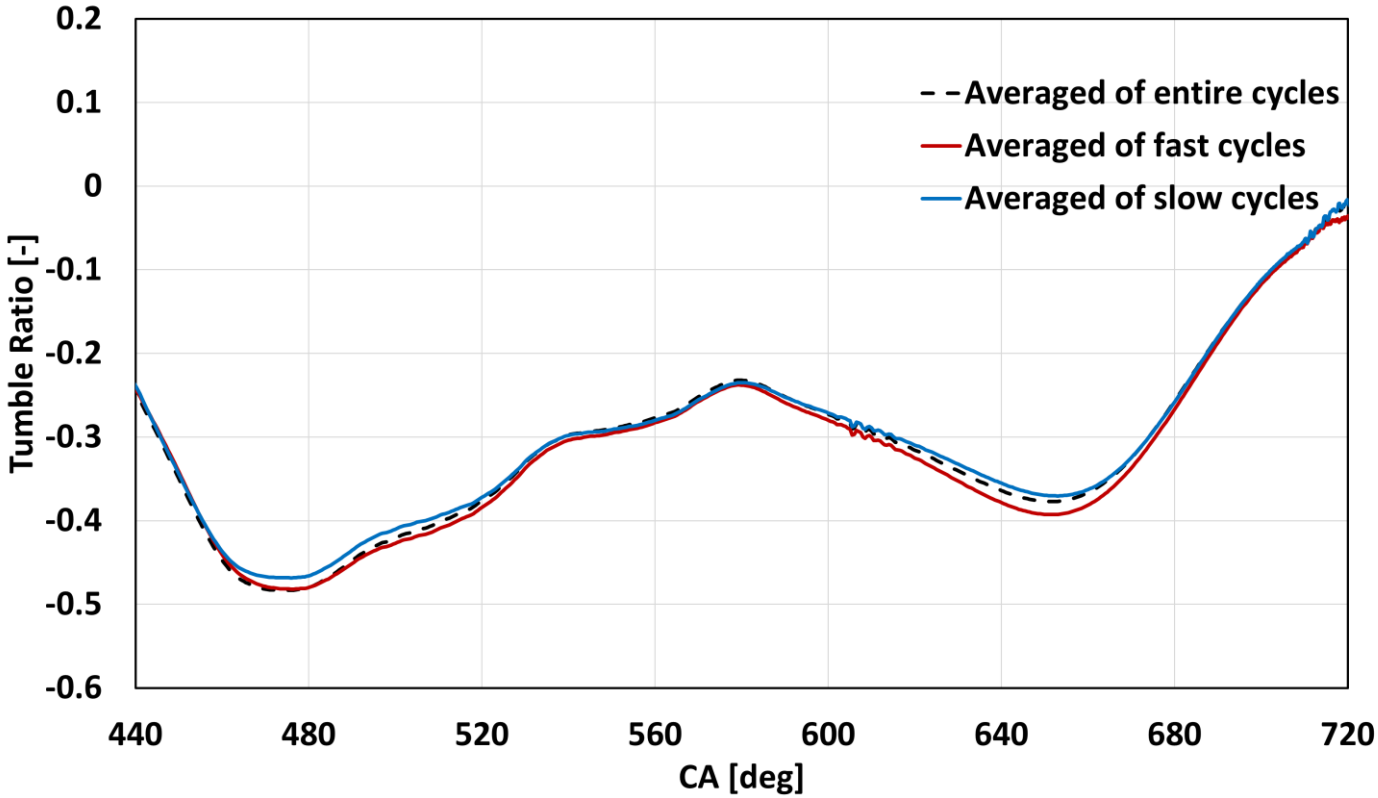

Figure 7.11 Comparison of tumble Y ratio. Black dotted line: Averaged value of entire cycles, Red solid line: Averaged value of fast cycles, Blue solid line: Averaged value of slow cycles

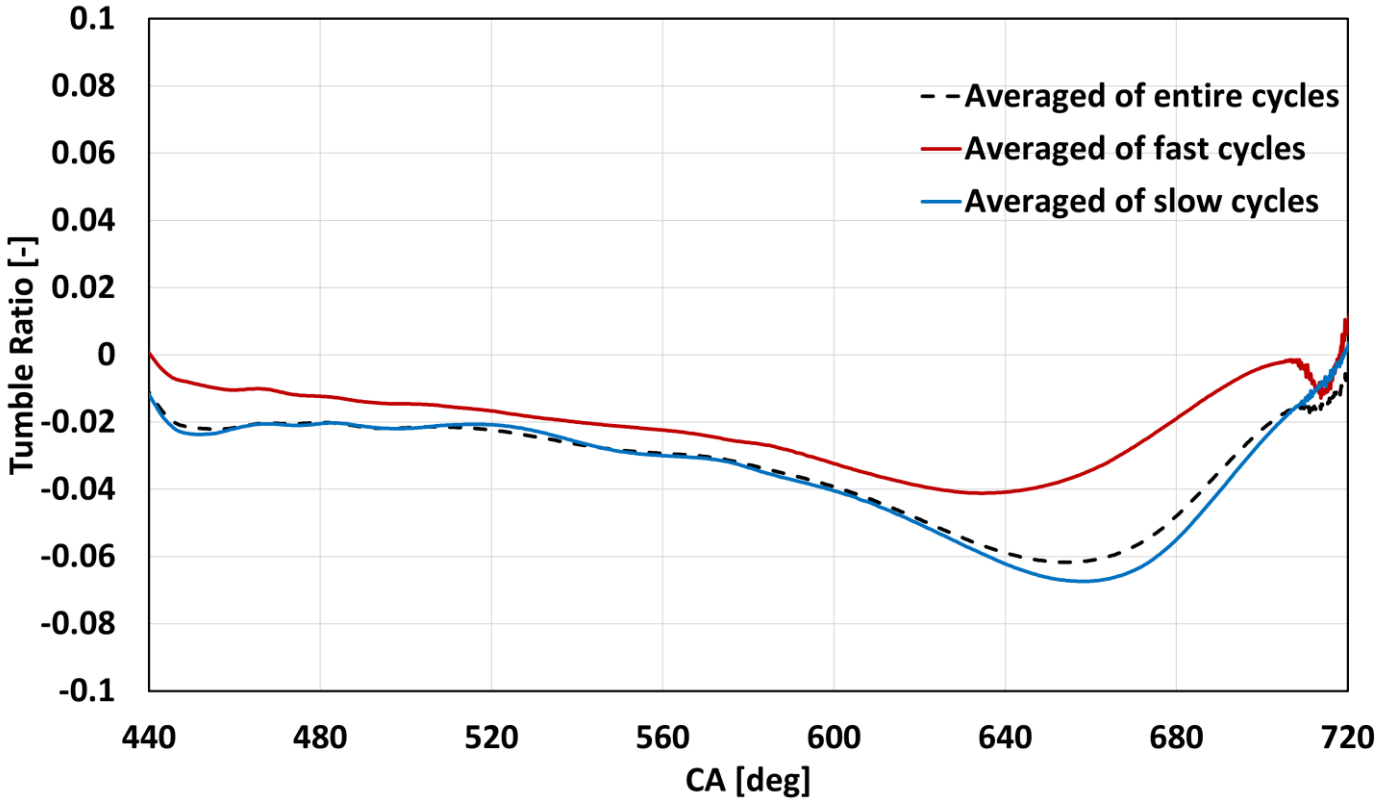

Figure 7.12 Comparison of tumble X ratio. Black dotted line: Averaged value of entire cycles, Red solid line: Averaged value of fast cycles, Blue solid line: Averaged value of slow cycles

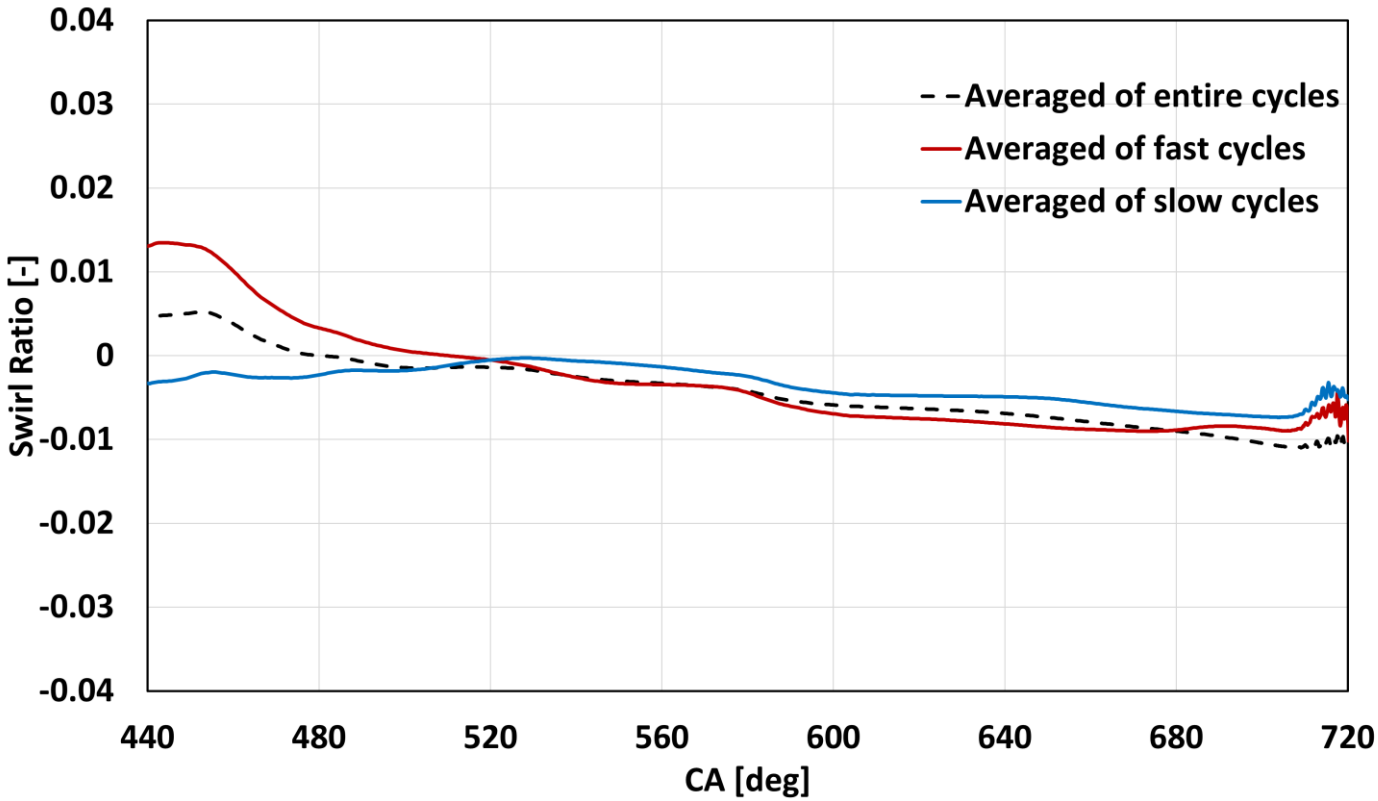

Figure 7.13 Comparison of swirl ratio. Black dotted line: Averaged value of entire cycles, Red solid line: Averaged value of fast cycles, Blue solid line: Averaged value of slow cycles

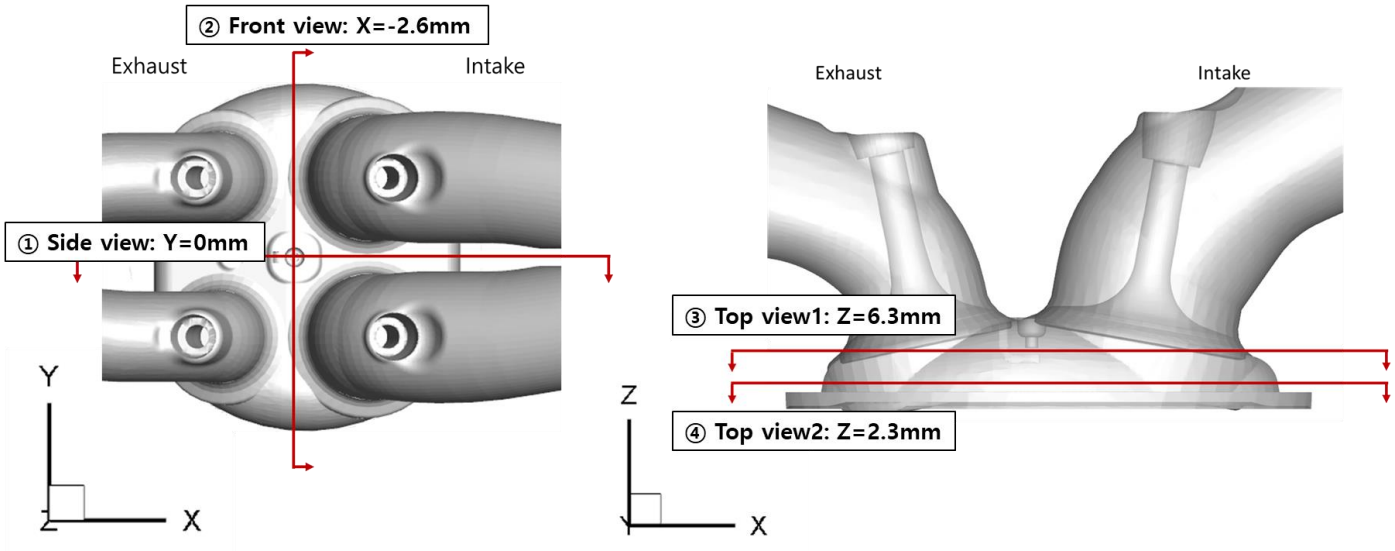

Figure 7.14 Analysis sections: ① Side view: Y=0mm, ② Front view: X=-2.6mm, ③ Top view1: Z=6.3mm, ④ Top view2: Z=2.3mm

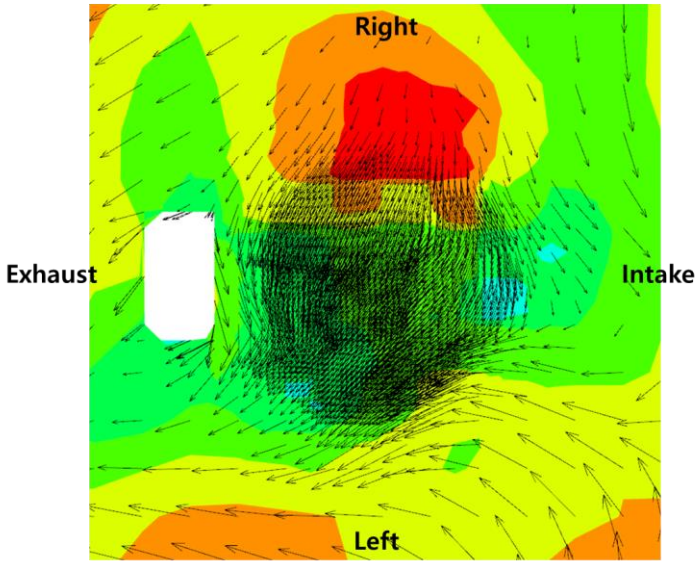

(a)

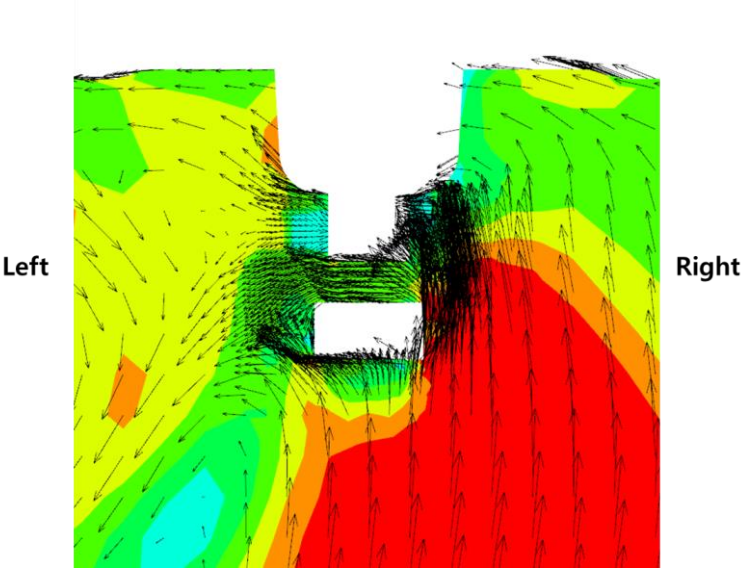

(b)

Figure 7.15 The vector field of 5th cycle at 699 CA. (a) Top view1 (Z=6.3mm), (b) Front view (X=-2.6mm)

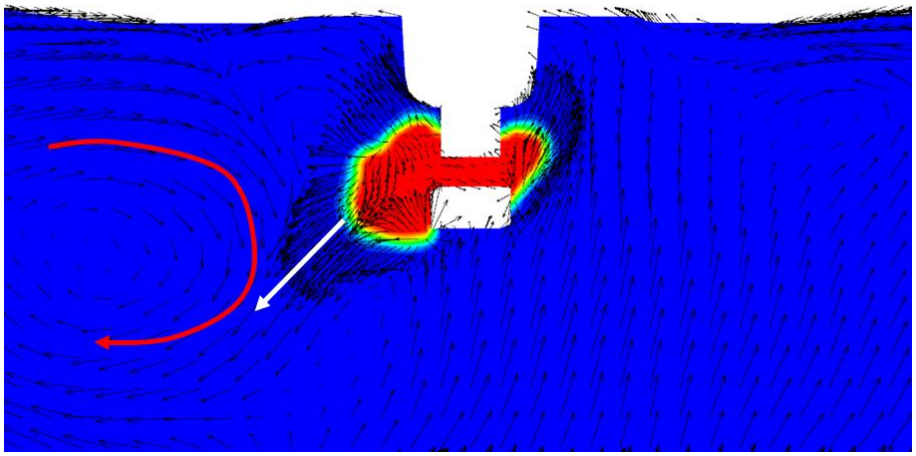

(a)

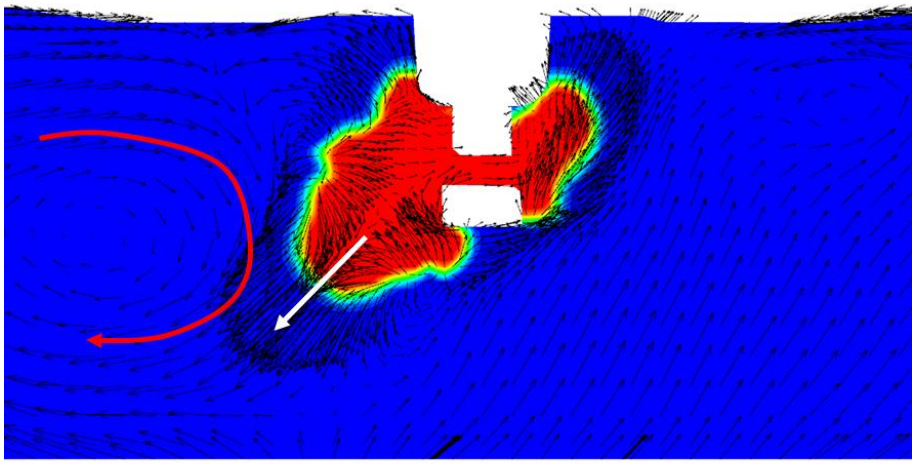

(b)

Figure 7.16 Progress variable and vector field of 5th cycle on front view (X=-2.6mm). (a) 703 CA, (b) 704 CA

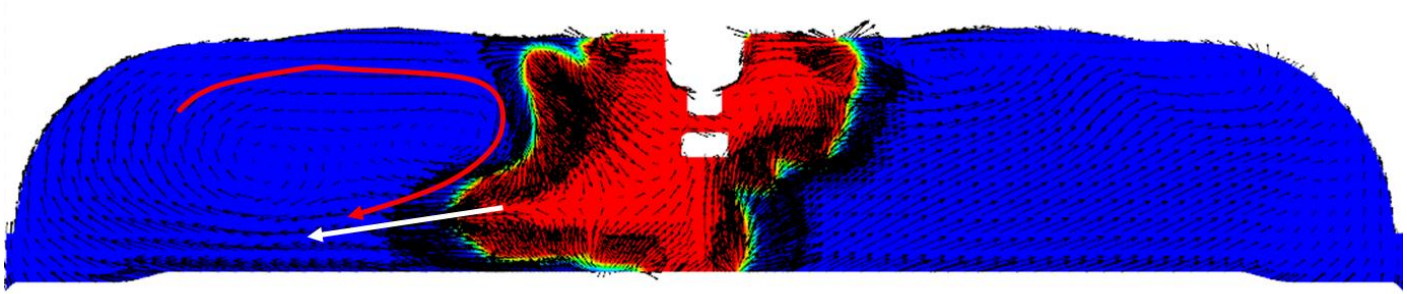

(a)

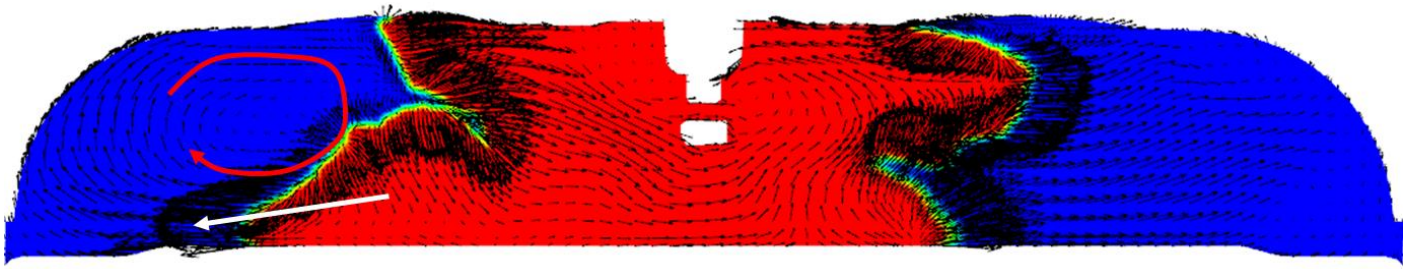

(b)

Figure 7.17 Progress variable and vector field of 5th cycle on front view (X=-2.6mm). (a) 710 CA, (b) 716 CA

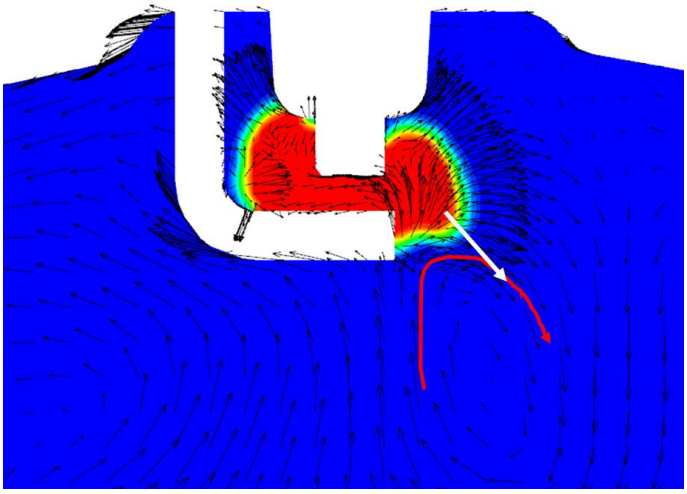

(a)

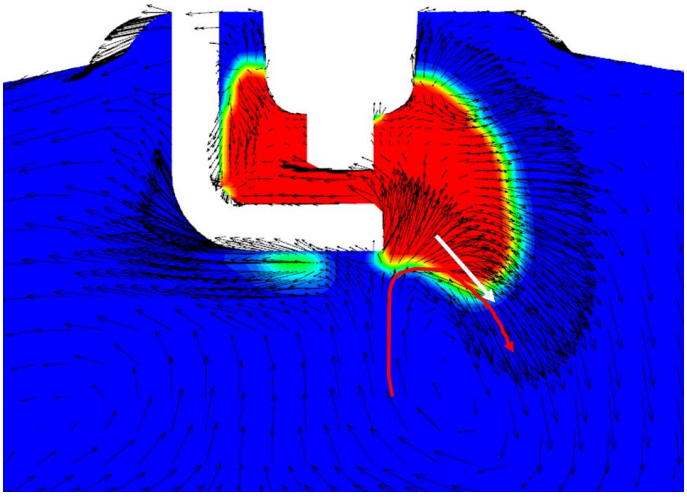

(b)

Figure 7.18 Progress variable and vector field of 5th cycle on side view (Y=0mm). (a) 703 CA, (b) 704 CA

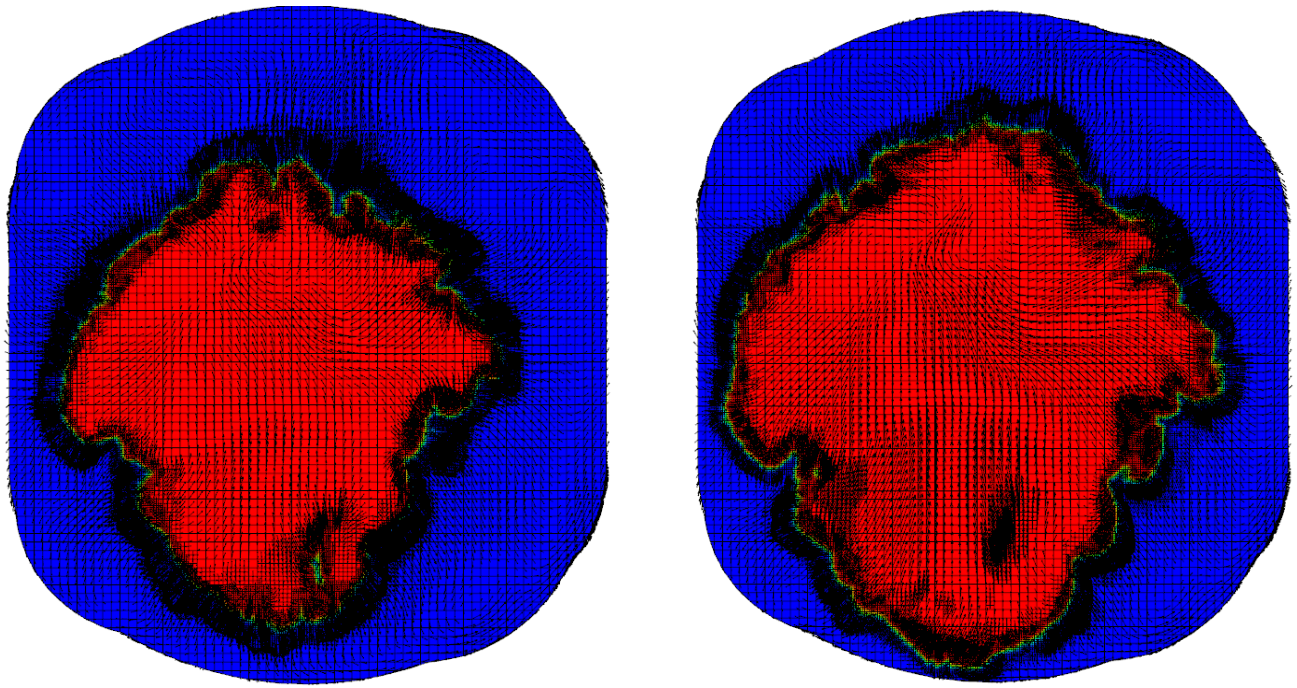

(a) (b)

Figure 7.19 Progress variable and vector field of 5th cycle on top view2 (X=2.3mm). (a) 720 CA, (b) 723 CA

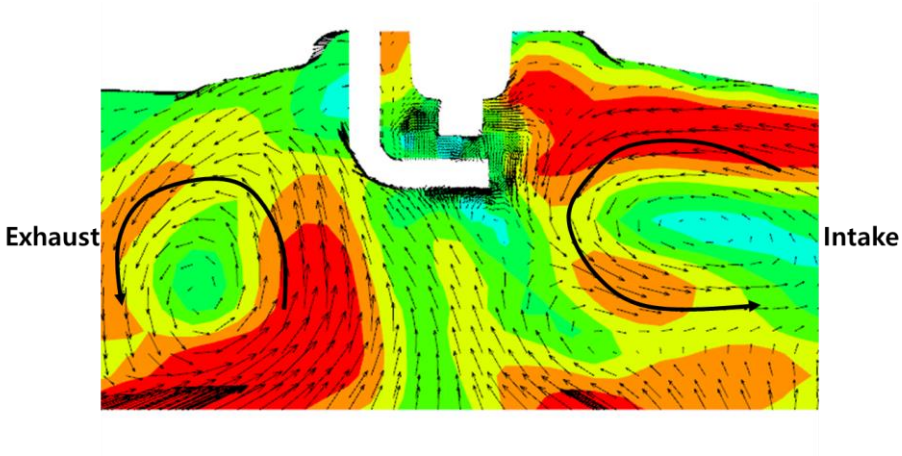

(a)

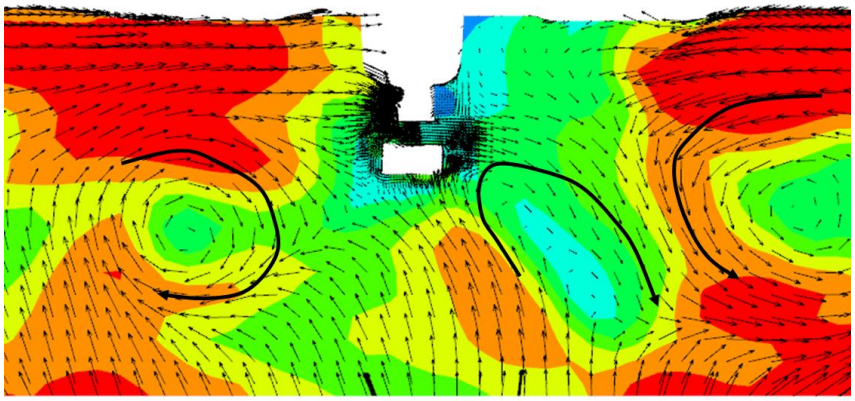

(b)

Figure 7.20 The vector field of 4th cycle at 699 CA. (a) Side view (Y=0mm), (b) Front view (X=-2.6mm)

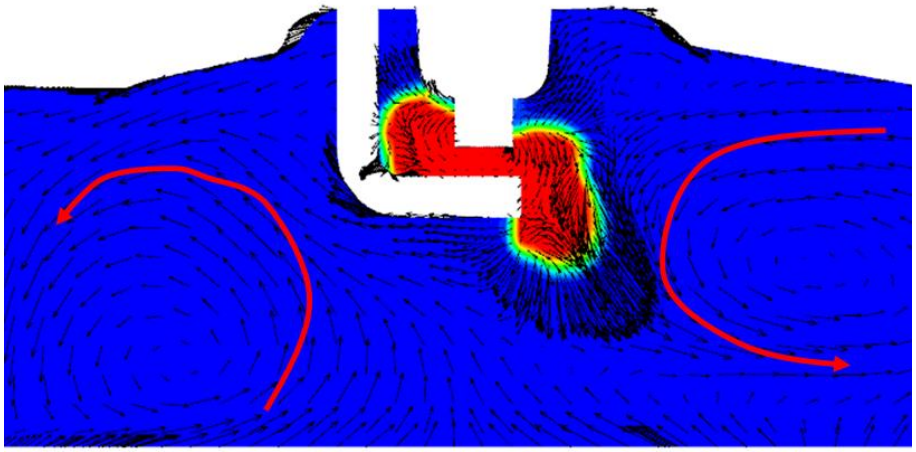

(a)

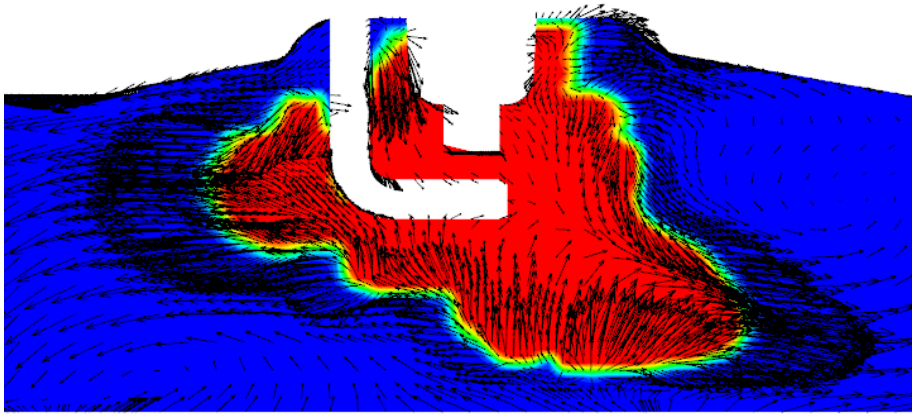

(b)

Figure 7.21 Progress variable and vector field of 4th cycle on side view (Y=0mm). (a) 705 CA, (b) 709 CA

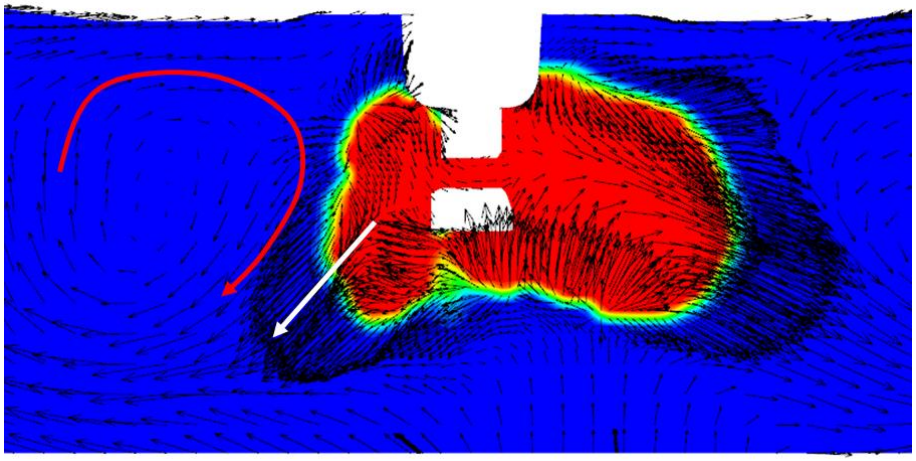

(a)

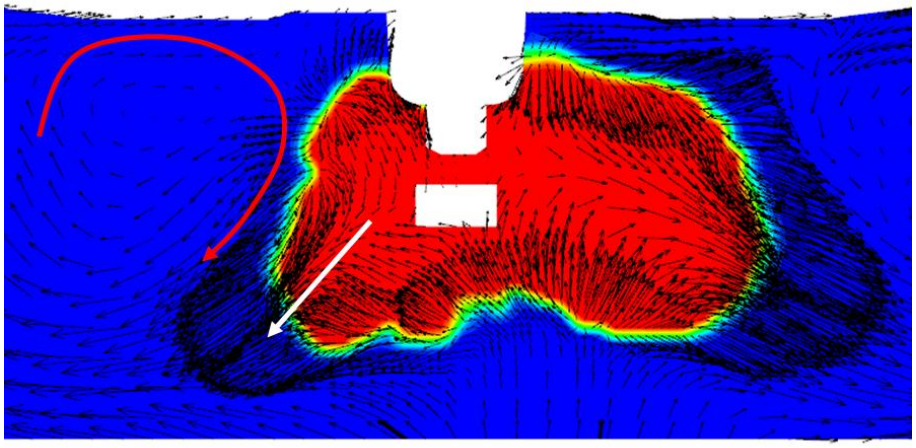

(b)

Figure 7.22 Progress variable and vector field of 4th cycle on front view (X=-2.6mm). (a) 707 CA, (b) 708 CA

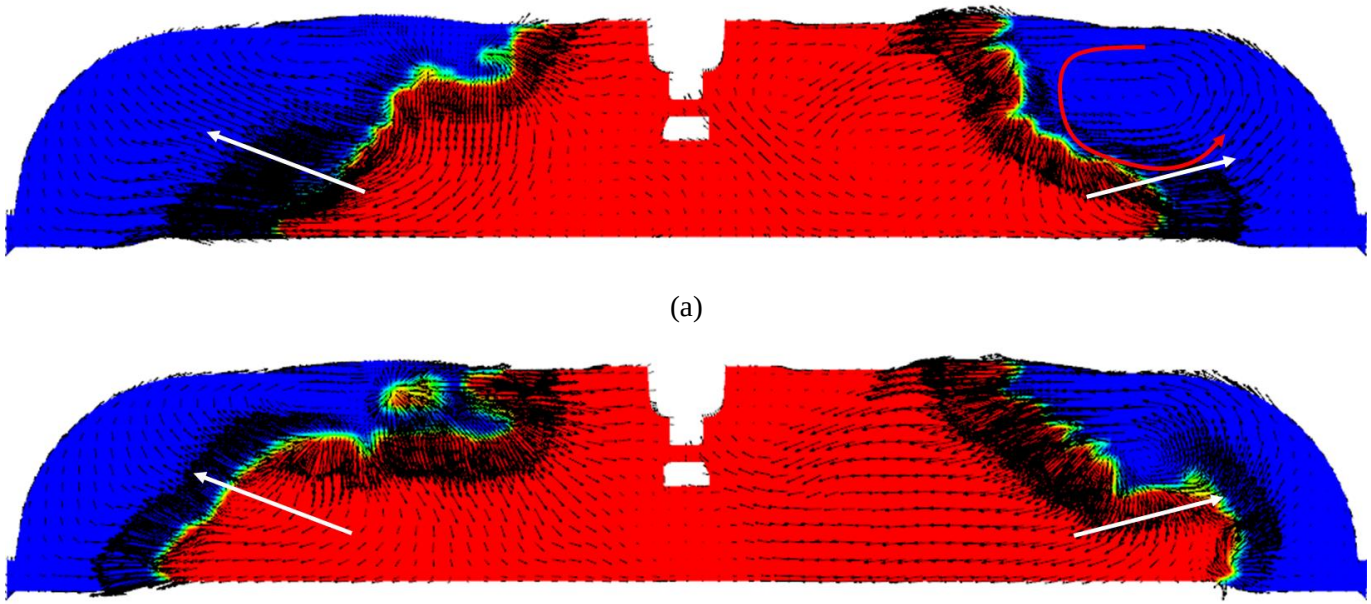

(a)

(b)

Figure 7.23 Progress variable and vector field of 4th cycle on front view (X=-2.6mm). (a) 717 CA, (b) 720 CA

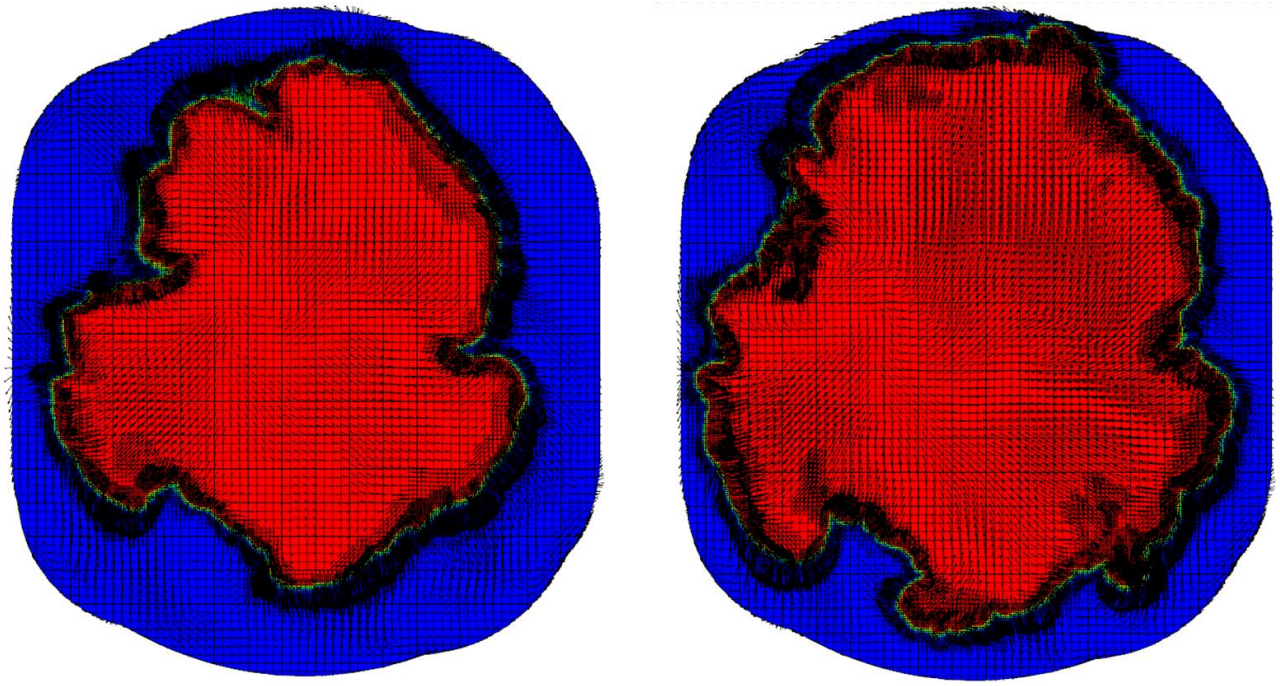

(a) (b)

Figure 7.24 Progress variable and vector field of 4th cycle on top view2 (X=2.3mm). (a) 720 CA, (b) 723 CA

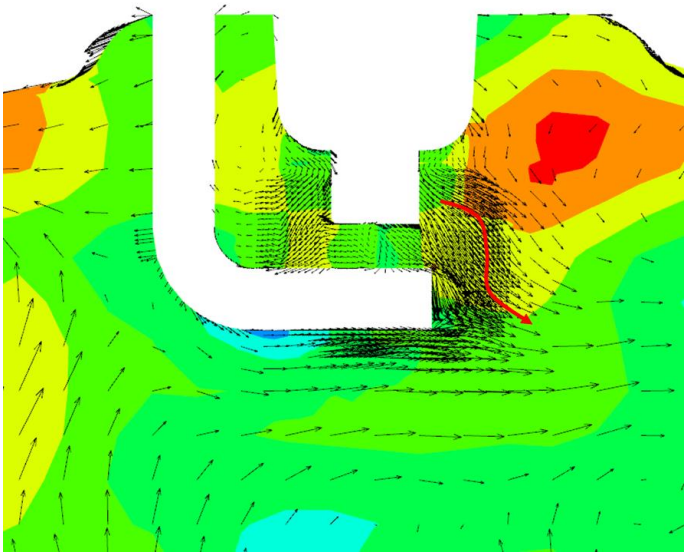

(a)

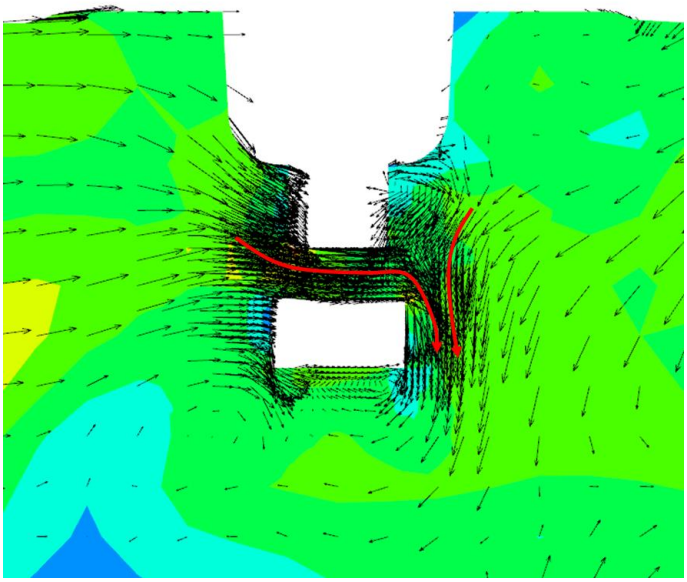

(b)

Figure 7.25 The vector field of 18th cycle at 699 CA. (a) Side view (Y=0mm), (b) Front view (X=-2.6mm)

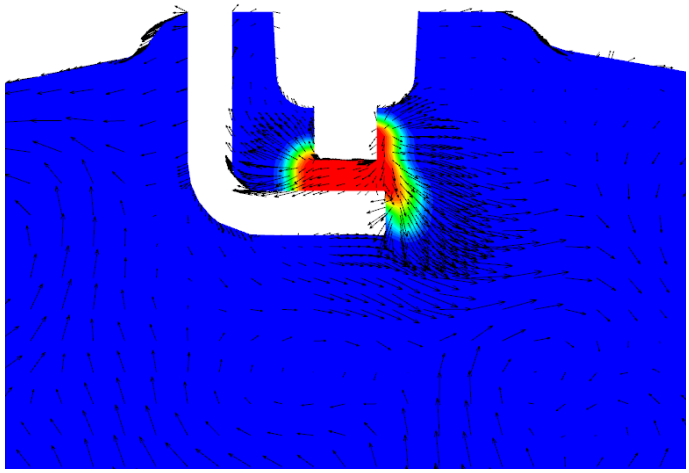

(a)

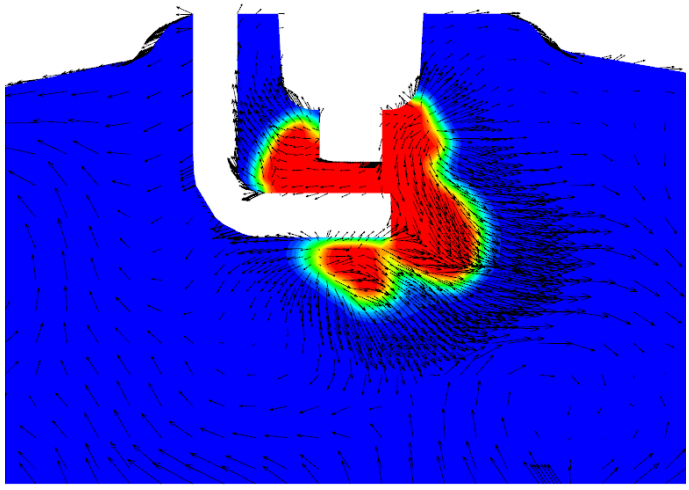

(b)

Figure 7.26 Progress variable and vector field of 18th cycle on side view (Y=0mm). (a) 703 CA, (b) 705 CA

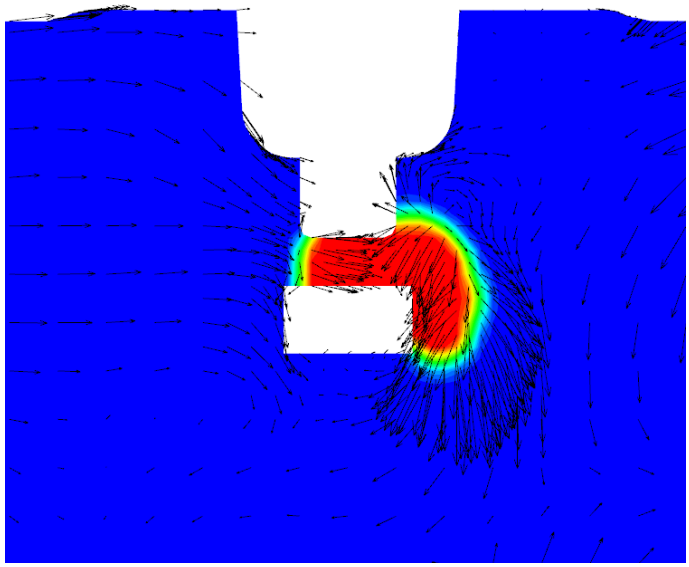

Figure 7.27 Progress variable and vector field of 18th cycle on front view (X=-2.6mm) at 702 CA.

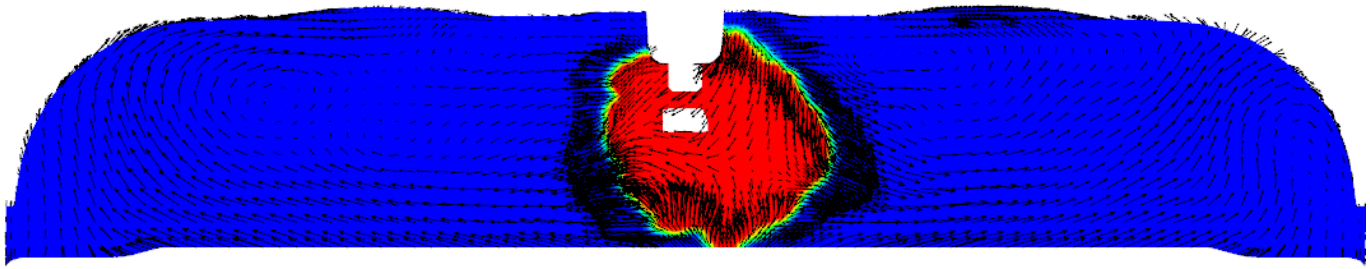

(a)

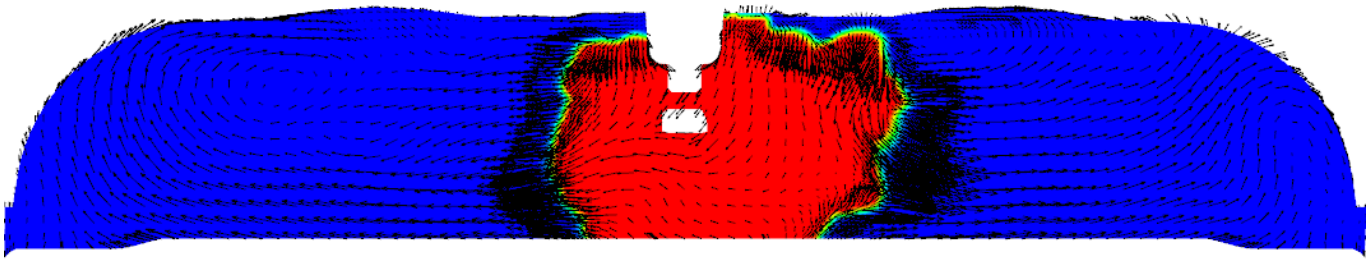

(b)

Figure 7.28 Progress variable and vector field of 18th cycle on front view (X=-2.6mm). (a) 709 CA, (b) 712 CA

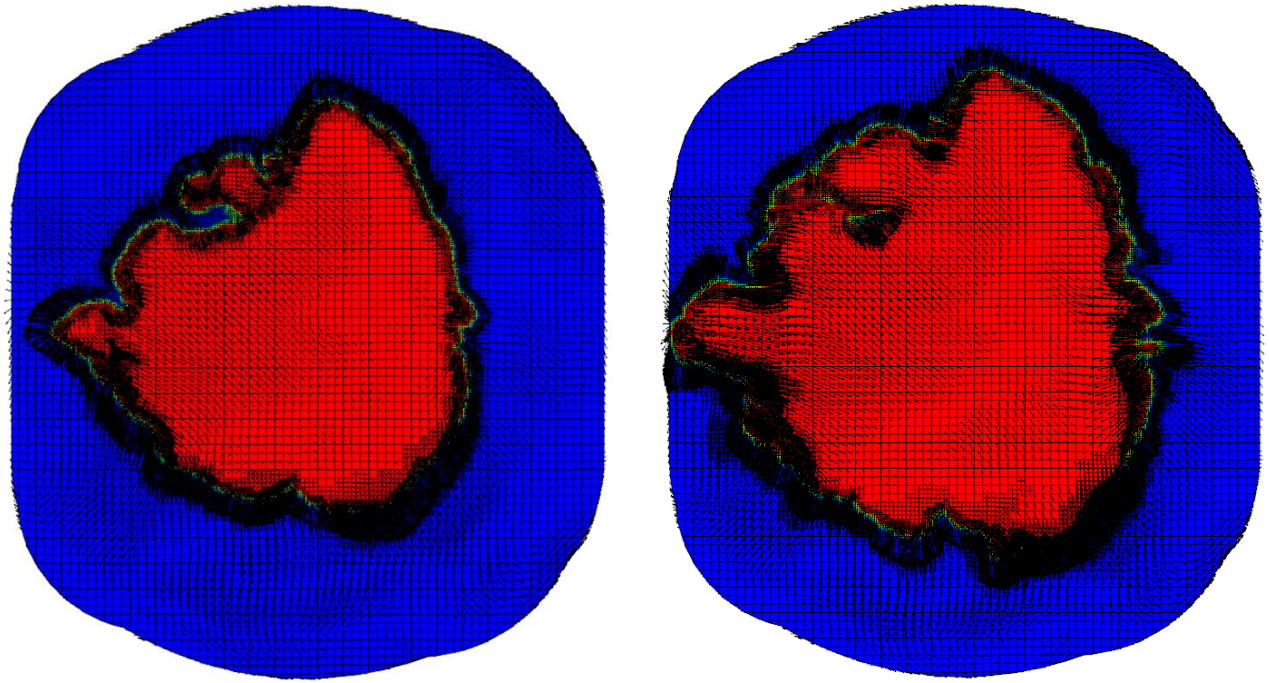

(a) (b)

Figure 7.29 Progress variable and vector field of 18th cycle on top view2 (X=2.3mm). (a) 720 CA, (b) 723 CA

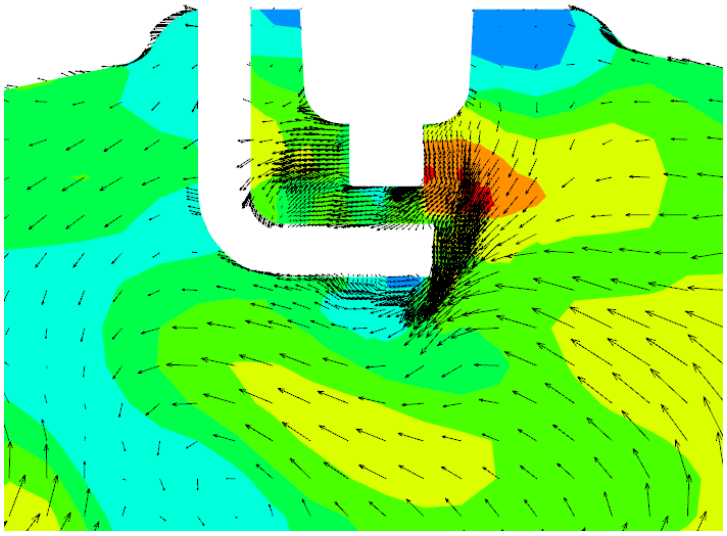

(a)

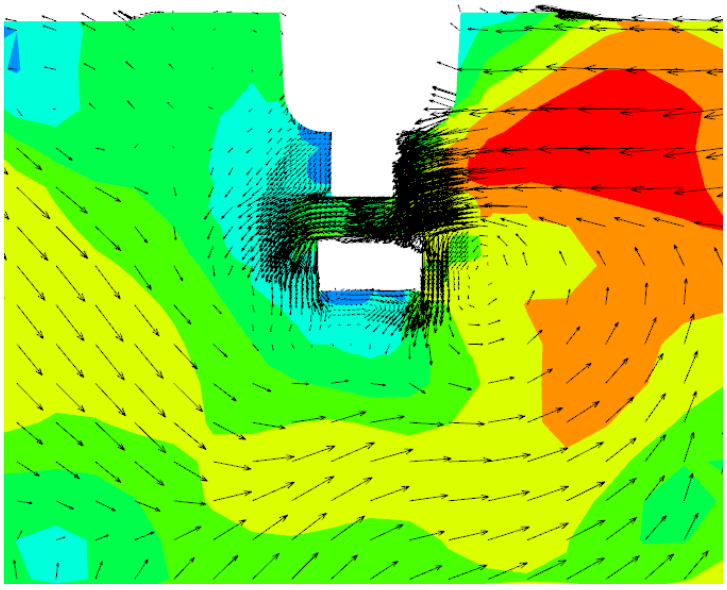

(b)

Figure 7.30 The vector field of 23th cycle at 699 CA. (a) Side view (Y=0mm), (b) Front view (X=-2.6mm)

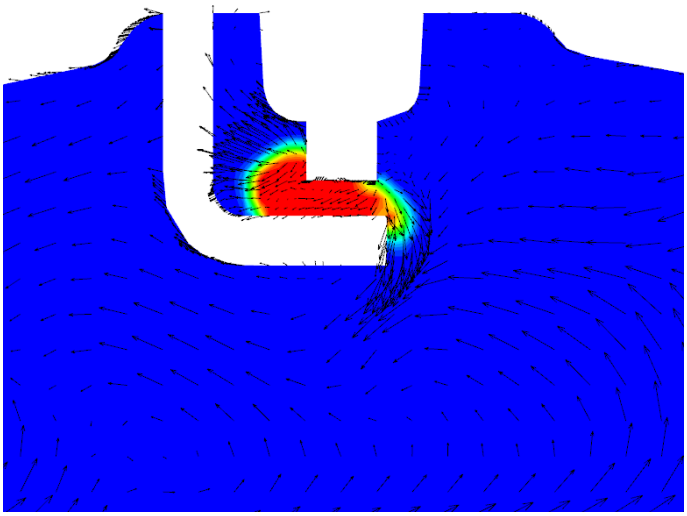

(a)

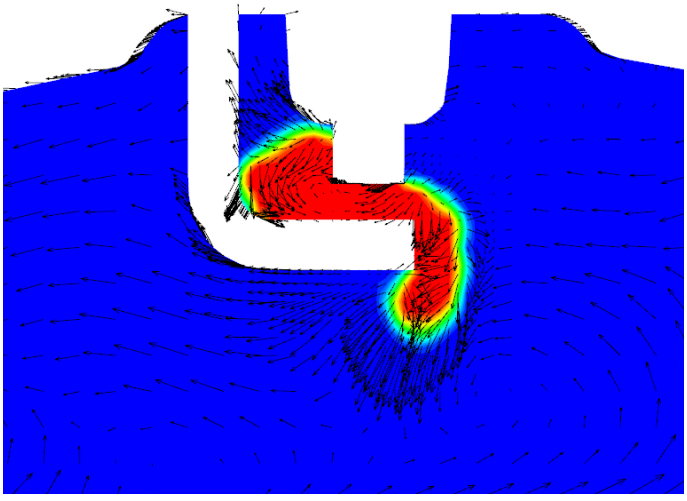

(b)

Figure 7.31 Progress variable and vector field of 23th cycle on side view (Y=0mm). (a) 703 CA, (b) 705 CA

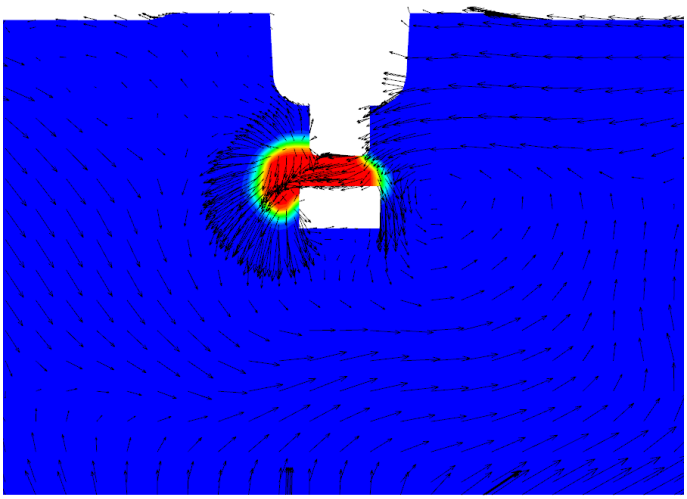

(a)

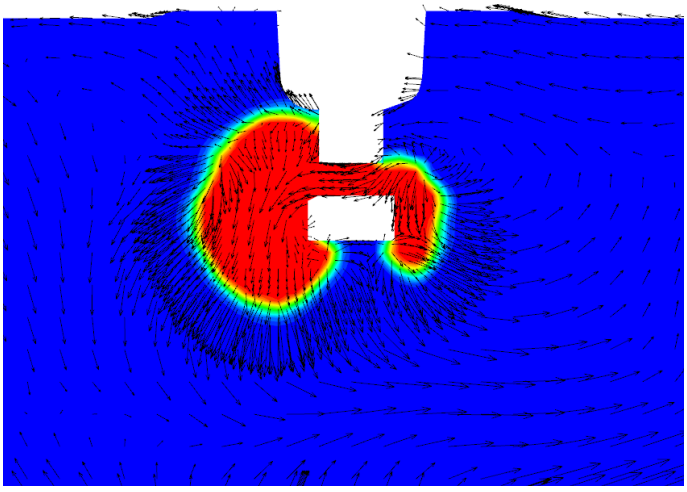

(b)

Figure 7.32 Progress variable and vector field of 23th cycle on front view (X=-2.3mm). (a) 702 CA, (b) 705 CA

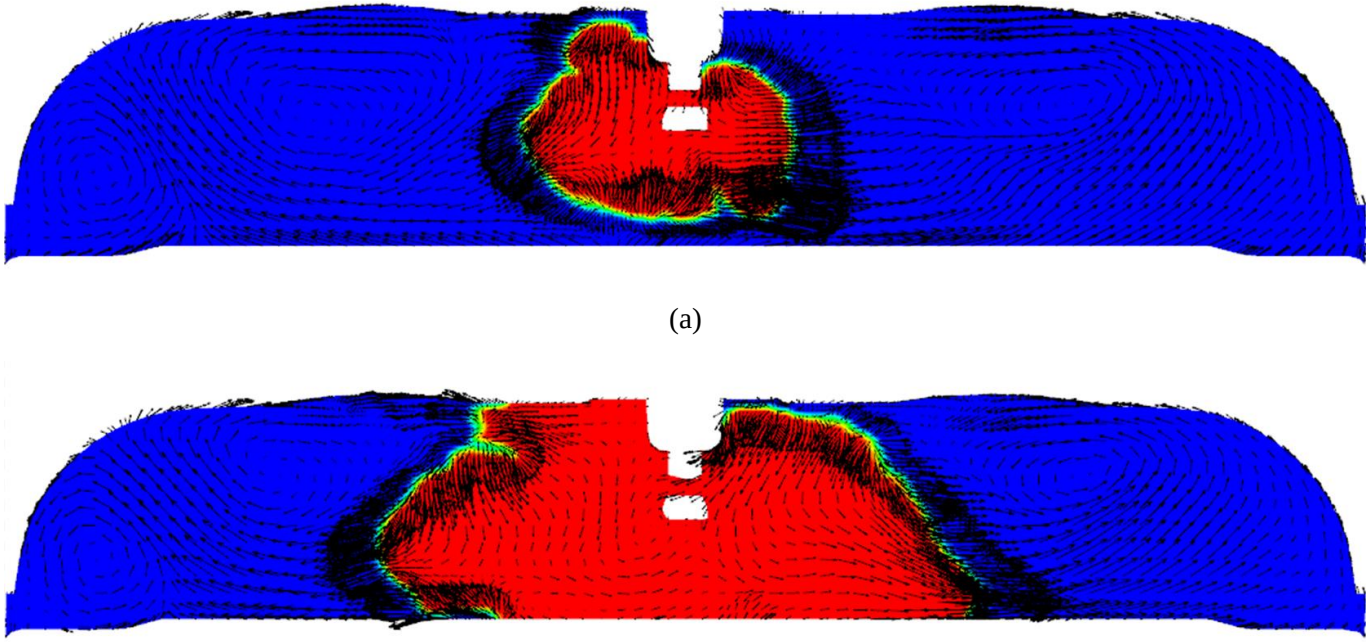

(a)

(b)

Figure 7.33 Progress variable and vector field of 23th cycle on front view (X=-2.6mm). (a) 709 CA, (b) 715 CA

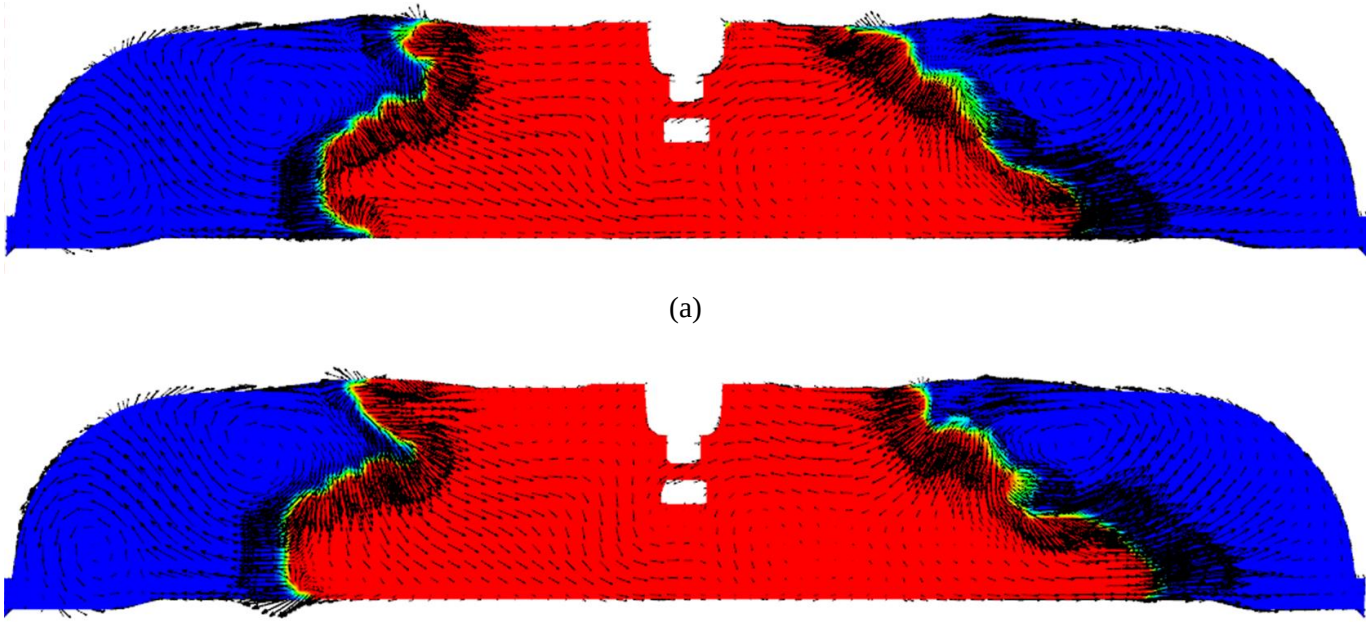

(a)

(b)

Figure 7.34 Progress variable and vector field of 23th cycle on front view (X=-2.6mm). (a) 718 CA, (b) 720 CA

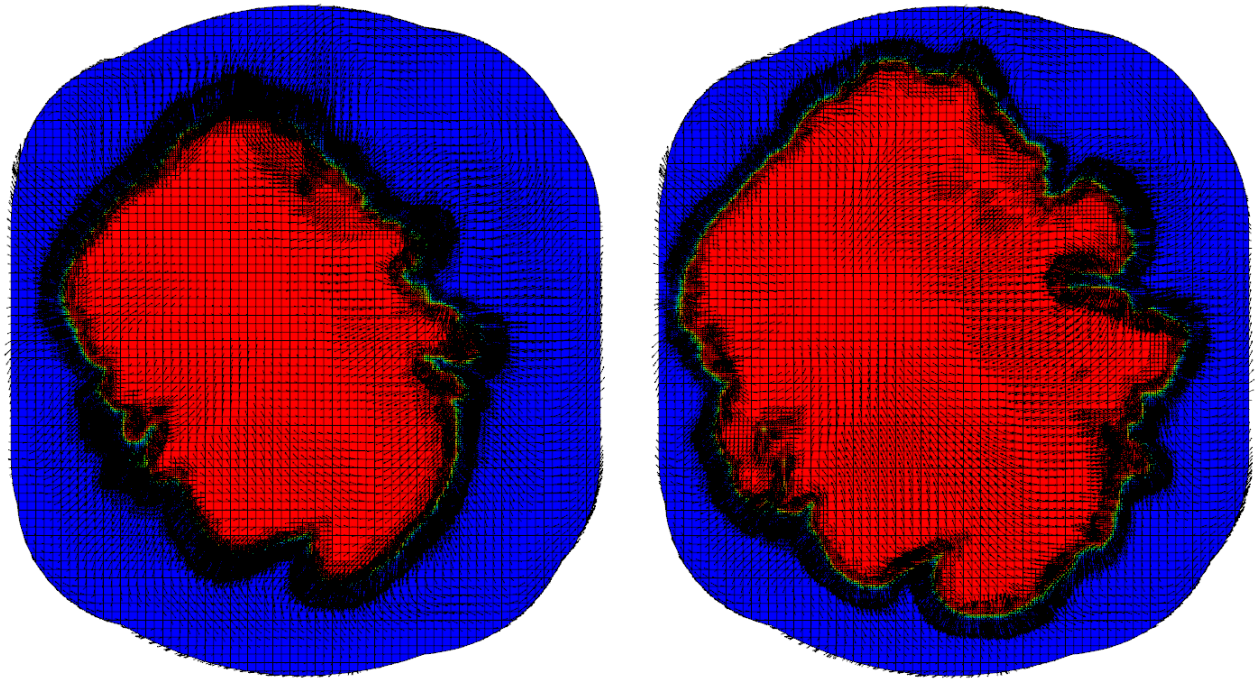

(a) (b)

Figure 7.35 Progress variable and vector field of 23th cycle on top view2 (X=2.3mm). (a) 720 CA, (b) 723 CA

7.4 Method for Reduction of CCV

7.4.1 Investigation of the Controllable Source of CCV

The factors affecting the CCV are the small scale turbulent flow and the local vortex which is the large scale turbulent flow. The way how to control the factors to reduce the CCV is investigated. It is generally known that the strong tumble flow can also lead to stronger turbulence. Therefore, at first, the controllability of the small scale turbulent flow and the tumble ratio is investigated. Next, the controllability of the local vortices is analyzed

Two cycles of the fastest and the slowest combustion phase are used to evaluate the controllability of turbulence flow: the 4th cycle is the fastest cycle, the 29th cycle is the slowest cycle as shown in Figure 7.6. In Figure 7.36, the SGS turbulent velocity distribution of the fastest and the slowest combustion cycle at the maximum intake valve lift timing is shown. There is no noticeable difference in the SGS turbulent velocity of two cycles from intake port to intake valve. There is also no noticeable difference in the vector field comparison similar to the comparison of the SGS turbulent velocity as shown in Figure 7.37.

The velocity field of two cycles during the compression process is analyzed. In Figures 7.38 and 7.39, the flow field is shown on the side view (Y=0mm) to investigate the tumble motion. Due to the flat piston shape, the tumble motion is not observed at 630 CA (Figure 7.38) and 660 CA (Figure 7.39). At 695 CA just before the ignition timing, the flow field of two cycles show randomness motion rather than the typical tumble motion as shown in Figure 7.40. Unlike the flow field observed in the side view, an organized flow motion is found in the front view. A strong wall flow on the left and right side is identified in the both the

fastest and the slowest combustion cycles during compression process as shown in Figure 7.41. In Figure 7.42, as compression progresses, a more organized wall flow is observed at 660 CA. As the wall flow in the fastest cycle is stronger than the wall flow in the slowest cycle as shown in Figure 7.42, the well-formed vortices can be observed in the fastest cycle just before ignition. In the front view, the importance of the wall flow to generate well-formed vortices is identified. Therefore, a new piston shape that can enhance the wall flow will be introduced and the result of reduced the CCV will be described in the following section.

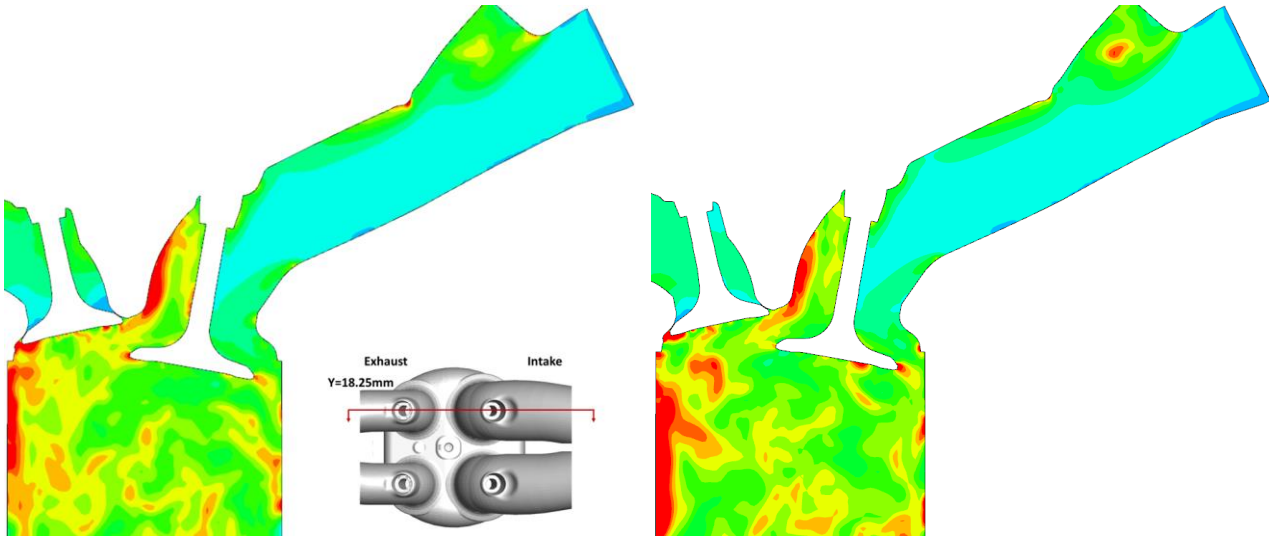

(a) (b)

Figure 7.36 The SGS turbulent velocity distribution of the fastest and the slowest combustion cycles on Y=18.25mm plane at the maximum intake valve lift timing (485 CA). (a) the fastest cycle (4th cycle), (b) the slowest cycle (29th cycle)

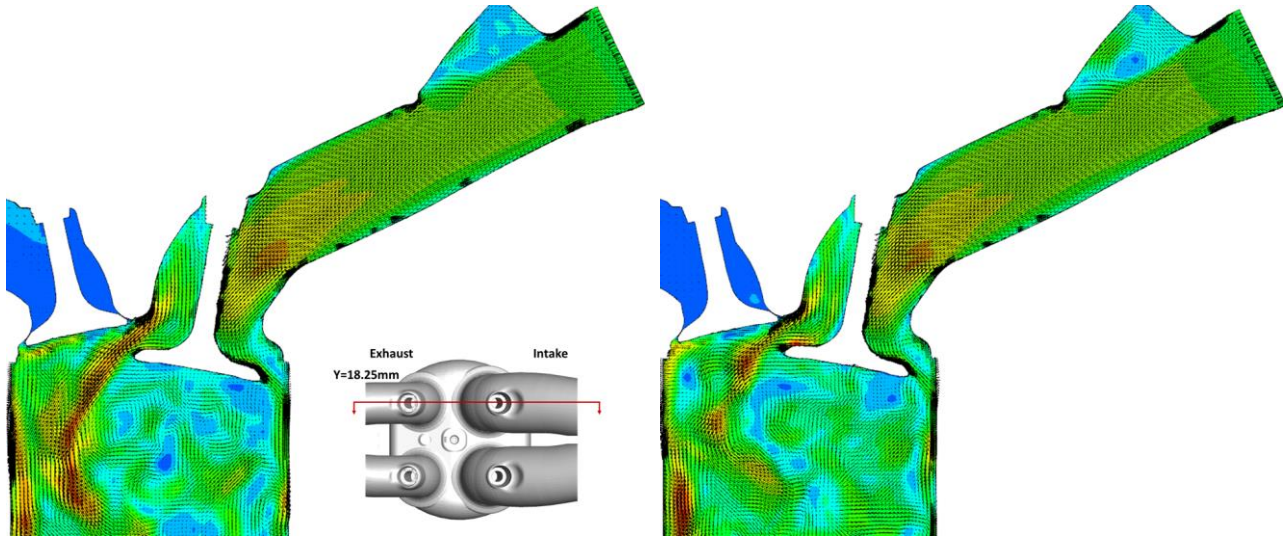

(a) (b)

Figure 7.37 The velocity distribution of the fastest and the slowest combustion cycles on Y=18.25mm plane at the maximum intake valve lift timing (485 CA). (a) the fastest cycle (4th cycle), (b) the slowest cycle (29th cycle)

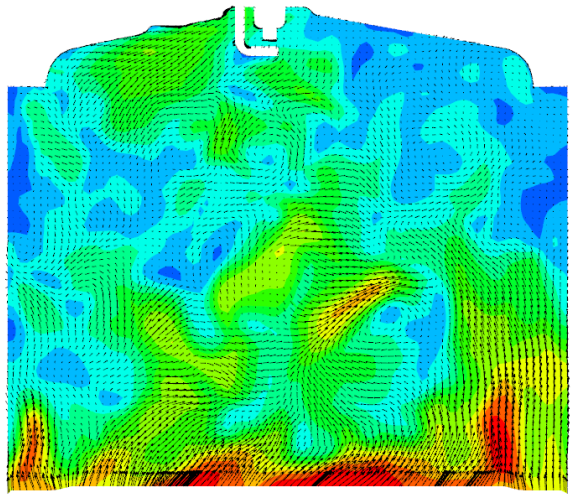

(a)

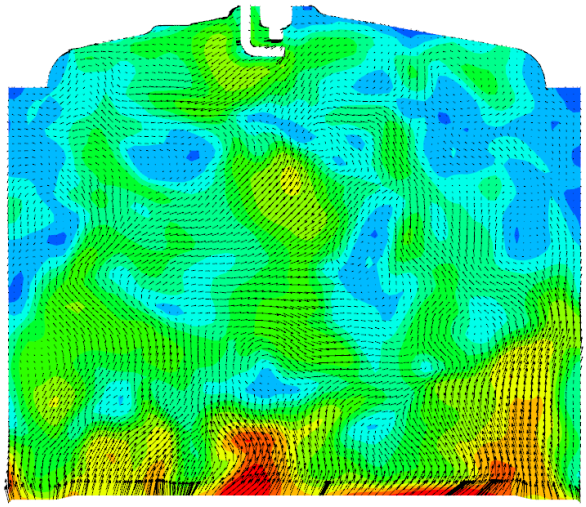

(b)

Figure 7.38 The velocity distribution of the fastest and the slowest combustion cycles on the side view (Y=0mm) at 630 CA. (a) the fastest cycle (4th cycle), (b) the slowest cycle (29th cycle)

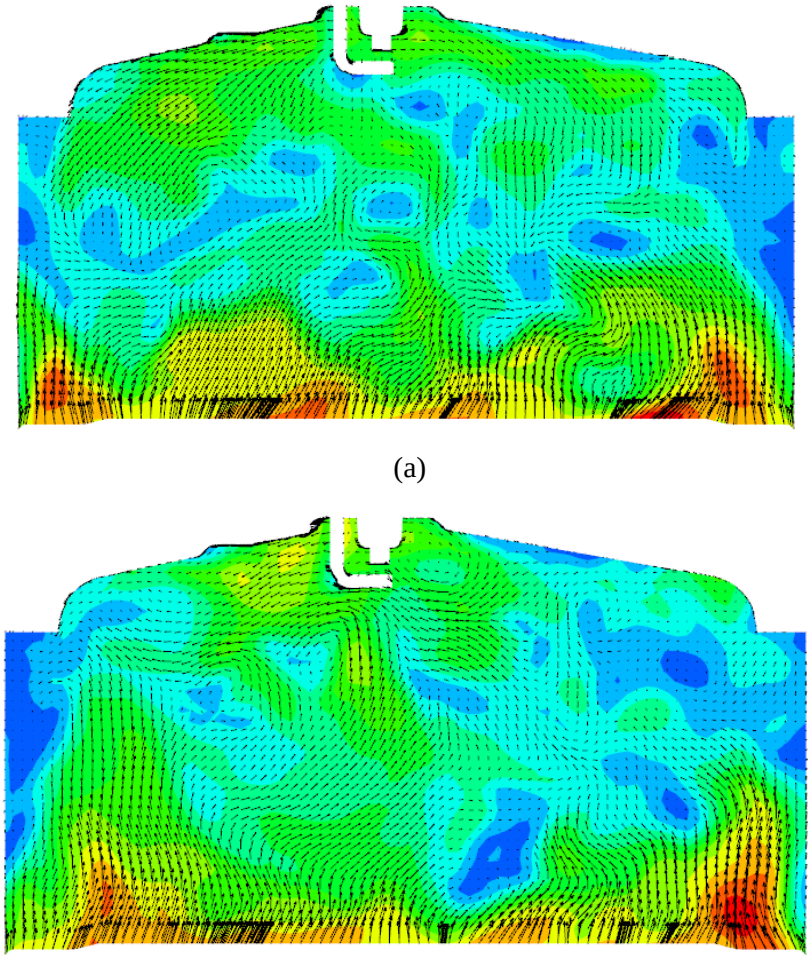

(a)

(b)

Figure 7.39 The velocity distribution of the fastest and the slowest combustion cycles on the side view (Y=0mm) at 660 CA. (a) the fastest cycle (4th cycle), (b) the slowest cycle (29th cycle)

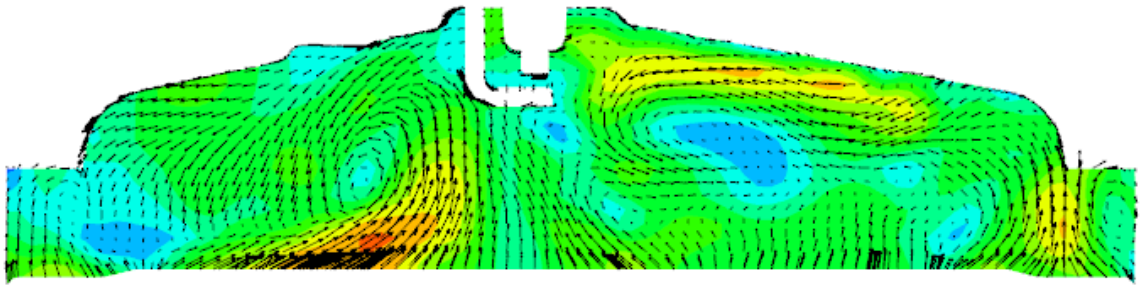

(a)

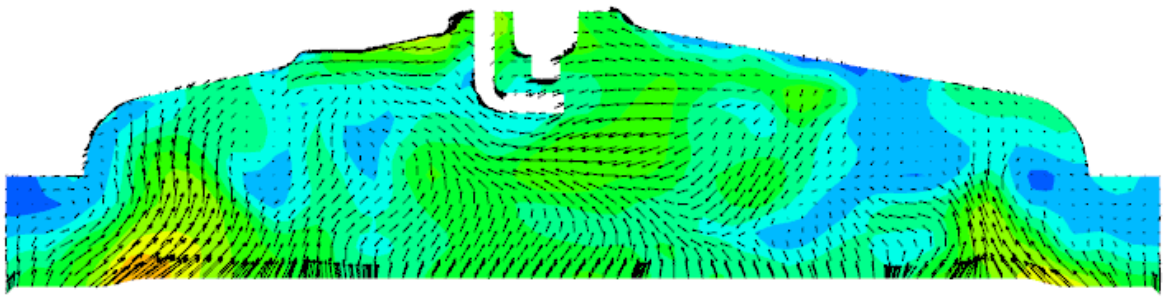

(b)

Figure 7.40 The velocity distribution of the fastest and the slowest combustion cycles on the side view (Y=0mm) at 695 CA. (a) the fastest cycle (4th cycle), (b) the slowest cycle (29th cycle)

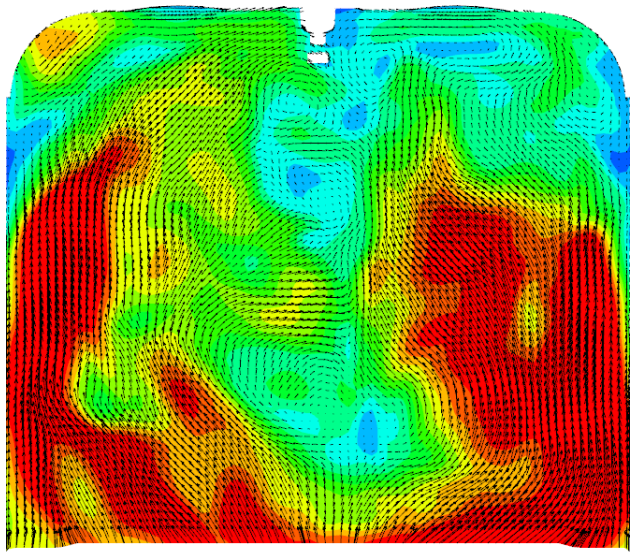

(a)

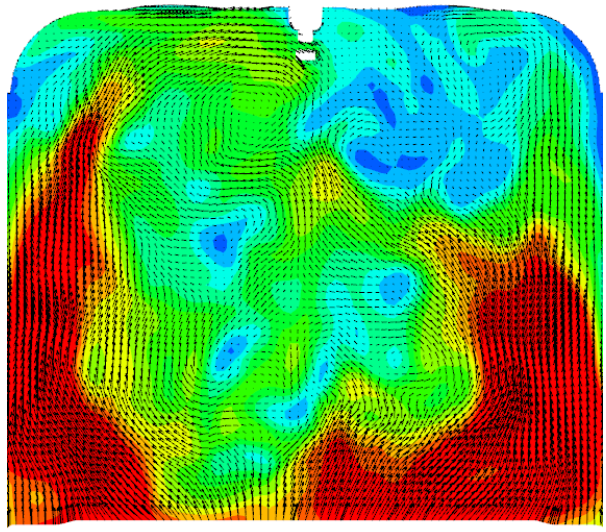

(b)

Figure 7.41 The velocity distribution of the fastest and the slowest combustion cycles on the front view (X=-2.6mm) at 630 CA. (a) the fastest cycle (4th cycle), (b) the slowest cycle (29th cycle)

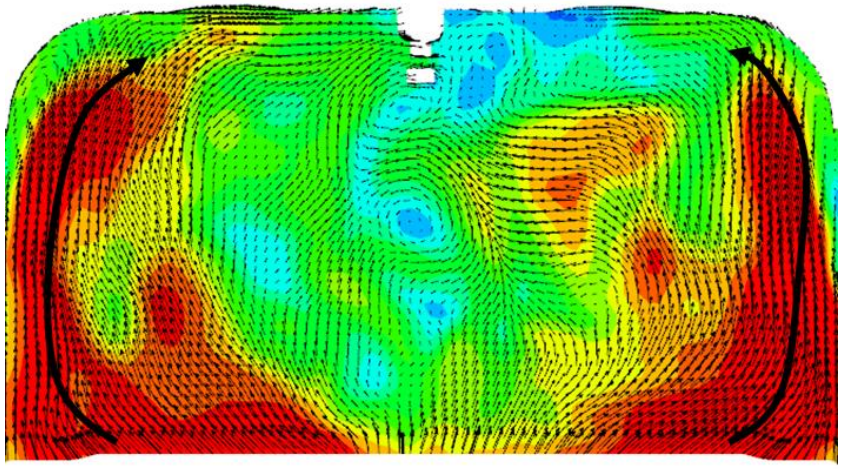

(a)

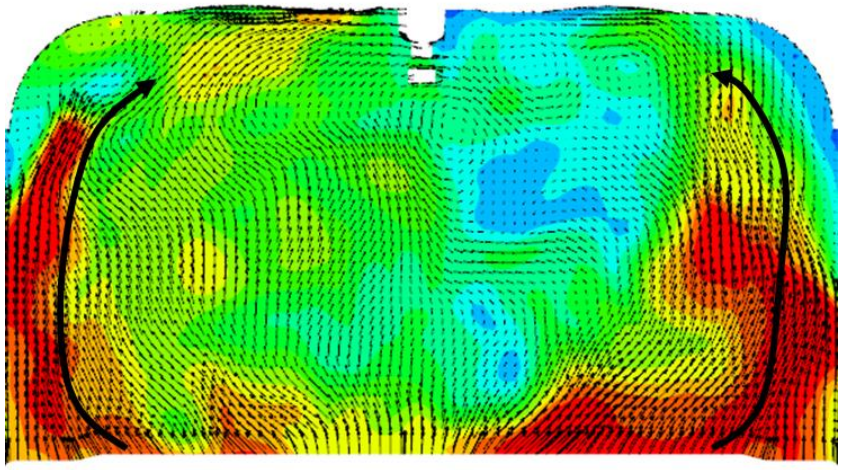

(b)

Figure 7.42 The velocity distribution of the fastest and the slowest combustion cycles on the front view (X=-2.6mm) at 660 CA. (a) the fastest cycle (4th cycle), (b) the slowest cycle (29th cycle)

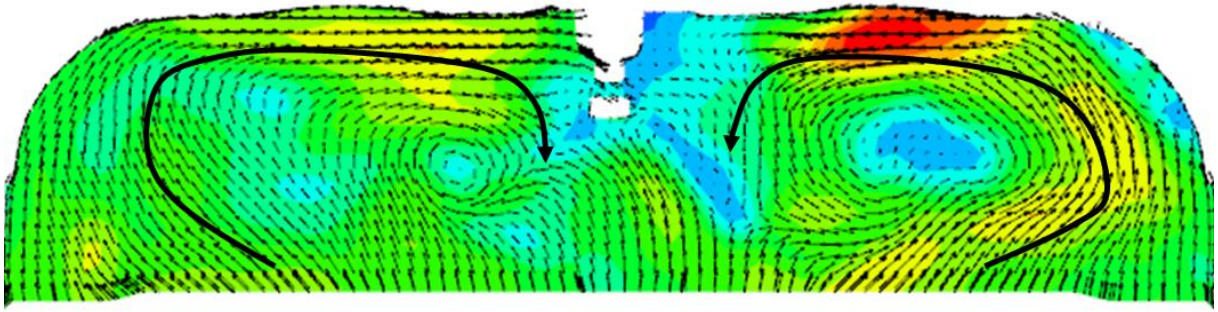

(a)

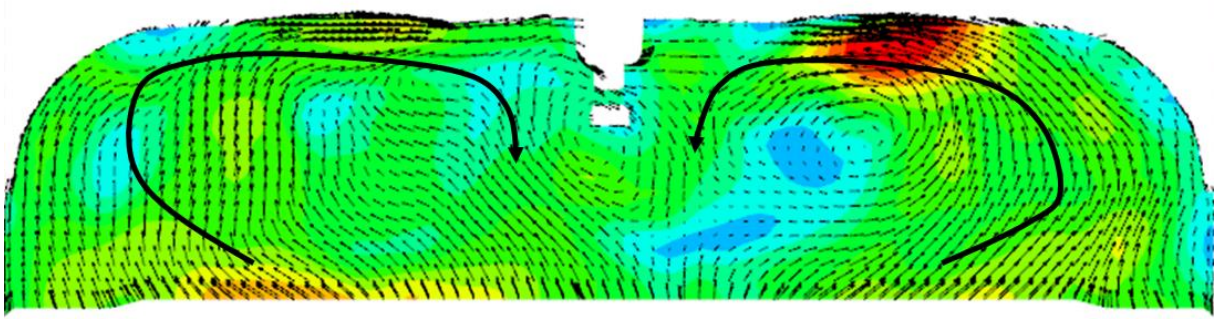

(b)

Figure 7.43 The velocity distribution of the fastest and the slowest combustion cycles on the front view (X=-2.6mm) at 695 CA. (a) the fastest cycle (4th cycle), (b) the slowest cycle (29th cycle)

7.4.2 Result of New Designed Piston

Figure 7.44 shows a new designed piston shape that enhances wall flow at the end of compression to make a vortex formation better. The width of the left and right sides is reduced by 2mm from 6.3mm to 4.3mm, and the height of the top of the piston is raised by 1mm to strengthen the wall flow. At first, the new designed piston is evaluated by using RANS approach. The numerical setup of RANS is identical to the numerical setup for LES introduced in chapter 6. except the turbulence model. Figure 7.45 shows the vector field of the base piston case and the new designed piston case on the front view (X=-2.6mm) at 695 CA. Vortices are observed in the both case. Due to the intended wall flow of the new piston case, the vortices of the new piston case is more distinctly generated than the base piston case.

The 14 LES cycles of the new piston case are conducted to compare the COV of peak pressure with base case. The numerical setup is the same as the base case described in chapter 6. The in-cylinder pressure curves of LES are compared with the experimental data in Figure 7.46. The range of pressure curves is narrower than the base case shown in Figure 7.1. Even though the sample of the new piston case is not enough, the trend of the reduced COV of peak pressure is observed in Figure 7.47. When the number of samples in the base case of LES is 14 cycles same as in the new case, the COV of peak pressure for the base case is 8.44% and the COV of the new case is 5.83%. Therefore, the enhanced vortices formation is effect for combustion CCV. However, the average combustion pressure is predicted to be somewhat lower than the experimental data. For quantitative comparison, the MFB values of the experiment, the base case and the new piston case are compared in Figure 7.48. Both the base and the new piston cases are well

matched with the experimental results up to the MFB 10. However, in the case of the new piston result, the MFB 90 value slows down as flame propagates.

The reason why the combustion of the new piston case slows down in the latter phase is identified in Figure 7.49. Figure 7.49 describes the vector field of the base and the new piston cases calculated by using RANS approach under the cold-flow condition at 715 CA when is the timing of the MFB 10. There is no flow separation in the base case, but the separations are identified on the left and right ends of the piston in the new piston case. Because of the unfavorable flow behavior, the flame propagation of the new piston case slows down in the latter phase. Because the new piston is designed only in terms of reducing the CCV, it results in the unintended consequence of slowed combustion speed. Nevertheless, it is identified that the formation of vortex by the enhanced wall flow plays an important role in reducing the combustion CCV. Furthermore, if the piston is well designed to form a flow that helps the combustion speed, both rapid combustion phase and the CCV reduction can be achieved.

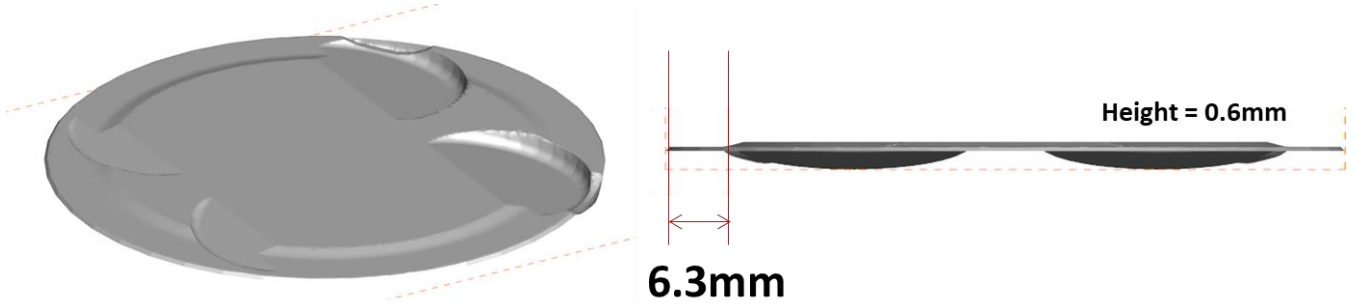

(a)

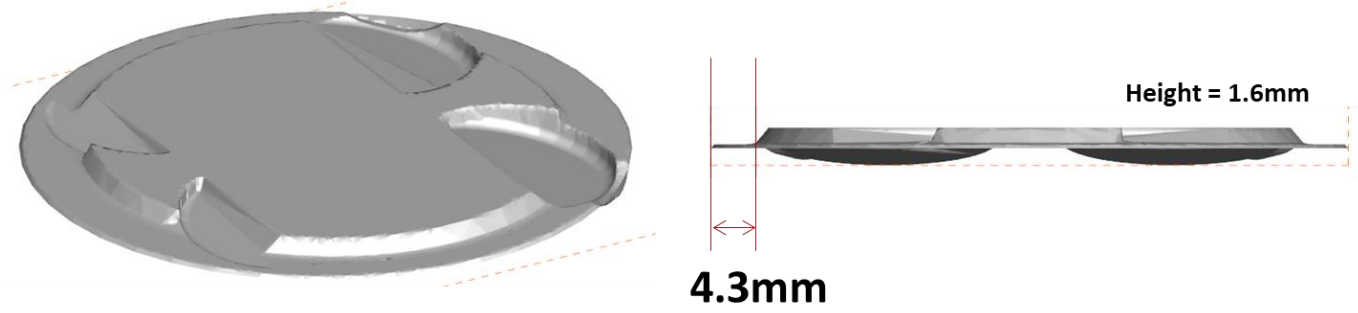

(b)

Figure 7.44 The base piston and new designed piston shape. (a) Base piston, (b) New piston

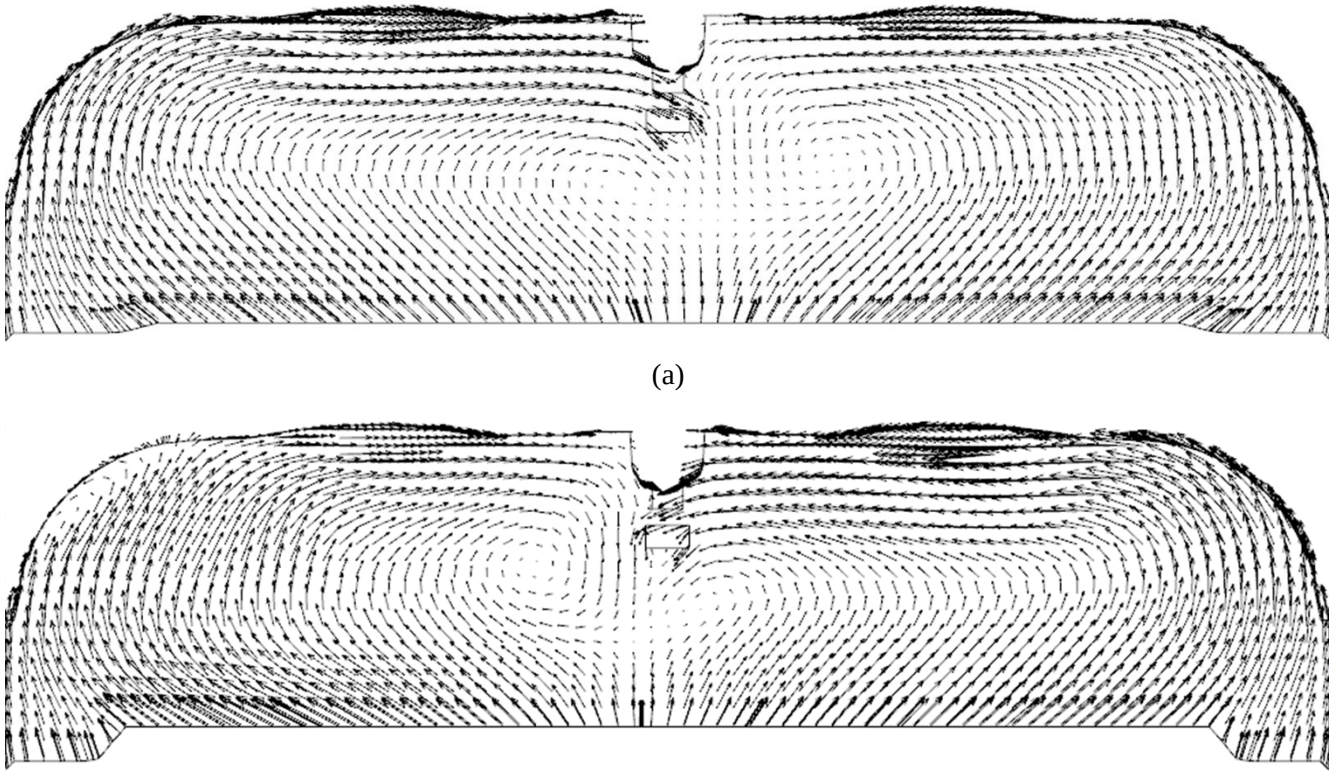

(a)

(b)

Figure 7.45 The vector field of the base piston case and the new piston case on the front view (X=-2.6mm) at 695 CA. (a) Base piston, (b) New piston

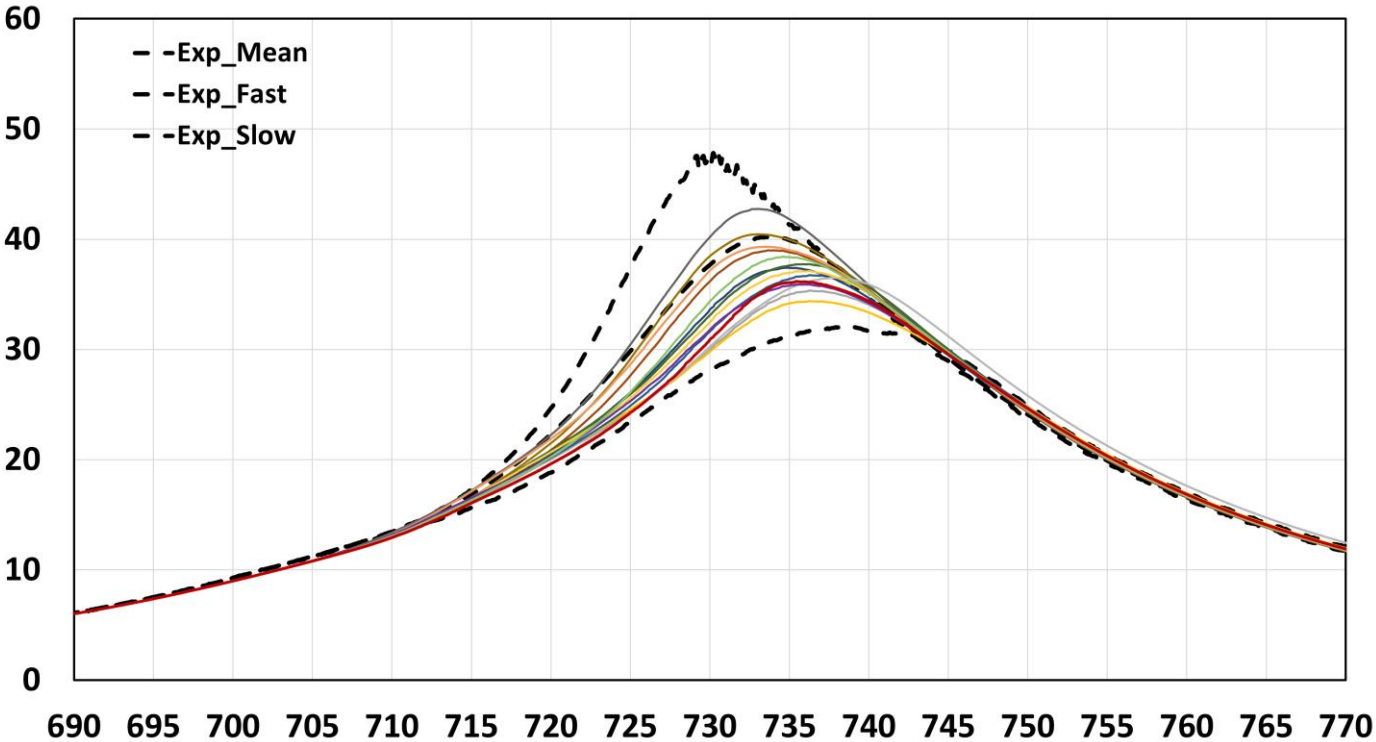

Figure 7.46 Comparison of in-cylinder pressure between LES (new piston) and experimental data

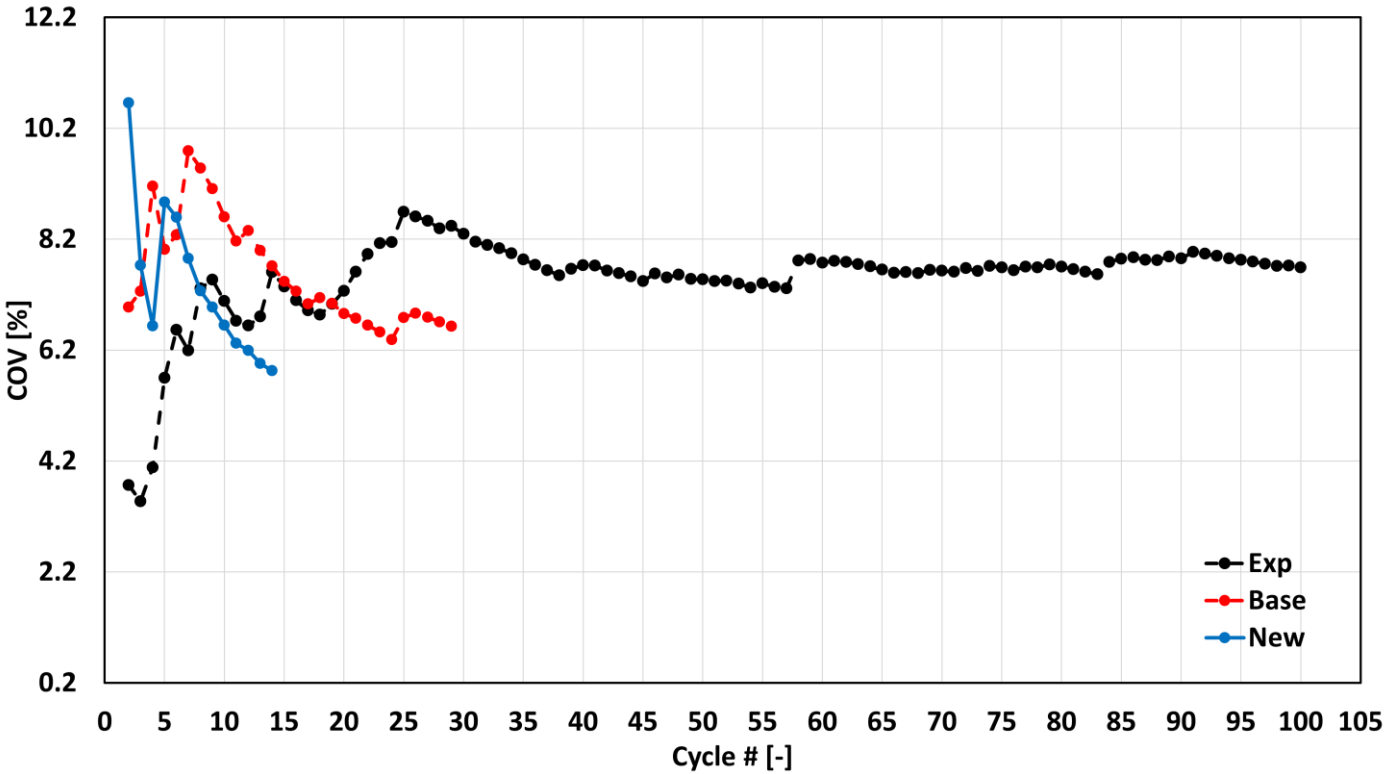

Figure 7.47 The cumulative COV of peak pressure. Black dotted line: experiments, red dotted line: base, blue solid line: new piston

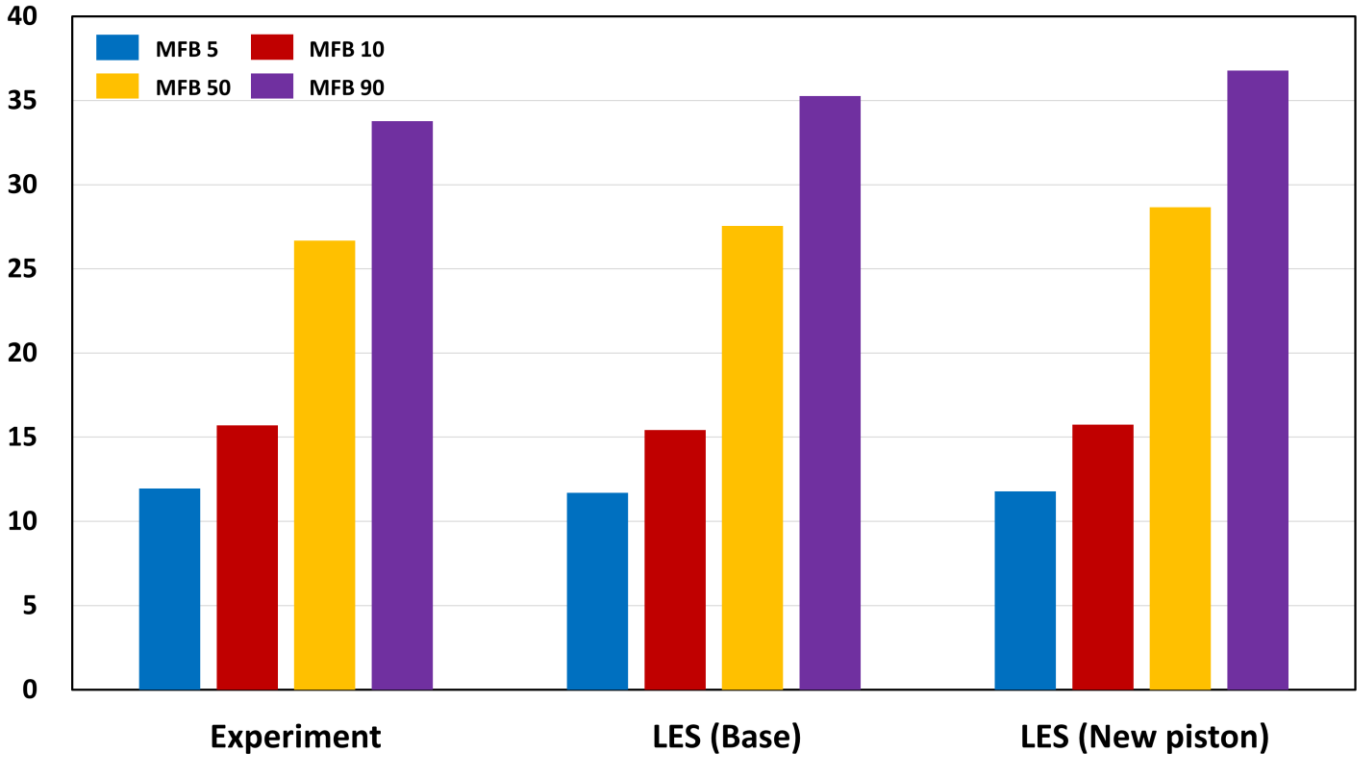

Figure 7.48 Comparison of MFB among experimental data, LES result of base case and LES result of new piston case

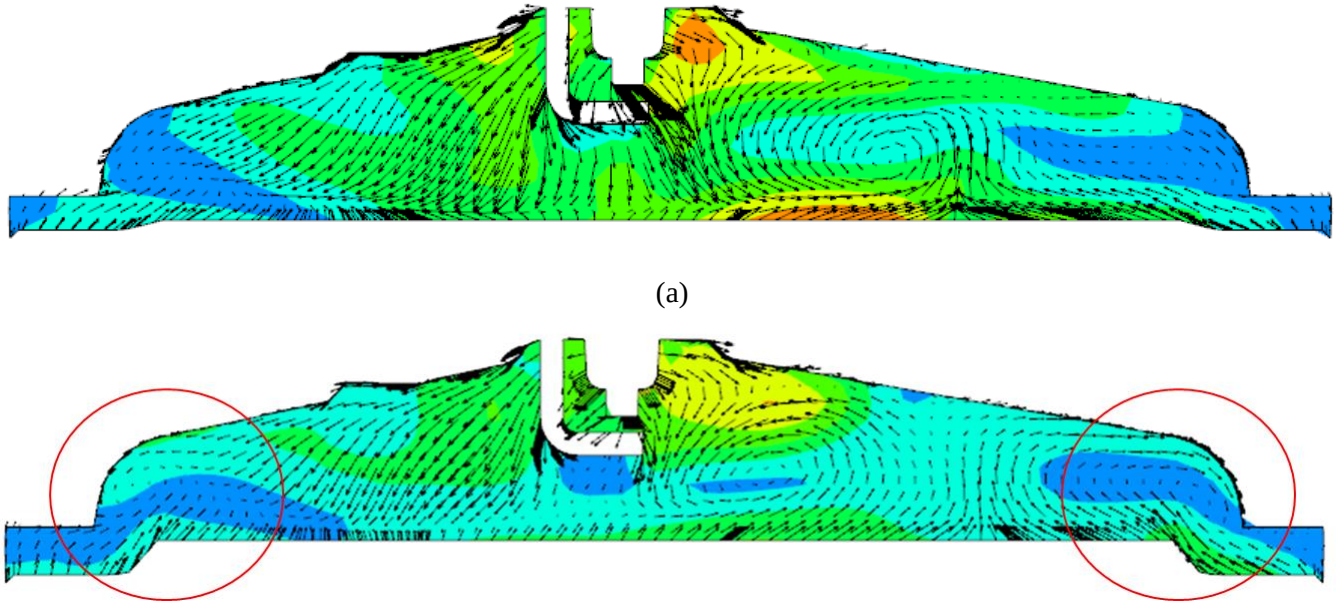

(a)

(b)

Figure 7.49 The comparison of vector field between base case and new piston case calculated by using RANS approach on the front view (X=-2.6mm) at 715 CA. (a) Base case and (b) New piston case

Chapter 8. Conclusions

In this study, the multi-cycle LES is conducted to reproduce the combustion CCV of the engine using the lagrangian ignition model reflecting the characteristics of LES. The investigation of the turbulent flow effect on the combustion CCV is conducted with the verified LES results. The main source of CCV is found and the guide to reduce the combustion CCV is provided.

First of all, the cold-flow engine simulation was conducted to evaluate the SGS turbulent model that could accurately simulate the in-cylinder flow motion. The PIV experimental data performed on the TCC-III single cylinder optical engine designed by University of Michigan and GM research center was used as validation data. Three SGS turbulent models were compared with the PIV data in terms of the velocity field in a combustion chamber. The most common used the static Smagorinsky model, the dynamic Smagorinsky and the 1-equation dynamic structure model with the transport equation for the SGS turbulent kinetic energy were compared. In terms of the prediction of velocity field, the dynamic Smagroinsky and the DSM were well matched with the PIV data. The LES quality index was used to assess the impact of the SGS turbulent model. The LES quality index can evaluate the contribution of the SGS model effect on the turbulent flow. Thanks to the superior concept of dynamically calculated model coefficient, the dynamic Smagorinsky and the DSM showed the proper contribution of the SGS model with 1mm of in-cylinder grid size, leading to reasonable computational cost. Although the accuracy of both the dynamic Smagorinsky model and the DSM was excellent, the DSM was adopted because of the numerical stability coming from the transport equation of the SGS turbulent kinetic energy and the theoretical advantages of the one-equation model.

To predict combustion phenomena, the G-equation combustion model was adopted. Pitsch [67] proposed the G-equation model for LES. The author derived the sub-filtered G-equation for the corrugated flamelets regime and the thin reaction flamelets regime based on the Peter's research [45]. The turbulent burning velocity for both the corrugated flamelets regime and the thin reaction flamelets regime is quite complicated with many model coefficients. The model coefficients are typically derived for RANS approach. Therefore, the adjustment of the model coefficient is necessary, but too many coefficients make it difficult to find proper values. Thus, it is important to identify which combustion regime belongs to under engine conditions to define the turbulent flame speed. Through RANS approach, it is verified that the target engine condition belongs to the corrugated flamelets regime. Therefore, the turbulent burning velocity is derived for the corrugated flamelets regime based on the Pitsch's work [67]. Finally, a very simple equation of the turbulent burning velocity with only one model coefficient is derived. The coefficient value is found with the validation of in-cylinder pressure against the experimental data.

The ignition model is developed for LES. At first, lagrangian particles are employed to predict the behavior of the ignition channel. The elongation of the ignition channel by turbulent flow can be reproduced. The secondary electric circuit model is used to calculate the spark energy, and it can predict the restrike and the end of ignition time. Immediately after the breakdown phase, the plasma channel at high temperature grows by the thermal expansion for a short time (~10μs). Generally, the thermal expansion is calculated using the 1D sub-cycle model, but it requires a lot of computational time, which is not suitable for multi-cycle LES. Therefore, in the present study, the empirical function is derived to predict the time, temperature and radius of the ignition channel after end of the arc phase. At first, the 1D simulation for the thermal expansion is conducted under various ambient temperature and pressure conditions to build the database. Next,

the empirical function is derived based on the database. After the thermal expansion, the channel grows by chemical reaction and flame propagation progresses. In the early stage, the flame is thin and unstable, so it is propagated by the laminar burning velocity. And over time, the flame is propagated by the turbulent burning velocity. The turbulent frame brush thickness term suitable for LES is introduced to predict the transition state between laminar flame propagation and turbulent flame propagation. Finally, when the channel is grown sufficiently, flame is propagated in the 3D field by the G-equation.

The multi-cycle engine simulation is performed using the SGS turbulent model, the combustion model and the developed ignition model. The accuracy of simulation is verified compared to the experimental data in terms of the in-cylinder pressure, the combustion phase and the COV of peak pressure. Next, the turbulent flow effect on the combustion CCV is investigated to find the source of the CCV. In this study, LES results are analyzed from two perspectives: the small scale turbulent flow and the large scale turbulent flow. In LES, the small scale turbulent flow is realized by the SGS turbulent velocity and the large scale turbulent flow is reflected in the velocity field. Before the ignition timing, the volume averaged SGS turbulent velocity in in-cylinder is analyzed. During the compression process, the SGS turbulent velocity of the fast combustion cycles increased than the SGS turbulent velocity of the slow cycles, and after ignition, the SGS turbulent velocity of the fast cycles around the flame surface continued to be greater. However, when the correlation between the SGS turbulent velocity and the MFB 50 is analyzed, it is found that the SGS turbulent velocity has an effect on the combustion speed but it is not absolute.

Next, the large scale turbulent flow effect on the combustion CCV is investigated. First of all, the tumble ratios, typical large scale turbulent flow, is analyzed. The negligible effect of the secondary tumble and swirl is observed.

However, the conversion of the energy contained in the main tumble into the SGS turbulent velocity during the compression process is identified. To analyze the direct effect of the large scale turbulence flow on combustion, the representative four cycles of velocity field and the flame propagation are analyzed. It is turned out that he local vortex effect is an important factor for the combustion CCV. The velocity distribution and the SGS turbulent velocity field are investigated to find out the controllable factor to reduce the CCV. Finally, the possibility of reducing the combustion CCV is found by enhancing the wall flow to generate intended vortices.

The new piston is designed to strengthen the wall flow. RANS approach is used to evaluate the effect of the new piston shape before performing multi-cycle LES. Based on RANS result, the multi-cycle LES of the new piston shape is conducted and compared with the base case in terms of the combustion CCV. The new designed piston case results in the lower CCV than the base piston case. However, because of the unintended flow separation on the end of the piston, the combustion speed is slower than the base case. The drawback of the new piston can be easily improved by a design change. Finally, despite of the slow combustion speed, the new piston shape can reduce the combustion CCV.

This research includes study of the SGS turbulent model for the ICE, the combustion model, the ignition model and the effect of turbulent flow on the combustion CCV. From the results, the main source of the CCV and the possibility of the controllability are found. The new piston results show the reduced CCV of combustion. Therefore, this study can contribute to provide the guide how to analyze and reduce the combustion CCV in SI engines.

Chapter 9. Bibliography

[1] Sources of Greenhouse Gas Emissions, United States Environmenatl Protection Agency (EPA). Available from: https://www.epa.gov/ghgemissions/sources-greenhouse-gas-emissions

[2] K. Min, Future IC Engine Technology: Toward Near Zero CO2 and Exhaust Emissions, china Engine Technology Summit, 2020.

[3] B. John, Heywood, Internal combustion engine fundamentals, Pub: McGraw Hill International Editions, (1988).

[4] X. Baby, A. Dupont, A. Ahmed, W. Deslandes, G. Charnay, M. Michard, A new methodology to analyze cycle-to-cycle aerodynamic variations, in, SAE Technical Paper, 2002.

[5] J. Bode, J. Schorr, C. Krüger, A. Dreizler, B. Böhm, Influence of three-dimensional in-cylinder flows on cycle-to-cycle variations in a fired stratified DISI engine measured by time-resolved dual-plane PIV, Proceedings of the Combustion Institute, 36 (2017) 3477-3485.

[6] T. Fujikawa, Y. Nomura, Y. Hattori, T. Kobayashi, M. Kanda, Analysis of cycle-by-cycle variation in a direct injection gasoline engine using a laser-induced fluorescence technique, International Journal of Engine Research, 4 (2003) 143-153.

[7] S. Hokimoto, T. Kuboyama, Y. Moriyoshi, M. Iida, T. Watanabe, Analyses of Cycle-to-Cycle Variation of Combustion and In-Cylinder Flow in a Port Injection Gasoline Engine Using PIV and PLIF Techniques, in: SAE Technical Paper Series, 2017.

[8] S. Fontanesi, A. D'Adamo, S. Paltrinieri, G. Cantore, C. Rutland, Assessment of the Potential of Proper Orthogonal Decomposition for the Analysis of Combustion CCV and Knock Tendency in a High Performance Engine, in: SAE Technical Paper Series, 2013.

[9] D. Goryntsev, A. Sadiki, M. Klein, J. Janicka, Large eddy simulation based analysis of the effects of cycle-to-cycle variations on air–fuel mixing in realistic DISI IC-engines, Proceedings of the Combustion Institute, 32 (2009) 2759-2766.

[10] M. Schmitt, R. Hu, Y.M. Wright, P. Soltic, K. Boulouchos, Multiple Cycle LES Simulations of a Direct Injection Natural Gas Engine, Flow, Turbulence and Combustion, 95 (2015) 645-668.

[11] N. Van Dam, C. Rutland, Understanding In-Cylinder Flow Variability Using Large-Eddy Simulations, Journal of engineering for gas turbines and power, 138 (2016).

[12] S. Pischinger, T. Korfer, Heading towards Higher Diesel Powertrain Efficiencies - Tailored Electrificatio and Hybridization, SIA Powertrain Conference, 2016.

[13] E. Zervas, Correlations between cycle-to-cycle variations and combustion parameters of a spark ignition engine, Applied Thermal Engineering, 24 (2004) 2073-2081.

[14] B. Huang, E. Hu, Z. Huang, J. Zheng, B. Liu, D. Jiang, Cycle-by-cycle variations in a spark ignition engine fueled with natural gas–hydrogen blends combined with EGR, International Journal of Hydrogen Energy, 34 (2009) 8405-8414.

[15] Y. Chen, Y. Wang, R. Raine, Correlation between cycle-by-cycle variation, burning rate, and knock: A statistical study from PFI and DISI engines, Fuel, 206 (2017) 210-218.

[16] D.C. Haworth, Large-eddy simulation of in-cylinder flows, Oil & Gas Science and Technology, 54 (1999) 175-185.

[17] L. Thobois, G. Rymer, T. Souleres, T. Poinsot, Large-eddy simulation in IC engine geometries, SAE Transactions, (2004) 1192-1209.

[18] B. Enaux, V. Granet, O. Vermorel, C. Lacour, L. Thobois, V. Dugué, T. Poinsot, Large Eddy Simulation of a Motored Single-Cylinder Piston Engine: Numerical Strategies and Validation, Flow, Turbulence and Combustion, 86 (2010) 153-177.

[19] C. Angelberger, X. Yang, T.-W. Kuo, Correlation of CCV Between In-Cylinder Swirl Ratio and Polar Velocity Profile in Valve Seat Region Using LES Under Motored Engine Condition, Oil & Gas Sciences and Technology – Revue d'IFP Energies nouvelles, 72 (2017).

[20] C. Chen, M.M. Ameen, H. Wei, C. Iyer, F. Ting, B. Vanderwege, S. Som, LES Analysis on Cycle-to-Cycle Variation of Combustion Process in a DISI Engine, in: SAE Technical Paper Series, 2019.

[21] A. d'Adamo, S. Breda, S. Fontanesi, G. Cantore, LES Modelling of Spark-Ignition Cycle-to-Cycle Variability on a Highly Downsized DISI Engine, SAE International Journal of Engines, 8 (2015) 2029-2041.

[22] S. Fontanesi, S. Paltrinieri, G. Cantore, LES Analysis of Cyclic Variability in a GDI Engine, in: SAE Technical Paper Series, 2014.

[23] V. Granet, O. Vermorel, C. Lacour, B. Enaux, V. Dugué, T. Poinsot, Large-Eddy Simulation and experimental study of cycle-to-cycle variations of stable and unstable operating points in a spark ignition engine, Combustion and flame, 159 (2012) 1562-1575.

[24] Y. Yu, D. Splitter, S. Kim, Predicting Cycle-to-cycle Variations in a Spark-ignition Engine using Multi-cycle Large Eddy Simulation, in, Oak Ridge National Lab.(ORNL), Oak Ridge, TN (United States), 2019.

[25] M. Ghaderi Masouleh, K. Keskinen, O. Kaario, H. Kahila, S. Karimkashi, V. Vuorinen, Modeling cycle-to-cycle variations in spark ignited combustion engines by scale-resolving simulations for different engine speeds, Applied Energy, 250 (2019) 801-820.

[26] S. Fontanesi, A. d'Adamo, C.J. Rutland, Large-Eddy simulation analysis of spark configuration effect on cycle-to-cycle variability of combustion and knock, International Journal of Engine Research, 16 (2015) 403-418.

[27] A. Robert, K. Truffin, N. Iafrate, S. Jay, O. Colin, C. Angelberger, Large-eddy simulation analysis of knock in a direct injection spark ignition engine, International Journal of Engine Research, 20 (2018) 765-776.

[28] C. Chen, P. Pal, M. Ameen, D. Feng, H. Wei, Large-eddy simulation study on cycle-to-cycle variation of knocking combustion in a spark-ignition engine, Applied Energy, 261 (2020).

[29] M.M. Ameen, M. Mirzaeian, F. Millo, S. Som, Numerical Prediction of Cyclic Variability in a Spark Ignition Engine Using a Parallel Large Eddy Simulation Approach, Journal of Energy Resources Technology, 140 (2018).

[30] S. Som, R. Scarcelli, J. Kodavasal, E. Pomraning, S. Wijeyakulasuriya, D.M. Probst, Predicting Cycle-to-Cycle Variation With Concurrent Cycles in a Gasoline Direct Injected Engine With Large Eddy Simulations, Journal of Energy Resources Technology, 142 (2020).

[31] O. Reynolds, Iv. on the dynamical theory of incompressible viscous fluids and the determination of the criterion, Philosophical transactions of the royal society of london.(a.), (1895) 123-164.

[32] J. Smagorinsky, General circulation experiments with the primitive equations: I. The basic experiment, Monthly weather review, 91 (1963) 99-164.

[33] J.W. Deardorff, A numerical study of three-dimensional turbulent channel flow at large Reynolds numbers, Journal of Fluid Mechanics, 41 (2006) 453-480.

[34] D. Lilly, On the application of the eddy viscosity concept in the inertial sub-range of turbulence. 1966, NCAR Manuscript.

[35] P.J. Mason, N.S. Callen, On the magnitude of the subgrid-scale eddy coefficient in large-eddy simulations of turbulent channel flow, Journal of Fluid Mechanics, 162 (2006).

[36] U. Piomelli, P. Moin, J.H. Ferziger, Model consistency in large eddy simulation of turbulent channel flows, Physics of Fluids, 31 (1988).

[37] A. Yoshizawa, Statistical theory for compressible turbulent shear flows, with the application to subgrid modeling, The Physics of fluids, 29 (1986) 2152-2164.

[38] M. Germano, U. Piomelli, P. Moin, W.H. Cabot, A dynamic subgrid-scale eddy viscosity model, Physics of Fluids A: Fluid Dynamics, 3 (1991) 1760-1765.

[39] A. Yoshizawa, A statistically-derived subgrid model for the large-eddy simulation of turbulence, Physics of Fluids, 25 (1982).

[40] A. Yoshizawa, K. Horiuti, A statistically-derived subgrid-scale kinetic energy model for the large-eddy simulation of turbulent flows, Journal of the Physical Society of Japan, 54 (1985) 2834-2839.

[41] R.H. Kraichnan, The structure of isotropic turbulence at very high Reynolds numbers, Journal of Fluid Mechanics, 5 (1959) 497-543.

[42] V.C. Wong, A proposed statistical-dynamic closure method for the linear or nonlinear subgrid-scale stresses, Physics of Fluids A: Fluid Dynamics, 4 (1992) 1080-1082.

[43] S. Ghosal, T.S. Lund, P. Moin, K. Akselvoll, A dynamic localization model for large-eddy simulation of turbulent flows, Journal of Fluid Mechanics, 286 (2006) 229-255.

[44] E. Pomraning, Development of large eddy simulation turbulence models, Uni-versity of Wisconsin-Madison, 2000, in, Ph. D. thesis.

[45] N. Peters, Turbulent combustion, in, IOP Publishing, 2001.

[46] D. Spalding, Mixing and chemical reaction in steady confined turbulent flames, in: Symposium (International) on Combustion, Vol. 13, Elsevier, 1971, pp. 649-657.

[47] B.F. Magnussen, B.H. Hjertager, On mathematical modeling of turbulent combustion with special emphasis on soot formation and combustion, in: Symposium (international) on Combustion, Vol. 16, Elsevier, 1977, pp. 719-729.

[48] D. Veynante, L. Vervisch, Turbulent combustion modeling, Progress in energy and combustion science, 28 (2002) 193-266.

[49] S. Pope, Computations of turbulent combustion: progress and challenges, in: Proc. Combust. Inst, Vol. 23, 1990, pp. 591-612.

[50] C. Dopazo, Recent developments in pdf methods, Turbulent reacting flows, (1994) 375-474.

[51] T. Hulek, R.P. Lindstedt, Joint Scalar-velocity pdf Modelling of Finite Rate Chemistry in a Scalar Mixing Layer, Combustion Science and Technology, 136 (1998) 303-331.

[52] S.B. Pope, A Monte Carlo Method for the PDF Equations of Turbulent Reactive Flow, Combustion Science and Technology, 25 (2008) 159-174.

[53] S.B. Pope, PDF methods for turbulent reactive flows, Progress in energy and combustion science, 11 (1985) 119-192.

[54] A.R. Kerstein, A Linear- Eddy Model of Turbulent Scalar Transport and Mixing, Combustion Science and Technology, 60 (1988) 391-421.

[55] A.R. Kerstein, Linear-eddy modelling of turbulent transport. Part 3. Mixing and differential molecular diffusion in round jets, Journal of Fluid Mechanics, 216 (2006) 411-435.

[56] A.R. Kerstein, Linear-eddy modelling of turbulent transport. Part 6. Microstructure of diffusive scalar mixing fields, Journal of Fluid Mechanics, 231 (2006) 361-394.

[57] A.R. Kerstein, Fractal Dimension of Turbulent Premixed Flames, Combustion Science and Technology, 60 (1988) 441-445.

[58] A.R. Kerstein, Linear-Eddy Modeling of Turbulent Transport. Part 4. Structure of Diffusion Flames, Combustion Science and Technology, 81 (1992) 75-96.

[59] P.A. McMurthy, S. Menon, A.R. Kerstein, A linear eddy sub-grid model for turbulent reacting flows: Application to hydrogen-air combustion, in: Symposium (International) on Combustion, Vol. 24, Elsevier, 1992, pp. 271-278.

[60] S. Menon, A.R. Kerstein, Stochastic simulation of the structure and propagation rate of turbulent premixed flames, in: Symposium (International) on Combustion, Vol. 24, Elsevier, 1992, pp. 443-450.

[61] K. Bray, J.B. Moss, A unified statistical model of the premixed turbulent flame, Acta Astronautica, 4 (1977) 291-319.

[62] K.C. BRAY, Recent developments in BML Model of premixed turbulent combustion, Turbulent reacting flows, (1994).

[63] P.A. Libby, F.A. Williams, Turbulent reacting flows, Academic press, 1994.

[64] J. Duclos, D. Veynante, T. Poinsot, A comparison of flamelet models for premixed turbulent combustion, Combustion and flame, 95 (1993) 101-117.

[65] F.E. Marble, J.E. Broadwell, The coherent flame model for turbulent chemical reactions, in, PURDUE UNIV LAFAYETTE IN PROJECT SQUIDHEADQUARTERS, 1977.

[66] H. Pitsch, A G-equation formulation for large-eddy simulation of premixed turbulent combustion, Annual Research Briefs, (2002) 3-14.

[67] H. Pitsch, A consistent level set formulation for large-eddy simulation of premixed turbulent combustion, Combustion and flame, 143 (2005) 587-598.

[68] S.B. Pope, Turbulent flows, in, IOP Publishing, 2001.

[69] Z. Warsi, Conservation form of the Navier-Stokes equations in general nonsteady coordinates, AIAA Journal, 19 (1981) 240-242.

[70] A. Leonard, Energy cascade in large-eddy simulations of turbulent fluid flows, Adv. Geophys. A, 18 (1974) 237-248.

[71] U. Piomelli, W.H. Cabot, P. Moin, S. Lee, Subgrid-scale backscatter in turbulent and transitional flows, Physics of Fluids A: Fluid Dynamics, 3 (1991) 1766-1771.

[72] J.W. Deardorff, A numerical study of three-dimensional turbulent channel flow at large Reynolds numbers, Journal of Fluid Mechanics, 41 (1970) 453-480.

[73] I. Ko, A. D'Adamo, S. Fontanesi, K. Min, Study of LES Quality Criteria in a Motored Internal Combustion Engine, in: SAE Technical Paper Series, 2017.

[74] I. Ko, K. Min, F. Rulli, A. D'Adamo, F. Berni, S. Fontanesi, Investigation of Sub-Grid Model Effect on the Accuracy of In-Cylinder LES of the TCC Engine under Motored Conditions, in: SAE Technical Paper Series, 2017.

[75] P. Schiffmann, S. Gupta, D. Reuss, V. Sick, X. Yang, T.W. Kuo, TCC-III Engine Benchmark for Large-Eddy Simulation of IC Engine Flows, Oil & Gas Science and Technology – Revue d'IFP Energies nouvelles, 71 (2015).

[76] P. Abraham, D. Reuss, V. Sick, High-Speed Particle Image Velocimetry Study of In-Cylinder Flows with Improved Dynamic Range, in, SAE International, 2013.

[77] F. di Mare, R. Knappstein, M. Baumann, Application of LES-quality criteria to internal combustion engine flows, Computers & Fluids, 89 (2014) 200-213.

[78] S.B. Pope, Ten questions concerning the large-eddy simulation of turbulent flows, New Journal of Physics, 6 (2004) 35-35.

[79] W.L. Nelson, Petroleum refinery engineering, McGraw-Hill, 2018.

[80] S. Yang, R.D. Reitz, C.O. Iyer, J. Yi, Improvements to combustion models for modeling spark-ignition engines using the G-equation and detailed chemical kinetics, SAE International Journal of Fuels and Lubricants, 1 (2009) 1009-1025.

[81] S. Yang, E. Pomraning, M. Jia, Simulations of gasoline engine combustion and emissions using a chemical-kinetics-based turbulent premixed combustion modeling approach, Proceedings of the Institution of Mechanical Engineers, Part D: Journal of Automobile Engineering, 231 (2017) 743-765.

[82] H.J. Curran, P. Gaffuri, W.J. Pitz, C.K. Westbrook, A comprehensive modeling study of iso-octane oxidation, Combustion and flame, 129 (2002) 253-280.

[83] C. Westbrook, H. Curran, W. Pitz, J. Griffiths, C. Mohamed, S. Wo, The effects of pressure, temperature, and concentration on the reactivity of alkanes: Experiments and modeling in a rapid compression machine, in: Symposium (international) on combustion, Vol. 27, Elsevier, 1998, pp. 371-378.

[84] M. Mehl, W. Pitz, M. Sjöberg, J.E. Dec, Detailed kinetic modeling of low-temperature heat release for PRF fuels in an HCCI engine, in, SAE Technical Paper, 2009.

[85] C.V. Naik, W.J. Pitz, C.K. Westbrook, M. Sjöberg, J.E. Dec, J. Orme, H.J. Curran, J.M. Simmie, Detailed chemical kinetic modeling of surrogate fuels for gasoline and application to an HCCI engine, SAE Transactions, (2005) 1381-1387.

[86] J.C.G. Andrae, Comprehensive chemical kinetic modeling of toluene reference fuels oxidation, Fuel, 107 (2013) 740-748.

[87] K. Lee, Y. Kim, K. Min, Development of a reduced chemical kinetic mechanism for a gasoline surrogate for gasoline HCCI combustion, Combustion Theory and Modelling, 15 (2010) 107-124.

[88] J.C.G. Andrae, R.A. Head, HCCI experiments with gasoline surrogate fuels modeled by a semidetailed chemical kinetic model, Combustion and flame, 156 (2009) 842-851.

[89] J.C.G. Andrae, A kinetic modeling study of self-ignition of low alkylbenzenes at engine-relevant conditions, Fuel Processing Technology, 92 (2011) 2030-2040.

[90] H.J. Curran, W. Pitz, C. Westbrook, G. Callahan, F. Dryer, Oxidation of automotive primary reference fuels at elevated pressures, in: Symposium (International) on Combustion, Vol. 27, Elsevier, 1998, pp. 379-387.

[91] M. Mehl, J.Y. Chen, W.J. Pitz, S.M. Sarathy, C.K. Westbrook, An Approach for Formulating Surrogates for Gasoline with Application toward a Reduced Surrogate Mechanism for CFD Engine Modeling, Energy & Fuels, 25 (2011) 5215-5223.

[92] Ö.L. Gülder, Correlations of laminar combustion data for alternative SI engine fuels, in, SAE Technical Paper, 1984.

[93] M. Metghalchi, J.C. Keck, Burning velocities of mixtures of air with methanol, isooctane, and indolene at high pressure and temperature, Combustion and flame, 48 (1982) 191-210.

[94] S. Yang, R.D. Reitz, Integration of a continuous multi-component fuel evaporation model with an improved G-equation combustion and detailed chemical kinetics model with application to GDI engines, in, SAE Technical Paper, 2009.

[95] Z. Zhao, J.P. Conley, A. Kazakov, F.L. Dryer, Burning velocities of real gasoline fuel at 353 K and 500 K, SAE Transactions, (2003) 2624-2629.

[96] S. Jerzembeck, N. Peters, P. Pepiotdesjardins, H. Pitsch, Laminar burning velocities at high pressure for primary reference fuels and gasoline:

Experimental and numerical investigation, Combustion and flame, 156 (2009) 292-301.

[97] O. Mannaa, M.S. Mansour, W.L. Roberts, S.H. Chung, Laminar burning velocities at elevated pressures for gasoline and gasoline surrogates associated with RON, Combustion and flame, 162 (2015) 2311-2321.

[98] L. Sileghem, V.A. Alekseev, J. Vancoillie, K.M. Van Geem, E.J.K. Nilsson, S. Verhelst, A.A. Konnov, Laminar burning velocity of gasoline and the gasoline surrogate components iso-octane, n-heptane and toluene, Fuel, 112 (2013) 355-365.

[99] Y.H. Liao, W.L. Roberts, Laminar Flame Speeds of Gasoline Surrogates Measured with the Flat Flame Method, Energy & Fuels, (2016).

[100] J. Kim, K. Min, Modeling laminar burning velocity of gasoline using an energy fraction-based mixing rule approach, Proceedings of the Institution of Mechanical Engineers, Part D: Journal of Automobile Engineering, 233 (2018) 1245-1258.

[101] F. Williams, The mathematics of combustion, SIAM, Philadelphia, 97 (1985).

[102] R. Maly, M. Vogel, Initiation and propagation of flame fronts in lean CH4-air mixtures by the three modes of the ignition spark, in: Symposium (international) on combustion, Vol. 17, Elsevier, 1979, pp. 821-831.

[103] L. Fan, G. Li, Z. Han, R.D. Reitz, Modeling Fuel Preparation and Stratified Combustion in a Gasoline Direct Injection Engine, SAE Transactions, 108 (1999) 105-119.

[104] J. Duclos, O. Colin, Arc and Kernel Tracking Ignition Model for 3D Spark Ignition Engine Calculations, 5th Int, in: Symp. on Diagnostics and Modeling of Combustion in Internal Combustion Engines, COMODIA, 2001.

[105] R.N. Dahms, M.C. Drake, T.D. Fansler, T.W. Kuo, N. Peters, Understanding ignition processes in spray-guided gasoline engines using high-speed imaging and the extended spark-ignition model SparkCIMM. Part A: Spark channel processes and the turbulent flame front propagation, Combustion and flame, 158 (2011) 2229-2244.

[106] R.N. Dahms, M.C. Drake, T.D. Fansler, T.W. Kuo, N. Peters, Understanding ignition processes in spray-guided gasoline engines using high-speed imaging and the extended spark-ignition model SparkCIMM, Combustion and flame, 158 (2011) 2245-2260.

[107] O. Colin, K. Truffin, A spark ignition model for large eddy simulation based on an FSD transport equation (ISSIM-LES), Proceedings of the Combustion Institute, 33 (2011) 3097-3104.

[108] J. Song, M. Sunwoo, A Modeling and Experimental Study of Initial Flame Kernel Development and Propagation in SI Engines, in, SAE International, 2000.

[109] S. Refael, E. Sher, A theoretical study of the ignition of a reactive medium by means of an electrical discharge, Combustion and flame, 59 (1985) 17-30.

[110] T. Lucchini, L. Cornolti, G. Montenegro, G. D'Errico, M. Fiocco, A. Teraji, T. Shiraishi, A Comprehensive Model to Predict the Initial Stage of Combustion in SI Engines, in: SAE Technical Paper Series, 2013.

[111] S. Falfari, G.M. Bianchi, Development of an Ignition Model for S.I. Engines Simulation, in, SAE International, 2007.

[112] J.D. Cobine, Gaseous conductors: theory and engineering applications, (1958).

[113] R. Herweg, R.R. Maly, A Fundamental Model for Flame Kernel Formation in S. I. Engines, SAE Transactions, 101 (1992) 1947-1976.

[114] A. D'Angola, G. Colonna, C. Gorse, M. Capitelli, Thermodynamic and transport properties in equilibrium air plasmas in a wide pressure and temperature range, The European Physical Journal D, 46 (2007) 129-150.

[115] J. Kim, R.W. Anderson, Spark Anemometry of Bulk Gas Velocity at the Plug Gap of a Firing Engine, SAE Transactions, 104 (1995) 2256-2266.

[116] S. Sayama, M. Kinoshita, Y. Mandokoro, T. Fuyuto, Spark ignition and early flame development of lean mixtures under high-velocity flow conditions: An experimental study, International Journal of Engine Research, 20 (2018) 236-246.

[117] J. Ewald, N. Peters, On unsteady premixed turbulent burning velocity prediction in internal combustion engines, Proceedings of the Combustion Institute, 31 (2007) 3051-3058.

[118] 조석원, Study on the Effect of Cylinder Wall Temperatures on Knock Characteristics in Spark-Ignited Engine, in: 가솔린 엔진에서 실린더 벽면 온도가 노킹 현상에 미치는 영향에 관한 연구, 서울 : 서울대학교 대학원, 서울, 2018.

국 문 초 록

현재 전 세계 대기오염 문제가 중요한 이슈로 떠오르고 많은 나라들이 이 문제를 해결하기 위해 노력하고 있다. 내연기관 차량의 배기가스 배출량을 줄이기 위해 전 세계적으로 배출가스 규제가 강화되었다. 2014년부터 미국은 Tier 3 배기배출물 규정을 유럽연합은 EURO 6 규정을 채택하고 있다. 현재 연비 규제인 CO2도 매년 강력하게 강화되고 있다. 강화된 CO2 규정을 충족시키기 위해, 고효율 엔진의 개발은 각 차량 제조사에 의해 활발하게 이루어지고 있다. 고효율 엔진 개발에서 핵심은 열효율 증가이다. 열효율을 높이기 위해 많은 기술이 개발되어 양산 엔진에 적용되고 있다. 그러나 현재 엔진 개발에 가장 큰 장애물로 연소 사이클 간 편차가 있다. 따라서 사이클 편차에 대한 연구도 활발히 진행되고 있다. 사이클 편차에 영향을 미치는 원인은 다양하고 복잡하기 때문에, 실험 연구를 통해 사이클 편차의 근본 원인에 대한 상세한 연구를 실시하기 어렵다. 따라서 대안으로 3D 시뮬레이션을 활용한 연구가 활발히 진행되고 있다.

본 연구에서는, 연소의 사이클 편차 현상을 Large-Eddy Simulation (LES) 유동 해석 방법을 이용하여 재현하고 사이클 편차의 원인에 대한 연구를 진행한다. 현재 LES를 이용한 엔진 시뮬레이션은 아직까지 미숙한 단계이다. 따라서 정확한 시뮬레이션을 위해 각 물리적 현상을 구현할 수 있는 모델을 구현해야 한다. 먼저, 3개의 sub-grid scale (SGS) 난류 모델을 단기통 광학 엔진의 (TCC-III) particle image velocimetry (PIV) 측정 결과로 평가하였다. PIV 데이터와 비교

한 유동장 및 예측된 SGS 난류속도에 대한 분석을 바탕으로 본 연구에서는 dynamic structure model (DSM)이 채택되었다.

둘째로, G-equation 모델을 연소 모델로 선택하였다. G-equation 모델은 Pitsch[1]에 의해 LES 적용 가능 하도록 개발되었다. 이 모델은 corrugated flamelets regime과 thin reaction flamelets regime에서 사용될 수 있다. 연소 속도 모델은 두 연소 환경에 포함된 난류 연소를 모사하기 위해 상당히 복잡하다. 따라서 본 연구에서는 RANS를 이용하여 대상 엔진 작동 조건의 연소 환경을 찾아 내었고, 연소 환경은 corrugated flamelets regime에 속한 것을 확인 하였다. 따라서 기존의 G-equation 연소 모델을 corrugated flamelets regime에 맞도록 변경 하였다.

셋째로, LES의 특성을 반영한 점화 모델이 개발되었다. Lagrangian 개념을 이용하여 점화 채널을 구현하고, 2차 전기 회로 모델을 이용하여 점화 에너지, 리스트라이크, 점화 시간 종료 등을 예측하였다. 본 연구에서 개발된 점화 모델의 주요 특징 중 하나는 아크 페이즈 중 열 팽창 현상을 구현을 위해 간단한 경험 함수를 이용한다는 것이다. 아크 페이즈 후, 점화 해널은 화학 반응에 성장하고 화염 전파가 진행된다. 난류 화염 두께는 층류 화염 전파와 난류 화염 전파 사이의 천이 상태를 예측하기 위해 도입되었다. 마지막으로 점화 채널이 충분히 커지면 G-equation 의해 3D 계산 영역에서 화염 전파가 구현된다.

마지막으로 30개의 LES 사이클을 수행하여 연소의 사이클 편차 원인을 분석하고 실험 데이터를 이용하여 시뮬레이션의 정확도를 검증하였다. 연소의 사이클 편차의 원인은 주로 작은 규모의 난류 유동

과 큰 규모의 난류 유동에서 나온다. 난류 모델로 구현된 작은 규모의 난류 유동과 큰 규모의 난류 유동에 속한 텀블 값을 같이 분석 하였다. 작은 규모의 난류 유동은 텀블 값과 관계가 있다는 사실을 파악하였다. 큰 규모 난류 유동 측면에서는 국부적인 유동의 소용돌이가 화염 전파에 미치는 영향을 유동장을 상세히 분석하여 확인되었다. 특히 2차 텀블면에서 벽면 유동에 의해 생성되는 소용돌이가 연소의 사이클 편차에 미치는 중요한 요인임을 밝혀 내었다. 벽면 유동에 의한 소용돌이 형성을 강화하기 위해 새로운 피스톤 현상을 설계 하였다. 새로운 피스톤 형상의 결과는 베이스 피스톤보다 연소의 CCV가 줄어들었다. 본 연구는 향후 엔진 개발을 위해 연소 CCV의 원인을 조사하는 방법과 연소 CCV를 줄이는 방법에 대한 방법론을 제시한다.

주요어: 전기점화 엔진, LES, 전산유체역학, 사이클 편차, 점화모델, 난류모델

학 번: 2013-20641